SEMICONDUCTORS VOLUME 32, NUMBER 5 MAY 1998

## REVIEW

# Nanometer-size atomic clusters in semiconductors—a new approach to tailoring material properties

M. G. Mil’vidskiĭ and V. V. Chaldyshev

*State Scientific Research and Planning Institute for the Rare-Earth Industries (Giredmet), 109017 Moscow, Russia*

(Submitted November 12, 1997; accepted for publication November 14, 1997)
Fiz. Tekh. Poluprovodn. **32**, 513–522 (May 1998)

In this paper the physical mechanisms and fundamental methods of obtaining nanometer-size atomic clusters in semiconductors are discussed, along with the possibility of controlling the properties of these clusters and those of the resulting cluster-containing materials. A number of electronic properties of semiconductors containing nanometer-sized clusters are considered, along with potential uses of these materials in electronics. © *1998 American Institute of Physics.* [S1063-7826(98)00105-7]

## 1. INTRODUCTION

The traditional approach to controlling the properties of semiconductor materials is to dope them with impurities, which creates well-defined energy levels in the band gap. In pursuit of this goal, several problems are encountered: correct choice of a doping impurity with the necessary properties, optimizing the amount of this dopant and method of doping, and obtaining crystallographically perfect, high-quality single crystals or epitaxial films which do not contain defects or unwanted impurities that could significantly affect the properties of the doped material. The successful solution to these problems in many important areas of applications has led to the rapid progress of semiconductor electronics. However, in several cases this traditional approach comes up against fundamental limitations arising from the absence in nature of impurities with suitable properties, low solubility limits of atoms of many impurities in the semiconductor crystal lattice, high concentrations of electrically active intrinsic defects in the lattice of the doped material, etc. For this reason, a new method of controlling the properties of semiconductors has been actively pursued in recent years. This method is based on creation of nanometer-size clusters in the semiconducting matrix made up of impurity atoms, atoms of the intrinsic semiconductor components, and intrinsic point defects of the crystal lattice.

In this article we will discuss the physical mechanisms and basic methods of obtaining and controlling properties of semiconductors that contain nanometer-sized clusters, as well as a number of electronic properties of these semiconductors.

## 2. GENERATION OF CLUSTERS

To begin with, we should formulate the concept of an atomic cluster in the context of this paper. By an atomic cluster we mean an atomic-scale aggregate (perhaps with the participation of intrinsic point defects of the crystal lattice) which alters the energy state of the components that make it up and the way they affect the fundamental properties of the semiconductor matrix, while leaving the phase state of the basic material unaffected. In contrast with clusters that form in gaseous or liquid phases, in our case the cluster forms in the crystal lattice of a semiconductor. This crystalline matrix is found to have a considerable influence on all the stages of cluster formation, and also on the properties of the final product.

### 2.1. Reasons for cluster formation

In general, the motive force that creates a cluster arises from the system’s attempt to reach a state with minimum free energy. However, in real systems the equilibrium state of a multicomponent system is seldom reached, due to energetic or kinetic limitations. Hence, in the majority of cases we are dealing with metastable structures, which nevertheless can be quite stable and can affect the properties of the semiconductor material to a considerable degree.

In general, when a cluster forms in the crystal lattice of a semiconductor, we can write the change in the free energy of the system in the form

$$\Delta F = -\Delta F_v + \Delta F_s + \Delta F_{el}, \qquad (1)$$

where $\Delta F_v$ is the change in free energy resulting from the system’s transition to a more favorable energy state. For example, when a solid solution decomposes, the motive force arises from supersaturation. $\Delta F_s$ is the change in free energy due to creation of the cluster surface, and $\Delta E_{el}$ is the change in free energy due to elastic deformation of the cluster and the surrounding material.

The surface contribution to the change in free energy of the system is most important for clusters of small size, while the influence of elastic deformation increases with increasing cluster size. Rigorous quantitative estimates of these quantities are difficult to obtain, since they require construction of an exact model of a cluster. Therefore, concepts like the ''crystal lattice'' or ''surface'' of a cluster are often quite nominal in character.

It is possible to obtain quantitative results in the simplest cases. For example, when clusters of intrinsic interstitial atoms ($Si_i$) form in a silicon crystal lattice due to supersaturation of the corresponding solid solution, it is reasonable to assume that the excess $Si_i$ atoms occupy interstitial sites that are fairly close together and couple to one another like regular atoms of the lattice. Because interstitial sites in the silicon lattice form a diamond structure that is analogous to regular occupation of sites by atoms, the cluster that forms can be regarded as a small silicon ''crystal'' placed in the crystal lattice of the primary crystal.

Because of the rather large distances between interstitial sites of the silicon crystal lattice, the contribution of elastic strain energy to the change in the free energy of the system can be ignored in this case. The free energy of a crystal with a cluster (compared to a perfect crystal with the same number of atoms) increases only because of the unsaturated (dangling) bonds of the peripheral cluster atoms, which are only partially bonded to the cluster because a normal bond requires four neighbors. The change in free energy caused by the creation of a cluster with $n$ interstitial atoms is

$$\Delta F(n) = -f_v n + f_s m, \tag{2}$$

where $f_v = kT\log(C_i/C_i^e)$ is the change in free energy due to supersaturation (the motive force for cluster formation), $m$ is the number of dangling bonds, and $f_s$ is the excess free energy per dangling bond, a quantity that is amenable to fairly rigorous quantitative estimates We give this example in order to demonstrate the fundamental approaches to the problem of cluster formation. In the next section we will consider the possible reasons for formation of atomic clusters in semiconductors in more detail.

### 2.2. Stable complexes of impurities and intrinsic point defects

Elastic, Coulomb, or chemical interactions with the participation of atoms of the host material, dopant or residual impurity atoms, or intrinsic point structural defects, can lead to the formation of various types of complexes in a semiconductor. This type of cluster formation has been investigated quite deeply for germanium, silicon, gallium arsenide, and a number of other semiconductors (see, for example, Refs. 1 and 2). Therefore, in this article we will not pause to discuss it in detail. We note only that the stability of many of the complexes that form as a result of these interactions is quite high (including stability against heating to relatively high temperatures) and that such complexes can strongly affect the properties of the semiconductor by acting as efficient centers for radiative and nonradiative recombination. To a considerable degree they also determine the compensation, concentration, nature of scattering of charge carriers, photosensitivity, and a number of other important material characteristics.

There are many ways to control the processes that lead to complex formation. Some of these are: the various types of irradiation and thermal processing (including combinations of these) such as laser and rapid thermal annealing, plasma-chemical etching, compound doping, various methods of gettering fast-diffusing impurities and defects, and ion implantation. Good results are obtained when nontraditional methods are used to modify the state of an ensemble of point structural defects in a crystal, such as doping with isovalent impurities[3] and rare-earth element impurities,[4] or chemical-thermal processing (e.g., oxidation and nitridization of silicon). Also worth noting is the technique of using atomic hydrogen to passivate electrically active and recombination-active centers in crystals.

### 2.3. Decomposition of supersaturated solid solutions

If doping or residual impurities are present at the surface of a single crystal or epitaxial film in concentrations that exceed their solubility in the semiconductor over a sufficiently broad temperature range, the corresponding supersaturated solid solutions form and then proceed to decompose. This decomposition can take place either during the growth process itself, as the single-crystal or epitaxial structure cools down from the crystallization temperature, or in the course of subsequent thermal processing or other kinds of external manipulation of the material. Supersaturated solid solutions can consist not only of impurities but also structural point defects (vacancies or interstitial atoms), as well as excess atoms of the semiconductor components, whose solubility in the semiconductor matrix exhibits a steep temperature dependence.

The formation of supersaturated impurity solid solutions is characteristic of strongly doped single crystals and epitaxial structures in a wide range of semiconducting materials. A typical example of the formation of supersaturated solid solutions of residual impurities is oxygen in silicon single crystals grown by the Czochralski method. A multitude of investigations have demonstrated that in the majority of cases of practical importance, energy and kinetic limitations prevent the decomposition of supersaturated impurity semiconductor solutions from reaching an equilibrium state for the corresponding systems. As a rule, the decomposition process is ''frozen'' at the stage where metastable impurity-containing precipitates form (atomic clusters of a characteristic composition). The stability of these precipitates is fairly high, and they are found to have a strong effect on the properties of the semiconductor. Typical manifestations of these effects in strongly doped single crystals of Ge, Si, GaAs, and other semiconductors[1,5] are ''impurity polytropy,'' characteristic changes in the degree of compensation, concentration, and mobility of charge carriers, luminescence, and other properties connected with it, and the formation of oxygen-containing thermal donors in silicon single crystals.[6]

When solid solutions that are supersaturated with structural point defects decompose, the products are vacancy accumulations, clusters of interstitial atoms, and also ''insertion''-type clusters. An example of the last is clusters of arsenic in gallium arsenide grown by MBE at low temperature,[7] which allows the capture of atoms of excess arsenic at concentrations up to 2 atomic %. Depending on

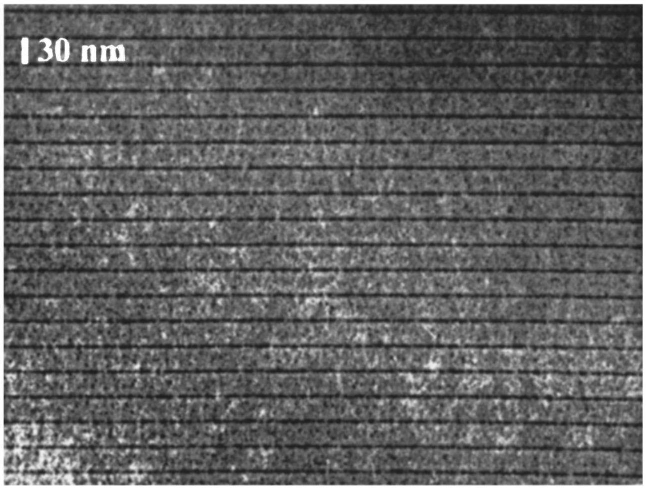

FIG. 1. Electron-microscope images of a superlattice of arsenic clusters in GaAs created by $\delta$-doping with indium during molecular-beam epitaxy at 200° and a subsequent anneal at 500°. The thickness of the GaAs layers between the two-dimensional layers of As clusters is 30 nm.

their dimensions, such clusters have a characteristic crystal structure that differs from the structure of elementary arsenic and from the structure of the surrounding GaAs matrix.[8]

The decomposition of supersaturated solid solutions, like cluster formation, can be controlled and monitored. The basic control methods in this case are:

1) Choice of optimal thermal conditions for growth. Here of paramount importance is to correctly choose the temperature and crystallization rate, the temperature gradients at the phase boundary, and post-crystallization cooling regime of the single crystals or epitaxial structures.

2) The use of multistep thermal processing of the single crystals or epitaxial structures.

3) Local control of cluster seeding. An example of this is the $\delta$-doping of GaAs layers grown by low-temperature MBE with Si donor or isovalent In impurity atoms (Fig. 1). In these $\delta$-doped epitaxial films, under certain conditions of doping and thermal processing it is possible to obtain two-dimensional layers of uniformly distributed nanometer-sized arsenic clusters in a GaAs matrix.[9] For the case of silicon doping, this effect is a result of the Coulomb interaction between the clusters and Si donor atoms located at sites of the gallium sublattice. When isovalent In impurity atoms are used, the controlled seed formation is due to local strain in the crystal lattice near the $\delta$-layers of indium. In this case, regions of the GaAs host with no clusters are present near the two-dimensional layers of clusters. Under certain conditions of growth, doping, and thermal processing of the material, these ''depletion regions'' near the two-dimensional layers of clusters will overlap, and it is possible to achieve almost complete ordering of the distribution of arsenic clusters in the growth direction. Note that without this controlled precipitation, which is determined by rigorous conditions for doping and thermal processing, the distribution of As clusters throughout the bulk of the GaAs film is for the most part disordered and well described by the Lifshitz–Slezov theory.[10]

4) The use of various external perturbations (chemical-thermal and plasma-thermal processing, irradiation, etc.) to regulate the state of an ensemble of structural point defects in the crystal host. This method requires some further explanation. The fact is that atomic clusters are created and grow in size in the early stages of the decomposition. This is accompanied by an increase in the elastic strain energy of the resulting complexes, and system reacts to this perturbation either by emitting clusters of intrinsic interstitial atoms into the crystal lattice or by generating or absorbing vacancies (creation of impurity-vacancy complexes). For this reason, any change in the state of the structural point defect ensemble in the system (injection of structural point defects from outside or creation of sinks for structural point defects) will strongly affect the rate of cluster formation processes associated with the decomposition of the supersaturated solid solution (see, for example, Ref. 10).

### 2.4. Ordering and disordering of semiconductor solid solutions

Most of the physical processes that occur in multicomponent semiconductor solid solutions are described in terms of statistical distributions of the components over sites of the crystal lattice. However, the semiconductor materials that make up these solid solutions have different lattice parameters. This causes elastic distortions to appear in the crystal lattice of the solid solution, and can lead to phase transitions that lower the elastic energy of the system, accompanied by the appearance of short- or long-range order (or superstructures), and also to clustering. A typical manifestation of this kind of energy instability in a system is spinodal decomposition.

When the distribution of components of the solid solution deviates from statistical (random), its properties are strongly affected (e.g., changes in the width of the band gap, charge carrier scattering, luminescence spectrum and phonon spectrum, plasticity, etc.). Depending on the growth conditions or subsequent thermal processing, the same solid solution can exhibit both ordering effects and spinodal decomposition (see, for example, Ref. 12).

As before, the effective methods for controlling these processes are: choice of optimal thermal conditions for growth and subsequent thermal processing regimes of single crystals or epitaxial structures, and regulation of the state of the structural point defect ensemble in the crystal lattice of the resulting solid solution. In this connection, the crystallographic orientation of the growth surface and its atomic structure play a nontrivial role in the formation of quantum-well structures (including quantum dots) in epitaxial compositions.

It is noteworthy that the processes of self-organization, ordering and disordering involve substantial mass transport. This hinders and often prevents them from occurring in the bulk crystalline phase. Conditions for the formation of clusters via spinodal decomposition and ordering are more favorable right at the growth surface during epitaxial growth, followed by subsequent regrowth. In this case it is possible to create various low-dimensional inclusions dominated by

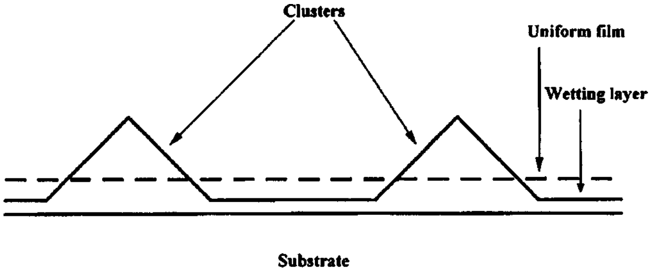

FIG. 2. Formation of clusters according to the Stranskii–Krastanov mechanism as part of the transformation of an epitaxial film grown on a substrate with a different lattice parameter. The dashed line is the uniform film; the solid line shows the three-dimensional islets and thin wetting layer.

quantum-well effects: two-dimensional ($\delta$-doped structures, quantum wells, and superlattices), one-dimensional (quantum wires) or zero-dimensional (quantum dots). In the last case it is necessary to generate nanometer-size islets on the growing surface.

Conditions for implementing this kind of clustering are most favorable during vapor-phase and molecular-beam epitaxy. In contrast to the methods discussed earlier, islet nucleation provides a wider range of possibilities for regulating the number, composition, and size of the clusters, as well as the way they are distributed in the crystal lattice of the epitaxial host. This opens up new and efficient ways to modify the fundamental properties of traditional semiconductors, and to create fundamentally new semiconducting systems with predictable properties.

Contemporary technologies for generating quantum dots are based on the Stranski-Krastanov crystallization process. When a thin epitaxial film is deposited on a substrate with a different crystal lattice parameter, its free energy given by Eq. (1) depends on the thickness of the film and its surface geometry.[13] If the film surface is kept planar as it grows, the surface energy $F_s$ does not change, but the elastic strain energy $F_{el}$ increases linearly. However, this situation becomes energetically unfavorable when a certain critical film thickness is reached. The minimum free energy of the system will then correspond to the formation of three-dimensional islets at the growth surface (Fig. 2). The bases of these islets are strongly strained, since they are adjacent to the substrate. However, the elastic strain decreases with distance from the substrate boundary. Thus, the fundamental motive force for clustering here is decreasing the strain energy.

The approach described above has been successfully used to generate clusters (quantum dots) of InAs and InGaAs on the surface of a GaAs substrate (Fig. 3), and has been applied to many other systems using molecular-beam and gas-phase epitaxial technologies.[14]

An important feature of this clustering technique is the fact that the clusters form right at the growth surface, where there is considerably more ''freedom'' than in the bulk of the matrix crystal lattice. Successful implementation of this technique, especially when the structures being grown are quantum wires or dots, requires the development of methods to fine-tune the potential well of the growth surface. To accomplish this, various methods can be used to regulate the atomic structure of the substrate surface, as well as nonthermal methods to locally perturb the surface combined with nonthermal methods to locally stimulate the processes of epitaxial growth (irradiation, ion implantation, etc.). A nontrivial role is played by precise control of the composition and supersaturation of the gas phase right at the crystallization front, as well as the mechanisms and kinetics of the crystallization process itself.

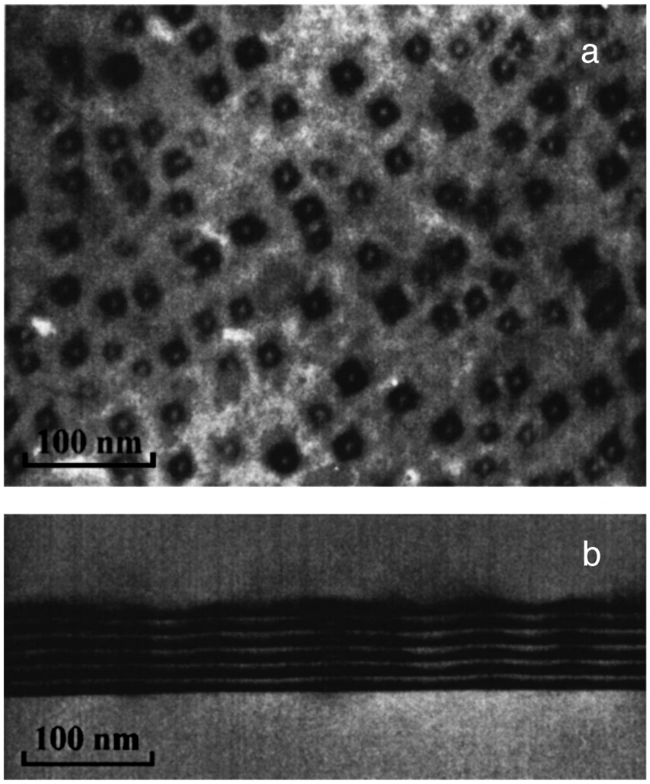

FIG. 3. Electron-microscope images in the growth plane (a) and cross-sectional view (b) of the bulk of vertically superimposed InGaAs quantum dots grown in an epitaxial GaAs layer.

### 2.5 Materials with high cluster densities

The methods described above allow us to create clusters of various kinds in a variety of semiconducting materials. However, the fraction of clusters does not exceed 1–2% of the total material volume (for As clusters in GaAs), and in many cases it is considerably less. However, methods exist that allow us to obtain materials in which the clusters occupy an appreciable, if not a large, portion of its volume. Among these methods, the most obvious is direct deposition of ''free'' semiconducting clusters (nanoclusters) on the corresponding substrate (Fig. 4). The clusters are supplied by a supersaturated nonequilibrium medium created by laser evaporation of a solid-state target.[15] The products of the evaporation are sent to a supersonic nozzle, where they are rapidly cooled in an atmosphere of buffering inert gas, and clusters form. The resulting beam of clusters is then analyzed and subjected to size-selection using time-of-flight mass spectrometers. The accuracy of existing mass spectrometers is entirely adequate to select out polyatomic clusters in a rather wide range of total numbers of atoms. We can also vary and specify deviations from ordinary crystalline stoichi-

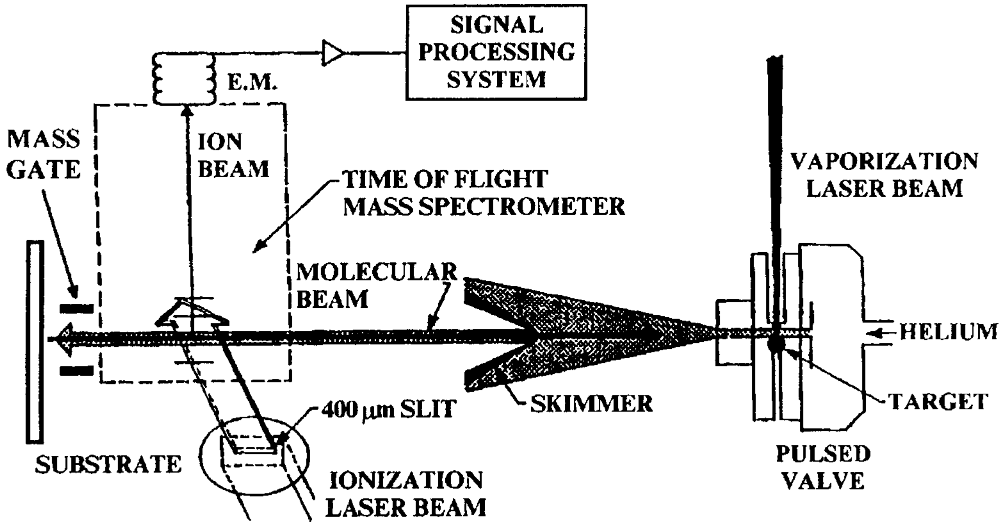

FIG. 4. Sketch of apparatus for depositing clusters.

ometry in clusters of semiconducting compounds. Although this is a very promising way to create new cluster (nanocrystalline) materials, at this time it is still very cumbersome and expensive, and has not found wide applications.

The possibility of using biotechnological processes to obtain nanocrystallites is of considerable interest. An example of their successful use is the synthesis of CdS nanocrystallites described in Ref. 16. In this process, certain peptides are used to transport sulfur to cadmium ions deposited on a substrate surface. As a result, a unique mosaic made up of CdS nanocrystallites, most of which were 21 Å in size, was obtained. Such biotechnological processes could lead to new ways of fabricating nanocrystalline media. However, research in this area is still in the initial stages, and it is still too early to evaluate their real promise. Meanwhile, the most widely used methods of obtaining nanocrystallites are still the traditional methods of crystallization on profiled and porous substrates.

At this time, a method that is extensively used to obtain nanocrystalline material is based on using the initial stages of crystallization in film-like structures based on hydrogenated amorphous semiconductors. Thin-film structures based on hydrogenated amorphous silicon $a$-Si : H and related materials have been intensely studied over the past two decades, and are now widely and successfully used in systems for recording and imaging information, harnessing solar energy, electrophotography, sensor technology, etc. A promising way to further extend the possibilities of this new class of semiconductors is to use them to create ''nanocrystalline media,'' whose compositions are made up of a large number of nanometer-size ''crystals'' incorporated into the amorphous matrix as it crystallizes. The nanocrystals that form in this case are essentially atomic clusters that grow not in a crystal lattice (as in previous cases) but rather in an amorphous medium. In this case the amorphous matrix provides rather ''comfortable'' conditions for the growth of practically unstressed clusters. Depending on the size and volume density of the nanocrystals, the fundamental properties of these thin-film structures, especially the width of its band gap, can be varied in a very wide range.

This kind of nanocrystalline composite is most simply created by laser annealing or rapid thermal annealing of a hydrogenated amorphous film. The extensive experimental material accumulated to date attests to the possibility of creating thin-film structures with controllable dimensions and bulk densities of nanocrystals uniformly distributed within the amorphous matrix. The day will come when the problem of providing high temporal stability for these nanocrystalline composites will also be solved.

Another example of a cluster material is porous silicon. This material is obtained by electrochemical (photoelectrochemical) processing of films of crystalline Si, resulting in a structure made up of nanometer-size clusters and filaments. The pores between these structures are also nanometer-sized. The structure of a film of porous silicon can be controlled by varying the current density and concentration of chemical reagents in the electrochemical reaction, or by doping and preliminary processing of the original film. Since the discovery of efficient red-orange luminescence in porous silicon in 1990,[17] this material has attracted a great deal of attention. The structure and properties of porous silicon have been the subject of a multitude of papers and special reviews (see, for example, Ref. 18); therefore, we will not pause here to discuss this material in any degree of detail. We mention only that, despite their very different starting materials, porous silicon and nanocrystalline silicon often exhibit similar properties. In particular, both materials luminensce in the red portion of the spectrum.[18,19]

## 3. EFFECT OF CLUSTERS ON THE ELECTRONIC PROPERTIES OF A MATERIAL AND THE USE OF SEMICONDUCTORS CONTAINING CLUSTERS

The presence of clusters in a semiconducting host can significantly effect the fundamental properties of the semiconductor. In the next sections of this paper, we briefly consider the fundamental mechanisms for this effect and show that in a number of cases the use of clusters allows us to create unique materials and device structures.

### 3.1. Local levels in the band gap

By virtue of the small size of a cluster, the wave function of an electron within it is bounded by a potential barrier in all three directions, and the electronic density of states has a $\delta$-like form. Thus, clusters can create localized levels in the band gap of the semiconductor, similar to the levels of ordinary impurities. Well-known examples of this occurrence are the energy levels of complexes consisting of a structural point defect and an impurity.

Of course, the creation of a suitable set of cluster levels in a semiconductor is a rather difficult problem. In contrast to ordinary doping, creating a system of clusters requires fine control of an entire ensemble of structural point defects and impurities. Nevertheless, the use of clusters is clearly indicated when no point impurity exists in nature that could lead to the required electronic level in the semiconductor, or when the solubility of a suitable impurity is too small. The more complex structure of clusters provides many possibilities for creating electronic levels. An example of this is the well-studied transformation of thermal donor levels in silicon when the material is thermally processed.[6]

### 3.2 "Buried" Schottky barriers

When metallic clusters that contain a sufficiently large number of atoms are embedded into a semiconductor host, they can affect the properties of the material through a mechanism that is distinct from ordinary doping. This mechanism was proposed by Warren and co-authors in Ref. 20 to explain the properties of gallium arsenide containing clusters of semimetallic arsenic.

It is known that when a metal makes contact with a semiconductor, a Schottky barrier forms. In this case, the Fermi level of the semiconductor usually is pinned at the heterojunction boundary at a certain point in the band gap. For contacts between the majority of metals and gallium arsenide, the Fermi level is pinned near the middle of the band gap, leading to depletion regions in both $n$-type and $p$-type conducting materials. The width of the depletion region depends on the magnitude of the conductivity of the semiconductor.

Since arsenic is a semimetal, an assembly of arsenic clusters in GaAs can be viewed as a system of multiple "buried" Schottky barriers, each of which is surrounded by a depletion region (Fig. 5). For the moderate impurity concentrations used in traditional semiconductor doping, the size of this depletion region is considerably larger than the intrinsic size of the cluster. At sufficiently high concentrations of clusters, the local depletion regions created by the latter overlap and extend throughout the entire volume of the semiconductor (Fig. 5b). As a result, the GaAs host should become semi-insulating, which is in fact observed experimentally. Moreover, the high concentration of clusters and the presence of built-in electric fields should facilitate the rapid trapping and recombination of nonequilibrium charge carriers, and in fact the characteristic lifetime of a charge carrier in GaAs containing arsenic clusters is experimentally measured to be less than 1 ps.

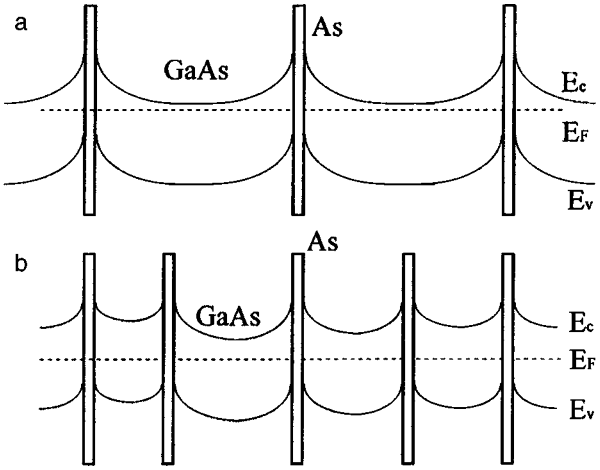

FIG. 5. Model of "buried" Schottky barriers formed by As clusters in an $n$-type GaAs host. a—low cluster concentration, b— high cluster concentration.

High resistivity combined with a phenomenally low lifetime for charge carriers and high crystallinity makes GaAs with arsenic clusters extremely attractive for various applications in ultrafast semiconductor electronics. Among these are photodetectors with active regions consisting of GaAs with arsenic clusters, whose response times are measured to be less than 1 ps, as well as field-effect transistors and integrated microcircuits where this material is used as a buffer to increase the breakdown voltage at the gate and to eliminate many parasitic effects in the channel.

### 3.3 The band gap and control of properties

When clusters make up most of its bulk, changes in their dimensions and concentration will lead to changes in the fundamental properties of a semiconductor, e.g., the width of the band gap, the value of the conductivity, energies of the fundamental optical transitions, etc. This opens up possibilities for creating new semiconductor materials with properties that differ considerably from those exhibited by the same semiconductors in the single-crystal or amorphous states. There is no doubt that the greatest interest focuses on realizing these possibilities in silicon, the workhorse material of contemporary semiconductor electronics.

It is well known that both crystalline and amorphous silicon possess low efficiencies for radiative recombination and thus are unsuitable for making light-emitting devices. This disadvantage is due to fundamental physics. In the first case, it arises from the indirect structure of the bands, while in the second case it is due to spatial separation and localization of charge carriers. However, in 1990 it was discovered that porous silicon can generate intense luminescence in the visible region of the spectrum at room temperature.[17] Efficient luminescence was also observed from silicon films consisting of a mixture of nanocrystalline and amorphous phases.[19]

Currently there are two models used to explain the efficient luminescence from cluster (porous or nanocrystalline) silicon. One model invokes the effect of size quantization of electrons in the clusters. This effect explains the ability of cluster silicon to emit in the visible region of the spectrum (bulk crystal silicon has a band gap 1.1 eV wide, which corresponds to the IR region). It also explains the dependence of the radiation wavelength on cluster size observed in experiment.

Another model that explains the luminescence of cluster silicon uses the fact that a system of clusters has a gigantic surface on which atoms of silicon can form various types of bonds, e.g., Si–H and Si–O–H. The model identifies the electronic transitions in these molecular groups as the source of the luminescence. This model explains the extreme sensitivity of the luminescence parameters to the composition of surface coatings, thermal processing, and various physical and chemical perturbations.

Neither the quantum-well model nor the molecular luminescence model can individually describe the properties of cluster silicon completely. In order to explain real systems, with their extremely complicated structures, it is probably necessary to take into account both effects. This is all the more so in that the division of these phenomena into ''surface'' and ''bulk'' categories is clearly nominal for nanometer-size clusters.

The fundamental problems that have to be solved in order to extend the practical usefulness of cluster silicon luminescence are ensuring stability of the material parameters and finding a way to efficiently inject charge carriers. These problems will be solved once the nature of the phenomena observed is understood and the material structure is under control. In particular, changing the atomic fraction of clusters in nanocrystalline silicon makes it possible to change its electrical conductivity by several orders of magnitude (Fig. 6).[21]

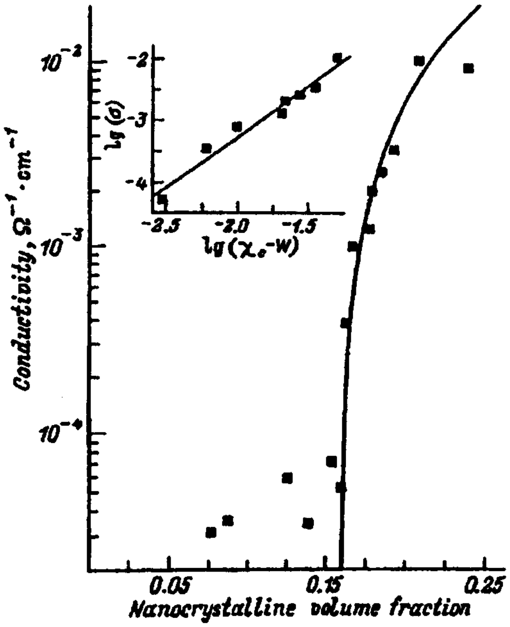

FIG. 6. Dependence of the conductivity on the volume fraction of nanocrystalline phase in silicon films with mixed amorphous—nanocrystalline composition. The points are experiment, the solid curves are a calculation based on percolation theory.

### 3.4 Quantum-dot lasers

Direct proof that the spectrum of electronic states of clusters in a semiconductor can resemble atomic spectra was obtained in studies of microcathodoluminescence of InAs quantum dots in a GaAs host.[22] It was observed that an isolated quantum dot gives a narrow (0.15 meV) luminescence line, whose width did not vary with temperature. The $\delta$-function-like electronic spectrum of quantum dots is of fundamental importance for their use in semiconductor lasers. It is anticipated that lasers made of quantum dots will possess high differential gain, low threshold currents, and high temperature stability of the threshold current.[23] Intensive investigations of the atomic structure and electronic properties of quantum dots carried out in recent years have made it possible to design structures (Fig. 7) and fabricate quantum-dot lasers that confirm these expectations.[14] By using a system of vertically superimposed InGaAs quantum dots in the active region of a GaAs structure, it was possible to fabricate lasers with threshold currents as low as 90 A/cm$^2$ at 300 K. These lasers exhibited ultrahigh stability of the threshold current: the value of 50 A/cm$^2$ for the latter was almost independent of temperature[24] in the range 77–220 K.

Thus, even present-day quantum-dot lasers have fundamental parameters that are competitive with the best semiconductor quantum-well lasers, and are greatly superior to them with regard to threshold current stability. In the near future we can expect further progress in designing such lasers as device structures are optimized and new materials are used for the host and quantum dots.

### 3.5 Single-electron transport

Consider a metallic cluster (for definiteness, a spherical cluster with radius $R$) placed in a dielectric medium with permittivity $\varepsilon$. The potential of this cluster is

$$U = q/C, \tag{3}$$

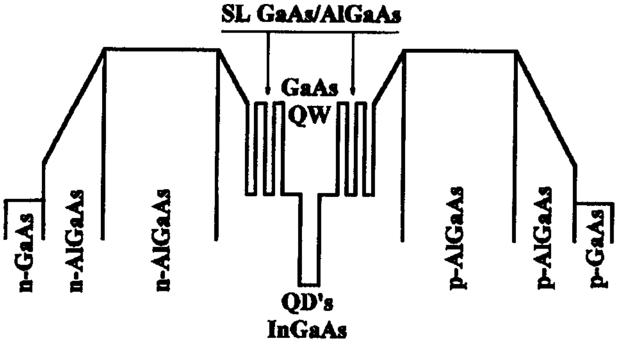

FIG. 7. Schematic diagram of a semiconductor laser with an aggregate of quantum dots (the $QD$'s are InGaAs) in an active region (a $QW$ made of GaAs).

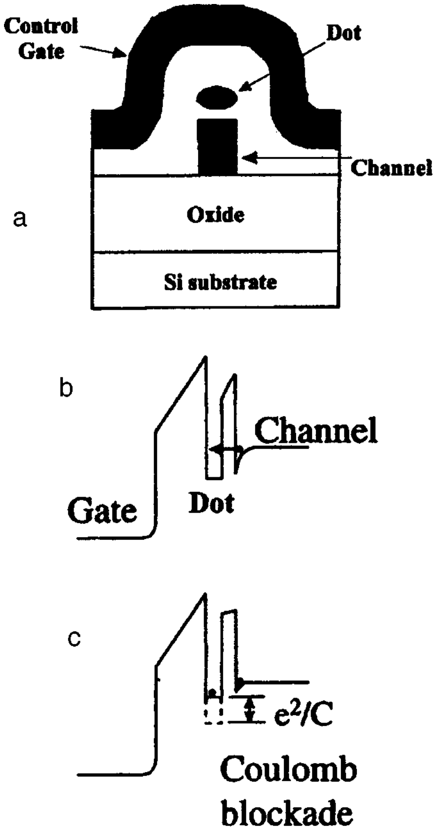

FIG. 8. Single-electron memory device with a nanometer-size cluster as a floating gate. The schematic illustration of the structure (a) and energy diagram before (b) and after (c) shows trapping of an electron by the cluster. The trapping of one electron leads to blocking of the narrow channel due to Coulomb blockade.

where $q$ is the electron charge, and $C = \varepsilon R$ is the capacitance. For a cluster with dimensions of a few nanometers, the capacitance is $\sim 10^{-18}$ F. Therefore, one electron placed in such a cluster creates a potential of order 0.1 V, which is found to be sufficient for Coulomb blockade of the transport of other electrons. This opens up possibilities for creating a new class of so-called single-electron devices. Several types of device structures of this kind have been developed: single-electron memory elements (Fig. 8), field-effect transistors controlled by a single electron on the gate, the single-electron analog of a bipolar transistor, a ''single-electron pump,'' etc. At present, practical realizations of these structures usually require the use of precision lithography of thin metallic films or semiconductor layers with a two-dimensional electron gas. Because the spatial resolution characteristics of lithography usually do not permit objects of sufficiently small size to be made, the operating temperatures of these devices are limited to liquid helium or below. However, it is worth noting that significant progress has been made in recent years in harnessing this technology. For example, Guo *et al.*[25] have reported fabricating a single-electron memory that operates at room temperature, based on a field effect transistor with a very narrow channel and a floating nanometer-size gate. In light of these size limitations, there can be no doubt that using the cluster-forming methods described in Sec. 2 of this paper to obtain a system of nanometer-size clusters is an extremely promising way to fabricate single-electron devices operating at room temperature.

## 4. CONCLUSION

We have discussed the basic approaches to creating and controlling systems of nanometer-size clusters in semiconductors, and the patterns of their behavior. Although clusters in semiconductors are only now beginning to attract the close attention of researchers, there has already been considerable progress in the technology of cluster formation. In a number of practically important cases, it has been possible to control the chemical compositions, sizes, concentration, and spatial locations of clusters in a semiconductor.

The progress made in the technology of obtaining clusters allows us even today to use them in semiconductor electronics devices. The biggest success is in the creation of semiconductor lasers with quantum dots and the use of GaAs layers containing arsenic clusters in ultrafast photodetectors, transistors, and integrated microcircuits. In the near future we can count on the creation of efficient light-emitting devices based on cluster silicon, and the fabrication of single-electron devices operating at room temperature.

As a whole, the study of fabrication methods for structures and properties of nanometer-size clusters is, in our view, one of the most promising directions for contemporary physics and semiconductor technology to follow.

We wish to thank E. V. Astrova, N. A. Bert, Yu. G. Musikhin, A. B. Pevtsov, A. A. Suvorova, and V. M. Ustinov for providing us with experimental data and for useful discussions.

This work was supported by the Russian Fund for Fundamental Research and the Russian Science Ministry (program on ''fullerenes and atomic clusters'').

[1] M. G. Mil'vidskiĭ and V. B. Osvenskiĭ, *Structural Defects in Single-Crystal Semiconductors* (Metallurgiya, Moscow, 1984) [in Russian].
[2] V. V. Emtsev and T. V. Mashovets, *Impurities and Point Defects in Semiconductors* (Radio i Svyaz, Moscow, 1981) [in Russian].
[3] M. G. Mil'vidskiĭ, N. S. Rytova, and E. V. Solov'eva, in *Problems in Crystallography* (Nauka, Moscow, 1987), V. 3, p. 215 [in Russian].
[4] *Rare Earth Doped Semiconductors*, MRS Symposium Proc. V. 301, edited by G. S. Pomrenke, P. B. Klein, and D. W. Lander (Pittsburg, USA, 1993).
[5] V. I. Fistul', *Heavily Doped Semiconductors* (Nauka, Moscow, 1965) [in Russian].
[6] V. V. Voronkov, Semicond. Sci. Technol. **8**, 2037 (1993).
[7] F. W. Smith, A. R. Calawa, C. L. Chen, M. J. Mantra, and L. J. Mahoney, Electron. Dev. Lett. **9**, 77 (1988).
[8] N. A. Bert and V. V. Chaldyshev, Fiz. Tekh. Poluprovodn. **30**, 1889 (1996) [Semiconductors **30**, 988 (1996)].
[9] N. A. Bert, V. V. Chaldyshev, D. I. Lubyshev, and V. V. Preobrazhenskiĭ, Fiz. Tekh. Poluprovodn. **29**, 2232 (1995) [Semiconductors **29**, 1170 (1995)].
[10] I. M. Lifshitz and V. V. Slezov, Zh. Éksp. Teor. Fiz. **35**, 479 (1958) [Sov. Phys. JETP **8**, 331 (1959)].
[11] V. V. Voronkov and M. G. Mil'vidskiĭ, Kristallografiya **33**, 471 (1988) [Sov. Phys. Crystallogr. **33**, 278 (1988)].
[12] E. V. Solov'eva, M. G. Mil'vidskiĭ, A. I. Belogorokhov, G. I. Vinogradova, D. T. Gogoladze, L. M. Dolginov, N. V. Mal'kova, V. M. Novikova, and A. N. Osipova, Fiz. Tverd. Tela (Leningrad) **25**, 965 (1991) [Sov. Phys. Solid State **25**, 551 (1991)].
[13] A. A. Chernov, *Contemporary Crystallography* (Nauka, Moscow, 1980), V. 3, p. 7 [in Russian].

[14] Zh. I. Alferov, Physica Scripta **68**, 32 (1996).
[15] M. L. Cohen and W. Knight, *Phys. Today* No. 12, 43 (1990).
[16] C. T. Dameron, R. N. Reese, R. K. Mehra, A. R. Korton, P. J. Carrol, M. L. Steigerwald, L. E. Brus, and D. R. Winge, *Nature* **338**, 596 (1989).
[17] L. T. Canham, Appl. Phys. Lett. **57**, 1046 (1990).
[18] *Porous Silicon. Science and Technology*, edited by J.-C. Vial and J. Derrier (Springer-Verlag, Berlin, 1995).
[19] E. Edelberg, S. Bergh, R. Naone, M. Hall, and E. S. Aydil, Appl. Phys. Lett. **68**, 1415 (1996).
[20] A. C. Warren, J. M. Woodall, J. L. Freeouf, D. Grischkowski, D. T. McInturff, M. R. Melloch, N. Otsuka, Appl. Phys. Lett. **57**, 1331 (1990).
[21] V. G. Golubev, V. Yu. Davydov, A. V. Medvedev, A. B. Pevtsov, and N. A. Feoktistov, Fiz. Tverd. Tela (St. Petersburg) **39**, 1348 (1997) [Phys. Solid State **39**, 1197 (1997)].
[22] M. Grudmann, J. Christen, N. N. Ledentsov, J. Bohrer, D. Bimberg, S. S. Ruvimov, P. Werner, U. Richter, U. Gosele, J. Heidenreich, V. M. Ustinov, A. Yu. Egorov, A. E. Zhukov, P. S. Kop'ev, and Zh. I. Alferov, Phys. Rev. Lett. **74**, 4043 (1995).
[23] Y. Arakawa and H. Sakaki, Appl. Phys. Lett. **40**, 939 (1982).
[24] Zh. I. Alferov, N. A. Bert, A. Yu. Egorov, A. E. Zhukov, P. S. Kop'ev, A. O. Kosogov, I. L. Krestnikov, N. N. Ledentsov, A. V. Lunev, M. V. Maksimov, A. V. Sakharov, V. M. Ustinov, A. F. Tsatsul'nikov, Yu. M. Shernyakov, and D. Bimberg, Fiz. Tekh. Poluprovodn. **30**, 351 (1996) [Semiconductors **30**, 194 (1996)].
[25] L. Guo, E. Leobandung, and S. Y. Chou, Appl. Phys. Lett. **70**, 850 (1997).

Translated by Frank J. Crowne

# ATOMIC STRUCTURE AND NON-ELECTRONIC PROPERTIES OF SEMICONDUCTORS

## How the type of bombarding ion affects the formation of radiation defects in silicon

M. Yu. Barabanenko, A. V. Leonov, V. N. Mordkovich, and N. M. Omel'yanovskaya

*Institute for Problems in Microelectronics and Ultrapure Materials, Russian Academy of Sciences,*
*142432 Chernogolovka, Russia*

(Submitted June 30, 1997; accepted for publication September 15, 1997)
Fiz. Tekh. Poluprovodn. **32**, 523–526 (May 1998)

The method of nonstationary capacitance was used to study how the chemical nature of implanted ions affects the creation of electrically active defects in silicon. Oxygen $O^+$ and nitrogen $N^+$ ions were implanted into Si at a target temperature of 300 K, in doses of $2\times10^{11}\text{cm}^{-2}$ with energies of 75 keV, and argon $Ar^+$ ions were implanted in a dose of $7\times10^{10}\text{cm}^{-2}$ with energies of 150 keV, in such a way that all the samples of $n-$ and $p-$Si received approximately the same number and spatial distribution of primary radiation defects. It was observed that the spectrum of stable radiation defects depends on the nature of the bombarding ion. Thus, the DLTS spectrum of $n$-Si irradiated by $O^+$ ions has three peaks, whereas the spectrum of $n-$Si implanted by $N^+$ ions exhibited only one of these peaks. The DLTS spectra of samples of $n-$ and $p-$Si implanted by $O^+$ and $N^+$ ions revealed peaks of reverse (anomalous) polarity, whose energy positions matched the most clearly defined DLTS peaks of silicon samples with the opposite type of conductivity. © *1998 American Institute of Physics.* [S1063-7826(98)00205-1]

### 1. INTRODUCTION

According to contemporary descriptions,[1] stable radiation defects resulting from ion bombardment of silicon are the result of processes that include formation of cascades of displaced atoms, spatial separation of interstitial atoms and silicon vacancies, and quasichemical reactions with the participation of interstitials and vacancies. The type and concentration of radiation-induced damage centers are determined entirely by the intensity of generation, concentration, and mobility of primary point defects, and also the initial density of sinks for these defects in the host. The generation of primary defects is specified by the ratio of masses of the ions and target atoms, along with the energies, dose, and current density of the ions. Diffusive motion of the defects is determined by the target temperature. In all of this, the individual properties of ions as chemical elements were disregarded. This approach is based on the fact that when Si is irradiated even by light ions, the number of interstitials and vacancies created greatly exceeds the number of implanted impurities.[2] Therefore, the contribution of specific properties of impurity atoms, for example their chemical activity, to the character of evolution of the ensemble of point defects is assumed to be negligible. The nature of the impurities manifests itself only when the host is strongly supersaturated, for example during ion-beam synthesis of layers of new phases in Si,[3,4] when the implantation dose exceeds values of $10^{17}$–$10^{18}$ $\text{cm}^{-2}$. However, the authors of Ref. 5 have asserted that the difference in chemical activity between hydrogen and helium explains the different behavior of radiation defects in Si implanted by small doses of the ions $H^+$ and $He^+$. This prediction by the authors of Ref. 5 has recently been confirmed by quantum-chemical calculations[6] of the effect of hydrogen on the behavior of intrinsic point defects in Si.

In this paper we set forth the observed experimental features of the formation of the simplest radiation-defect complexes in silicon implanted by extremely low doses of oxygen and nitrogen ions.

### 2. EXPERIMENTAL CONDITIONS

Samples of $n$-Si (KEF-20, $\langle 100\rangle$) and $p$- Si (KDB-20, $\langle 100\rangle$) with oxygen concentrations of $\sim 7\times10^{17}\text{cm}^{-3}$ and nitrogen concentrations of $\sim 10^{16}\ \text{cm}^{-3}$ were irradiated by $O^+$ and $N^+$ ions with energies of 75 keV in single doses of $2\times10^{11}\text{cm}^{-2}$ at ion-current densities of 1.25 nA/cm$^2$, and also by $Ar^+$ ions with energies of 150 keV at a dose of $7\times10^{10}\ \text{cm}^{-2}$, at current densities of 0.5 nA/cm$^2$, and a target temperature of 300 K. The doses and implantation energies were determined by requiring that approximately equal numbers and spatial distributions of primary displaced Si atoms be created by the ions. According to calculations based on the program TRIM,[2] the total number of displaced atoms created by $O^+$ and $N^+$ ions actually should equal $7\times10^{13}$, by $Ar^+$ ions $9\times10^{13}$ for line displaced-atom densities of $2\times10^7$ and $8\times10^7$ $\text{ion}^{-1}\cdot\text{cm}^{-1}$ respectively. The concentrations of oxygen and nitrogen at the maxima of the ion range distribution were $\sim 10^{16}\ \text{cm}^{-3}$. The small ion doses were chosen so as to avoid generating particles made up of new chemical phases, e.g., $SiO_2$ and $Si_3N_4$ (Refs. 3 and 4), which would affect the radiation defect spectrum. Under these conditions, we should expect the irradiated layers to have the same properties if the type of ion has no effect.

TABLE I. Depth location of radiation defect levels and their literature identification (Refs. 7–9).

| Peak | Energy | | Type of defect |
|---|---|---|---|
| $E_1$ | $E_c - 0.18$ eV | | $A$-center (O+$V$) |
| $E_2$ | $E_c - 0.46$ eV | | Divacancy $V_2$ |
| $E_3$ | $E_c - 0.5$ eV | | Multivacancy complex |
| $E_4$ | $E_c - 0.23$ eV | | Divacancy $V_2$ |
| $H_1$ | | $E_v + 0.1$ eV | Not identified |
| $H_2$ | | $E_v + 0.28$ eV | $K$-center ($V$-O-C) |
| $H_3$ | | $E_v + 0.38$ eV | Not identified |

The parameters of the deep levels created by radiation defects were determined by deep-level transient spectroscopy (DLTS). In order to make the measurements, Schottky barriers were created on the front side of the irradiated samples by thermal sputtering in vacuum (Au on $n$-Si and Al on $p$-Si), while ohmic contacts were formed on the back side. The DLTS spectra were measured at constant reverse bias equal to $\mp 1$ V, with filling pulse amplitudes of $\pm 1$ and $\pm 0.85$ V for $n$- and $p$-type Si, respectively. For the doping levels and biases used, the width of the space charge region was approximately 3 $\mu$m, which ensured complete overlap of the damaged region for these energies of the implanted ions. The two amplitudes for the filling pulse (1 and 0.85 V) allowed us to characterize the spatial distribution of the defects. The observed electrically active centers in the spectra of Si were identified based on literature descriptions,[7–9] and are reported in Table I. Table II lists the relative concentrations of deep levels whose value in units of the concentration of majority charge carriers in Si exceeds $10^{-3}$.

## 3. RESULTS AND DISCUSSION

It is clear from Fig. 1 and Table II that the DLTS spectrum corresponding to $n$-Si (O$^+$) contains three peaks.[1] In contrast, the spectrum of $n$-Si (N$^+$) exhibits only one peak, which corresponds to the deep level $E_2$, although the concentration of energetically active centers contributed by N$^+$ ions is higher than the total concentration of defects generated by O$^+$ ions. The spectrum of $n$- Si (Ar$^+$) has three peaks, as in the case of $n$-Si (O$^+$), and one additional peak $E_4$ (see Table II). Note that the DLTS method allows us to follow only electrically active defects, which are only a fraction of the total number of radiation defects in silicon. This probably explains the larger total number of radiative defects observed in experiment when $n$-Si is irradiated by nitrogen compared to irradiation with oxygen (see the right column of Table II).

TABLE II. Ratio of concentrations of energetically active centers to the concentration of primary charge carriers in silicon. In the right column Q we list the total values.

$n$-Si

| Ion | $E_1$ | $E_2$ | $E_3$ | $E_4$ | $\Sigma E_i$ |
|---|---|---|---|---|---|
| O$^+$ | 0.001 | 0.062 | 0.010 | | 0.072 |
| N$^+$ | | 0.102 | | | 0.102 |
| Ar$^+$ | 0.007 | 0.075 | 0.010 | 0.001 | 0.092 |

$p$-Si

| Ion | $H_1$ | $H_2$ | $H_3$ | $\Sigma H_i$ |
|---|---|---|---|---|
| O$^+$ | 0.002 | 0.057 | 0.015 | 0.074 |
| Ar$^+$ | 0.001 | 0.100 | 0.035 | 0.136 |

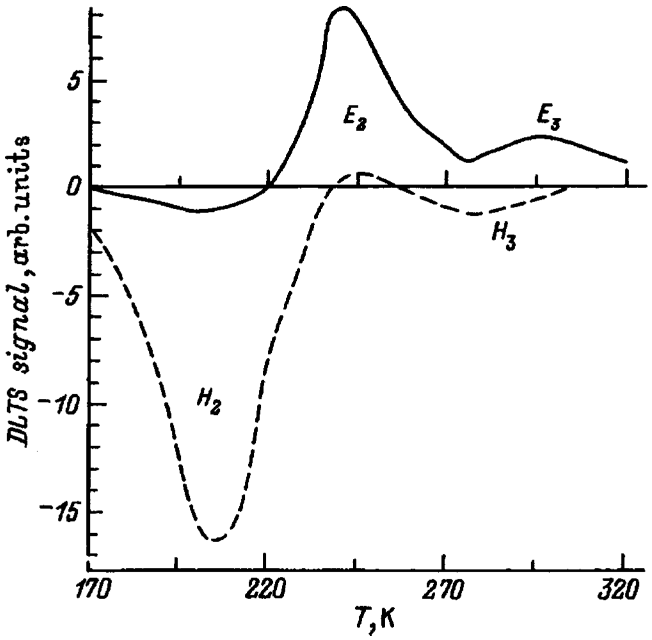

FIG. 1. DLTS spectra of samples of $n$-Si (solid curves) and $p$-Si (dashed curves) implanted by oxygen ions at a dose of $2\times 10^{11}$cm$^{-2}$ and energy of 75 keV at a temperature of 300 K. The peaks on the solid and dashed curves corresponding to the same temperature are denoted by the same symbol: $H_2$ or $E_2$.

In the lower section of Table II we record concentrations of deep levels in $p$-Si. According to this data, there is no fundamental difference in the DLTS spectra of samples implanted by O$^+$ and Ar$^+$ ions; in both cases the same types of radiation defects are observed.

The DLTS spectra of samples with either type of conductivity irradiated by O$^+$ or N$^+$ ions exhibit peaks of reverse polarity (anomalous), despite the fact that carrier injection from a Schottky barrier was excluded. This is because the amplitude of the filling pulse did not exceed the value of the reverse bias in the measurements. Usually, the amplitude of the anomalous peaks was quite small. The exception was the spectrum of $p$- Si (N$^+$), in which the anomalous peaks had a considerable magnitude and, by superimposing on top of the normal peaks, prevented us from interpreting the spectrum of this sample.

The authors of Refs. 10 and 11 investigated the appearance of anomalous peaks in the DLTS spectra of silicon with Schottky barriers irradiated by protons and boron ions. In contrast to the results of these papers, in our experiments we found that the energy positions of the anomalous peaks corresponded approximately to the energies of the most distinct maxima in the spectra for silicon with the opposite type of conductivity. In fact, the maximum of the anomalous peak in the spectrum of $p$-Si (peak $E_2$ on the dashed curve in Fig. 1) and the maximum of the largest peak in magnitude observed in the spectrum of $n$-Si (peak $E_2$ on the solid curve in Fig. 1) correspond approximately to the same measurement temperature. In the same way, we correlate the peaks $H_2$ of the dashed and solid curves on the figure. Note that during scanning of a ''recessed'' layer of silicon, i.e., when a reverse bias of -1 V was applied and the filling pulse amplitude was no larger than $+0.85$ V, the $E_2$ and $H_2$ peaks were absent from the spectra obtained. This implies that defects associated with these peaks are located near the crystal surface.

The appearance of anomalous peaks in the DLTS spectra of implanted samples of Si is also associated with the nature of the implanted ions. In fact, no anomalous peaks are seen for implantation by $Ar^+$ ions, but do appear in Si irradiated by $O^+$ and $N^+$ ions.

As we have already noted, the DLTS spectra of $n$-Si($O^+$) and $n$-Si($N^+$) samples (see Table II) are quite different. In the $n$-Si($N^+$) spectrum we observed neither the peak $E_1$ characteristic of a $A$-center nor peak $E_3$ corresponding to multivacancy complexes. At the same time, the divacancy peak $E_2$ is the largest feature in all the samples. The absence of $A$-centers in $n$-Si($N^+$) allows us to conclude that quasi-chemical reactions with participation of vacancies take place within the cascade of displaced atoms. If this were not so, i.e., if the vacancies were scattered away from the cascade of displaced atoms and the reactions took place in the surrounding matrix, we would observe roughly the same number of $A$-centers both in $n$-Si($O^+$) and in $n$-Si($N^+$). An important detail here is that the concentrations of oxygen in $n$-Si($O^+$) and $n$-Si($N^+$) samples are practically the same, because implantation of $O^+$ ions leads to negligible changes in the volume concentration of oxygen in silicon. In fact, as was noted previously, the starting samples contain oxygen at a level of $\sim 7\times 10^{17}\mathrm{cm}^{-3}$, while at the maximum of the ion range distribution the concentration of oxygen has a value of order $10^{16}$ cm$^{-3}$.

Thus, for insignificant differences in the concentrations of impurites between samples of $n$-Si implanted by oxygen and nitrogen, we observed (see Table II) a considerable difference in the concentrations of $A$-centers– at least an order of magnitude (the precision of the DLTS method is $10^{-4}$ in the relative units used in Table II).

## 4. CONCLUSIONS

The experiments discussed in this paper were set up so as to ensure as far as possible the same characteristics of the primary radiation defects in the silicon samples during implantation of the different ions. Under these conditions we observed an effect of the type of ion on the formation of secondary radiation defects: 1) the defect spectra in $n$-Si implanted by ions of oxygen and nitrogen differed qualitatively; 2) anomalous peaks were observed in the DLTS spectra of samples of $n$- and $p$-Si implanted by oxygen and nitrogen ions, and were not observed after irradiation by argon ions. In addition, we discovered a correlation in the energy positions of normal and anomalous peaks with DLTS spectra of silicon with opposite types of conductivity; defects responsible for the appearance of these peaks were observed in the skin layer of the crystals. It is especially important to note the following interrelationship: nitrogen atoms predominantly form divacancies in $n$-Si, while generating larger anomalous peaks in the DLTS spectrum of $p$-Si samples.

The authors are grateful to O. V. Feklisov and N. A. Yarykina for assistance in measuring the DLTS spectra.

1)Later on in this paper we will use the notation $k$-Si ($M^+$) to indicate that we are considering electron-doped ($k=n$) or hole-doped ($k=p$) silicon irradiated by M ions.

---

[1] J. Gulai, *Handbook of Ion Implantation*, I.F. Ziegler, Ed. (Elsevier, Amsterdam, 1992).
[2] J. R. Biersack and L. G. Haggmark, Nucl. Instrum. Methods **174**, 257 (1980).
[3] P. L. F. Hemment, E. Maydell-Ondrusz, and K. S. Stevens, Vacuum **34**, 203 (1984).
[4] T. Tsujide, M. Nojiri, and H. Kitagawa, J. Appl. Phys. **51**, 1605 (1980).
[5] A. I. Aleshin, L. S. Smirnov, and V. F. Stas', Fiz. Tekh. Poluprovodn. **17**, 551 (1983) [Sov. Phys. Semicond. **17**, 348 (1983)].
[6] V. M. Pinchuk, A. N. Nazarov, V. S. Lysenko, and T. V. Yanchuk, Fiz. Tekh. Poluprovodn. **30**, 2133 (1996) [Semiconductors **30**, 1111 (1996)].
[7] V. S. Vavilov, V. F. Kisilev, and B. N. Mukashev, *Defects in Silicon and at its Surface* (Nauka, Moscow 1990) [in Russian].
[8] L. G. Kimerling and J. L. Benton, Physica B **116**, 297 (1983).
[9] M. O. Aboelfotoh and B. G. Svensson, Phys. Rev. B **52**, 2522 (1995).
[10] M. A. Tranwaert, J. Vanhellemont, E. Simoen, C. Claeys, B. Johlander, L. Adams, and P. Clauws, IEEE Trans. Nucl. Sci. **39**, 1747 (1992).
[11] I. V. Antonova and S. S. Shaĭmeev, Fiz. Tekh. Poluprovodn. **29**, 605 (1995) [Semiconductors **29**, 315 (1995)].

Translated by Frank J. Crowne

SEMICONDUCTORS VOLUME 32, NUMBER 5 MAY 1998

# Creation of vicinal facets on the surface of gallium arsenide with orientations close to (100) under conditions of nonequilibrium mass transfer

M. V. Baĭzer, V. Yu. Vitukhin, I. V. Zakurdaev, and A. I. Rudenko

*Ryazan State Radio Engineering Academy, 391000 Ryazan, Russia*

(Submitted June 7, 1997; accepted for publication October 30, 1997)
Fiz. Tekh. Poluprovodn. **32**, 527–530 (May 1998)

The method of low-energy electron diffraction is used to investigate surfaces of GaAs misaligned by 3° from (001) as they are heated in vacuum to a temperature of $T=550$ °C in the field of a temperature gradient $\nabla T \simeq 50$ deg/cm. When no $\nabla T$ is present, a $(1\times4)$ structure forms at the surface, which is preserved under annealing for 1 hour. In the presence of $\nabla T$, reflection doublets appear along the direction [110], indicating a faceted surface. Analogous behavior is observed after the crystals are annealed with no $\nabla T$ at $T=$ 650–700 °C, when the evaporation of arsenic becomes noticeable. The calculated value of the atomic heat of transport $Q^*$ of 2.3 eV is close to $Q^*$ for transition metals, where it is associated with phonon drag by the atoms. © *1998 American Institute of Physics.* [S1063-7826(98)00305-6]

## 1. INTRODUCTION

In recent years, attention has focused on the faceting of vicinal surfaces of GaAs crystals in connection with the problem of making low-dimensional quantum structures. In Ref. 1 it was shown theoretically, and in Ref. 2 experimentally, that it is possible to use faceted surfaces to grow structures with one-dimensional electron gases. In Ref. 3 facet length was observed to affect the size of InAs quantum dots on the surface of GaAs. The authors of Ref. 4 formulated the problem of creating echelons of steps of rectangular form covering the entire surface of the crystal.

In Refs. 4 and 5 the authors used scanning tunneling microscopy (STM) to observe faceting of surfaces with orientations close to (100). In GaAs crystals, the facet surface energy ($\gamma$) varies with surface orientation in the order $\gamma(100)>\gamma(110)>\gamma(111)$, so that when the crystals are annealed under conditions of thermodynamic equilibrium, facets (‘‘natural roughness’’) are most likely to form on surfaces that are close in orientation to (111), while vicinal facets that are close in orientation to (100), and certain orientations close to (110), should be stable against faceting. The authors of Ref. 4 noted that the observed reconstruction of the vicinal (100) surface could possibly be related both to nonuniformity of the substrate heating temperature and to the flux of arsenic at the surface, as well as to noncongruent decomposition of the GaAs.

In this paper, low-energy electron diffraction (LEED) is used to study the change in morphology of the surface of GaAs crystals during annealing, both under conditions close to thermodynamic equilibrium and under conditions that are quite far off equilibrium, when significant evaporation of arsenic takes place and atoms drift along the surface under the action of a temperature gradient.

## 2. EXPERIMENTAL METHOD AND RESULTS

The objects of our investigation were vicinal surfaces misoriented by 3° with respect to (001) toward [110] [referred to in what follows as vicinal (001) surfaces] and by 4° relative to (110) toward [010] [vicinal (110) surfaces]. Films 400 $\mu$m thick were cut from a single crystal of brand AGChT-1 gallium arsenide, doped with tellurium to a concentration $N=(4— 5)\times10^{18}$ cm$^{-3}$. The surface of the films was processed by standard methods used in molecular beam epitaxy technology.[5] In the final stage, rectangular samples with dimensions $10\times15$ mm$^2$ cut from the films were further processed by electropolishing in a 3% solution of NaOH, which passivated the surface and made it possible to monitor the surface morphology using a scanning tunneling microscope operating under atmospheric conditions.[6] On the STM images we could see both atomically smooth regions and regions covered with a periodic profile of facets with a mean

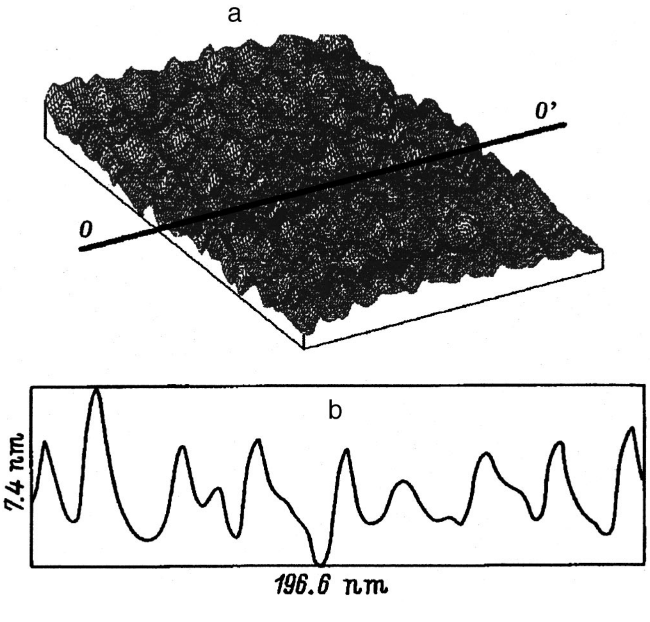

FIG. 1. STM image of faceted surface of gallium arsenide after passivation: a—three-dimensional image of a section with area ~297×196 nm$^2$, b—cross section along the direction $O-O'$.

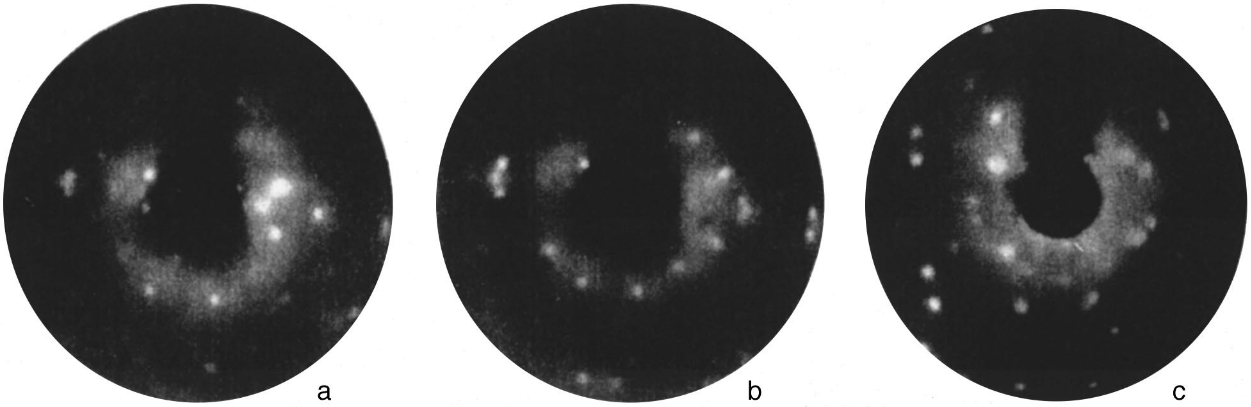

FIG. 2. Electron-diffraction patterns of a vicinal (001) GaAs surface subjected to high-temperature annealing: a— starting image after ion cleaning at $T=610$ °C for $t = 10$ min; b—after an additional anneal at $T=620$ °C for $t = 10$ min; c—after an additional anneal at $T=650$ °C for $t = 20$ min.

terrace width of approximately 20 nm and height 7 nm (Fig. 1). The facets, which occupied a large portion of the sample surface, are presumably the result of etching the surface during chemical processing.

The samples were simultaneously annealed and investigated by low-energy electron diffraction in a combination apparatus based on a Riber high-vacuum chamber at a pressure $p=2\times10^{-8}$ Pa. Cleanliness of the surface was monitored by Auger-electron spectroscopy. The apparatus was equipped with a system for ion etching. The samples were glued to the crystal holder with 7N pure indium foil. The temperature of the crystal holder $T$ was measured using an alumel-chromel thermocouple. The electron-diffraction patterns were observed at room temperature, the electron energy was varied from 110 to 130 eV. The diameter of the electron beam at the sample surface was roughly 1 mm.

After preliminary annealing of the samples at $T=600$ °C, the remainder of the carbon (~ 3% of a monolayer) was removed by ion etching. The density of argon ions was 3 $\mu$A/cm$^2$ at an energy of 500 eV. In order to recover the amorphized layer, after ion etching the samples were annealed for 10 min at $T=610$ °C. The electron-diffraction pattern for vicinal (001) after annealing is shown in Fig. 2a. Reflections without any well-defined symmetry appeared, and paired reflections (doublets) were visible, which suggested structural imperfection of the surface. Samples prepared in a similar fashion were annealed in different regimes.

*1. High-temperature annealing. Vicinal (001).* The temperature was gradually raised to 700 °C. Figure 2b shows the electron-diffraction pattern after the first anneal at $T=620$ °C for 10 min. The number of reflections is practically unchanged, but the distance between reflections that form doublets increases (compare with Fig. 2a). As the temperature is raised above 650 °C (for an anneal time of 20 min), the brightness of the reflections and their number increase, and the majority of the reflections appear in the form of doublets (Fig. 2c). Evaporation of arsenic atoms leads to coagulation of the gallium atoms into droplets, which is revealed by the ring-like arrangement of the reflections. Examination of a sample after annealing in the aperture of the electron microscope showed the presence of facets at the surface oriented along [110]; the edges of the facets are decorated with gallium droplets. The pattern observed is close to the STM image of the surface of vicinal (001) after annealing at a temperature of 670 °C under excess arsenic pressure, as shown in Ref. 5. Annealing at $T=700$ °C for 60 min leads to an increase in the size of the facets against a background of growth in the size of the gallium droplets. Steps are clearly visible in an optical microscope, and the length of a terrace is 5 to 7 $\mu$m; gallium droplets are located along the edges of the step. The surface of the sample acquires a matted form.

*2. Low-temperature anneal. Vicinal (001).* After annealing at $T=610$ °C (Fig. 2a), the temperature was lowered to $T=550$ °C and the sample was annealed for 30 min. The electron-diffraction pattern is shown in Fig. 3a. The reflections are aligned along the direction [110] forming a $(1\times4)$ structure. Intermediate reflections and doublets are not observed. The surface is level. Two anneals in succession for 15 minutes apiece do not change the pattern of reflections.

*3. Low-temperature anneal. Vicinal (110).* The regimes of annealing are analogous to previous. The electron- diffraction pattern is shown in Fig. 3b. A $(1\times1)$ structure forms. This structure is characteristic for the (110) facet. The surface is level, and no facet formation is observed.

*4. Low-temperature anneal in the field of a temperature gradient. Vicinal (001).* After annealing at $T=610$ °C, the temperature in the zone of observation behind the surface is lowered to $T=550$ °C and the annealing takes place in a nonuniform distribution of temperature along the sample. The temperature gradient was $\nabla T\simeq$ 50 deg/cm, and its direction coincided with the [110] direction. The annealing lasted 30 min. The electron-diffraction pattern (Fig. 4) is similar in form to that obtained for the high- temperature anneal. Elements of the $(1\times4)$ structure are preserved against a background of emerging intermediate reflections and doublets.

## 3. DISCUSSION OF RESULTS

It is clear from the electron-diffraction patterns (Figs. 3a and 3b) that annealing of vicinal (001) and vicinal (110)

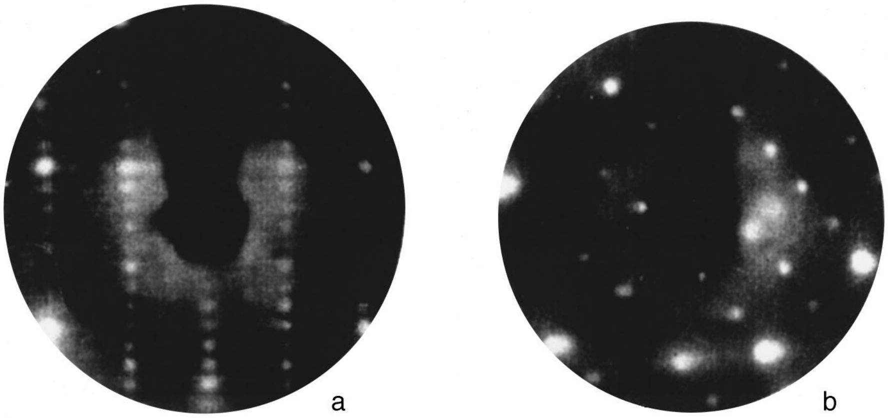

FIG. 3. Electron-diffraction pattern of the surface of GaAs subjected to low-temperature annealing: a—vicinal (001) after annealing at $T=550$ °C for $t = 30$ min; b—vicinal (110) after annealing at $T=550$ °C for $t = 30$ min.

under conditions close to thermodynamic equilibrium, when evaporation of arsenic from the surface is compensated by diffusion from the bulk,[7] does not cause facets to form. In contrast, facets form easily during short-period anneals on surfaces close in orientation to (111), which has the minimum surface energy, even when $T=300$ °C.[7] The process is identical to that observed in metals,[8] i.e., for vicinal surfaces of GaAs that are close in orientation to (100) and (110), which do not have the minimal surface energy, the faceting is probably caused by the diffusion process kinetics. The mechanism for formation of facets during sublimation or condensation of atoms has been studied in many papers, for example, for vicinal (110) of GaAs in Ref. 9. Therefore, we will concentrate on the process of faceting due to thermal diffusion of atoms.

The process of faceting caused by thermal diffusion or electrodiffusion of atoms has a threshold character. The external force causing the mass transport must exceed the force caused by the curvature of the surface (the Laplace pressure).[10] According to the thermodynamics of irreducible processes, the force that causes thermal diffusion of atoms can be written in the form

$$F=(Q^*/T)\nabla T, \tag{1}$$

where $Q^*$ is the heat of transport (the effective amount of heat transported by an atom during the diffusion process).

Semiconductors are characterized by a large phonon contribution to the process of thermal conduction. A flux of phonons as quasiparticles gives rise to a flux of atoms (the phonon wind). The phonon contribution to the heat of transport is[11]

$$Q^*=\frac{\sigma}{v}\kappa T, \tag{2}$$

where $\sigma$ is the cross section for scattering of phonons by activated (diffusing) atoms, $v$ is the velocity of sound, and $\kappa$ is the phonon contribution to the thermal conductivity.

For GaAs we can take the following: the minimum value of $\sigma\sim10^{-15}$ cm$^2$ (Refs. 11 and 12), $v=4\times10^5$ cm/s, and $\kappa=0.16$ W/cm·K at $T=900$ K.[12] Substituting these values into Eq. (1), we obtain $Q^*=$ 2.3 eV. The contributions of kinetic and electronic mechanisms to the atomic drag are estimated to be negligible compared to the value due to phonons.

Substituting the computed value of $Q^*$ into Eq. (1), $\nabla T=$ 50 deg/cm and $T=820$ K, we obtain $F=$ 0.14 eV/cm. For transition metals the threshold value of the external force that causes faceting is 0.2 to 0.3 eV/cm.[8] Since the surface energy of GaAS is 1.5 to 2 times lower than the surface energy of transition metals, the value we obtain for $F$ is close to threshold.

Based on the growth rate of the facets we can estimate the coefficient of surface diffusion of atoms $D_s$. Assuming that the mass transport takes place within the developing facet, which is confirmed by the STM studies of electrodiffusion-driven faceting on silicon reported in Ref. 13, it is not difficult to calculate the rate of drift of the atoms. When a GaAs crystal is annealed for $t=30$ h under conditions where $\nabla T=$ 150 deg/cm and the anneal temperature in the zone of observation at the surface is $T=550$ °C, we observed the formation of wave-like facets with a period of up to 6 $\mu$m and a height of 1 $\mu$m. The formation of such facets is possible for atomic drift rates $V=1\times10^{-8}$cm$^2$/s. Using

FIG. 4. Electron-diffraction pattern of vicinal (001) facet of GaAs annealed in the field of a temperature gradient $\nabla T\simeq$ 50 deg/cm, $T=550$ °C, for $t=30$ min.

the formula $V=(D_s/kT)F$ we then find $D_s=2\times 10^{-9}\,\text{cm}^2/\text{s}$. The authors of Ref. 9 found that $D_s=2.5\times 10^{-9}\,\text{cm}^2/\text{s}$ for the (110) facet, and the authors of Ref. 14 found $D_s=0.4\times 10^{-9}\,\text{cm}^2/\text{s}$ for the (001) facet. This latter value of $D_s$ was obtained for migration of gallium along a surface enriched by gallium. In Ref. 14 it is shown that the surface diffusion of gallium along a surface enriched by arsenic is two orders of magnitude lower. From this we may assert that the observed faceting process is determined by the thermal diffusion of gallium along the crystal surface and the calculated value of $Q^*$ probably applies to a gallium atom.

Thus, these studies have shown that formation of echelons of steps on vicinal surfaces of GaAs close in orientation to (100) is possible when the crystals are annealed under conditions where evaporation or condensation of arsenic takes place, or when the flow of atoms is organized along the surface by thermal diffusion or electrodiffusion.

[1] A. Monakov and A. Shik, *Abstracts of Invited Lectures of the International Symposium on ''Nanostructures''* (St. Petersburg, Russia, 1994), p. 159.

[2] V. I. Kadushkin, V. A. Kul'bachinskiĭ, E. V. Bogdanov, and A. P. Senichkin, Fiz. Tekh. Poluprovodn. **28**, 1889 (1994) [Semiconductors **28**, 1042 (1994)].

[3] N. N. Ledentsov, M. V. Maksimov, G. É. Tsyrlin, V. N. Petrov, and G. M. Gur'yanov, Fiz. Tekh. Poluprovodn. **29**, 1295 (1995) [Semiconductors **29**, 671 (1995)].

[4] A. O. Golubok, G. M. Gur'yanov, N. N. Ledentsov, V. N. Petrov, Yu. B. Samosenko, S. Ya. Tipisev, and G. É. Tsyrlin, Fiz. Tekh. Poluprovodn. **28**, 516 (1994) [Semiconductors **28**, 317 (1994)].

[5] A. O. Golubok, G. M. Gur'yanov, N. N. Ledentsov, V. N. Petrov, Yu. B. Samosenko, S. Ya. Tipisev, and G. É. Tsyrlin, Fiz. Tekh. Poluprovodn. **28**, 903 (1994) [Semiconductors **28**, 526 (1994)].

[6] V. Yu. Vitukhin, I. V. Zakurdaev, O. V. Kireeva, and A. I. Rudenko, Bull. Russ. Acad. Sci., Ser. Phys. **60**(7), 180 (1996) [in Russian].

[7] A. J. Van Bommel, J. E. Crombeen, and T. G. Van Oirschat, Surf. Sci. **72**, 95 (1978).

[8] I. V. Zakurdaev, O. V. Kireeva, and A. I. Rudenko, Bull. Acad. Sci. USSR, Phys. Ser. **40**(8), 1554 (1976) [in Russian].

[9] M. Krishnamurthy, M. Wassermeier, D. R. Williams, and P. M. Petroff, Appl. Phys. Lett. **62**, 1922 (1993).

[10] Ya. E. Geguzin and Yu. S. Kaganovskiĭ, *Diffusion Processes at the Surface of a Crystal* (Energoatomizdat, Moscow, 1984), p. 124 [in Russian].

[11] V. B. Fiks, *Ionic Conductivity in Metals and Semiconductors* (Nauka, Moscow, 1969), p. 296 [in Russian].

[12] G. Drabl and G. Goldsmit, *Thermal Conductivity of Semiconductors* [Russian trans., IL, Moscow, 1963], p. 266.

[13] H. Tokumoto, K. Miki, Y. Morito, T. Sato, M. Iwatsuki, M. Suzuki, and T. Fukuda, Ultramicroscopy **42–44**, 816 (1992).

[14] S. Nagata and T. A. Tanaka, J. Appl. Phys. **48**, 940 (1977).

Translated by Frank J. Crowne

SEMICONDUCTORS VOLUME 32, NUMBER 5 MAY 1998

## ELECTRONIC AND OPTICAL PROPERTIES OF SEMICONDUCTORS

# A quantum-well model and the optical absorption edge in structurally nonuniform *a*-Si:H-based alloys

B. G. Budagyan, A. A. Aĭvazov, D. A. Stryakhilev, and E. M. Sokolov

*Moscow Institute of Electrical Engineering, 103498 Moscow, Russia*

(Submitted June 10, 1997; accepted for publication October 2, 1997)
Fiz. Tekh. Poluprovodn. **32**, 531–536 (May 1998)

This paper describes studies of the microstructure and optical absorption edge of films of $a$-Si : H and $a$- SiN$_x$ : H alloys ($x = 0.0$–$0.72$), obtained by decomposing gas mixtures in an rf glow discharge. For the $a$-Si : H films, the gas mixture was monosilane diluted by hydrogen, for the $a$-SiN$_x$ : H alloys it was $SiH_4 + NH_3$. Structurally nonuniform films with ''device-quality'' optoelectronic characteristics were obtained when the rates of growth were increased (to 8 Å/s). Atomic force microscopy and infrared absorption spectroscopy are used to identify a characteristic feature of the microstructures of these films: the presence of islets $\sim$500 Å in diameter, whose boundaries are formed by clusters of hydrogen atoms (in the case of $a$-Si : H) or of hydrogen and nitrogen (in the case of $a$-SiN$_x$ : H). In this case the optical band gap of $a$-Si : H ($a$-SiN$_x$ : H) is determined by the concentration of SiH (SiN) bonds in the interior of the islets and is not sensitive to changes in the content of hydrogen (nitrogen) at their boundaries. This result is explained by a quantum-well model which takes into account the characteristic sizes of the microstructures formed by hydrogen or nitrogen atoms.
[S1063-7826(98)00405-0]

## 1. INTRODUCTION

Since hydrogenated amorphous silicon ($a$-Si : H) and alloys based on it are very attractive materials for making a multitude of electronic devices (solar energy elements, thin-film field effect transistors, photodetectors, light emitting devices, etc.), their physical properties have been the subject of many investigations. A fact of particular interest to researchers is the interrelation between structural peculiarities and the distribution of electronic states. This is explained by the tendency to develop the most detailed descriptions (''optimal material''), where the impact on practical applications is greatest (solar cells, thin-field effect transistors, and various types of photodetector setups) and by the fact that $a$-Si : H, due to its availability and the feasibility of controlling its material properties as it is made, is an extremely convenient object for studying the regularities of electronic spectra in amorphous semiconductors.

A series of papers[1–4] have identified several factors that affect the position and shape of the optical absorption edge in $a$-Si : H. The most important of these is structural disorder,[1,2] which acts to distort the lines and bond angles of the amorphous silicon network compared to the ideal diamond structure, and the influence of atoms of other kinds, such as hydrogen, carbon, nitrogen, etc.[3,4] However, it has also been shown that simply invoking the dependence of the shape of the optical absorption edge on these structure-related factors cannot explain the multitude of existing experimental data.

The most important qualitative model that can reproduce the fundamental features of the electronic spectra of $a$-Si : H, starting from compositional nonuniformity of the material, is the quantum-well model proposed by Brodsky.[5] Quantitative calculations based on this model[6,7] allow us to obtain good agreement with experimental results for the parameters of the electron state distribution near the zone edge and in the band gap; however, they disregard the possible existence of various kinds of microstructures in $a$-Si : H and related alloys made up of atoms such as hydrogen, carbon, nitrogen, etc.

In this paper we investigate the interrelation between the optical band gap and microstructures in $a$-Si : H and $a$-SiN$_x$ : H, and discuss our results within the framework of a quantum-well model modified so as to take into account the characteristic dimensions of microstructures formed by atoms of hydrogen and nitrogen.

## 2. EXPERIMENT

Films of $a$-Si : H were obtained by rf decomposition of monosilane diluted with hydrogen in the ratio $10\%SiH_4 + 90\%H_2$. The frequency at which the glow discharge was excited was 13.56 MHz.

In order to obtain films with varying hydrogen content and different microstructures, the deposition conditions, i.e., the various combinations of discharge power, pressure, and gas discharge rate, were varied in the following limits: the specific power of the rf discharge $W=0.10$–$0.18$ W/cm$^2$, pressure $P=1$–$2.5$ Torr, and gas flow rate $Q=30$–$100$ cm$^3$/min. The temperature of the substrate was maintained at a constant level of 300 °C.

These fabrication regimes ensured deposition of films with thickness 0.8–1.4 $\mu$m at growth rates of 3.3–7.3 Å/s.

Samples of $a$-SiN$_x$ : H were obtained by decomposing the mixture (10% SiH$_4$ + 90% H$_2$ + NH$_3$). The substrate temperature, pressure, and specific rf power (13.56 MHz) in the discharge were 220 °C, 0.38 Torr, and 0.3 W/cm$^2$, respectively. The films were deposited in the presence of various partial pressures of ammonia (0–0.03 Torr), so that films of $a$-SiN$_x$ : H were obtained with compositions $x = 0$–$0.72$.

Plates of glass and single-crystal Si (KDB-10) were used as substrates.

The morphology of the film surface was investigated with an atomic force microscope (AFM) made by the NT-MDT company (Russia). The cantilever of the microscope, whose tip had a radius of curvature of 20 nm, was made of silicon nitride. The measurements were made in the contact regime with a resolution of 8–25 Å and a scanning rate of 100 000–300 000 Å/s (Ref. 8).

The film composition and local configurations made up of atoms of hydrogen and nitrogen were identified by infrared (IR) spectroscopy. IR spectra of films on single-crystal silicon substrates were measured in a two-beam spectrometer SPECORD-M80. The film components were identified according to the method proposed in Ref. 9. First, we used the width of the absorption band centered at 630 cm$^{-1}$ to estimate the concentration of bound hydrogen. Then, by resolving the band, whose main peak is at 2000 cm$^{-1}$, into two peaks with frequencies 2000 and 2100 cm$^{-1}$, we were able to estimate the so-called microstructure parameter $R = I_{2100}/(I_{2000} + I_{2100})$, where $I_{2000}$ and $I_{2100}$ denote integrals of the absorption taken over the corresponding peaks. We then could calculate values of the concentration of hydrogen in the form of single and clustered SiH bonds starting from the total hydrogen content and value of the microstructural parameter $R$.[10]

According to identification given in Refs. 11 and 12, infrared spectra of the alloys $a$-SiN$_x$ : H, contain features that correspond to the bonds SiH, SiN, and NH. In order to define the total concentration of nitrogen in the films we used peak intensities at 850 and 3350 cm$^{-1}$ (Ref. 13).

The optical transmission spectra of $a$-Si : H and $a$-SiN$_x$ : H films were measured using a two-beam spectrometer SPECORD-M40 in the wavelength range 300– 900 nm. Based on this data we calculated the absorption spectra of samples corresponding to interband transitions and estimated the value of the optical band gap by the method of Tauc.

## 3. RESULTS

*a-Si : H films.* Typical images of the surface of $a$- Si : H films obtained in the atomic force microscope are shown in Fig. 1. It is clear that the film has a nonuniform structure in which islets and inter-islet boundaries can be distinguished. The characteristic dimensions of these islets range from 300 to a few thousand angstroms.

In Fig. 2 we plot the optical band gap $E_G$ versus the total concentration of hydrogen [H], as well as the concentrations of single ([SiH]) and clustered ([SiH$_x$]) SiH bonds. Is is clear that only Fig. 2b, where $E_G$ is plotted as a function of [SiH], suggests a monotonic dependence. In contrast, Figs. 2a and 2c, where $E_G$ is plotted versus [H] and [SiH$_x$], exhibit no correlation between the quantities being plotted.

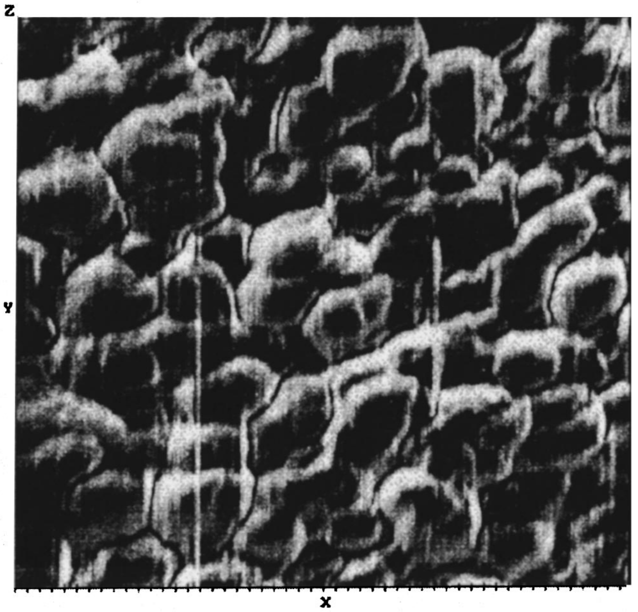

FIG. 1. Typical image of the surface of a $a$-Si : H film obtained by the method of atomic force microscopy.

*a-SiN$_x$: H films.* As shown in Ref. 12, several types of local environment for the SiN bond are possible in $a$-SiN$_x$ : H alloys, with differing longitudinal vibrational frequencies. The corresponding infrared absorption bands are shown in Fig. 3. A strong symmetric peak dominates the spectra of all the samples at a wave number 850 cm$^{-1}$. For the two samples with the minimum nitrogen content

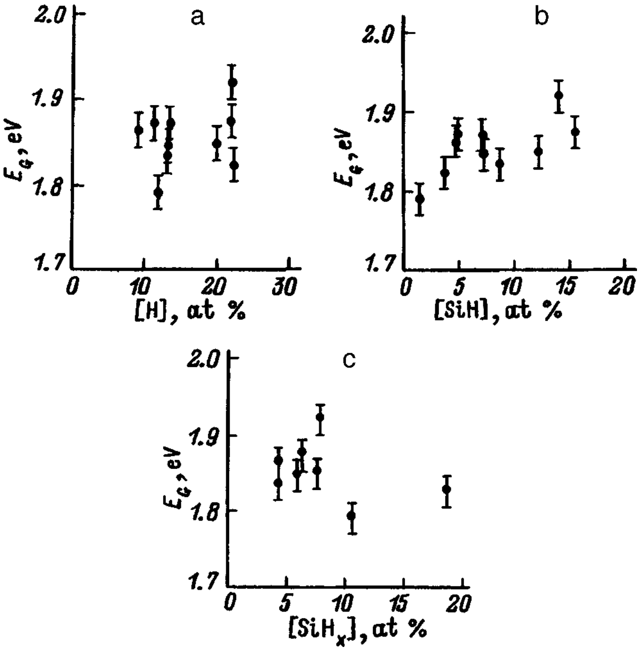

FIG. 2. Dependence of the optical band-gap $E_G$ on the total content of hydrogen [H] (a), and also on the concentration of isolated (b) and clustered (c) [SiH] bonds.

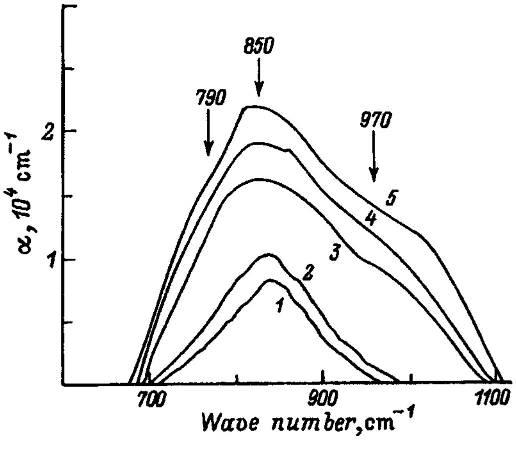

FIG. 3. Infrared absorption bands caused by longitudinal vibrations of SiN bonds in $a$-SiN$_x$ : H alloys with varying nitrogen content. [N]/[Si]: *1* — 0.13, *2* — 0.17, *3* — 0.53, *4* — 0.62, *5* — 0.72.

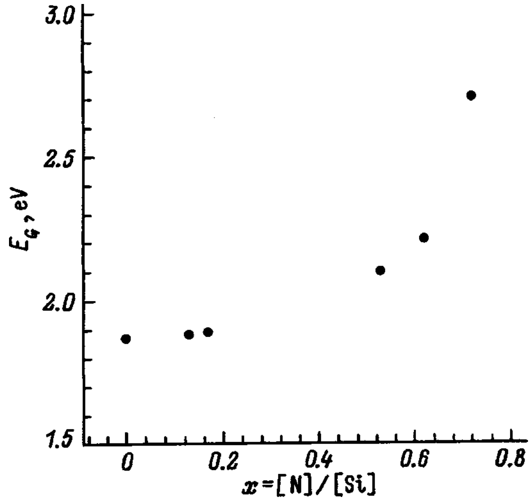

FIG. 5. Dependence of the optical band gap on nitrogen content in $a$-SiN$_x$ : H alloys.

($x$ = 0.13 and $x$ = 0.17), this peak was the only spectral feature observed in the range 700–1000 cm$^{-1}$. An increase in nitrogen concentration is accompanied by the appearance of features at 790 and 970 cm$^{-1}$, which correspond to nitrogen atom surrounded by three Si atoms and Si$_4$N$_9$ clusters, which cause the shape of the band to change and become asymmetric.

In the $a$-SiN$_x$ : H alloys, increasing the nitrogen content leads to an increase in the frequency of the principal peak of the longitudinal vibrational band for SiH bonds (Fig. 4). This fact, together with the presence of a strong peak at 850 cm$^{-1}$ (Fig. 3), implies that a characteristic local structure in our $a$-SiN$_x$ : H films consists of nitrogen and hydrogen atoms bonded to the same silicon atom.[12]

The dependence of the optical band gap on nitrogen content in $a$-SiN$_x$ : H films is shown in Fig. 5. At comparatively low concentrations of nitrogen ($x \leqslant 0.17$) the optical band gap does not differ from that of a $a$-Si : H film obtained for the same values of discharge power, pressure, and substrate temperature (1.87 ± 0.02 eV), at least within the error limits for the method used to determine it. However, when $x$=0.53–0.72, we find that $E_G$ increases from 2.11 to 2.72 eV.

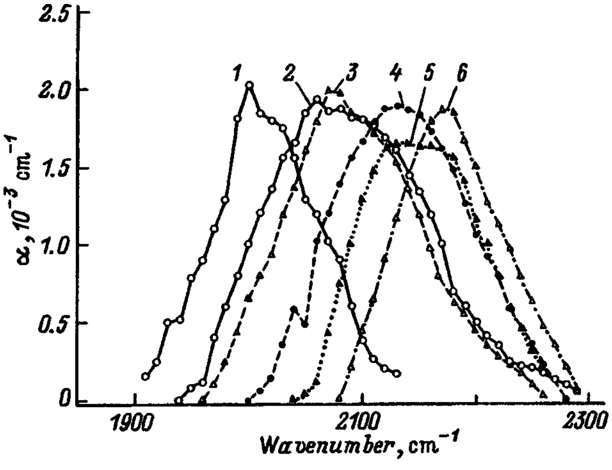

FIG. 4. Infrared absorption bands caused by longitudinal vibrations of SiH bonds in $a$-SiN$_x$ : H alloys with varying nitrogen content. [N]/[Si]: *1* — 0, *2* — 0.13, *3* — 0.17, *4* — 0.53, *5* — 0.62, *6* — 0.72.

We previously investigated the microstructures of $a$-Si : H and $a$-SiN$_x$ : H films obtained under analogous fabrication conditions by transmission electron microscopy (TEM). A description of our experimental method and the TEM images themselves are given in Ref. 14. For films of $a$-Si : H and $a$-SiN$_x$ : H we observed a nonuniform structure with clearly delineated ''islets.'' In this case the characteristic dimensions (400–500 Å) and shape of the islets were similar to those observed in surface images obtained by AFM (Fig. 1). As we have shown, the islets have a higher density and are made up primarily of Si–Si bonds, whereas hydrogen concentrates primarily along the boundaries of these islets, forming polyhydride configurations with clustered SiH bonds. Thus, for $a$-Si : H the value of [SiH] gives the concentration of bound hydrogen in the bulk of the islets, whereas that of [SiH$_x$] should be assigned to hydrogen at internal boundaries.

Modifications of the microstructure in $a$-SiN$_x$ : H alloys of intermediate composition ($x$=0.13 and 0.17) are associated primarily with decreased hydrogen content at the internal boundaries. In light of the spatial correlation between SiH and SiN bonds, and also the TEM results mentioned above, we should assign the infrared absorption band with frequency 850 cm$^{-1}$ (longitudinal vibrations of the SiN bond), and the peak shifted towards high frequencies corresponding to longitudinal vibrations of the bond SiH, to N and H atoms located within the internal boundaries. At the same time, atoms of nitrogen located within the islet interior are responsible for the absorptions at 790 and 970 cm$^{-1}$. Thus, in alloys with low nitrogen content ($x$=0.13 and 0.17) the SiN bonds are located primarily along the grain boundaries, whereas in alloys with higher concentrations of nitrogen the SiN bonds also appear within the bulk of the material.

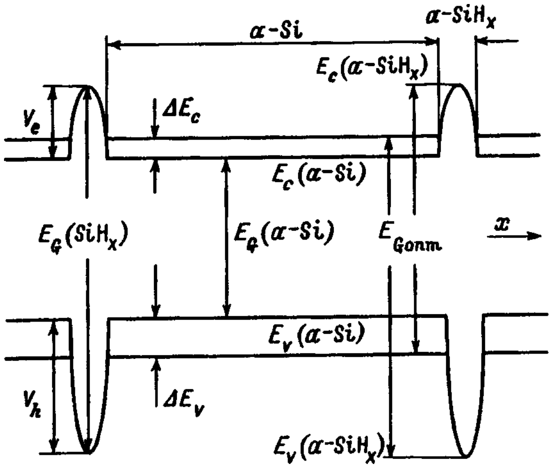

FIG. 6. Sketch of energy bands in the Brodsky quantum-well model.

## 4. QUANTUM-WELL MODEL

A sketch of the energy bands of $a$-Si : H corresponding to the quantum-well model is shown in Fig. 6. According to Ref. 5, $a$-Si : H consists of a wide-gap phase corresponding to regions with increased hydrogen content ($a$-SiH$_x$), and a narrow-gap phase consisting of practically ''pure'' amorphous silicon. Electrons with energies from $E_C(a\text{-Si})$ to $E_C$ $(a\text{- Si})+V_e$ and holes with energies from $E_V(a\text{- Si})\text{-}V_h$ to $E_V$ $(a\text{-Si})$ are localized. Here $V_e$ and $V_h$ are the values of the corresponding potential barriers.

The quantities $\Delta E_C$ and $\Delta E_V$ denote energies of stationary states of electrons and holes in potential wells, and depend on the particle effective mass, the values of the corresponding potential barriers, and the sizes of the potential wells. According to the Brodsky model,[5] the optical absorption edge is determined by transitions between pairs of states with energies $E_V(a\text{-Si})\text{-}V_h$ and $E_C(a\text{-Si})+\Delta E_C$, or $E_V$ $(a\text{-Si})\text{- }\Delta E_V$ and $E_C(a\text{-Si})+V_e$. Thus, we can use the values of these steady-state energies averaged over the ensemble of potential wells to discuss the dependence of the optical width of the band gap on the concentration of hydrogen and the nature of its distribution. Since the position of the valence-band edge is much more sensitive to hydrogen content in $a$-Si than the position of the conduction-band edge, we restrict the discussion to the behavior of the average value of steady-state energies for holes.

In order to discuss the dependence of the optical width of the band gap on the hydrogen concentration, it is necessary to calculate the quantity

$$\langle \Delta E_V \rangle (x) = \int_0^\infty \Delta E_V(V) f_v(V,x) dV, \tag{1}$$

where $\langle \Delta E_V(x) \rangle$ is the energy of a hole stationary state averaged over the potential well ensemble, $\Delta E_V(V)$ is the energy of a stationary state corresponding to a potential well with volume $V$, and $f_v(V,x)$ is the probability density for the distribution of potential wells as a function of hydrogen concentration $x$. Equation (1) implies that the sensitivity of the optical band gap to changes in the hydrogen content of the film is given by the distribution of quantum-well volumes. Using the results of Ref. 7, we write the following expression for the function $f_v(V,x)$ for a uniform distribution of hydrogenic clusters:

$$f_v(V,x) = \begin{cases} \lambda(x)\exp(-\lambda(x)V), & \text{V} \geqslant 0, \\ 0, & \text{V} < 0. \end{cases} \tag{2}$$

In Eq. (2), $\lambda(x)$ is the average number of SiH clusters per unit volume for a given hydrogen concentration $x = [\text{H}]/[\text{Si}]$. The function $\lambda(x)$ is determined by the dimensions of the hydrogen clusters and grows monotonically with increasing $x$.

The average potential-well volume for the distribution (2) is determined by $\lambda(x)$:

$$\langle V \rangle (x) = \frac{1}{\lambda(x)}. \tag{3}$$

In what follows, we will propose a certain modification of the approach given in Ref. 15 in order to take into account the effect of the dimensions of the hydrogenic microstructures. Relation (3) will be used in order to relate the function $\lambda(x)$ to characteristic dimensions of the experimentally observed microstructures.

Let us assume that

$$\lambda(x) = \gamma x \tag{4}$$

is a linear dependence, where $\gamma$ is the coefficient of proportionality. Citing the well-known results of nuclear magnetic resonance (NMR) studies of Ref. 16, O'Leary *et al.*[7] proposed that the dominant type of hydrogen bonding was via clusters which consist of six SiH bonds and which occupy a volume equivalent to a unit cell in a Si crystal (160 Å$^3$). Using Eqs. (3) and (4), we find that the quantity $\gamma$ for this case is $\sim 10^{-3}$ Å$^{-3}$ (for $x = [\text{SiH}]/[\text{Si}] \sim 0.1$), and that the average diameter of a potential well is roughly 10 Å. However, in our $a$-Si : H films we observed a structure with characteristic dimensions $\geqslant$ 300 Å, which corresponds to $\gamma \sim 10^{-7} - 10^{-8}$ Å$^{-3}$ for the same hydrogen concentration.

The average value of the steady-state energy of an ensemble of potential wells with identical shapes and identical values of the potential barrier height $U_0$ can be written as

$$\langle \Delta E_V \rangle (x) = U_0(1 - \exp(-V_{\text{crit}}\lambda(x))) + \int_{V_{\text{crit}}}^\infty \Delta E_V(V) f_v(V) dV, \tag{5}$$

where the ''critical'' volume $V_{\text{crit}}$ is the maximum volume for which stationary levels coincide with the edge of the continuous spectrum, i.e., $\Delta E_V = V_h$.

The value of critical volume $V_{\text{crit}}$ and the dependence of the steady-state energy on the volume of the potential well $\Delta E_V(V)$ are determined by the height of the energy barrier $U_0$ and the effective mass $m^*$ of the particles (in our case, holes). For spherical potential wells[7,17] we have

$$V_{\text{crit}} = \frac{\pi^4}{6} \left( \frac{h^2}{2m^* U_0} \right)^{3/2} \tag{6}$$

and

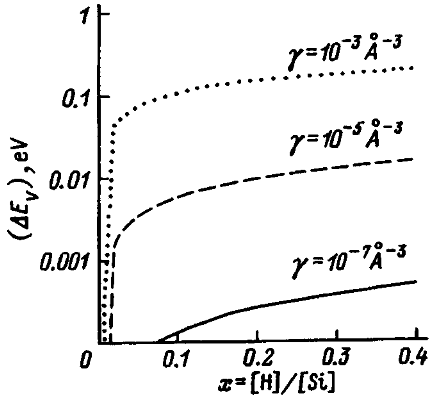

FIG. 7. Width of the optical band gap of $a$-Si : H versus hydrogen content. The three curves correspond to three different methods for distributing the hydrogen determined by the value of the parameter $\gamma$.

$$k\cdot\cot(kL)=-\sqrt{\frac{2m^{*}U_0}{h^2}-k^2}, \tag{7}$$

where $k=\sqrt{2m^{*}(U_0-|E'|)}$, $V=\frac{4}{3}\pi L^3$, $E'=U_0-E$, and $E$ is the energy of a particle measured from the bottom of a potential well.

Values of the model parameters were chosen from the following considerations. The effective mass of a hole, in accordance with Ref. 5, was assumed to be $m_h^{*}=0.5m_0$, where $m_0$ is the free electron mass. In order to estimate the height of the barrier for holes, we must determine the band gap for the narrow-gap and wide-gap phases, and also the value of the energy barrier for electrons. For the first we take the well-known extrapolated value of 1.6 eV,[1] corresponding to zero hydrogen concentration. According to Ref. 5, the value of the energy barrier for electrons can be estimated by starting from the activation energy for drift mobility. This quantity usually is about 0.1 eV for $a$-Si : H.[15] In estimating the band gap of the wide band phase, we follow Refs. 5 and 7, where $E_G(\mathrm{SiH}_x)\approx$ 2 eV. Thus, the value of the potential-barrier height for holes $V_h=E_G(\mathrm{SiH}_x)-E_G(a\text{-Si})-V_e$ is 0.3 eV.

The average steady-state energy $\langle E_V\rangle=E_G(a\text{-}Si{:}H)-E_G(a\text{-Si})$ is plotted versus hydrogen content in Fig. 7 for various values of $\gamma$. The largest change in $\langle E_V\rangle$ with hydrogen content (which increases by $\sim$ 0.3 eV as $x$ increases from 0.1 to 0.4) is observed for $\gamma=10^{-3}$ Å$^{-3}$. In this case the quantity $d\langle\Delta E_V\rangle/d[\mathrm{H}]$ (which is an estimate of the longitudinal $dE_G/d[\mathrm{H}]$) amounts to approximately 0.01 eV/atomic %, which is in good agreement with the data of Ref. 1. On the other hand, for $\gamma=10^{-5}-10^{-7}$ Å$^{-3}$ the quantity $\langle\Delta E_V\rangle$ is nearly independent of hydrogen content.

The functions shown in Fig. 7 allow us to determine the "dissolved" and "clusterized" forms of SiH bonds within the framework of this model. The dissolved form of the SiH bond ($\gamma\sim10^{-3}$) includes single bonds and fairly small clusters, which are formed by a few SiH bonds and which occupy a volume of the same order of magnitude as the unit cell of single-crystal silicon. If this kind of hydrogen bonding is predominant, then the average size of the "islands" (potential wells) is $\sim$10 Å, and the optical width of the band gap of the two-phase system is strongly dependent on the hydrogen content.

The clusterized form presumes the presence of larger-scale clusters that form nonuniformities (internal boundaries) with characteristic dimensions of several tens of nanometers ($\gamma\sim10^{-5}-10^{-7}$). A change in the content of hydrogen in the clusterized phase has practically no effect on the optical band gap.

This model can also be extended to the case of alloys of Si with nitrogen, carbon, and other elements, whose binding energy to Si is larger than the Si–Si bond energy. It is obvious that quantum-well models for these alloys differ primarily in the values of the energy barriers $V_e$ and $V_h$, which suggests that the optical band gap is sensitive to changes in composition for a preset value of $\gamma$, which is determined by the characteristic dimensions of the microstructure. At the same time, the qualitative regularities that determine the dependence of $E_G$ on these characteristic distances (i.e., the dependence of $\langle\Delta E_V\rangle$ on $\gamma$) will remain as before.

From the experimental data shown in Sec. 3 of this paper, it follows that the optical band gaps of $a$-Si : H and $a$-SiN : H alloys are determined by the number of SiH (SiN) bonds in the interior of the islets and do not depend on their concentration near the internal boundaries. In the framework of the quantum-well model as we have modified it, the case where the islet interior contains isolated hydrogen (nitrogen) or relatively small clusters corresponds to a high value of $\gamma$ ($\sim10^{-3}$ A$^{-3}$), and consequently strong sensitivity of $E_G$ to changes in the film composition (Fig. 7). If, however, atoms of hydrogen or nitrogen form a microstructure with characteristic dimensions that are approximately several hundred angstroms (boundaries of the islets), then $E_G$ is virtually independent of the concentration of hydrogen (nitrogen) atoms. Thus, our modification of the quantum-well model qualitatively reproduces the experimental dependence of the optical band gap of $a$-Si : H and $a$-SiN$_x$ : H films on composition and on the characteristic dimensions of the microstructure formed by hydrogen and nitrogen atoms.

## CONCLUSIONS

1. We have investigated the microstructure and optical absorption edge of structurally nonuniform $a$-Si : H and $a$-SiN$_x$ : H alloys obtained by decomposing silane-containing gas mixtures diluted by hydrogen in an rf glow discharge. AFM, TEM, and IR spectroscopy data all indicate that the fundamental microstructural elements in these films are islets enriched by Si along whose boundaries hydrogen is concentrated (in the case of $a$-Si : H) or hydrogen and nitrogen (in the case of $a$-SiN$_x$ : H). The characteristic size of these islets is $\sim$ 500 Å.

2. We have established that the value of the optical band gap of the films is determined by the hydrogen content (for $a$- Si : H) or nitrogen content (for $a$-SiN$_x$ : H), gases which are contained in the interior of grains, and that it does not depend on the concentration of these elements in the intergrain boundary region.

3. A modification of the well-known "quantum-well

model'' is proposed. In this model we take into account the characteristic size of the microstructure formed by hydrogen, nitrogen atoms, etc. This modified model satisfactorily explains the experimentally observed dependences of the optical band gap for $a$-Si : H-band alloys on their composition and microstructure.

We wish to thank V. Kh. Kudoyarova, and also to the NT-MDT Company, specifically, V. Bykov, A. Galoganov, and S. Nesterov, for collaboration in carrying out the experiments and for a discussion of the results.

The investigations whose results are reported in this article were carried out with the financial support of the INTAS Program (Contract No. 94-4352).

[1] G. D. Cody, Semicond. Semimet. **21B**, 11 (1984).
[2] M. B. Schubert, H.-D. Mohring, E. Lotter, and G. H. Bauer, IEEE Trans. **36**, 2863 (1989).
[3] A. P. Sokolov, A. P. Shebanin, O. A. Golikova, and M. M. Mezdrogina, J. Non-Cryst. Solids **137/138**, 99 (1991).
[4] J. Robertson, Philos. Mag. **63**, 47 (1991).
[5] M. H. Brodsky, Solid State Commun. **36**, 55 (1980).
[6] A. A. Klochikhin, Phys. Rev. B **52**, 979 (1995).
[7] S. K. O'Leary, S. Zukotinsky, and J. M. Pierz, J. Appl. Phys. **78**, 4282 (1995).
[8] B. G. Budagyan, A. Aivazov, A. Yu. Sazonov, A. A. Popov, and A. E. Berdnikov, *Mater. Res. Soc. Spring Meeting* (San Francisco, USA, 1997).
[9] A. A. Langford, M. L. Fleet, B. P. Nelson, W. A. Lanford, and N. Maley, Phys. Rev. B **45**, 367 (1992).
[10] S. Chattopadhay, S. N. Sharma, R. Banarjee, D. M. Bhusari, S. T. Kshirsagar, Yan Chen, and D. L. Wiliamson, Appl. Phys. Lett. **76**, 5208 (1994).
[11] J. W. Osenbach and W. R. Knolle, J. Appl. Phys. **60**, 1408 (1986).
[12] G. Lucovsky, J. Yang, S. S. Chao, J. E. Tyler, and W. Czubatyj, Phys. Rev. B **28**, 3234 (1983).
[13] E. Bustarret, M. Bensouda, M. C. Habrard, J. C. Bruyere, S. Pouline, and S. C. Gujrathi, Phys. Rev. B **38**, 8171 (1988).
[14] B. G. Budagyan, A.A. Aivazov, and A. Yu. Sazonov, Physica B **193**, 195 (1994).
[15] J. M. Marshall, R. A. Street, and M. J. Thompson, Philos. Mag. B **54**, 51 (1986).
[16] J. Baum, K. K. Gleason, A. Pines, A. N. Garroway, and J. A. Reimer, Phys. Rev. Lett. **56**, 1377 (1986).
[17] L. D. Landau and E. M. Lifshitz, *Quantum Mechanics: Nonrelativistic Theory* (3rd ed. Pergamon Press, Oxford, 1977)[Russ. orig. Nauka, Moscow, 1989].

Translated by Frank J. Crowne

# Stimulated-emission spectrum arising from interband absorption of a picosecond optical pulse in a thin layer of GaAs

I. L. Bronevoĭ and A. N. Krivonosov

*Institute of Radio Engineering and Electronics, Russian Academy of Sciences, 103907 Moscow, Russia*

(Submitted October 1, 1997; accepted for publication October 10, 1997)
Fiz. Tekh. Poluprovodn. **32**, 537–541 (May 1998)

Pumping a thin layer of GaAs with a high-power picosecond optical pulse leads to nonstationary edge emission. Experimental data are obtained for the way the time-integrated power spectrum of this emission varies with beam diameter and energy of the optical pump pulse. These data are sufficient to confirm the stimulated nature of the emission, whose duration is in the picosecond time range. © *1998 American Institute of Physics.* [S1063-7826(98)00505-5]

It is well known (see, e.g., Refs. 1–4) that interband absorption of a high-power ultrashort light pulse in a thin layer of direct-gap semiconductor leads to high-power, recombination-induced edge emission (referred to simply as emission in what follows) with an anomalously fast (picosecond) rise time. Within ~ 10 ps after the end of the excitation pulse, the emission decays, i.e., the duration of the emission pulse is in the picosecond time range. It is assumed that this emission is a stimulated emission which arises as a result of amplification of spontaneous emission in the photoexcited semiconductor. This assumption is based on the following evidence. First of all, the characteristic relaxation time of the emission is considerably shorter than the relaxation time for spontaneous emission in GaAs, which is ~ 1 ns. Secondly, emission is not observed until the carrier concentration exceeds threshold, that is when $\mu_e - \mu_h > E_g$ (Ref. 3), and an optical gain spectrum appears in the photoexcited medium, as observed, e.g., in Refs. 5 and 6 (here $\mu_e$ and $\mu_h$ are the quasi-Fermi levels of electrons and holes, and $E_g$ is the band gap).

However, it must be acknowledged that the available experimental data on this emission are clearly inadequate. We cannot obtain an exact representation of the characteristics of this emission *a priori*, since no existing theory can describe how the nonstationary (picosecond) stimulated emission in the thin semiconductor layer without a resonator depends on the parameters of the high-power, ultrashort, optical pump pulse. Such a theory must take into account the following phenomena: the nonstationary nature of the optical pumping; the substantial heating of the electron-hole plasma that generates the emission, which is caused by the excitation light and the emission itself;[7–11] the strong mutual coupling between the cooling of the electron-hole plasma and the radiation intensity;[9,11] the nonstationary and nonuniform spatial distribution of the electron-hole plasma;[11] etc. In light of this situation, experimental studies are needed to obtain a picture of how the emission is affected by the beam diameter $F$ and energy density $D_{\text{ex}}$ of the excitation pulse (also called the pump pulse). This paper describes our ongoing efforts to obtain such a picture. In our work, the duration of the pump pulse was 14 ps. We explain the effect of the beam paramaters on the emission as follows. Varying the energy density $D_{\text{ex}}$ should vary the rate of charge-carrier photogeneration and population inversion, while varying the beam diameter $F$ should vary the diameter of the active region of the medium that amplifies the light. However, measuring the dependences of the emission energy density on the diameter $F$ and excitation energy density $D_{\text{ex}}$ does not, in itself, offer sufficiently convincing proof of the stimulated nature of the emission. Such proof is obtained by investigating the emission spectrum. One of the most characteristic and well-studied properties of stimulated emission in semiconductors (see, e.g., Refs. 12–15) is narrowing of the emission spectrum, which takes place when spontaneous emission in a semiconductor is amplified by optical pumping. In our work we measured the emission spectrum at various values of energy density $D_{\text{ex}}$ of the excitation light pulse and beam diameter $F$. The behavior of the measured spectra qualitatively corresponds to changes in the spectrum predicted by the theory of steady-state stimulated emission in a laser medium without a resonator[16] and from the results of model calculations of stationary stimulated emission in a GaAs laser.[17] This has borne out the following experimental results: 1) the width of the emission spectrum decreases as the energy density $D_{\text{ex}}$ of the excitation pulse and the diameter $F$ increase once saturation is achieved; 2) the decrease in the emission spectral width $\Delta\hbar\omega_s$ has a universal character as a function of the product $D_{\text{ex}}F$; 3) the emission spectrum becomes concentrated in the longer-wavelength region as the energy density $D_{\text{ex}}$ or diameter $F$ increases. We emphasize that the observed narrowing of the emission spectrum and its concentration in the longer-wavelength region as the energy density of the excitation pulse increases is opposite to what should occur if the radiation were spontaneous. Amplification by optical pumping of the semiconductor causes the spectrum of spontaneous emission, according to Ref. 18, to become broader and to spread to the short-wavelength region.

The small number of experimental papers that investigate light emitted when a semiconductor without a resonator is pumped by ultrashort light pulses is probably a result of the following circumstances. First of all, exciting the emission requires a source of ultrashort, high-power light pulses.

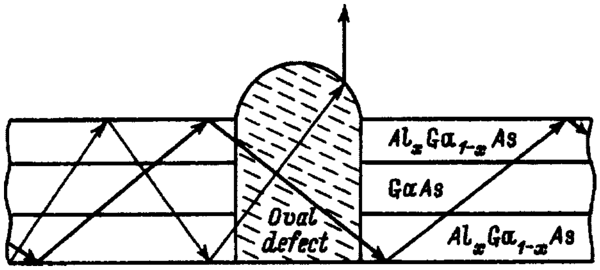

FIG. 1. Postulated scheme for output of radiation (shown by arrows) from a sample to the outside.

It is desirable that the photon energy $\hbar\omega_{\text{ex}}$ of this excitation light exceed the width of the band gap $E_g$ by only a small amount, so that the temperature $T_c$ of the resulting electron-hole plasma does not exceed the temperature of the crystal lattice by too much (for example, in Ref. 3 $T_c \simeq 470$ K). This facilitates the appearance of the emission. Secondly, it is necessary to find a way to guide the emission from the semiconductor layer to the outside. Epitaxial layers of semiconductors are waveguides. If the layer of semiconductor is ideally fabricated, strongly amplified spontaneous emission can escape to the outside only in the longitudinal direction, and even in this direction its escape is prevented by absorption in the unexcited portion of the sample. This is especially true for experiments at room temperature, as was shown in Ref. 1. Moreover, any emission that does reach the ends of the sample is reflected back. In this paper we identify characteristic features of stimulated emission by investigating the spectrum of light emitted orthogonal to the epitaxial layer, although it is often assumed that only spontaneous or slightly amplified emission can propagate in this direction. For readily apparent reasons, escape of light in the direction orthogonal to the layer can be mediated only by what heretofore has been called imperfections in the morphology of the heterostructure surface, part of which is the GaAs active layer under study (the heterostructure is described below). The imperfect morphology is due to so-called oval defects. These are a type of defect specific to molecular-beam epitaxy, the method used to grow the heterostructure. Oval defects range from 2 to 100 $\mu\text{m}^2$ in size (see Ref. 19), and are distributed quite uniformly over the sample (on the scale of the excited sample area). Figure 1 shows in a simplified way how they can facilitate the escape of light to the surface.

Our experiments were carried out at room temperature $T_R$. The sample under study was a $Al_{0.22}Ga_{0.78}As$–GaAs–$Al_{0.4}Ga_{0.6}As$ heterostructure with layer thicknesses $1.3-1.5-1.2$ $\mu$m grown on a (100) GaAs substrate. The concentration of background impurities in the heterostructure was $<10^{15}$ cm$^{-3}$. The substrate was etched away over an area of $4\times4$ mm$^2$. The layers of $Al_xGa_{1-x}As$, whose purpose was to stabilize surface recombination and provide mechanical hardness, were transparent to the light used in the experiment, for which $\hbar\omega<1.7$ eV. The sample was illuminated with 14-ps high-power light pulses, incident on the sample at an angle of $\sim10°$ with respect to the normal at its surface. The photon energy of the excitation light $\hbar\omega_{\text{ex}}=1.485$ eV exceeded the band gap of GaAs by 60 meV. Interband absorption of the excitation light occurs only in the GaAs layer. The variation in intensity of the light over the cross section of the excitation beam was approximately Gaussian. These experiments were carried out for different values of the optical pulse energy and beam diameter $F$. Following the method described in Ref. 20, we measured the edge emission spectrum (integrated over time) propagating within a solid angle of $\sim 4°$. The axis of the angle coincides with the normal to the epitaxial layer emerging from the excited region. For convenience in analyzing the measurement results we calculated the energy density of the excitation light pulse $D_{\text{ex}}$ and energy density of the emission pulse, both the spectral density of the latter $d_s$ and $D_s$, the integral of this quantity over the spectrum. These calculations were based on measurements of the corresponding energies integrated over time and the diameter of the excitation beam (at half-height). Hence, the quantities $D_{\text{ex}}$, $d_s$, and $D_s$ are integrated over time and averaged over the cross section of the photoexcited region of the sample. Translation of charge carriers along the sample within the emission time was not included in the calculation. This is permissible if the charge carrier motion is diffusive, since estimates indicate that the diffusion length is is considerably smaller than $F$. There will be a redistribution of the electron-hole plasma along the sample since this plasma is being created by interband absorption of the emitted light within the GaAs layer, but it is unclear whether this effect should be taken into account. At this time, calculations[11] of such a redistribution of the electron-hole plasma have only been done for the one-dimensional case.

Figure 2a shows the experimental dependence of the emission energy density $D_s$ on the energy density of the excitation pulse $D_{\text{ex}}$. The experimental results are well approximated by a linear dependence, which intersects the $D_{\text{ex}}$ axis at a certain value $D^0_{\text{ex}}$. The value of $D^0_{\text{ex}}$, commonly referred to as the threshold value, is discussed in more detail in Refs. 2 and 4. The threshold nature (in this sense) of the linear increase in emission energy with pumping gain is characteristic of stimulated emission. Analogous linear dependences are observed in studies of stimulated emission driven by various pumping methods, for example, in GaInAsP layers,[4] in superluminescent diodes made of gallium arsenide,[14] and in $Al_xGa_{1-x}As$/GaAs double heterostructure lasers.[21] Note that for values of $D_{\text{ex}}$ beyond the limits of the plot shown in Fig. 2a (because the energy of the excitation pulse is limited, this happens only when $F=0.2$ $\mu$m) the function $D_s(D_{\text{ex}})$ exhibits a tendency to saturate.

It is clear from Fig. 2a that as the diameter $F$ varies from 0.7 to 0.2 mm, the function $D_s(D_{\text{ex}})$ remains nearly constant. Of course, the parameters $D_{\text{ex}}$ and $F$ must affect the stimulated emission. However, the integrated function $D_s(D_{\text{ex}},F)$ measured for optical pumping by ultrashort pulses is not suitable for studying the processes that are characteristic of stimulated emission, because the energy density of the emission $D_s$ is determined by an integer number of electron-hole pairs that are photogenerated within the time of excitation of the pulse and then radiatively recombine. In other words, the energy density of the emission pulse is determined largely by interband absorption of the excitation light pulse that generates the electron-hole plasma.

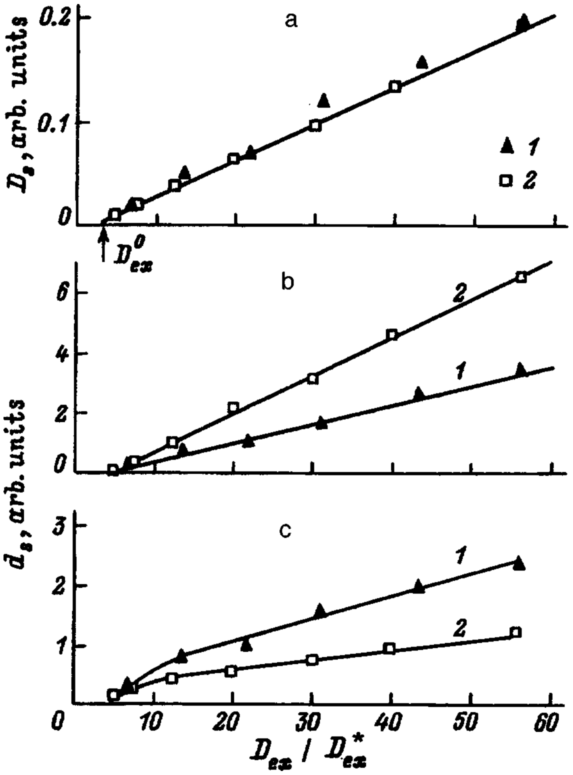

FIG. 2. Dependence of the emission energy density integrated over the spectrum $D_s$ (a), the emission energy density $d_s$ at $\hbar\omega_s=1.39$ eV (b), and at $\hbar\omega_s=1.42$ eV (c), on the energy density of the excitation pulse $D_{ex}$. $\hbar\omega_{ex}=1.485$ eV, $F$, mm: *1* — 0.2, *2* — 0.7. $D^*_{ex}$ —normalizing quantity.

However, it is noteworthy that when the diameter $F$ changes, a change is observed in the dependence of the emission energy density (at fixed photon energy) $d_s$ on the energy density of the excitation $D_{ex}$ (see Figs. 2b and 2c). This is probably a real manifestation of the stimulated nature of the emission, connected with a change in the dimensions of the active medium that amplifies the emission. However, the analysis of such dependences (also measured in Ref. 2) is hindered by the absence of a theory for the emission mentioned above. The stimulated nature of the emission manifests itself more clearly in changes of the emission spectrum as the beam diameter $F$ changes and the energy density of the excitation pulse $D_{ex}$ changes. The remaining portion of this paper is devoted to this topic.

The characteristic shape of the emission spectra observed is shown in Fig. 3. For the minimum excitation energy density $D_{ex}$ used we observed spectra similar to the spectrum in Fig. 3b for $F=0.2$ mm and still characteristic of spontaneous emission. The following facts suggest this conclusion. First of all, the maximum in the spectrum of edge emission energy density $d_s$ is located at a photon energy of $\hbar\omega^m_s\simeq E^0_g$, where $E^0_g$ is the band gap of the "unexcited" sample (see Fig. 4). Secondly, the width of the emission spectrum (at half-height) $\Delta\hbar\omega_s$ actually slightly exceeds the value of $1.8kT_R$ (see Fig. 5), which is characteristic of spontaneous luminescence at room temperature;[22] this increase in the spectral width beyond $1.8kT_R$ is explained by broadening of the spontaneous emission spectrum with increasing electron-hole plasma temperature $T_c$. The temperature $T_c$ in our experiments should exceed $T_R$, because the kinetic energy of the photogenerated electron-hole pairs, which equals $\hbar\omega_{ex}-E_g$, exceeds $kT_R$.

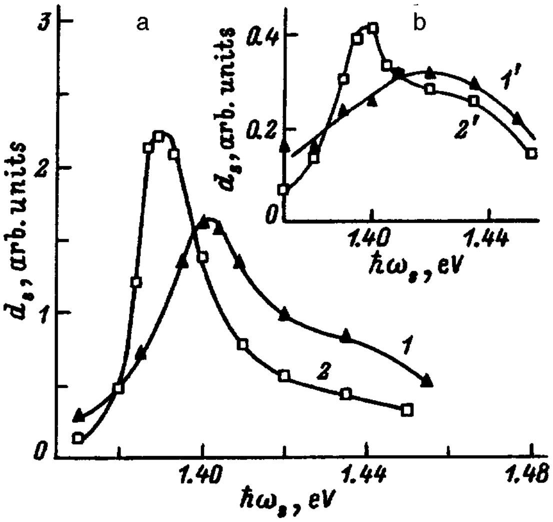

FIG. 3. Emission energy density spectra $d_s$ from GaAs at $\hbar\omega_{ex}=1.485$ eV. a: *1* - -$D_{ex}=22\,D^*_{ex}$, $F=0.2$ mm; *2* — $D_{ex}=20\,D^*_{ex}$, $F=0.7$ mm. *b*: *1′* — $D_{ex}=6.8\,D^*_{ex}$, $F=0.2$ mm; *2′* - -$D_{ex}=7.5\,D^*_{ex}$, $F=0.7$ mm. $D^*_{ex}$ — normalizing quantity.

As the excitation energy density $D_{ex}$ increases, we observe a decrease in the emission spectral width $\Delta\hbar\omega_s$ (see Fig. 5). Further increases in $D_{ex}$ lead to slowing and eventual saturation of the decrease in $\Delta\hbar\omega_s$. This observed decrease in the width of the spectrum, as we have already said, is proof of the stimulated nature of the emission. Conversely, for spontaneous emission the width of the radiation spectrum ought to increase with increased pumping according to Ref. 18.

Changes in $F$, i.e., the characteristic diameter of the active region, change the dependence of the width of the emission spectrum on the energy density of the excitation $D_{ex}$ as well (see Fig. 5). For the larger diameter $F=0.7$ mm, the spectral width $\Delta\hbar\omega_s$ decreases much more rapidly with increasing $D_{ex}$, and the function $\Delta\hbar\omega_s=f(D_{ex})$ saturates at a smaller $D_{ex}$ than it does for $F=0.2$ mm. However, the

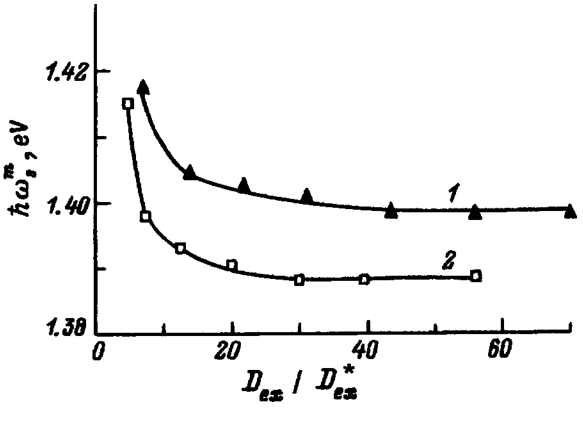

FIG. 4. Dependence of the photon energy $\hbar\omega^m_s$ corresponding to the maximum in the emission spectrum on $D_{ex}$ for $\hbar\omega_{ex}=1.485$ eV. $F$, mm: *1* — 0.2, *2* — 0.7. $D^*_{ex}$ — normalizing quantity.

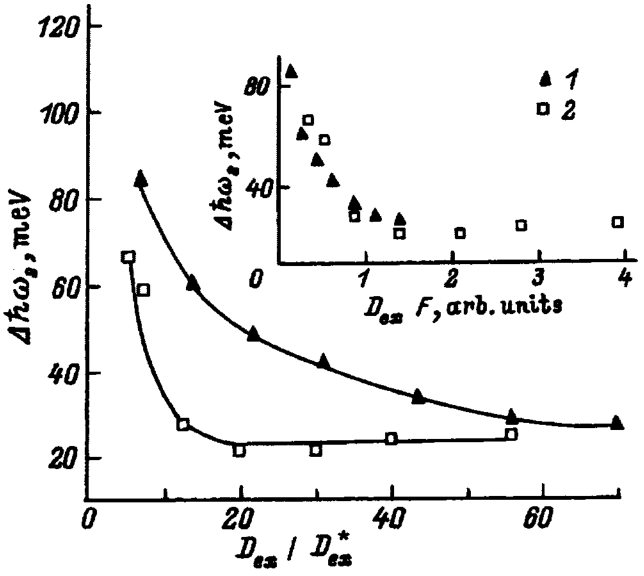

FIG. 5. Dependence of the width of the emission spectrum $\Delta\hbar\omega_s$ on $D_{ex}$ for $\hbar\omega_{ex}=1.485$ eV. $F$, mm: *1* — 0.2, *2* — 0.7. The inset shows the corresponding dependence of $\Delta\hbar\omega_s$ on $D_{ex}F$. $D^*_{ex}$ — normalizing quantity.

change in $F$ does not affect the value of $\Delta\hbar\omega_s$ at which the function $\Delta\hbar\omega_s=f(D_{ex})$ saturates. This fact is revealed by measurements in which $D_{ex}$ is further increased beyond the range shown in Fig. 5. It is noteworthy that when the value of $\Delta\hbar\omega_s$ at saturation is measured for various samples, it is found to increase with increasing defectiveness of the crystal structure of the sample (the sample investigated in this paper was the best one we had). The degree of imperfection is estimated by $x$-ray diffraction.

Let us use the theory developed in Ref. 16 for steady-state stimulated emission in a laser medium without a resonator and extrapolate its conclusions regarding narrowing of the emission spectrum to GaAs in particular. This theory takes into account the spatial nonuniformity of the emission gain, but does not include the specific features of the semiconductor. According to Ref. 16, the stimulated emission spectrum should narrow with increasing radiation energy by no more than a factor of $\sim 3$. After this, the width of the spectrum is almost unchanged as the optical energy increases. This conclusion of the theory is in agreement with the experimental function $\Delta\hbar\omega_s=f(D_{ex})$ shown in Fig. 5. In this case we must take into account that the excitation energy density $D_{ex}$ is proportional to the emission energy density $D_s$. Note that this conclusion could not be confirmed, e.g., in experiments using semiconductor lasers. Lasers are most often used for studying stimulated emission, but the narrowing of the spectrum in these devices is in large degree due to the resonator. In the theory of Ref. 16 it was also shown that increasing the length of active medium should lead to a narrowing of the stimulated emission spectrum. This qualitatively explains the change in the experimental function $\Delta\hbar\omega_s=f(D_{ex})$ described above with changing diameter $F$ shown in Fig. 5.

The inset in Fig. 5 shows the results of measuring the function $\Delta\hbar\omega_s=f(D_{ex})$ for $F$ = 0.2 and 0.7 mm in the form $\Delta\hbar\omega_s=f(D_{ex}F)$. Note that for both diameters the experimental points lie on almost the same curve. This also agrees with the conclusions of the theory of Ref. 16 that for stimulated emission (i.e., amplified spontaneous emission) the form of the function $\Delta\hbar\omega_s=f(\alpha L)$ is universal for a given spontaneous emission spectrum (here $L$ is the length of the active medium, and $\alpha$ is a value of the gain coefficient proportional and close in magnitude to the maximum of the spectrum, which should increase with increasing $D_{ex}$). We point out that it is not yet clear whether the spontaneous emission spectra in our experiment would differ from each other for fixed $D_{ex}F$ but different $F$.

Increasing the diameter $F$ (for fixed energy density $D_{ex}$) also leads to concentration of the emission spectrum in the longer-wavelength spectral region (see Fig. 3). The peak of the spectrum shifts toward longer wavelengths when the diameter is increased from 0.2 to 0.7 mm at fixed excitation energy density $D_{ex}$ (see Fig. 4) by an amount that first increases with increasing $D_{ex}$, and then saturates. For the moment we suggest two possible reasons for the observed shift in the emission spectrum as $F$ changes. First of all, the shift in the emission spectrum could be a result of saturation of the emission gain at the short-wavelength end of the spectrum, which should happen with increasing $F$. This conclusion holds for a semiconductor laser (with steady-state, high-power optical pumping), as shown by self-consistent calculations of the spatially nonuniform distribution of charge carrier concentration and photon emission density.[17] According to Ref. 17, the carrier concentration falls off from the center of the photoexcited region to its edge, while the photon density, conversely, increases. Secondly, the shift in the spectrum as the diameter $F$ changes could be explained qualitatively by taking into account that increasing $F$ increases the probability of intraband absorption of an emission photon. As $F$ increases, enhanced heating of the electron-hole plasma due to intraband absorption of the emission will decrease the population inversion of energy levels by charge carriers. This follows from the theory of Ref. 23. In this case a narrowing of the gain spectrum will occur towards the long-wavelength side (coinciding with the edge of the band). This also should lead to concentration of the emission towards the longer-wavelength region.

Thus, we have experimentally observed the following properties of the emission spectrum: 1) A decrease in the width of the emission spectrum which saturates as the energy density $D_{ex}$ of the excitation pulse increases and as the diameter of the beam $F$ increases; 2) a universal character of the decrease in width $\Delta\hbar\omega_s$ of the emission spectrum as a function of the product $D_{ex}F$; 3) concentration of the emission at longer wavelengths as the excitation energy $D_{ex}$ increases and as the diameter $F$ increases. Our qualitative discussions of these properties indicate that all of them are characteristic of stimulated (amplified spontaneous) emission in a semiconductor without a resonator. To sum up, in the absence of a theory we have obtained a experimental picture of the changes in the time-integrated power spectrum of nonstationary edge emission in a thin layer of GaAs with changing beam diameter and energy of the high-power picosecond optical pump pulse. Our picture provides the necessary confirmation of the stimulated nature of this emission, whose duration, as shown in previous papers (see Refs. 1 and 2, etc.) lies in the picosecond time range. This confirmation is needed, in particular, to analyze a whole series of effects[5,20,24] that occur in a photoexcited electron-hole plasma with the participation of light.

This work was carried out with the financial support of the Russian Fund for Fundamental Research (Project 95-02-05871) and GKNT Russia.

The authors are deeply grateful to Yu. D. Kalafati for detailed discussions of this work and for valuable advice.

[1] D. Hulin, M. Joffre, A. Migus, J. L. Oudar, J. Dubard, and F. Alexandre, J. de Physique **48**, 267 (1987).

[2] N. N. Ageeva, I. L. Bronevoĭ, E. G. Dyadyushkin, and B. S. Yavich, JETP Lett. **48**, 276 (1988).

[3] N. N. Ageeva, I. L. Bronevoi, E. G. Dyadyushkin, V. A. Mironov, S. E. Kumekov, and V. I. Perel', Solid State Commun. **72**, 625 (1989).

[4] A. M. Fox, R. J. Manning, and A. Miller, J. Appl. Phys. **65**, 4287 (1989).

[5] I. L. Bronevoi, A. N. Krivonosov, and T. A. Nalet, Solid State Commun. **98**, 903 (1996).

[6] J. P. Foing, D. Hulin, M. Joffre, M. K. Jackson, J. L. Oudar, C. Tanguy, and M. Combescot, Phys. Rev. Lett. **68**, 110 (1992).

[7] I. L. Bronevoĭ, S. E. Kumekov, and V. I. Perel', JETP Lett. **43**, 473 (1986).

[8] S. E. Kumekov and V. I. Perel', Zh. Éksp. Teor. Fiz. **94**, 346 (1988) [Sov. Phys. JETP **67**, 193 (1988)].

[9] Yu. D. Kalafati and V. A. Kokin, JETP Lett. **50**, 495 (1989).

[10] N. N. Ageeva, V. A. Borisov, I. L. Bronevoi, V. A. Mironov, S. E. Kumekov, V. I. Perel', and B. S. Yavich, Solid State Commun. **75**, 167 (1990); N. N. Ageeva, I. L. Bronevoi, V. A. Mironov, S. E. Kumekov, and V. I. Perel', Solid State Commun. **81**, 969 (1992).

[11] Yu. D. Kalafati, V. A. Kokin, H. M. Van Driel, and G. R. Allan, in *Hot Carriers in Semiconductors*, Karl Hess *et al.* Eds. (Plenum Press, N. Y., 1996), p. 587.

[12] D. N. Nasledov, A. A. Rogachev, S. M. Ryvkin, and B. V. Tsarenkov, Fiz. Tverd. Tela (Leningrad) **4**, 1062 (1962) [Sov. Phys. Solid State **4**, 782 (1962)].

[13] A. Yariv and R. C. C. Leite, J. Appl. Phys. **34**, 3410 (1963).

[14] L. N. Kurbatov, S. S. Shakhidzhanov, L. V. Bystrova, and V. V. Krapukhin, Fiz. Tekh. Poluprovodn. **4**, 2025 (1970) [Sov. Phys. Semicond. **4**, 1739 (1970)].

[15] T. George, M. A. Khan, S. Krishnankutty, R. A. Skogman, J. N. Kuznia, and D. T. Olson, Appl. Phys. Lett. **65**, 520 (1994).

[16] L. W. Casperson, J. Appl. Phys. **48**, 256 (1977).

[17] E. O. Goebel, O. Hildebrand, and K. Lohnert, IEEE J. Quantum Electron. **QE-13**, 848 (1977).

[18] F. Stern, J. Appl. Phys. **47**, 5382 (1976).

[19] P. S. Kop'ev, S. V. Ivanov, A. Yu. Yegorov, and D. Yu. Uglov, J. Cryst. Growth **96**, 533 (1989).

[20] I. L. Bronevoi, A. N. Krivonosov, and V. I. Perel', Solid State Commun. **94**, 805 (1995).

[21] H. C. Casey and M. B. Panish, *Heterostructure Lasers* (Academic Press, London, 1978).

[22] A. P. Levanyuk and V. V. Osipov, Usp. Fiz. Nauk **133**, 427 (1981) [Sov. Phys. Usp. **24**, 187 (1981)].

[23] Yu. D. Kalafati and V. A. Kokin, Zh. Éksp. Teor. Fiz. **99**, 1793 (1991) [Sov. Phys. JETP **72**, 1003 (1991)].

[24] N. N. Ageeva, I. L. Bronevoi, V. A. Mironov, S. E. Kumekov, and V. I. Perel', in *Mode-Locked Lasers and Ultrafast Phenomena*, G. B. Altshuler, Ed. [Proc. SPIE **1842**, 70 (1992)]; I. L. Bronevoi, A. N. Krivonosov, and V. I. Perel', Solid State Commun. **94**, 363 (1995).

Translated by Frank J. Crowne

SEMICONDUCTORS VOLUME 32, NUMBER 5 MAY 1998

# Effect of the diameter of the photoexcited region on the picosecond relaxation of bleaching in a thin layer of GaAs

I. L. Bronevoĭ and A. N. Krivonosov

*Institute of Radio Engineering and Electronics, Russian Academy of Sciences, 103907 Moscow, Russia*

(Submitted October 1, 1997; accepted for publication October 10, 1997)
Fiz. Tekh. Poluprovodn. **32**, 542–545 (May 1998)

It is found experimentally that the relaxation of bleaching in GaAs, which takes place when charge carriers are photogenerated by a high-power picosecond optical pulse, is slowed as the beam diameter $F$ increases. Relaxation of the bleaching is caused by a decrease in the concentration of carriers due to recombination-induced superluminescence in GaAs. It is found that as the diameter $F$ increases, the rate of superluminescence recombination slows, although the intensity of the superluminescent emission should increase. This apparent contradiction is explained with the help of theory. © *1998 American Institute of Physics.* [S1063-7826(98)00605-X]

In this paper we investigate the relaxation of bleaching in a thin layer of GaAs. Bleaching (increased transparency) is observed during photogeneration of an electron-hole plasma (EHP) by high-power optical pulses with duration 14 ps. The bleaching reflects a change in the sum of populations of nonequilibrium charge carriers in energy levels of the valence and conduction bands that are connected by direct optical transitions.[1] Our experiments were carried out at room temperature $T_R$. The photogenerated electron-hole plasma concentration was large enough that recombination- induced superluminescence occurs. In Ref. 1 we established that when the photogeneration of an electron-hole plasma is interrupted, superluminescent recombination on a picosecond time scale ensures relaxation of the electron-hole plasma concentration (and accordingly the bleaching) down to a certain residual level. According to Ref. 1, when this residual level is reached, the temperature $T_c$ of the electron-hole plasma becomes approximately equal to room temperature $T_R$, the superluminescence decays, and further relaxation of the electron-hole plasma concentration and bleaching proceed much more slowly with a characteristic time comparable to the spontaneous recombination time in gallium arsenide of $\sim 1$ ns.

As the diameter $F$ of the photoexcited region in the GaAs layer increases, the intensity of superluminescent emission should increase, and we should expect the rate of superluminescent carrier recombination to increase as well. This should speed up the ''picosecond'' relaxation of the bleaching to its residual level. However, in this paper we observe experimentally the opposite—the ''picosecond'' relaxation of the bleaching down to a residual level is slowed as the diameter $F$ of the exciting beam increases. This fact is qualitatively explained using the theory of Ref. 2.

Our sample consisted of a $Al_{0.22}Ga_{0.78}As$–GaAs–$Al_{0.4}Ga_{0.6}As$ heterostructure with layer thicknesses 1.3–1.5–1.2 $\mu$m and impurity concentrations $<10^{15}$ cm$^{-3}$. The width of the $x$-ray diffractive reflection curve, which characterizes the degree of imperfection of the GaAs crystal lattice, was 29 angular seconds. The layers of $Al_xGa_{1-x}As$ were transparent to the light used. Bleaching was investigated by the ''excite-probe'' method (see Ref. 1). The duration of the excitation $(ex)$ and probing $(p)$ pulses was 14 ps. The change in light intensity over the cross section of the excitation and probe beams was approximately Gaussian. The probe beam passed through the central portion of the photoexcited region of the sample. The ratio $\log(T^1/T^0)$, which characterizes bleaching (where $T$ is the transparency of the sample, and labels 1 and 0 denote the presence and absence of the excitation, respectively) and the average energy density (over the beam cross section) of the excitation pulse $D_{\text{ex}}$ were calculated from measurements of the time-integrated energy of the probe and excitation pulses and the diameter of the excitation beam $F$ (at half-height of the intensity distribution). The spectra (integrated over time) of the light emitted when the sample is photoexcited were measured as in Ref. 3.

Figure 1 shows the time dependence of the bleaching for a pulse energy density $D_{\text{ex}}=56\,D_{\text{ex}}^*$ (where $D_{\text{ex}}^*$ is a normalizing quantity) and a fixed ratio of the diameters of the excitation $(F)$ and probe $(f)$ beams equal to 2. For the larger excitation beam diameter $F = 0.7$ mm the bleaching falls off with time more slowly and reaches its residual level $\sim 15$ ps later than for $F = 0.2$ mm. The residual bleaching for the diameter $F = 0.7$ mm was smaller than for $F = 0.2$ mm. Based on the decay of the bleaching we define a characteristic time $\tau_r$ for ''picosecond'' relaxation of the bleaching down to its residual level (see the inset in Fig. 1). Figure 2 shows the decay of the bleaching measured at a fixed diameter $f$ of the probe beam. In both experiments, the changes in the bleaching relaxation (Figs. 1 and 2) indicate that the time $\tau_r$ increases with increasing diameter $F$ and follows the same functional law (see Fig. 3).

In Ref. 1 it was shown experimentally that when the residual bleaching is reached for the diameter $F = 0.7$ mm, the energy distribution of the electron-hole plasma corresponding to this residual bleaching for $T_c \simeq T_R$ could be approximately characterized by the conditions

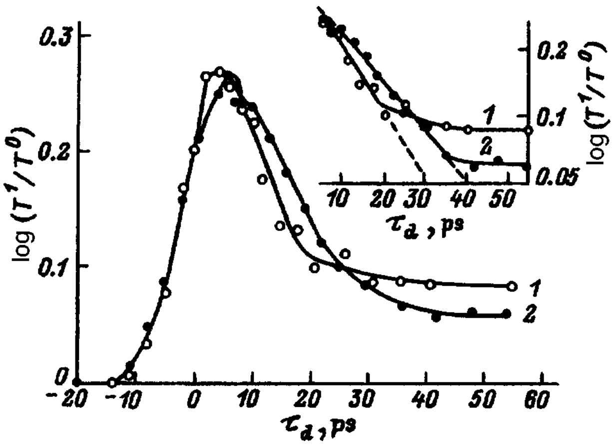

FIG. 1. Change in the bleaching of GaAs with delay time $\tau_d$ between excitation and probe pulses for $\hbar\omega_{\rm ex}=1.485$ eV and $\hbar\omega_p=1.568$ eV: *1*—$F=0.2$ mm, $f=0.1$ mm; *1*—$F=0.7$ mm, $f=0.35$ mm;. The inset shows the decay of the bleaching on a semilogarithmic scale. From these curves we find that $\tau_r=19$ ps for $F=0.7$ mm, and $\tau_r=15$ ps for $F=0.2$ mm.

$$n=p,\quad \mu_e=\mu_h\simeq E_g, \tag{1}$$

where $n$ and $p$ are, respectively, the concentrations of electrons and holes, $\mu_e$ and $\mu_h$ are the quasi-Fermi levels of the electrons and holes, and $E_g$ is the width of the band gap. Condition (1) corresponds to the maximum concentration of electron-hole plasma for which there is no longer a population inversion. In this paper, the residual bleaching decreases as the diameter $F$ increases (see Fig. 1). It is probable that for small diameters $F$ the superluminescence decays, and the residual bleaching level is reached while a certain population inversion still remains. The fact that for different diameters $F$ the superluminescence terminates at different levels of residual bleaching is confirmed by measurement of the time dependence of the bleaching (see Fig. 4) and emission from the sample when the energy density $D_{\rm ex}=12\,D^*_{\rm ex}$. For the diameter $F=0.2$ mm the maximum and residual bleaching are practically the same. The width of the emission spectrum $\Delta(\hbar\omega)$ is equal in this case to 62 meV, which corresponds to spontaneous emission (see Ref. 4); i.e., superluminescence is not triggered at this diameter. At a diameter $F=0.7$ mm we observe "picosecond" relaxation of the bleaching down to its residual level, which is lower than for $F=0.2$ mm. At $F=0.7$ mm the width of the emission spectrum $\Delta(\hbar\omega)=28$ meV. The narrower emission spectrum for $F=0.7$ mm confirms that superluminescence is triggered.[5] We emphasize that although the residual bleaching also increases with increasing beam diameter $F$ (probably because the superluminescence decays at a higher concentration of the electron-hole plasma), for fixed $F$ the residual bleaching remained nearly constant with changing excitation energy density $D_{\rm ex}$ (as we noted previously in Refs. 6 and 7).

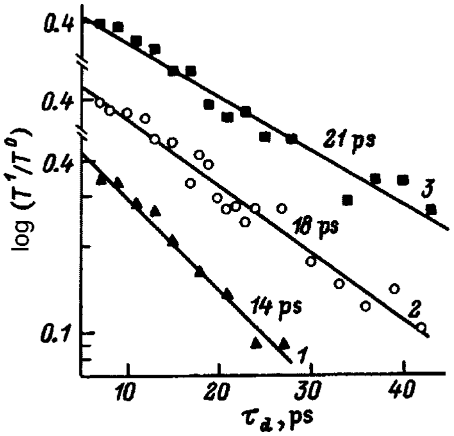

FIG. 2. Decay of the bleaching in GaAs with delay time $\tau_d$ between excitation and probe pulses (on a semilogarithmic scale) for $f=0.17$ mm, $\hbar\omega_{\rm ex}=1.513$ eV, $\hbar\omega_p=1.568$ eV. $F$, mm: *1* — 0.24, *2* — 0.35, *3* — 1.1. Values of $\tau_r$ are shown on the figure.

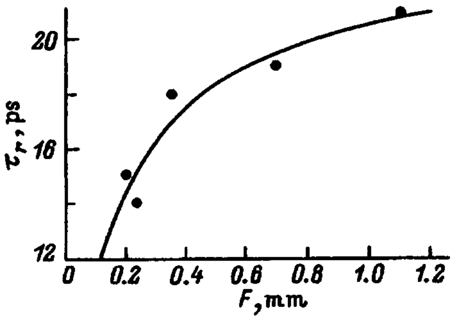

FIG. 3. Experimental dependence of the characteristic relaxation time $\tau_r$ on the diameter of the excitation beam $F$ for $\hbar\omega_p=1.568$ eV (dots). The solid curve is the theoretical dependence $\tau_r=(2/3)(A+B\tau_pT_c^{1/2}E_g)\tau_h$; the parameters $A$ and $B$ chosen for the best approximation of experimental data are given in the text.

Let us discuss the "picosecond" relaxation of the bleaching. Since the energy of an excitation photon $\hbar\omega_{\rm ex}$ is not much larger than $E_g$, the temperature of the photoexcited electron-hole plasma should only slightly exceed the lattice temperature (for example in Ref. 2, when $\hbar\omega_{\rm ex}=1.52$ eV, the electron-hole plasma temperature did not exceed 470 K). In this case, the observed change in bleaching primarily reflects a change in the electron-hole plasma concentration (this is confirmed by experimental spectra of the bleaching at various electron-hole plasma temperatures and concentrations,[8] and also calculated spectra that separately illustrate the effect of temperature changes and concentration changes of the electron-hole plasma on the bleaching[7]). The decay of the concentration of photogenerated electron-hole plasma begins several picoseconds after the intensity of the excitation light passes through its maximum, when the electron-hole plasma

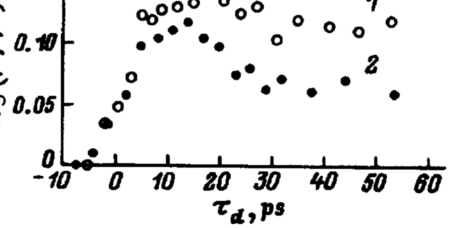

FIG. 4. Variation of bleaching in GaAs with delay time $\tau_r=(2/3)(A+B\tau_pT_c^{1/2}E_g)\tau_h$ between excitation and probe pulses for $\hbar\omega_{\rm ex}=1.485$ eV, $\hbar\omega_p=1.568$ eV. $F$, mm: *1* — 0.2, *2* — 0.7.

begins to cool.[8] During cooling the charge carriers make transitions from the higher to the lower energy levels that are subject to population inversion. The recombination-induced superluminescence that occurs over picosecond times[9,10] does not allow the inversion band to increase significantly[1,11] and the concentration of the electron-hole plasma decreases as the electron-hole plasma cools. If we ignore the small fraction of the electron- hole plasma concentration whose subtraction causes the population inversion to disappear, then the energy distribution of the electron-hole plasma within the cooling time can be characterized by conditions (1). It is not difficult to show that in this approximation the electron-hole plasma concentration $n$ must vary with temperature as $T_c^{3/2}$, which is confirmed by the values of $n$ and $T_c$ determined from the experiments in Ref. 8. Note that the presence of recombination-induced superluminescence leads to additional heating of the electron-hole plasma (see Refs. 2, 12 and 13). This heating should slow the cooling of the electron-hole plasma compared to the case where there is no superluminescence. The characteristic cooling time for the electron-hole plasma in GaAs in the presence of superluminescence was determined within the theory of Ref. 2 to be:

$$\tau_T \simeq (A + B\tau_p T_c^{1/2} E_g)\tau_h , \tag{2}$$

where $A = 6.2$, $B = 0.34$, $\tau_h \simeq$ 0.8 ps is the cooling time of the electron-hole plasma due to emission of LO-phonons; $\tau_T$, $\tau_p$, and $\tau_h$ are measured in ps, $T_c$ in K, and $E_g$ in eV. The first term in Eq. (2) takes into account heating of the electron-hole plasma arising from the fact that the energy of charge carriers that participate in the superluminescent recombination is smaller than the average energy of carriers in the electron-hole plasma. The second term takes into account heating of the electron-hole plasma due to intraband absorption of the superluminescent emission. The time $\tau_p$ is a characteristic time for the motion of a superluminescence photon in the active medium without leaving the medium or being absorbed. For the sample under study, which has waveguiding properties when the number of optically sensitive defects in the crystal lattice is small, we can set $\tau_p^{-1} \simeq c(\gamma + F^{-1})$, where $\gamma$ is the intraband absorption of light, and $c$ is the velocity of light in the medium.

Note that the theory of Ref. 2 basically describes relaxation of the electron-hole plasma in a semiconductor laser with optical pumping, and that according to the assertions made in Ref. 2, Eq. (2) is qualitatively correct for GaAs without a resonator. The theory allows us to use an exponential to approximate the dependence of the electron-hole plasma temperature $T_c$ on time for $T_c > T_R$. The results of numerical simulation[13] confirm that in the central portion of the photoexcited region, where the bleaching was also investigated, it is permissible to approximate the time-dependent decrease in electron-hole plasma temperature by an exponential from the time when the superluminescence first appears until the residual bleaching is reached.

The probe photon energy $\hbar\omega_p = 1.568$ eV was chosen (according to the data of Ref. 8) so that the measured bleaching should vary with the concentration $n$ of the electron-hole plasma. Since $n \sim T_c^{3/2}$, the theory of Ref. 2 predicts that the characteristic time for the measured relaxation of the bleaching should be determined by the expression $\tau_r \simeq (2/3)\tau_T$. The theoretical dependence obtained for $\tau_r$ describes the experimental results if we agree that $A$ = 8.5, $B$ = 0.57 (see Fig. 3). The difference between the fitting parameters $A$ and $B$ and the values obtained from theory is entirely acceptable if we are only attempting qualitative agreement. The values $T_c = 400$ K and $n = 2.8 \times 10^{18}$ cm$^{-3}$ averaged over the time in which the bleaching falls to its residual level were determined by using the dependence of the bleaching on $n$ and $T_c$ given in Ref. 8. The coefficient $\gamma = 54$ cm$^{-1}$ was estimated from the concentration $n$ according to Ref. 14.

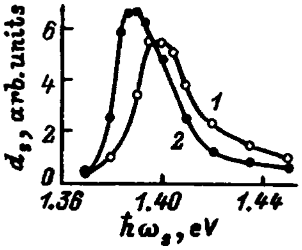

FIG. 5. Energy density spectra $d_s$ (averaged over the photoexcited sample area) for pulses of light emitted from GaAs when $\hbar\omega_{\mathrm{ex}} = 1.485$ eV. $F$, mm: *1* — 0.2, *2* — 0.7..

Let us clarify why the superluminescent recombination should slow down as $F$ increases, which explains the observed slowing of the ''picosecond'' relaxation of the bleaching. As $F$ increases, the probability of intraband absorption of a superluminescence emission photon in the region of GaAs, where the electron-hole plasma is excited, increases. In this case, according to the theory of Ref. 2, the heating of the electron-hole plasma due to intraband absorption of the emitted light will decrease the population inversion and amplification coefficient of the emission $\alpha_\omega$ so much that, although the superluminescent intensity $B_\omega$ increases with increasing diameter of the active GaAs region, the rate of stimulated (superluminescent) recombination $(dn/dt) \sim \int \alpha_\omega(n,T) B_\omega d\omega$ decreases (here $\omega$ is the frequency of the radiation, and the integral is taken over the spectral gain band).

As $F$ increases, the width of the gain spectrum for the light should decrease due to the decreasing population inversion mentioned above. The difference in width of the gain spectra at different diameters $F$ (and the slightly differing concentrations of electron-hole plasma) should lead to concentration of superluminescence in the longer-wavelength region as $F$ increases. This is confirmed by emission spectra from a sample measured at $D_{\mathrm{ex}} = 56\, D_{\mathrm{ex}}^{*}$ (see Fig. 5). The width (at half-height) of the spectra $\Delta(\hbar\omega)$ corresponds approximately to the estimate from theory[5] of the superluminescence spectral width when the decrease in $\Delta(\hbar\omega)$ with increasing gain saturates.

Thus, the experimentally observed slowing of ''picosecond'' relaxation of bleaching observed in this paper as the diameter $F$ of the photoexcited GaAs region increases is probably explained by a mechanism of slowing of superluminescent recombination based on the theory of Ref. 2 and qualitatively discussed above.

This work was carried out with the financial support of the Russian Fund for Fundamental Research (Project 95-02-05871) and GKNT Russia.

The authors are deeply grateful to Yu. D. Kalifati for detailed discussion of this work and for valuable advice.

Fax: (905) 203-8414 (Bronevoi)
E-mail: bil@mail.cplire.ru (Bronevoi)

---

[1] N. N. Ageeva, I. L. Bronevoi, E. G. Dyadyushkin, V. A. Mironov, S. E. Kumekov, and V. I. Perel’, Solid State Commun. **72**, 625 (1989).

[2] Yu. D. Kalafati and V. A. Kokin, Zh. Éksp. Teor. Fiz. **99**, 1793 (1991) [Sov. Phys. JETP **72**, 1003 (1991)].

[3] I. L. Bronevoi, A. N. Krivonosov, and V. I. Perel’, Solid State Commun. **94**, 805 (1995).

[4] A. P. Levanyuk and V. V. Osipov, Usp. Fiz. Nauk **133**, 427 (1981) [Sov. Phys. Usp. **24**, 187 (1981)].

[5] L. W. Casperson, J. Appl. Phys. **48**, 256 (1977).

[6] I. L. Bronevoi, R. A. Gadonas, V. V. Krasauskas, T. M. Lifshitz, A. S. Piskarskas, M. A. Sinitsyn, and B. S. Yavich, JETP Lett. **42**, 395 (1985).

[7] N. N. Ageeva, I. L. Bronevoi, V. A. Mironov, S. E. Kumekov, and V. I. Perel’, in *Mode-Locked Lasers and Ultrafast Phenomena*, edited by G. B. Altshuler [Proc. SPIE **1842**, 70 (1992)].

[8] I. L. Bronevoĭ, S. E. Kumekov, and V. I. Perel’, JETP Lett. **43**, 473 (1986).

[9] D. Hulin, M. Joffre, A. Migus, J. L. Oudar, J. Dubard, and F. Alexandre, J. de Physique **48**, 267 (1987).

[10] N. N. Ageeva, I. L. Bronevoĭ, E. G. Dyadyushkin, and B. S. Yavich, JETP Lett. **48**, 276 (1988).

[11] I. L. Bronevoi, A. N. Krivonosov, and T. A. Nalet, Solid State Commun. **98**, 903 (1996).

[12] N. N. Ageeva, I. L. Bronevoi, V. A. Mironov, S. E. Kumekov, and V. I. Perel’, Solid State Commun. **81**, 969 (1992).

[13] Yu. D. Kalafati, V. A. Kokin, H. M. Van Driel, and G. R. Allan, in *Hot Carriers in Semiconductors*, Karl Hess *et al.*, Eds. (Plenum Press, N. Y. 1996), p. 587.

[14] J. S. Blakemore, J. Appl. Phys. **53**, R123 (1982).

Translated by Frank J. Crowne

# Distinctive features of the far-infrared reflection spectra of the semimagnetic semiconductors $Hg_{1-x}Mn_xTe_{1-y}Se_y$

A. I. Belogorokhov, V. A. Kul'bachinskiĭ, P. D. Mar'yanchuk, and I. A. Churilov

*M. V. Lomonosov State University at Moscow, 119899 Moscow, Russia*

(Submitted August 11, 1997; accepted for publication October 16, 1997)
Fiz. Tekh. Poluprovodn. **32**, 546–548 (May 1998)

Reflection spectra of single crystals of $Hg_{1-x}Mn_xTe_{1-y}Se_y$ ($0.01<x<0.14$, $y=0.01$) in the far-infrared range (10–600 $cm^{-1}$) are investigated at 300 and 77 K. A series of new phonon modes is observed, in addition to the longitudinal and transverse modes corresponding to the ternary compounds. © *1998 American Institute of Physics.* [S1063-7826(98)00705-4]

## 1. INTRODUCTION

Semimagnetic semiconductors, or dilute magnetic semiconductors, consist of solid solutions in which atoms of one of the components are replaced by atoms of a transition element $M$ with an uncompensated magnetic moment. At this time, much is known about the magnetic and transport properties of many semimagnetic semiconductors, including the $A^{II}_{1-x}M_xB^{VI}$ compounds, i.e., semimagnetic semiconductors such as $Hg_{1-x}Mn_xTe$ and $Hg_{1-x}Mn_xSe$.[1–3] For instance, it is known that $Hg_{1-x}Mn_xSe$ has $n$-type conductivity, whereas $Hg_{1-x}Mn_xTe$ usually has $p$-type conductivity. Adding Se to $Hg_{1-x}Mn_xTe$ is expected to lead to defect compensation, thereby allowing us to regulate the type of conductivity and defect concentration of the latter.

There are far fewer papers in which the optical properties of semimagnetic semiconductors like $Hg_{1-x}Mn_xTe$, $Hg_{1-x}Mn_xSe$ are discussed. Most of the the existing studies use magnetooptics,[1–3] although there is also some data on the effect of current carrier concentration on the infrared spectra of HgTe, $Hg_{1-x}Mn_xTe$, and $Hg_{1-x}Mn_xSe$.[4–7]

Our interest is in the synthesis and study of optical properties of the narrow-gap semimagnetic semiconductor $Hg_{1-x}Mn_xTe_{1-y}Se_y$. In this paper we have investigated its reflection spectrum in the far-infrared range.

## 2. EXPERIMENTAL METHOD

Single crystals of $Hg_{1-x}Mn_xTe_{1-y}Se_y$ were grown by the Bridgman method from chemically pure components. For the measurements, samples were cut from ingots by the electroerosion method, yielding samples with characteristic dimensions $6\times6\times0.2\ mm^3$. The manganese content was determined more accurately by measuring the absolute value of the magnetic susceptibility at room temperature. $X$-ray, microprobe analysis, and magnetic measurements established that the samples contained no inclusions of other phases, and that they were homogeneous. The uniformity of the samples was also monitored by measuring the Hall coefficient $R_H$ over the length of the samples. (The values of $R_H$ did not differ by more than a few percent in the samples we chose to study, which attests to their high degree of uniformity.)

Our samples had mirror-like polished surfaces, with compositions $y=0.01$ and $x=0.01$, 0.03, 0.05, and 0.14. The concentrations and mobilities of current carriers for the single crystals we investigated are listed in Table I. The transport properties of $Hg_{1-x}Mn_xTe_{1-y}Se_y$ involve electrons and two groups of holes, in contrast to $Hg_{1-x}Mn_xTe$, where only electrons and holes in an impurity acceptor band contribute, or $Hg_{1-x}Mn_xSe$, where only electrons contribute. One set of holes in $Hg_{1-x}Mn_xTe_{1-y}Se_y$ probably consists of holes from the impurity acceptor band, which is also characteristic of materials like $Hg_{1-x}Mn_xTe$, while the other set consists of band holes.[8]

It is well known that the near-surface region has a significant influence on the electric and galvanomagnetic properties of semiconductor solid solutions based on mercury telluride.[9] In order to eliminate this effect, we subjected our samples to chemical-mechanical polishing immediately before making the measurements, followed by a further chemical etch. Special investigations showed that exposure of the etched samples to air for a few days did not change their properties, i.e., the near-surface region does not affect the results obtained.

The optical spectra were recorded with a IFS-113v spectrometer (Bruker) in the wave number range (10–600) $cm^{-1}$ at room temperature and liquid-nitrogen temperature. In this

TABLE I. Concentration of electrons $n$ and holes $p_1$ and $p_2$ for the mobility of electrons $\mu_c$ and holes $\mu_{p1}$, $\mu_{p2}$ for the samples of $Hg_{1-x}Mn_xTe_{1-y}Se_y$ investigated here at $T=4.2$ K.

| Sample No. | $x$ | $n$, $10^{20}m^{-3}$ | $\mu_c$, $m^2/V\cdot s$ | $p_1$, $10^{23}m^{-3}$ | $\mu_{p1}$, $m^2/V\cdot s$, | $p_2$, $10^{21}m^{-3}$ | $\mu_{p2}$, $m^2/V\cdot s$ |
|---|---|---|---|---|---|---|---|
| 1 | 0.01 | 0.1 | – 5.0 | 3.0 | 0.09 | 0.6 | 0.10 |
| 2 | 0.03 | 5.9 | – 1.6 | 1.8 | 0.10 | 0.53 | 0.13 |
| 3 | 0.05 | 5.3 | – 1.5 | 2.8 | 0.0715 | 7.2 | 0.20 |
| 4 | 0.14 | 0.3 | – 6.0 | 2.7 | 0.082 | 9.0 | 0.3 |

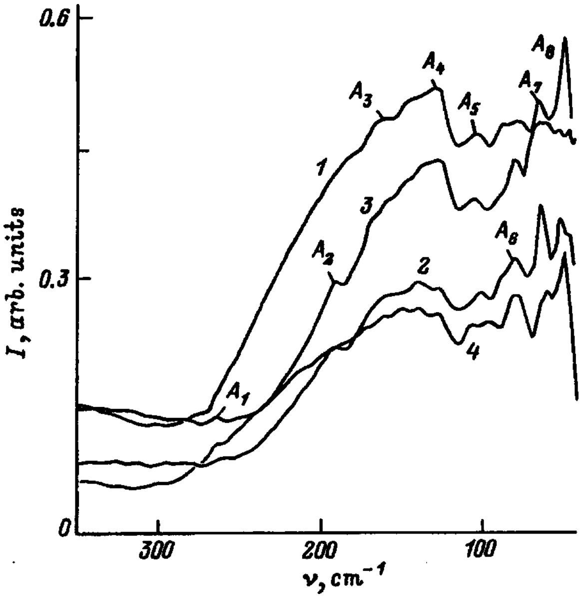

FIG. 1. Reflection spectrum $Hg_{1-x}Mn_xTe_{1-y}Se_y$ obtained at room temperature of samples 1–4.

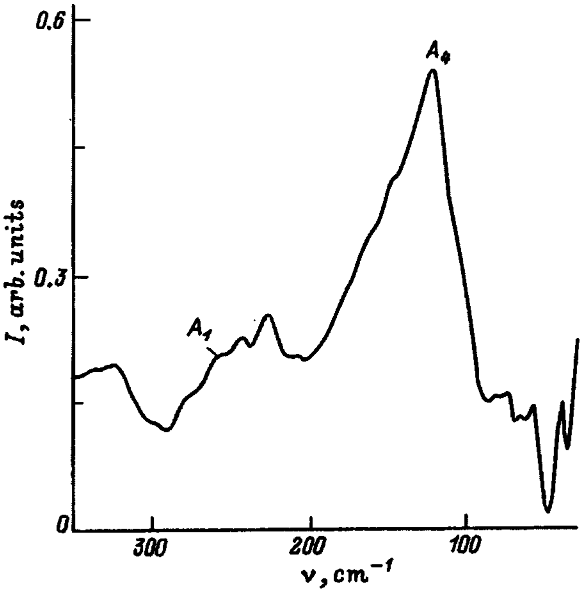

FIG. 2. Reflection spectrum of sample *1* at liquid-nitrogen temperature.

case, the wave number resolution was 0.5 $cm^{-1}$ over the entire spectral interval.

## 3. REFLECTION SPECTRA

Figure 1 shows the reflection spectra of samples *1–4* at room temperature. The letters indicate the characteristic positions of lattice modes. The deep washed-out minimum on the high-frequency side of the spectrum (around 280 $cm^{-1}$) corresponds to the spectral position of the mixed plasmon-phonon mode. This mode appears because of the high concentration of free charge carriers in the samples under study. The exact spectral positions of the lattice modes observed are listed in Table II. In Table II we also list values of the wave number corresponding to these modes at liquid-nitrogen temperature.

From a comparison of data taken at these two temperatures, it is clear that modes $A_1-A_3$, $A_7$ shift to longer wavelength portions of the spectrum as the temperature falls, whereas the positions of modes $A_4$ and $A_6$ do not change. At the same time, mode $A_5$ shifts towards the short-wavelength portion of the spectrum.

Figures 2 and 3 show reflection spectra at liquid-nitrogen temperatures for samples *1* and *2*, respectively. In Figs. 2 and 3 it is clear that as the temperature falls, the shape of the spectrum changes as the plasmon-phonon minimum moves toward the region of small wave numbers, which is a consequence of the decreasing free carrier concentration. For this reason, the spectrum acquires a more well-defined profile in the region of bulk lattice vibrations.

Mode $A_1$, whose position depends on temperature and on composition, was not observed previously in the ternary compound $Hg_{1-x}Mn_xTe$,[4]; therefore, we assign it to a local mode of selenium in the lattice of the quaternary compound $Hg_{1-x}Mn_xTe_{1-y}Se_y$.

Modes $A_2$ and $A_3$ correspond to transverse optical (TO) and longitudinal optical (LO) phonons. This follows from a comparison of our data with the results of Refs. 4 and 5. Modes $A_2$ and $A_3$ are practically unchanged as the composition changes and shift only slightly toward the low-energy region as the temperature decreases. The TO mode $A_2$ could correspond to vibrations of the binary component MnTe in the crystal lattice of the compound. We can also say this about mode $A_4$ (see Ref. 4).

Interpretation of mode $A_5$ depends on the literature source used: one paper assigns it to a local defect mode,[5] while another assigns it to LO phonons.[4] The four-

TABLE II. Spectral position of lattice modes $A_i$($cm^{-1}$) for $Hg_{1-x}Mn_xTe_{1-y}Se_y$ at room temperature (in parentheses—at liquid-nitrogen temperature).

| Sample No. | $x$ | $y$ | $A_1$ | $A_2$ | $A_3$ | $A_4$ | $A_5$ | $A_6$ | $A_7$ | $A_8$ |
|---|---|---|---|---|---|---|---|---|---|---|
| 1 | 0.01 | 0.01 | – | – | 156 | 125.0 | 97.5 | 72.8 | 60.9 | 43.8 |
| | | | (254) | ( – ) | (152.8) | (125.3) | ( – ) | (75.0) | (59.4) | (41.3) |
| 2 | 0.03 | 0.01 | 261 | 192.8 | 156.0 | 123.0 | 97.5 | 75.6 | 59.4 | 46.9 |
| | | | ( – ) | (186.6) | (153.1) | (122.5) | (105.6) | ( – ) | (55.6) | (38.1) |
| 3 | 0.05 | 0.01 | 265 | 189 | 156.0 | 122.5 | 101.0 | 75.5 | 60.0 | 47.8 |
| | | | (254) | (185.9) | (153.8) | (126.3) | (106.6) | (71.9) | (54.4) | ( – ) |
| 4 | 0.14 | 0.01 | 265.6 | 190.6 | 156.0 | 124.4 | 103.1 | 76.6 | 56.3 | 45.3 |
| | | | (256.2) | (185.9) | (154.0) | (124.4) | (108.1) | (72.5) | (53.8) | (23.4) |

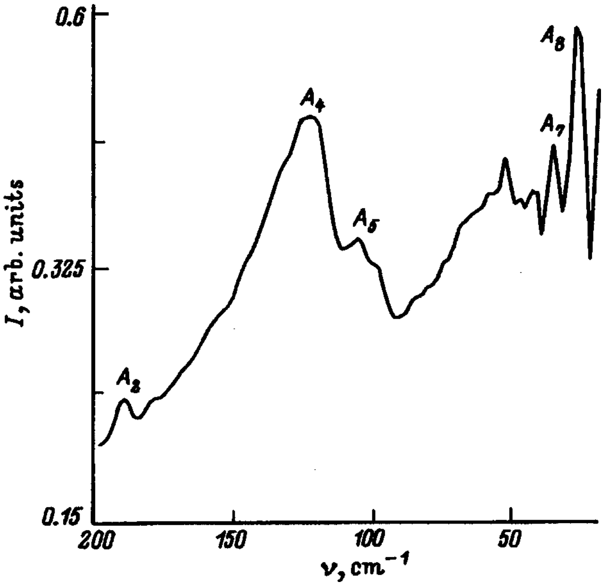

FIG. 3. Reflection spectrum of sample *2* obtained at liquid-nitrogen temperature.

component crystal $Hg_{1-x}Mn_xTe_{1-y}Se_y$ has defects that are characteristic of $Hg_{1-x}Mn_xTe$: vacancies of mercury, selenium, tellurium, interstitial mercury, etc. The Se atoms occupy vacancies, and new clusters appear or change their dimensions, depending on the situation. Change in the dimensions of clusters leads to changes in the vibrational spectrum of $Hg_{1-x}Mn_xTe_{1-y}Se_y$, for example, mode $A_5$ shifts toward higher energies as the Mn content $x$ increases.

## 4. DISTINCTIVE FEATURES OF THE REFLECTION SPECTRA IN THE SMALL-WAVE-VECTOR RANGE

A feature worth noting is the good resolution of modes $A_6-A_8$, which are present in the reflection spectra of nearly all the samples. As the temperature decreases, the amplitude of vibration of these modes increases. One reason for absorption of photons in this region of the spectrum could be optical transitions of carriers from the valence band to the impurity band with participation of phonons. The presence of this band in the materials under study was established in Ref. 8. It is located above the bottom of the conduction band by an energy of about 5 meV. This energy is comparable to the energy of transitions with participation of the phonons corresponding to modes $A_7$ and $A_8$. However, despite the single- phase nature of the sample, we cannot completely rule out the possible existence in the samples of a granular structure. If the dimensions of the grains were 20–50 $\mu$m, modes $A_7$ and $A_8$ could in principle be explained by local vibrations, i.e., bulk-confined acoustic phonons.

This work was supported by the Russian Fund for Fundamental Research Grants 96-15-96500 and 96-02-18853.

[1] J. K. Furdyna, J. Appl. Phys. **64**, R29 (1988).
[2] I. I. Lyapilin and I. M. Tsidil'kovskiĭ, Usp. Fiz. Nauk **146**, 35 (1985) [Sov. Phys. Usp. **28**, 349 (1985)].
[3] N. B. Brandt and V. V. Moshchalkov, Adv. Phys. **33**, 194 (1984).
[4] S. W. McKnight, P. M. Amirtharaj, and S. Perkowitz, Solid State Commun. **25**, 357 (1978).
[5] M. Grynberg, R. Le Toullec, and M. Balkanski, Phys. Rev. B **9**, 517 (1974).
[6] G. D. Coguric, Z. V. Popovich, D. Stajanovic, O. Zizic, and W. Konig, Solid State Commun. **77**, 555 (1991).
[7] O. Zizic, Z. V. Popovich, A. Milutinovich, and V. A. Kulbachinskii, Phys. Status Solidi B **168**, k103 (1991).
[8] V. A. Kulbachinskii, P. D. Maryanchuk, I. A. Churilov, M. Inoue, M. Sasaki, H. Negishi, and Y. Hara, Semicond. Sci. Technol. **10**, 463 (1995).
[9] V. I. Ivanov-Omskii, N. N. Berchenko, and A. I. Elizarov, Phys. Status Solidi A **103**, 11 (1987).

Translated by Frank J. Crowne

SEMICONDUCTORS VOLUME 32, NUMBER 5 MAY 1998

# Effect of ultraviolet irradiation on the luminescence and optical properties of ZnS : Mn films

Ya. F. Kononets, L. I. Veligura, and O. A. Ostroukhova

*Institute of Semiconductor Physics, Academy of Sciences of Ukraine, 252028 Kiev, Ukraine*

(Submitted August 29, 1997; accepted for publication October 26, 1997)
Fiz. Tekh. Poluprovodn. **32**, 549–553 (May 1998)

Changes have been observed and investigated in the electrooptic properties of ZnS : Mn films used in thin-film electroluminescent structures as a result of irradiation by ultraviolet pulses with energies per pulse much smaller than the threshold energy of laser annealing. It is found that in disordered ZnS : Mn films processes of defect generation are important even for below-threshold energies of the ultraviolet radiation pulses, and can facilitate the effective diffusion and activation of Mn atoms in the ZnS lattice. It is shown that short-time ultraviolet processing of thin-film electroluminescent structures improves their characteristics and, by making the preparation technology simpler and cheaper, allows structures with detector characteristics to be fabricated on low melting-point substrates. © *1998 American Institute of Physics.* [S1063-7826(98)00805-9]

Films of wide-gap compounds of the group II–VI (ZnS, CdS, etc.) are widely used in various optoelectronic systems, e.g., photodetectors or electroluminescent light sources. For example, thin-film electroluminescent structures based on ZnS : Mn films have been used successfully in planar displays for information imaging systems. The use of these thin-film electroluminescent structures is becoming more widespread as their preparation technology becomes cheaper and simpler.[1]

One commonly used technology operation in making these thin-film electroluminescent structures is an anneal at temperatures of 500–600 °C, which facilitates the crystallization processes in ZnS : Mn films and activates impurities. However, this anneal requires the use of refractory substrates and protective measures to prevent interlayer diffusion of impurities that degrade the characteristic of the layers. Laser annealing makes selective processing of the thin-film electroluminescent structures possible over their area or along the layers without heating the substrate or the other layers of the thin-film electroluminescent structure, which is especially important in fabricating multicolor structures.[1] However, since the threshold energy density for laser annealing exceeds 0.5 J/cm$^2$ (Ref. 2), high-power sources of ultraviolet radiation are needed, and it is necessary to carry out the laser annealing at excess pressures of inert gas in order to avoid cracking the layers.

Previously,[3] we observed that the photoluminescence intensity of ZnS : Mn films increased when they were exposed to light pulses from a LGI-21 laser with wavelength $\lambda = 337$ nm and energy density per pulse $E_i \geqslant 10^{-4}$ J/cm$^2$, which is considerably lower than the threshold energy density for laser annealing. We established that the magnitude of the effect depends both on the fabrication conditions for obtaining the ZnS : Mn films and on the intensity and duration of the ultraviolet irradiation (UV annealing). The goal of this paper is to investigate this effect in more detail in order to clarify its features and nature, as well as to evaluate the possibility of using it to make thin-film electroluminescent structures based on ZnS : Mn films.

## 1. TEST SAMPLES AND EXPERIMENTAL PROCEDURE METHOD

We studied films of ZnS : Mn 0.1–0.8 $\mu$m thick obtained by coevaporation of ZnS and MnS in vacuum onto a substrate made of glass or sapphire heated from below to a temperature $T_s = 100-180$ °C, with no thermal annealing and subjected to an additional thermal anneal in vacuum. The concentration $C_{\mathrm{Mn}}$ of manganese in the layers varied from 0 to 1 weight %. In order to study the effect of ultraviolet annealing on the electroluminescence properties, we fabricated the usual type of MISIM structure, in which a semiconductor (S) film of ZnS : Mn with thickness $\sim 0.6$ $\mu$m is enclosed between two insulating (I) $Al_2O_3$ layers, each of thickness $\sim 3$ $\mu$m. The lower electrode (M) was made of a layer of $In_2O_3$ on glass or sapphire, and the upper layer was made of aluminum. Before depositing the aluminum, some of the structures were subjected either to thermal annealing in vacuum at an anneal temperature $T_a = 300-500$ °C or to irradiation for 15–30 min by pulses from a LGI-21 laser ($E_i = 10^{-3}$ J/cm$^2$, repetition rate $f = 100$ Hz). In addition to UV radiation from the LGI-21 laser, we also used UV radiation selected by filters from a DRSh-250 mercury lamp in the range 313 or 365 nm.

We studied the transmission spectra and photoluminescence of the ZnS : Mn films, along with changes in the spectrum and PL intensity resulting from thermal annealing or UV processing, the kinetics of luminescence in the emission band of the $Mn^{2+}$ ions ($\lambda = 585$ nm) and in the band of so-called self-activated emission ($\lambda = 460$ nm). In studies of the spectral characteristics we used a KSBU-23 spectrometer. The time resolution for our measurements of photoluminescence kinetics excited by LGI- 21 pulses ($\tau_i = 10$ ns) was $\leqslant 10^{-6}$ s.

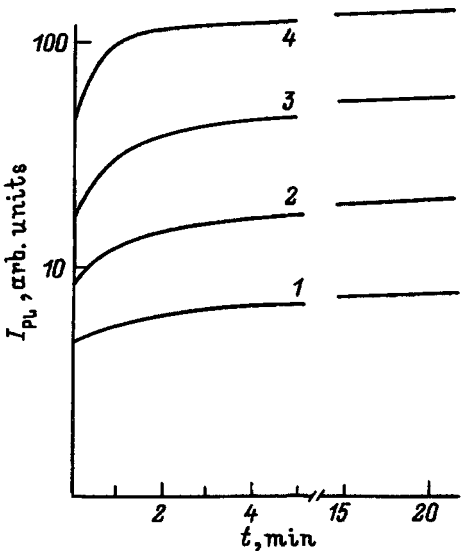

FIG. 1. Increase in PL intensity ($I_{PL}$) of a ZnS : Mn film ($T_s$=120 °C) irradiated by pulses of UV quanta. Energy density per pulse $E_i$, $10^{-3}$ J/cm$^2$: *1*—0.1, *2*—0.2, *3*—0.35, *4*—1.

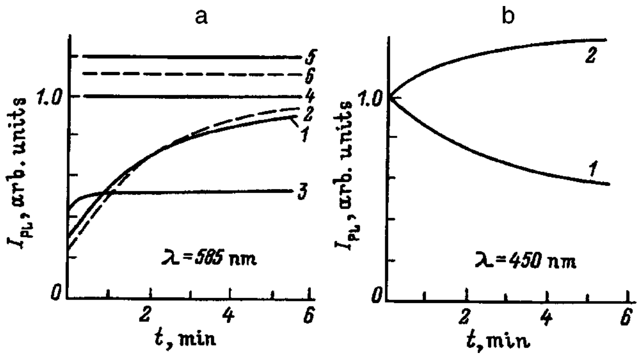

FIG. 2. Effect of irradiation time *t* by the LGI-21 laser on the PL intensity ($I_{PL}$) when λ=585 nm (a) and λ=450 nm (b). The irradiation regime is: $f$=100 Hz, $E_i=10^{-3}$ J/cm$^2$. a: a ZnS : Mn film without annealing (*1*), films subjected to thermal annealing at $T_a$=300, 400, 500 °C (*3,4,5*), and films subjected to additional $\gamma$ irradiation (*2*) and then thermally annealed at 400 °C (*6*). b: a ZnS : Mn film (*1*) and an undoped ZnS film (*2*).

We made multiple measurements on the three types of thin-film electroluminescent structures which we fabricated, i.e., original and subjected either to thermal annealing or UV annealing. These measurements were: voltage-brightness and voltage-charge characteristics, electroluminescent efficiency, defined as the ratio of the brightness of the structure to the current passing through it, and spectral and kinetic characteristics of the luminescence. In measuring the voltage-brightness and voltage-charge characteristics we used standard measurement methods. Electroluminescence was excited by a sinusoidal voltage at a frequency $f$=50–5000 Hz or by sign-changing rectangular pulses of duration 10–20 $\mu$s with rise times of ~0.5 $\mu$s. The latter were also used to study the growth and decay kinetics of the electroluminescence.

## 2. RESULTS AND DISCUSSION

Our studies showed that ZnS : Mn films obtained by deposition onto a substrate that was slightly heated from below ($T_s$<150 °C) exhibited an increase in the PL intensity $I_{PL}$ from the Mn$^{2+}$ ions with time *t* when the films are irradiated by pulses with energy density $E_i \geqslant 10^{-4}$ J/cm$^2$. The rate of growth of the PL intensity and its level at saturation depended not only on the intensity of the UV irradiation (Fig. 1) but also the technology for fabricating the films and their doping level. This effect is observed when the ZnS : Mn films are irradiated by quanta from the spectral region of band-band absorption (λ=313, 337 nm), and is not observed when the irradiating quanta are from the impurity absorption region (λ=365 nm). Disorder in ZnS : Mn films is generated by low deposition temperatures, increased doping levels, or additional $\gamma$-irradiation. It turns out that increasing this disorder enhances the effect of UV annealing.

Thus, when ZnS : Mn films ($T_s$=120 °C, $C_{Mn}$=0.6 weight %) are irradiated by pulses with energy $E_i=10^{-3}$ J/cm$^2$, the intensity of the photoluminescence from the Mn$^{2+}$ ions (Fig. 2a, curve *1*) increases after $t$=5 min by 28 to 88 % relative to the PL intensity of the same film subjected to thermal annealing at a temperature $T_a$=400 °C in vacuum for one hour (curve *4*). Subjecting such a film to an additional $\gamma$-irradiation ($10^7$ rad, curve *2*) under the same conditions increases its PL intensity by 22 to 94%. Thermal annealing such a sample also enhanced the intensity of its PL (curve *6*). The ultraviolet annealing effect, as follows from Fig. 2a, is significant for the initial films of ZnS : Mn (curves *1* and *2*), but decreases after thermal annealing and for $T_a$>400 °C is no longer observed. Note that increasing the deposition temperature above 180 °C also causes the ultraviolet anneal effect to disappear.

Ultraviolet annealing of ZnS : Mn films not only increases the PL from the Mn$^{2+}$ ions but also suppresses PL arising from self-activated emission (Fig. 2b, curve *1*), whereas the same kind of annealing of an undoped ZnS film causes the self-activated emission to increase (curve *2*). Some increase in the self-activated emission PL is also observed when films of undoped ZnS are $\gamma$-irradiated, which leads to the formation of Frenkel pairs ($V_{Zn}Zn_i$). The effect of UV annealing is stable, in that several years after annealing there is no noticeable change in the properties of the film.

Analysis of transmission spectra shows that UV annealing does not change the shape of the spectrum in the transparency region (λ>400 nm), i.e., during annealing no significant changes occur in the refractive index or degree of light scattering in the film. However, this type of anneal, like thermal annealing (Fig. 3, curves *1–3*, causes the absorption edge to become sharper. It is interesting to note that in undoped ZnS films UV annealing does not affect the shape of the absorption edge, whereas after thermal annealing (curve *4*) the absorption edge becomes sharper.

Figure 4 shows the results of measuring the voltage-brightness characteristics and electroluminescence efficiency for two types of structures—one with no UV annealing (curves *1* and *3*) and one with UV annealing (curves *2* and *4*). It is clear that annealing leads to a significant increase in the brightness and electroluminescence efficiency, and to steepening of the voltage-brightness characteristics. More-

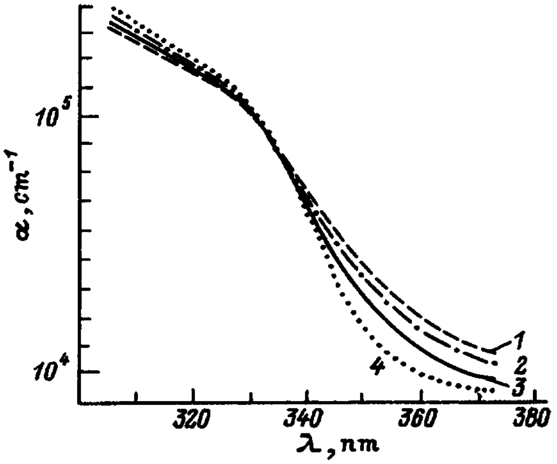

FIG. 3. Absorption edge of ZnS : Mn films ($T_s=120°$) unannealed (*1*) after UV annealing (*2*), and after thermal annealing at $T_a=500$ °C (*3*). *4*—Absorption edge of an undoped ZnS film ($T_s=120$ °C, $T_a=500$ °C). λ is the absorption coefficient.

over, the annealing also facilitates more stable operation of the thin-film electroluminescent structures, since after UV annealing they have more electrical breakdown strength and their characteristics are less subject to change during operation. Comparison of the parameters of these thin-film electroluminescent structures shows that with regard to brightness and electroluminescence efficiency the thin-film electroluminescent structures subjected to ultraviolet annealing are just as good as those subjected to thermal annealing at 450 °C in vacuum for 1 hour, and have greater electrical breakdown strength.

It is well known[1,4] that temperature annealing of ZnS : Mn films is necessary in order to increase the degree of crystallinity of the films, anneal out defects, and uniformly distribute and activate the Mn. Significant growth of crystallites is observed only for anneal temperatures $T_a > 500$ °C, while at lower temperatures the increased concentration of $Mn^{2+}$ ions replacing Zn is more important, since these latter centers luminescence efficiently. The same processes are characteristic of laser annealing, where recrystallization of the layer after rapid local heating leads to higher quality of the crystal structure and diffusion of impurities into lattice sites, where they become electrically or optically active.[2] In this case important roles are played not only by thermal heating, but also by the generation of thermoelastic strain, larger densities of electron-hole pairs, which enhance the diffusion rate of impurities, and the annealing and creation of defects.[5]

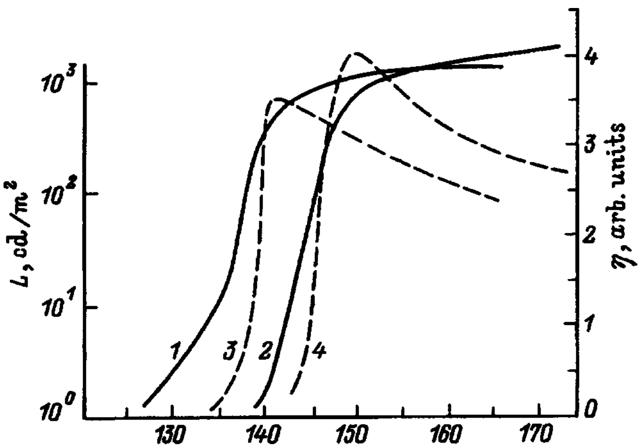

FIG. 4. Dependence of the brightness *L* (*1,2*) and electroluminescent efficiency *η* (*3,4*) on the magnitude of the voltage *U* applied to an initial thin-film electroluminescent structure (*1,3*) and to one that was UV annealed (*2,4*). $f = 5$ kHz.

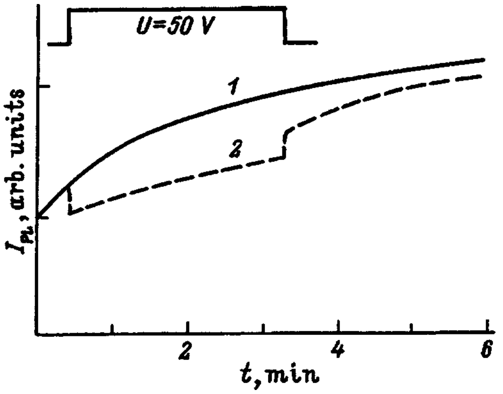

FIG. 5. Rate of UV annealing of a ZnS : Mn film without an applied voltage (*1*) and with an applied voltage (*2*). The voltage pulse shape is shown at the top of the figure.

The threshold energy for UV annealing is substantially lower than the laser annealing threshold ($10^{-4}$ versus 0.5 J/cm²), and under these annealing conditions the heating of the ZnS film does not exceed 10 °C. Annealing is observed only in the region where quanta generated by electron-hole pairs are absorbed, and is not observed when the films are irradiated through the upper Al electrode. Therefore, there is no reason to assign a dominant role to heating or thermoelastic stresses in the observed UV annealing effect.

In Fig. 5 we show the results of studies of how an electric field affects the kinetics of UV annealing. We found that applying a voltage (curve *2*) leads to quenching of the photoluminescence and weakening of its growth during UV exposure, and the PL intensity is smaller after the voltage is removed. The observed decrease in the rate of UV annealing in an electric field, due to quenching of the photoluminescence as a result of carrier separation and consequently a decreased electron-hole-pair density, indicates the significant influence of the latter on the UV annealing, although their density is smaller by several orders of magnitude than that required by a model of plasma annealing.[5]

Thus, none of the phenomena that could take place when an energy of $\sim 10^{-3}$ J/cm² is absorbed by a ZnS : Mn film—heating, thermoelastic strain, or electron-hole plasmas—can cause the recrystallization and lattice ordering that are characteristic of laser annealing. However, certain things are known[6] about generation of defects in semiconductors subjected to pulsed irradiation that suggest a decrease in the threshold energy for their formation. This decrease could be important in strongly disordered semiconductors when the effect of the deformation potential is combined with the heating, thermoelastic stress, and plasma generation that can occur when the semiconductor is irradiated by these pulses.[7]

Lowering the energy of defect formation can in turn stimulate the processes of impurity diffusion and activation.

The more efficient ultraviolet annealing observed in more disordered films suggests that this kind of annealing can lead not only to recrystallization of the lattice, but also to the creation and annihilation of defects. It is known that irradiation of CdS crystals[8] or ZnSe crystals[9] by light from an LGI-21 laser leads to the generation or annealing out of intrinsic defects. In ZnS, the threshold energies for defect formation are large, of order 5–6 eV (see Ref. 10) for the most probable of these—the $V_{\mathrm{Zn}}\mathrm{Zn}_i$ pair—and energy quanta in the range of 3.6 eV are probably insufficient to create defects in the ordered ZnS lattice. However, in strongly disordered ZnS films exposed to pulsed UV irradiation this energy could be considerably smaller; direct confirmation of this is probably the increased self-activated emission in undoped ZnS films under UV annealing (Fig. 2a, curve *2*) caused by recombination of electrons trapped at shallow donors (usually $\mathrm{Zn}_i$ or $\mathrm{Cl}_s$) and holes at centers which incorporate zinc vacancies ($V_{\mathrm{Zn}}$).[10]

Manganese in ZnS is an efficient luminescence center which replaces Zn in the cation sublattice; the process of inclusion of Mn occurs more efficiently when voids are present in the latter, i.e., zinc vacancies.[4] Usually, the decrease in self-activated emission observed when ZnS is doped with manganese is associated with a decreased number of these voids due to their occupation by manganese with the formation of an efficient luminescence center—the $\mathrm{Mn}^{2+}$ ion. The enhanced PL from $\mathrm{Mn}^{2+}$ ions observed when ZnS : Mn films are UV annealed is accompanied by a decrease in self-activated emission, which probably indicates stimulation by the UV irradiation of the processes that incorporate manganese atoms into the ZnS lattice where they become effective luminescence centers, since they are isoelectronically substituting for zinc atoms.

Obviously, in ZnS : Mn films deposited on weakly heated substrates (from below) there are many nonequilibrium defects, including inclusions of manganese atoms, that form a broad spectrum of states. In strongly compensated semiconductors, the shallow states are able to wash out the edge of the fundamental absorption band.[11] The changes in the shape of the absorption edge and the emission band of $\mathrm{Mn}^{2+}$ ions observed in the course of UV annealing of ZnS : Mn and ZnS films do not contradict the assertion that some of the shallow levels are converted into deep neutral levels, since manganese, which isoelectronically replaces zinc in the ZnS lattice, is neutral with respect to the latter.

In general, photoinduced changes in the PL intensity can be caused by changes in the concentration of recombination centers due to annealing[9] or generation of new defects[8] stimulated by impurity diffusion,[12] and by changes in the recombination characteristics of the luminescence centers. Our investigations of the luminescence spectra show that both the PL and EL spectra are dominated by a band associated with $\mathrm{Mn}^{2+}$ ions, since emission outside this band, including self-activated emission, is several orders of magnitude weaker. Although UV annealing makes the PL intensity of $\mathrm{Mn}^{2+}$ ions several times stronger, it gives rise only to a slight distortion of the spectrum, while the spectrum and kinetics of the luminescence and the absorption coefficient are essentially unchanged. This probably indicates that the increased PL from $\mathrm{Mn}^{2+}$ ions in films subjected to UV annealing is connected not with an increase in the efficiency of excitation or luminescence of the latter, but rather with the increase in the number of luminescence centers.

Thus, we have established that subthreshold UV power can generate intrinsic defects in ZnS : Mn films irradiated by pulses of UV light and stimulate diffusion and interstitial insertion of manganese atoms in the bulk of the crystallites, which leads to an increase in the number of luminescence centers. In this case the number of shallow states decreases, which affects the shape of the absorption edge, the emission band of manganese, the intensity and electroluminescence efficiency, and the steepness of the voltage-brightness characteristic. The decrease in concentration of shallow states, which can drift in an electric field, increases the electrical strength and improves the operating stability of thin-film electroluminescent structures after UV annealing. We have shown that UV annealing makes the process of fabricating these thin-film electroluminescent structures simpler and cheaper, and allows us to obtain them with suitable characteristics on cheap, low-melting substrates.

[1] Y. A. Ono, *Electroluminescent Displays* (Singapore, Scientific World, 1995).

[2] H. S. Reehal, J. M. Gallego, C. B. Edwards, Appl. Phys. Lett. **40**, 258 (1982).

[3] L. I. Veligura, Ya. F. Kononets, and O. A. Ostroukhova, in *Abstracts of International Conference on Luminescence* (FIAN, Moscow, 1994), p. 232 [in Russian].

[4] N. Yu and M. Senna, Appl. Phys. Lett. **64** , 424 (1995).

[5] V. I. Emel'yanov, Bull. Russ. Acad. Sci. Ser. Phys. **56**, 4147 (1992).

[6] R. V. Prudnikov, P. K. Kashkarov, and V. Yu. Timoshenko, Bull. Moscow State Univ. Ser. 3: Phys., Astronomy **36**(3), 61 (1995) [in Russian].

[7] V. I. Emeljanov and P. K. Kashkarov, Appl. Phys. A **55**, 161 (1992).

[8] G. P. Yablonskiĭ, Fiz. Tekh. Poluprovodn. **18**, 918 (1984) [Sov. Phys. Semicond. **18**, 570 (1984)].

[9] N. E. Korsunskaya, I. V. Markevich, M. D. Moin, A. Tanatar, and I. Yu. Shabliĭ, Fiz. Tverd. Tela (Leningrad) **24**, 3223 (1982) [Sov. Phys. Solid State **24**, 1829 (1982)].

[10] J. E. Nichols, J. J. Davis, and B. C. Covenott, J. Phys. C: Sol. State Phys. **12**, 370 (1979).

[11] V. I. Fistul', *Heavily Doped Semiconductors* (Plenum Press, New York, 1969) [Russ. orig. Nauka, Moscow, 1967].

[12] M. M. Sobolev, A. V. Abramov, N. G. Deryagin, A. G. Deryagin, V. I. Kuchinskiĭ, and M. I. Papentsev, Fiz. Tekh. Poluprovodn. **30**, 1108 (1996) [Semiconductors **30**, 587 (1996)].

Translated by Frank J. Crowne

# Natural nonuniformities in the height of a Schottky barrier

V. B. Bondarenko, Yu. A. Kudinov, S. G. Ershov, and V. V. Korablev

*St. Petersburg State Technical University, 195251 St. Petersburg, Russia*

(Submitted March 17, 1997; accepted for publication November 10, 1997)
Fiz. Tekh. Poluprovodn. **32**, 554–556 (May 1998)

This paper discusses natural nonuniformities in the height of a Schottky barrier caused by the discreteness of impurity charges randomly distributed in the depletion region. The parallel-diode model is used to show that these natural fluctuations in the effective barrier height at a metal-semiconductor junction, on the average, do not exceed $kT$ at room temperature for doping levels less than or equal to $10^{18}$ cm$^{-3}$. [S1063-7826(98)00905-3]

The lack of time-delay processes involving the accumulation and extraction of minority carriers, the possibility of creating sharp junctions, and other properties make Schottky contacts a necessary structural unit in the fabrication of electronic circuits. For this reason, it is especially important to describe these junctions and predict their parameters based on well-developed theories.

Real metal-semiconductor contacts are nearly always nonuniform to some degree. This is confirmed by direct measurement with scanning probes[1] and by analysis of the nonideality of current-voltage characteristics.[2,3] It is customary to link this fact with the defective nature of the boundary or, in general, to abstract it from the physical nature of the nonuniformities, modeling them, e.g., in Ref. 4, by spots with variable work function. A statistical approach was developed in Refs. 5 and 6 in order to construct a theory of excess current through metal-semiconductor junctions, and the effect of fluctuations in the magnitude of the impurity concentration (majority and compensated) on the Schottky barrier height was discussed as well.

Our goal in this paper is to show that even atomically smooth, abrupt, and defect-free contacts with no surface states unavoidably induce nonuniformities in the Schottky barrier, due to the discreteness of the charge of doping impurities at some well-defined value of the concentration (natural nonuniformities).

In describing the field and potential present in semiconductor depletion layers, the three-dimensional Poisson equation with a sum of $\delta$-functions on the right-hand side is replaced by its one-dimensional analog, whose solution leads to the well-known parabolic bending of the bands. The admissibility of this approximation is not in question if the extent of the depletion layer exceeds by many factors the average distance between atomic impurities. In this case it is possible to replace the discretely distributed bulk charge by a continuous distribution characterized only by the impurity concentration. In reality, however, at sufficiently high values of the band bending $U_0$ (greater than 0.1 eV) the average distance between charged donors $\langle d\rangle = N^{-1/3}$ is of the same order of magnitude as the width of the space-charge region, $L=(\varepsilon U_0/2\pi e^2 N)^{1/2}$ (where $\varepsilon \simeq 10$ is the dielectric constant of the semiconductor) over the full range of important, from the practical standpoint, doping levels, i.e., $N$ from $10^{16}$ to $10^{20}$ cm$^{-3}$. For example, when $U_0=0.2$ eV and $N=10^{18}$ cm$^{-3}$, we find that $\langle d\rangle = 10$ nm and $L=15$ nm. Thus, the effect of discreteness of the impurity charge cannot be ignored *a priori* in analyzing processes at the semiconductor surface and, in particular, at the metallic contact.

In Ref. 7 we calculated the distribution of electric field in the near-contact region of a Schottky junction, taking into account that the field in the space-charge region is generated by the fields of point charges of ionized impurities and their electrostatic images in the plane of the contact surface. The results of these calculations, presented in Ref. 7, showed that the value of the total field varies significantly along the surface and can exceed the value of the field in the one-dimensional model of band bending by one to two orders of magnitude. The electrostatic potential at the surface of a semiconductor in contact with a metal is smoothed out. However, if we take into account that a probe charge near the boundary feels the effect of the image force, we find that the height of the Schottky barrier depends on the value of the electrostatic field.

Computer simulation allows us to calculate the distribution of potential barrier height along the surface of the contact. However, even at rather small doping levels there are portions of the surface for which the barrier is so narrow that tunneling of electrons becomes important. In order to compare the results of our calculation with experiment, the effective Schottky height should be determined, i.e., the height of an equivalent classical barrier that gives the same current density through the junction.

In order to calculate the current through the junction we used the parallel-diode model.[8] Let us consider the case of rather small fluctuations in the electric field intensity in the near-contact region, which occurs at impurity concentrations less than or of the order of $10^{18}$ cm$^{-3}$. The requirement of rather weak variation of the field in the junction is necessary in order that we be able to use the parallel-diode model. The characteristic size of the model diodes should greatly exceed the wavelength of an above-barrier electron $\lambda$, which is true for these doping levels. The surface of the contact is divided into $n$ equal areas $S_i$, within which the potential is nearly one-dimensional. Let us also assume that the junction bias is small. We will assume that the external voltage drop occurs only across the depletion layer, i.e., $U=eFL$, where $F$ is the electric field applied to the junction. Taking into account the transparency of the barrier $D_i(E,F)$ and the equilibrium energy distribution of electrons, we can then write the thermionic emission current density from area $S_i$ in the form

$$j_i=(m^*ekT/2\pi^2\hbar^3)\int_0^\infty dED_i(E,F)$$

$$\times\ln\left\{\frac{1+\exp[(E_f-E)/kT]}{1+\exp[(E_f-E-U)/kT]}\right\}. \tag{1}$$

Here $m^*$ is the electron effective mass, $E_f$ is the Fermi level, and $E$ is the energy of an electron measured from the bottom of the conduction band. The transparency of the potential barrier in the quasiclassical approximation can be set equal to 1 for above-barrier electrons, while for below-barrier particles it is given by the expression

$$D_i(E,F)=\exp\left\{-[(2m^*)^{1/2}/\hbar]\int_b^a dz[U_i(z,F)-E]^{1/2}\right\}. \tag{2}$$

Here $a$ and $b$ are roots of the equation $U_i(z,F)=E$. The potential profile in Eq. (2) has the form

$$U_i(z,F)=U_0-e(F_{0i}-F)z-e^2/4\varepsilon z,$$

where the field $F_{0i}$ is the result of summing the fields of donor-image dipoles. Near the boundary within the area $S_i$ it is constant and depends on the specific position of the donors in the space-charge layer and on their number, i.e., the impurity concentration. The field calculations were already done in Ref. 7.

Now, according to our definition of the effective barrier, its height $U_{\text{eff}}$ should be determined from the condition that $j$ equal the value calculated using the classical formula

$$j=[m^*e(kT)^2/2\pi^2\hbar^3]\exp(-U_{\text{eff}}/kT)[\exp(U/kT)-1]. \tag{3}$$

In each model diode we have

$$U_{\text{eff}i}=kT\ \ln\{[m^*e(kT)^2/2\pi^2\hbar^3][\exp(U/kT)-1]/j_i\}. \tag{4}$$

Calculations show that for this model of a metal-semiconductor contact the distribution of effective values of the barrier along the boundary surface has a density that differs from a $\delta$-function. The results obtained nearly coincide with the distribution of values of electrostatic potential for a free semiconductor surface in the case of intrinsic delocalized surface states.[7] In Fig. 1 we plot the density $p(U_{\text{eff}})$ of the distribution of effective Schottky barrier heights for two doping levels of the semiconductor—$10^{16}$ and $10^{18}$ cm$^{-3}$. The widths of these curves, which characterize the degree of nonuniformity of the barrier height, are in the range 10–30 meV for these concentrations of impurities. The character of this distribution function density for the effective Schottky barrier height and its variation with increasing doping level qualitatively agree with the results of the experimental paper of Palm *et al.*[1] The quantitative disagreement, as mentioned in Ref. 7, could be associated with enhancement of the primary nonuniformities of the potential at the surface of the semiconductor when a metallic film is grown on top.

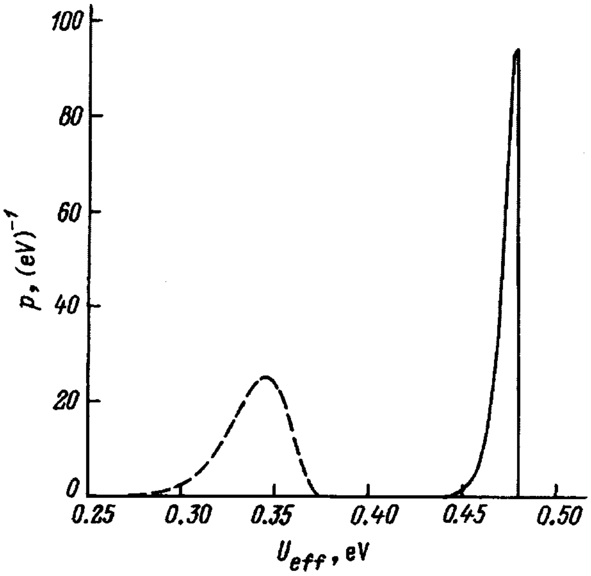

FIG. 1. Distribution density of the heights of effective Schottky barriers along the surface of a contact for a band bending $U_0=$ 0.5 eV and various doping levels: $10^{16}$ cm$^{-3}$—solid curve, $10^{18}$ cm$^{-3}$—dashed curve.

Thus, in this paper we have defined and calculated modelistically the effective Schottky barrier height. We have shown that even in the absence of other defects nonuniformity of the electrostatic potential in the metal-semiconductor contact is caused by the discrete charge of the doping impurities. These calcuations determine the theoretically possible limits on the ideality of a Schottky diode.

[1] H. Palm, M. Arbes, and M. Schulz, Phys. Rev. Lett. **71**, 2224 (1993).
[2] B. R. Nad, *Electron Transport in Compound Semiconductors* (Berlin–Heidelberg–N.Y. 1980).
[3] R. T. Turn, Appl. Phys. Lett. **58**, 2821 (1991).
[4] J. P. Sullivan, R. T. Tung, M. R. Pinto, and W. R. Graham, J. Appl. Phys. **70**, 7403 (1991).
[5] M. Ĕ. Raĭkh and I. M. Ruzin, Fiz. Tekh. Poluprovodn. **21**, 456 (1987) [Sov. Phys. Semicond. **21**, 283 (1987)].
[6] Kh. G. Nazhmudinov and T. A. Polyanskaya, Fiz. Tekh. Poluprovodn. **21**, 1737 (1987) [Sov. Phys. Semicond. **21**, 1053 (1987)].
[7] V. B. Bondarenko, Yu. A. Kudinov, S. G. Ershov, and V. V. Korablev, Fiz. Tekh. Poluprovodn. **30**, 2068 (1996) [Semiconductors **30**, 1078 (1996)].
[8] I. Ordomari and K. N. Tu, J. Appl. Phys. **51**, 3735 (1980).

Translated by Frank J. Crowne

# Distinctive features of the magnetoresistance of degenerately doped *n*-InAs and their influence on magnetic-field-dependent microwave absorption

A. I. Veĭnger, A. G. Zabrodskiĭ, and T. V. Tisnek

*A. F. Ioffe Physicotechnical Institute, Russian Academy of Sciences, 194021 St. Petersburg, Russia*

G. Biskupski

*University of Science and Technology, Lille, France*

(Submitted June 22, 1997; accepted for publication November 18, 1997)
Fiz. Tekh. Poluprovodn. **32**, 557–563 (May 1998)

Magnetic-field-dependent microwave absorption and electron spin resonance are used to investigate magnetoresistive effects in strongly doped $n$-InAs. It is shown that these effects can be traced back to negative, positive, or oscillatory magnetoresistance (i.e., the Shubnikov–de Haas effect). While the experimental data are in agreement with the predictions of theory in the latter two cases, for the negative magnetoresistance there are features that are difficult to interpret, especially the absence of any effect at very small fields, much smaller than the characteristic field $H_\varphi$ that appears in the theory of quantum corrections, and the two-dimensionality of bulk samples in fields much larger than $H_\varphi$ implied by the observed dependences on temperature and to some extent on the magnetic field. © *1998 American Institute of Physics.* [S1063-7826(98)01005-9]

## 1. INTRODUCTION

Changes in the microwave absorption of solids placed in a magnetic field can be due to a large variety of phenomena. The most important of these was discussed in Ref. 1, where it was noted that magnetoresistive effects are responsible for most of the magnetic-field dependence of the microwave absorption in semiconductors. The conduit for these effects is the resistivity $\rho$, which for a semiconductor in a weak magnetic field increases as the square of the applied magnetic field $H$:

$$\rho=\rho_0+\beta H^2, \tag{1}$$

where $\beta$ is a coefficient of proportionality. In degenerate semiconductors oscillations in the magnetoresistance are observed at sufficiently strong magnetic fields, which are quantum mechanical in nature. This is the well-known Shubnikov–de Haas effect, which can be used to determine the precise position of the Fermi level in a degenerate semiconductor among other things.

The phenomenon of negative magnetoresistance required a much longer time to explain. Negative magnetoresistance appears at low temperatures, especially in strongly doped semiconductors, and has been studied experimentally since the end of the 1950's in several materials including InAs.[2] At the beginning of the 1980's theoretical descriptions were developed for this phenomenon, based on the quantum-mechanical properties of charge carriers in disordered conductors (see Ref. 3). Subsequent comparison of this theory, called the ''theory of quantum corrections,'' with the huge volume of experimental material accumulated at the end of the 1980's, led researchers to conclude that it was sufficiently complete to model all the basic features of the phenomena observed,[4] in particular, their temperature and magnetic-field dependences.

It is noteworthy that the experiments used to study magnetoresistive effects in semiconductors have been primarily dc experiments. Therefore, it is interesting to identify what features of this phenomenon appear at microwave frequencies, when the skin effect begins to make itself felt. In this case any change in resistance in a magnetic field appears as a change in the microwave absorption, and ESR (electron spin resonance) spectroscopy can be used to measure the latter. This technique is now commonly used to investigate magnetic field-dependent microwave absorption in superconductors,[5] and also in the search for new superconducting phases in nonsuperconducting hosts.[1] In particular, the experiments described in Refs. 1 and 5 demonstrated the high sensitivity of this technique to changes in the microwave absorption in materials with large conductivity.

For this reason, we propose in this paper to address the problem of identifying the effect of magnetoresistance and, in particular, negative magnetoresistance, on the absorption of electromagnetic energy at microwave frequencies for the example of degenerate $n$-type InAs. We will show that it is possible to use ESR spectroscopy effectively[6] in these studies.

## 2. EXPERIMENTAL PROCEDURE

The high sensitivity of ESR spectroscopy to magnetoresistive effects in low-resistance materials is a consequence of a number of methodological and structural features. First of all, the sample under study is placed at an antinode of the magnetic microwave field of a cavity resonator; therefore, the latter preserves its high $Q$. Secondly, what is measured is not the microwave power absorption itself, but rather its derivative with respect to magnetic field. This allows us to distinguish the field-sensitive part of the microwave absorption from the part that does not depend on magnetic field, and record only the first of these, and also to use a narrowband amplifier to enhance the signal, which greatly increases the signal-to-noise ratio.

A further advantage of the ESR technique is the fact that the magnets used in ESR spectroscopy generate highly uniform magnetic fields, and the systems for controlling this field make it possible to fix the value of the field and maintain that value to an accuracy of four decimal places. The magnetic field is scanned automatically, which allows us to measure the dependence of the derivative of the microwave absorption with respect to magnetic field $dP/dH$ on magnetic field $H$ with high accuracy; both the magnetic field and the value of its derivative are fixed.

On the other hand, use of a microwave field leads to certain peculiar features of the measurement process compared to measuring the dc resistance of a sample. These features derive from the skin effect, which causes the microwave field to penetrate only a rather small distance into the sample, so that the change in microwave absorption is determined by the change in resistance of a narrow, near-surface layer, where the state of the sample surface can strongly affect the phenomenon being measured. This requires special attention to conditions at the surface.

The problem with using ESR spectroscopy for such measurements stems from the fact that absolute values of the change in sample resistance are highly nontrivial to measure in this case. Accuracy in this situation is presumed to be rather low (on the order of 20%),[6] and for absolute measurements it is better to use other methods.

Note also that the signal generated by an ESR spectrometer is determined by changes in the $Q$ of a resonator. Such changes can differ even in sign for samples whose resistances are very different. Thus, in high-resistivity materials (whose impedance is much larger than the characteristic impedance of the waveguide), examples of which are insulators with paramagnetic ions, the $Q$ of the resonator decreases with decreasing resistance $R$ since the losses reduce to zero as $R\rightarrow\infty$. However, in a material with high conductivity $\sigma$ the $Q$ decreases with decreasing conductivity, because the losses reduce to zero as $\sigma\rightarrow\infty$. For this reason, changes in sample conductivity that are opposite in sign for high-resistivity and low-resistivity materials lead to changes in the resonator $Q$ with the same sign.

In our investigations we used a E-112 ESR spectrometer built by Varian with an ESR-9 flow helium cryostat built by Oxford Instruments. The spectrometer magnet was capable of varying the magnetic field $H$ in the range -50 Oe$<$H$<$ $+$15 kOe. Small coils were inserted into the gap of the electromagnet, which created a constant counterfield on the order of 100 Oe at the location of the sample. This counterfield did not act on the magnetic-field pickup. The sample temperature could be held constant to good accuracy (0.1 K) in the range of temperatures from 3 to 300 K by varying the helium flow through the cryostat. In order to detect the derivative of the microwave absorption we superimposed an ac field on the slowly varying magnetic field with a frequency of $10^5$ Hz and amplitude of 1 Oe.

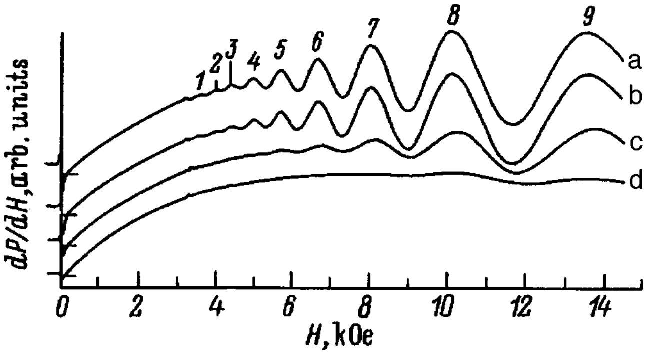

FIG. 1. Derivative of the microwave absorption $dP/dH$ as a function of magnetic field $H$ for a strongly doped crystal of $n$-InAs at $T$, K: a — 3.1, b — 3.8, c — 10, d — 20. The cutoffs on the ordinate correspond to zero values of $dP/dH$. The numbers above curve $a$ label maxima in the Shubnikov–de Haas oscillations. In the field $H\simeq$ 3.3 kOe the background ESR line is apparent for all the curves.

The experiments were carried out on ''metallic'' samples of $n$-type InAs with carrier concentrations of $5.5\times10^{16}$ cm$^{-3}$, mobilities of order 20 000 cm$^2$/(V·s), and resistivities of $6\times10^{-3}$ $\Omega\cdot$cm at 300 K. Our experimental procedure was the following. A sample of semiconductor with dimensions $0.8\times3.5\times9$ mm was placed in the cryostat, at the position of an antinode of the magnetic field in the resonator, and cooled down to the necessary temperature, after which the dependence of $dP/dH$ on $H$ was recorded. In this case the magnetic field increased from -50 Oe to the necessary positive value within 4 or 8 minutes.

## 3. EXPERIMENTAL RESULTS

Figure 1 shows the dependence of $dP/dH$ on magnetic field as the latter varies from -50 Oe to 15 kOe at various temperatures. Since we are dealing with a low-resistance material, the signal $dP/dH\sim dR/dH\sim d\rho/dH$. It is clear from the figure that a negative derivative of the magnetoresistance is observed only at sufficiently weak fields ($\leqslant$100 Oe), while in stronger fields the derivative of the magnetoresistance becomes positive. Note that this figure shows H-dependences of the derivative of the microwave absorption, and a change in sign of the derivative does not indicate a change in sign of the effect. The negative magnetoresistance reaches a maximum at a point where $dP/dH=0$, and then begins to decrease, becoming positive at fields much larger than the field where the derivative changes sign. However, the transition from a dependence characteristic of negative magnetoresistance to one characteristic of positive magnetoresistance takes place at lower fields, and is easily seen in the figure, appearing as a kink in the function $dP(H)/dH$ at a field of about 100 Oe. In fields $H>3500$ Oe, oscillations are clearly visible in the magnetoresistance (the Shubnikov–de Haas effect) at low temperatures. As the temperature rises, the two effects decrease in amplitude.

In Fig. 2 we show a more detailed picture of the function $dP(H)/dH$ in the negative magnetoresistance range for several temperatures in the range from 3.1 to 25 K. At low

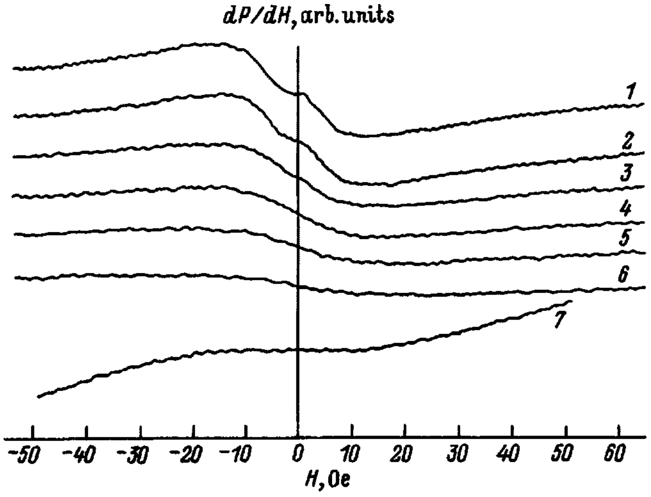

FIG. 2. Derivative of microwave absorption $dP/dH$ plotted versus magnetic field $H$ for the same sample of $n$- InAs as in Fig. 1, in the region of negative magnetoresistance at temperatures $T$, K: *1* — 3.1, *2* — 3.8, *3* — 5.7, *4* — 7.5, *5* — 10, *6* — 15, *7* — 25.

temperatures these functions contain four characteristic regions. At very weak fields $H \leqslant 1$ Oe the change in the derivative is small or entirely absent (at the lowest temperatures). The size of this region is comparable to the amplitude of the ac magnetic field that generates the signal for the derivative. Under these conditions the fine structure in this region (if any is present) cannot be determined. As the magnetic field increases to $H \simeq 1$ Oe, the absolute value of the derivative $|dP/dH|$ increases and goes over to a linear dependence on $H$:

$$\left|\frac{dP}{dH}\right| \sim H. \tag{2}$$

However, the range of fields in which this behavior is observed is not large (a few oersteds) and is followed by a segment on which $|dp/dH|$ reaches a maximum ($H$ of order 10 Oe). As the field increases further, $|dp/dH|$ begins to decrease, approaching zero sublinearly. The maximum value of $|dp/dH|$ decreases with increasing temperature, but the magnetic field at which this maximum is observed remains constant. Moreover, as the temperature increases, the feature near $H = 0$ (the first of the regions discussed above) gradually disappears.

## 4. OBSERVED NEGATIVE MAGNETORESISTANCE AND THEORY OF QUANTUM CORRECTIONS

Let us compare our results for the negative magnetoresistance with the theory set forth in Refs. 3 and 4. Note first of all that the magnetic field and temperature dependences of the magnetoresistance take different forms in the theory of quantum corrections, depending on the mechanisms that create them, i.e., weak localization or interference between electron-electron interactions in the diffusion and Cooper channels. Because the effect of electron-electron interactions on the magnetoresistance is, as a rule, much weaker than the effect of weak localization,[3] most of our conclusions will derive from the latter.

1. The characteristic magnetic field at which phase coherence of the particles that carry current is destroyed (which also leads to the appearance of the negative magnetoresistance) is determined by the ratio $H/H_\varphi$, where

$$H_\varphi = \frac{\hbar c}{4eD\tau_\varphi}, \tag{3}$$

where $\hbar$, $c$, and $e$ is the usual notation for well-known constants, $D$ is the particle diffusion, and $\tau_\varphi$ is the relaxation (breaking) time of the phase of the particle wave function.

2. The dependence of the negative magnetoresistance on magnetic field turns out to be different for different dimensions $d$ of the conducting structures. For $d=2$,

$$\sigma_2(H) - \sigma_2(0) = \frac{e^2}{2\pi^2\hbar} f_2\left(\frac{4DeH}{\hbar c}\tau_\varphi\right), \tag{4}$$

where

$$f_2(x) = x^2/24 \quad \text{for} \quad x \ll 1, \tag{5}$$

$$f_2(x) = \ln x \quad \text{for} \quad x \gg 1. \tag{6}$$

For $d = 3$,

$$\sigma_3(H) - \sigma_3(0) = \frac{e^2}{2\pi^2\hbar}\left(\frac{eH}{\hbar c}\right)^{1/2} f_3\left(\frac{4DeH}{\hbar c}\tau_\varphi\right), \tag{7}$$

where

$$f_3(x) = x^{3/2}/48 \quad \text{for} \quad x \ll 1, \tag{8}$$

$$f_3(x) = 0.605 \quad \text{for} \quad x \gg 1. \tag{9}$$

From Eqs. (4) and (5) it follows that for two-dimensional structures when $x \ll 1$ we have

$$\frac{d\sigma_2}{dH} \sim \frac{x}{12} \sim H, \tag{10}$$

i.e., in weak fields the derivative $d\sigma_2/dH$ should increase linearly with increasing magnetic field.

For two-dimensional systems when $x \gg 1$, i.e., in strong fields, from Eqs. (4) and (6) we obtain

$$\frac{d\sigma_2}{dH} \sim \frac{1}{x} \sim \frac{1}{H}, \tag{11}$$

i.e., as the field increases, the derivative should reduce to zero like $1/H$.

Analogous relations for three-dimensional structures have the following form. For $x \ll 1$ from Eqs. (7) and (8) we have

$$\frac{d\sigma_3}{dH} \sim x \sim H, \tag{12}$$

and for $x \gg 1$ from Eqs. (7) and (9) we have

$$\frac{d\sigma_3}{dH} \sim x^{-1/2} \sim H^{-1/2}. \tag{13}$$

Thus, it follows from Eqs. (10)–(13) that whereas in weak fields the derivatives of the negative magnetoresistance depend identically on magnetic field in two-dimensional and three-dimensional samples, in strong fields their asymptotic behaviors differ: In two-dimensional structures the derivative reduces to zero with increasing magnetic field much more rapidly than in three-dimensional structures.

3. The temperature dependence of the negative magnetoresistance also has a different form for two-dimensional and three-dimensional systems.[3,4] This is associated with the different dependences of $\delta\sigma(H)$ on $\tau_\varphi$ [see Eqs. (4) and (7)]. For any type of scattering $\tau_\varphi \sim T^{-n}$. For a two-dimensional system, when $x \gg 1$ and $H=\text{const}$, we thus obtain from Eq. (6) the expression

$$\delta\sigma_2(T) \sim -\ln T, \tag{14}$$

For three-dimensional systems, we have $f_3(x)=\text{const}$ when $x \gg 1$. However, this relation is correct only when $x \geqslant 100$. For smaller values of $x$, as shown in Ref. 4, we have

$$\delta\sigma_3(H,T) \sim H^{m+1/2}/T^{m+n}, \tag{15}$$

i.e., for $H=\text{const}$ we should observe a power-law dependence of $\delta\sigma_3(T)$. For $d\sigma/dH$ the dependences should be analogous.

Let us now turn to the relation between theory and our experimental data.

In the weak-field range $1 \leqslant H \leqslant 10$ Oe, in agreement with the theoretical relations (10) and (12), there actually is a segment of the experimental function shown in Fig. 2 on which $|dP/dH| \sim H$. However, in very weak fields $H \leqslant 1$ Oe this linearity is disrupted, and at the very lowest temperatures the resistance in this regime ceases to depend in any way on field. This effect is not associated with features of the apparatus for the following reasons. First of all, it disappears as the temperature rises. Secondly, in other materials which exhibit changes in the absorption at microwave frequencies at such weak fields (e.g., in type-I superconductors) the change in the derivative is recorded immediately starting from zero field. Thus, our experiments imply that there is a certain threshold field $H_0 \approx 1$ Oe for satisfying relations (10) or (12), which is not predicted by theory.

In order to compare the experiments with theory in the strong-field range $H \gg H_\varphi$, we replotted the function $dP(H)/dH$ on a log-log scale. Figure 3 shows a portion of the field in which the derivative decreases in absolute value, but remains negative. For comparison, we show straight lines *1* and *2* on this plot, which represent the theoretical dependences (13) and (11) predicted for $d=3$ and $d=2$, respectively. It is clear that, strictly speaking, the experimental curve cannot be approximated by the power-law dependences of either of the segments, which embody the predictions of quantum correction theory. A comparison with theory should be made in the field range $H \gg H_\varphi \approx 10$ Oe, i.e., at roughly 30 Oe. On the other hand, it is clear from Fig. 1 that the character of the magnetoresistance changes qualitatively at fields on the order of 100 Oe from a sharp dependence characteristic of negative magnetoresistance to a weaker dependence that is typical of positive magnetoresistance, although the sign in this case still corresponds to negative magnetoresistance. Thus, analysis based on the theory of negative magnetoresistance when $H \gg H_\varphi$ must be carried out in fields $100 \geqslant H \geqslant 30$ Oe. It is clear that in this range of fields approximation of the experimental dependence by Eq. (11) is more justifiable. In other words, the two-dimensional model is slightly preferable.

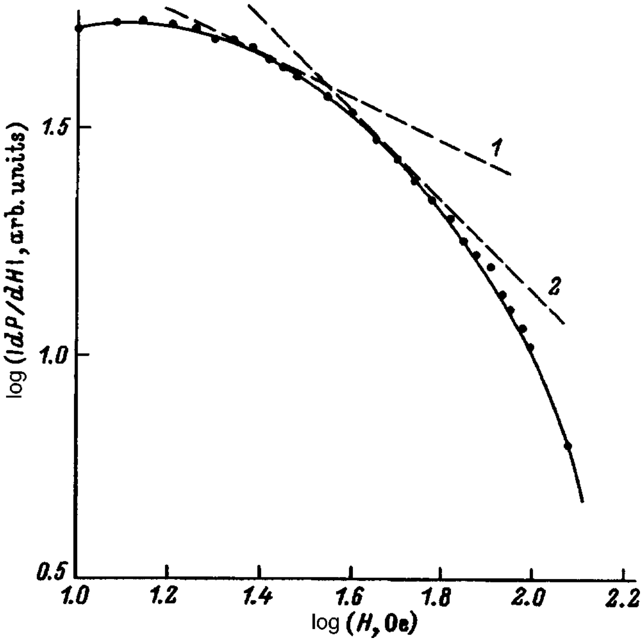

FIG. 3. Dependence of the derivative of the microwave absorption $|dP/dH|$ on magnetic field $H$ in the range 10 Oe$\leqslant H \leqslant$140 Oe at 3.1 K plotted on a log-log scale. The dashed straight lines are: *1* — $|dP/dH| \sim H^{-1/2}$, *2* — $|dP/dH| \sim H^{-1}$.

From a comparison of the experimental functions for $x \ll 1$ and $x \gg 1$ we find that $x \approx 1$ for $H \approx 10$ Oe. We thus obtain

$$H_\varphi = \frac{\hbar c}{4eD\tau_\varphi} \approx 10\ \text{Oe}, \tag{16}$$

which allows us to determine the diffusion length after the phase breaking time $\tau_\varphi$ in the sample under study

$$L_\varphi = \sqrt{D\tau_\varphi} \approx \left(\frac{\hbar c}{4H_\varphi e}\right)^{1/2} \approx 4\times 10^{-5}\text{cm}. \tag{17}$$

Let us now turn to an analysis of the temperature corrections. In Fig. 4 we plot the temperature dependence of the points $|dP/dH|_{\max}$ shown in Fig. 2 on a semilogarithmic scale (curve *1*). It is clear from the figure that this dependence is well described over most of its range by the relation

$$\frac{dP}{dH} \sim -\ln T, \tag{18}$$

which coincides with the theoretical function (14) for two-dimensional systems. However, Eq. (14) corresponds to the parameter $x \gg 1$, while Eq. (18) was obtained for $x \simeq 1$.

It should be noted that the temperature dependence of the conductivity, when $H=0$, also has the form[7]

$$\sigma(T) = \sigma_0 - A\ln T, \tag{19}$$

where $\sigma_0$ is the classical conductivity, and $A$ is a coefficient of proportionality. In this case it is clear that as the temperature increases the correction to the conductivity decreases,

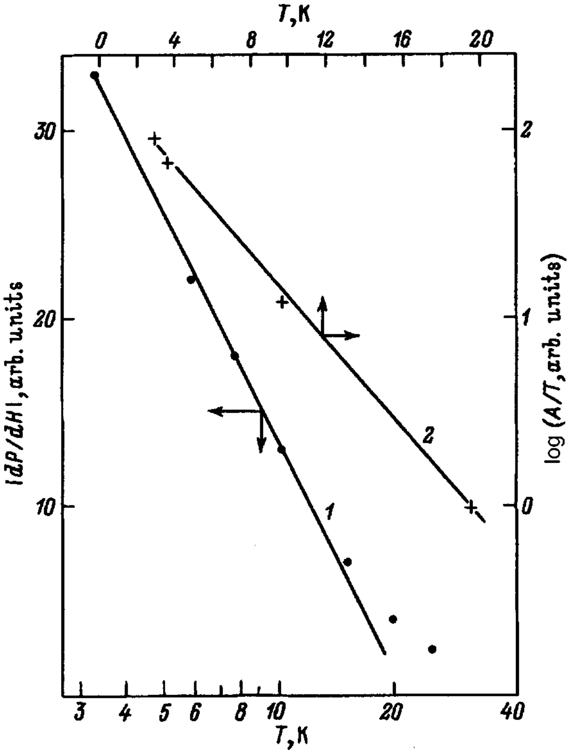

FIG. 4. Temperature dependences of the maximum value of $|dP/dH|$ in the range of negative resistance (curve *1*) and the ninth maximum of the oscillatory part of $|dP/dH|$ (*2*).

which also agrees with data from other experiments[4] on strongly doped semiconductors that are far from the metal-insulator transition.

Thus, it turns out that our bulk InAs sample behaves as if its dimensionality was close to two ($d=2$) with respect to its temperature-dependent, and to some extent magnetic-field-dependent, behavior, as expressed by the dependence of its negative magnetoresistance on magnetic field and temperature at microwave frequencies.

## 5. DISCUSSION OF "TWO-DIMENSIONALITY"

In the theory of quantum corrections (see, e.g., Ref. 3), two-dimensionality is determined by the ratio of the sample thickness $L$ to the phase-breaking length $L_\varphi$. In other words, the sample is assumed to be quasi-two-dimensional when

$$L \ll L_\varphi . \tag{20}$$

However, in our case, since we are making microwave measurements, the current carriers interact with the field only near the surface within the skin-depth layer. Therefore, it is only the loss of phase in this layer that is important for interaction with a microwave field, and we should replace Eq. (20) by the following criterion for the appearance of two-dimensionality:

$$L_\varphi \gg \delta, \tag{21}$$

where $\delta$ is the skin-depth layer. The quantity $\delta$ is determined either by the expression for the normal skin effect

$$\delta = \left( \frac{2}{\omega \mu_0 \sigma} \right)^{1/2}, \tag{22}$$

where $\omega$ is the frequency of the microwave field, $\mu_0$ is the magnetic permittivity in vacuum, and $\sigma$ is the conductivity of the sample, or by the expression for the anomalous skin effect

$$\delta = \left( \frac{4l}{3\omega \mu_0 \beta \sigma} \right)^{1/3}, \tag{23}$$

where $l$ is the mean-free path of a charge carrier, and $\beta$ is a numerical coefficient of order 10, which varies somewhat according to the nature of the reflection from the surface (specular or diffusive).

In order to estimate the width of the skin-depth layer we made samples of InAs with contacts and measured the conductivity at a temperature of 3 K. It turned out to be the same as at room temperature, which reflects the metallic nature of the conductivity. The value of $\delta \approx 4 \times 10^{-3}$ cm we obtain from Eq. (22) is two orders of magnitude larger than the phase-breaking length defined in Eq. (17). Thus, condition (21) is not satisfied in our case. Note that using Eq. (23) increases the value of $\delta$, so that inequality (21) was violated even more strongly.

Thus, the "two-dimensionality" of the negative magnetoresistance for the samples under study is observed in the microwave frequency range under anomalous conditions, when the skin depth is much larger than the phase-breaking length ($\delta \gg L_\varphi$). This discrepancy between experiment and theory has not yet found a satisfactory explanation and requires additional study.

## 6. SHUBNIKOV–de HAAS OSCILLATIONS IN THE MICROWAVE ABSORPTION

Shubnikov–de Haas oscillations are well-studied quantum magnetic effects observed in semiconductors with a degenerate electron gas at low temperatures (see, for example, Ref. 8). Their analysis allows us to determine the position of the Fermi level in the semiconductor under study and in a number of cases the relaxation time, according to which we can estimate the applicability of Eqs. (22) or (23), in particular, for calculating the skin depth. The origin of the oscillations shown in Fig. 1 is the well known fact that Landau levels successively intersect the Fermi level as the magnetic field increases. In this case the maximum change in the density of states occurs at the instant the Fermi level intersects the next Landau level. In Fig. 1 this corresponds to a maximum of $dP/dH$, since the maximum change in the density of states corresponds to a maximum change in the resistivity. When several magnetoresistive effects appear simultaneously in the function $dP(H)/dH$, maxima in the oscillations are determined much more precisely than the position of zero values of the oscillations, as in ordinary measurements of the dc resistance. Moreover, the accuracy of these measurements is increased due to the fact that recording the derivative eliminates the constant component of the sample resistance.

Below the Fermi level we always find an integer number of Landau levels, and when the Fermi level intersects the next Landau level, their number above the Fermi level decreases by one. Since the energy of the Landau level is

$$E_L=\frac{\hbar eH}{m^*c}, \tag{24}$$

multiplication of the value of the magnetic field $H_i$ for a given maximum of the derivative by a suitable integer $n_i$ gives the value of the magnetic field corresponding to the Fermi level; as the magnetic field increases, the value of the magnetic field for each successive maximum of $dP/dH$ must be multiplied by an integer that is one less than the number used to multiply the magnetic field at the previous maximum. Analysis of the oscillations in Fig. 1 shows that for magnetic fields at which the derivative $dP/dH$ is a maximum the following relations hold:

$$11H_1=10H_2=9H_3=8H_4=7H_5=6H_6=5H_7$$
$$=4H_8=3H_9=H_F=40.2\pm0.6\ \text{kOe},$$

i.e., oscillations are observed as the Fermi level successively crosses Landau levels three through eleven.

It is thus not difficult to find the position of the Fermi level, which determines the degree of degeneracy of the sample:

$$E_F=\hbar\frac{eH_F}{m^*c}=21.1\times10^{-3}\text{eV} \tag{25}$$

at the characteristic experimental temperatures 3–30 K; i.e., the degeneracy must be assumed strong. The value of $E_F$ which we found allows us to determine the electron concentration in the sample by the standard formula for semiconductors with a degenerate electron gas[8,9]

$$n=\frac{1}{3\pi^2}\left(\frac{2m^*E_F}{\hbar^2}\right)^{3/2}\approx5.7\times10^{16}\text{cm}^{-3},$$

which must be considered good agreement with the ‘‘passport’’ data presented above. The velocity of an electron at the Fermi surface is

$$v_F=\sqrt{\frac{2E_F}{m^*}}=4.7\times10^7 cm/s.$$

In order to estimate the mean-free path we use the relation

$$l=v_F\tau, \tag{26}$$

where $\tau$ is the momentum relaxation time. For a rough estimate of this time we use the temperature dependence of the amplitude of Shubnikov–de Haas oscillations, which has the form[7]

$$b=b_0T\exp[2\pi^2k(T_D+T)/\hbar\omega_c] \tag{27}$$

and which contains the so-called Dingle temperature

$$T_D=\frac{1}{\pi}\frac{\hbar}{\tau_c}, \tag{28}$$

where $\omega_c$ is the cyclotron frequency, and $\tau_c$ is the carrier relaxation time, which is the same order as $\tau$ in (26) and can serve as a guide in making rough estimates of the mean-free path. The value of $\tau_c$ determines the ‘‘natural’’ linewidth for cyclotron resonance, which corresponds to transitions between neighboring Landau levels.

The temperature $T_D$, in turn, can be obtained once we plot the curve[8] $\ln(A/T)=f(T)$, where in our case the coefficient $A=(dP/dH)_{osc}$ is the magnitude of the oscillatory part of $dP/dH$ for constant values of the magnetic field. This dependence is shown in Fig. 4 (curve *2*). On the figure the deviation from linear behavior is insignificant down to low temperatures. Therefore, we can conclude that $T_D\ll3$ K, and from Eq. (28) we obtain the estimate $\tau_c>10^{-12}$ s. Thus, from this experiment we can estimate only a lower limit on the relaxation time, and consequently $l>5\times10^{-5}$ cm. Thus, Eq. (22) appears to be more suitable for calculating $\delta$ in our case.

## 7. CONCLUSIONS

1. The use of ESR spectroscopy to investigate the magnetic field-dependent microwave absorption $P(H)\sim\rho(H)$ allows us to establish the existence of three characteristic regions of negative magnetoresistance in metallic InAs:

a) $H\leqslant H_0\simeq1$ Oe: the quantity $P(H)$ is actually independent of $H$. Such behavior is anomalous and not predicted by existing theory of quantum corrections:

b) 1 Oe$\leqslant H\leqslant10$ Oe, $H\ll H_\varphi$: here $|P|\propto H^2$, and this region of quadratic field dependence is described by the theory of quantum corrections for $d=2$, 3;

c) $H\geqslant10$ Oe, $H\gg H_\varphi$: strictly speaking, the function $P(H)$ does not have any power-law character, which is predicted by the quantum correction theory; however, the approximation of the theoretical dependence for $d=2$ is found to be preferred.

2. The temperature dependence of $P(H)$ in a field of order 10 Oe corresponds to the dependence that follows from the theory of quantum corrections when $d=2$.

3. ‘‘Two-dimensional’’ characteristics of the negative magnetoresistance in the microwave frequency range were observed in the sample under study under conditions where the skin depth was two orders of magnitude larger than the phase-breaking length ($l\gg L_\varphi$), where we should expect behavior characteristic for $d=3$. This disagreement between experiment and theory has not yet been satisfactorily explained and requires further study.

4. Use of ESR spectroscopy to study Shubnikov–de Haas oscillations allows us to increase the sensitivity of the measurements and broaden the temperature range where the effect is observed. At a temperature of 3 K, nine oscillations were observed, starting with eleven Landau levels below the Fermi level. We were able to observe oscillations up to a temperature of 30 K. From the temperature dependence of the amplitude of the oscillations it follows that the relaxation time in our sample was $\tau_c>10^{12}$ s, while the Dingle temperature was $T_D\ll3$ K.

Thus, the use of ESR to investigate magnetic-field dependent microwave absorption in low-resistance materials turns out to be a very effective way to study their quantum transport properties, i.e., Shubnikov-de Haas effect and quantum corrections to the conductivity on the metallic side of the metal-insulator transition.

We wish to thank T. A. Poyanskaya for useful discussion of the results of this work and for the participation of the Scientific Seminar of the Laboratory of Nonequilibrium Processes in Semiconductors, A. I. Ioffe Physicotechnical Institute of the Russian Academy of Science, for useful discussions.

The work was supported by the Russian Fund for Fundamental Research, Project 96-02-17936A and international grant 94-4435 from INTAS.

[1] A.I. Veinger, A.G. Zabrodskii, and T.V. Tisnek, Semicond. Sci. Technol. **8**, 368 (1995).

[2] N. V. Zotova, T. S. Logunova, and D. N. Nasledov, Fiz. Tverd. Tela (Leningrad) **5**, 3329 (1963) [Sov. Phys. Solid State **5**, 2439 (1963)].

[3] B. L. Altshuler and A. G. Aronov, in *Modern Problems in Condensed Matter Sciences*, V. M. Agranovich and A. A. Maradudin [Eds.], Vol. 10: *Electron–Electron Interaction in Disordered Systems* (North–Holland, Amsterdam e.a. 1985).

[4] T. A. Polyanskaya and Yu. V. Shmartsev, Fiz. Tekh. Poluprovodn. **23**, 3 (1989) [Sov. Phys. Semicond. **23**, 1 (1989)]; T. A. Polyanskaya, I. I. Saĭdashev, and Yu. V. Shmartsev, Fiz. Tekh. Poluprovodn. **17**, 1081 (1983) [Sov. Phys. Semicond. **17**, 679 (1983)].

[5] A. A. Romanova, Yu. M. Shvachko, and V. V. Ustinov, Usp. Fiz. Nauk **161**, 37 (1991) [Sov. Phys. Usp. **34**, 862 (1991)].

[6] C. P. Poole, *Experimental Techniques in Electron Spin Resonance* (Wiley, New York, 1966) (Russ. transl. Mir, Moscow, 1970), p. 558 [in Russian].

[7] B. L. Al'tshuler, Zh. Éksp. Teor. Fiz. **75**, 1330 (1978) [Sov. Phys. JETP **48**, 670 (1978)].

[8] K. Seeger, *Semiconductor Physics* (Springer-Verlag, Wien–N.Y. 1973) [Russ. transl. Mir, Moscow, 1977].

[9] G. E. H. Reuter and E. H. Sondheimer, Proc. Roy Soc. A **195**, 336 (1948).

Translated by Frank J. Crowne

SEMICONDUCTORS VOLUME 32, NUMBER 5 MAY 1998

# Hopping-induced energy relaxation with allowance for all possible versions of intercenter transitions

A. A. Kiselev

*A. F. Ioffe Physicotechnical Institute, Russian Academy of Sciences, 194021 St. Petersburg, Russia*

(Submitted September 15, 1997; accepted for publication November 26, 1997)
Fiz. Tekh. Poluprovodn. **32**, 564–569 (May 1998)

Hopping relaxation of localized excitons is discussed within a model that avoids the approximation of treating hopping to nearest-neighbor centers only, thereby lifting the model-imposed restriction on the largest concentration of localized states that can be treated. The general results are illustrated by an example in which the line shape of low-temperature exciton luminescence in the tail of localized states is calculated. © *1998 American Institute of Physics.* [S1063-7826(98)01105-3]

## 1. INTRODUCTION

A problem that arises in very different areas of the physics of disordered systems is the need for a microscopic description of the kinetics of localized particles. For example, fluctuations in the content of layers and (or) imperfect interfaces are the cause of structural disorder in semiconductor heterostructures, which to a considerable degree determines the properties of devices such as lasers, photodetectors, high-speed transistors, etc.[1] Since radiative recombination of localized excitons determines the low-temperature luminescence of undoped structures with quantum wells, the presence of disorder in these systems is directly reflected in the inhomogeneous broadening of the exciton luminescence line and its Stokes shift relative to the exciton absorption peak.[2,3] This makes spectroscopic measurements one of the most convenient methods for diagnosing the quality of nanostructures.

A number of papers in which the authors reduce the problem of describing the luminescence spectra to calculating a certain ''effective'' density of states for the localized excitons has been published.[4–8] In this case it is explicitly predicted that in the course of its energy relaxation an exciton rapidly (compared to the times for radiative or nonradiative recombination) reaches a state from which it cannot depart. These states contribute to the effective density of states. The difference between the absorption and luminescence spectra is thus connected with the difference between ordinary and effective densities of excitonic states.

In spectroscopic measurements with time resolution in the picosecond range, it turns out to be possible to track the dynamics of exciton energy relaxation via localized states.[9–11] A first-principles theoretical approach that is adequate for these experiments requires an accurate description of the exciton (or carrier) kinetics at the microscopic level, i.e., inclusion of the competition between processes of exciton recombination and transitions between states.[12–15] The schemes developed for these calculations are only adequate at low concentrations of localized centers, and take into account the possibility of hopping only between nearest-neighbor centers. In this approximation the collection of all possible chains of successive hops an exciton makes between localized centers distributed in space as it undergoes energy relaxation at low temperatures can be represented in the form of a tree which gradually grows more branches as the localization energy of the excitonic states decreases. In fact, within the approximation of nearest-neighbor center hopping there is exactly one chain of successive relaxation hops for each localized center. However, at higher concentrations of localized states it turns out to be necessary to include transitions to all centers in the immediate vicinity of the particle (see, e.g., Ref. 16, whose topic is donor-acceptor recombination in semiconductors).

In this paper we develop a first-principles microscopic theory of exciton relaxation in systems with disorder, which is equally applicable at low and at high concentrations of localized centers. The results are obtained within a model that approximately takes into account the possibility of localized particles making transitions to all centers in the local environment, and not simply to the nearest available center. A general finite-temperature balance equation, which does not depend on specific mechanisms for intercenter transitions or on the distribution functions of localized states with respect to energy, is derived. The method of calculation is illustrated for the example of high-temperature relaxation of excitons within an exponential (Urbach) tail of localized states. The distribution functions for excitons with respect to energy calculated under conditions of stationary excitation is compared with analogous results obtained within the approximation of nearest-neighbor hopping.

## 2. DISTRIBUTION FUNCTION OF LOCALIZED PARTICLES AND KINETIC EQUATIONS

Let the distribution of centers with respect to energy be given by a function $q(\varepsilon)$, where $\varepsilon$ is the localization energy of a state at a center. We assume the spatial distribution of localized centers is random and uncorrelated. Each center with a given energy $\varepsilon$ is characterized by a local configuration of neighbors: the set ${}^{\infty}\{\varepsilon_i, r_i\}$ of energies of the states of neighboring centers and distances to them (the space is assumed to be isotropic). Let us introduce a fictitious ''radius of sensitivity'' $R$ into our theory such that if $r_j>R$ hopping of a localized particle between these centers must necessarily be excluded from the discussion. Let the rate of transitions of a particle from a center with energy $\varepsilon$ to a center with energy $\varepsilon'$ be given by the function $\omega(\varepsilon,\varepsilon',r')$, which depends on the energies of these centers and the distance $r'$ between them. If this function falls off sufficiently rapidly with distance, then introduction of the radius of sensitivity $R$ is justified. When the mechanism of transitions between centers is by tunneling, $\omega$ turns out to be an exponential function of the distance $r'$, while for dipole-dipole interactions between excitonic states we have $\omega\sim r'^{-6}$ (see Ref. 13). Thus, we can exclude distant centers $(r_j>R)$ from the total set ${}^{\infty}\{\varepsilon_i,r_i\}$, which allows us to operate with finite sequences $\{\varepsilon_i,r_i\}$. Let us denote the average occupation of a state with energy $\varepsilon$ and $n$ neighbors ${}^{n}\{\varepsilon_i,r_i\}$ (within the radius of sensitivity $R$) by $f^n_\varepsilon\{\varepsilon_i,r_i\}$.

The probability density for finding a state with the set of neighbors ${}^{n}\{\varepsilon_i,r_i\}$ among the states with energy $\varepsilon$ is determined according to the Poisson formula by the expression

$$P^n_\varepsilon\{\varepsilon_i,r_i\}=\frac{\mathrm{e}^{-\rho V(R)}}{n!}\prod_{i=1}^{n} g(\varepsilon_i)S(r_i), \tag{1}$$

if the distribution of centers, as we assume, is random. Here $\rho=\int g(\varepsilon)d\varepsilon$ is the total concentration of localized centers, $V(r)$ and $S(r)$are the volume and area of the surface of a sphere of radius $r$ in the space with the system dimensionality, and $n!$ appears in the expression because of disordering of the set of neighboring centers ${}^{n}\{\varepsilon_i,r_i\}$. Note that the probability density for finding in $\varepsilon$ a state with $m+1$ neighbors, where the first state is $(\varepsilon',r')$ is (necessarily) simply $P^m_\varepsilon\{\varepsilon_i,r_i\}$.

For continuous generation of particles $\Gamma^{(0)}(\varepsilon)$, at the end of all transient processes a stationary regime is established with a state occupation function that depends on the local configuration of centers. Under conditions of stationary excitation, the occupation number $f^n_\varepsilon\{\varepsilon_i,r_i\}$ is found by balancing the arrival of particles in these states and their departure from them.

The arrival is determined by the generation of particles $\Gamma^{(0)}(\varepsilon)$ at the center and their hopping from neighboring centers (the hopping arrival channel). The arrival of localized particles via a single hopping channel can be represented in the form $\omega(\varepsilon',\varepsilon,r)f^{m+1}_{\varepsilon'}\{\varepsilon,r;\varepsilon_i,r_i\}$, where there are $n$ such channels in all. Among the neighbors of the center with energy $\varepsilon'$, there necessarily must be an initial center with energy $\varepsilon$ ; this pair is separated out explicitly in the notation for the population $f^{m+1}_{\varepsilon'}\{\varepsilon,r;\varepsilon_i,r_i\}$. Here and in what follows we assume that the average occupation of the states is small, i.e., the state to which the hopping takes place can be treated as empty.

Strictly speaking, the occupations of two neighboring centers are coupled to one another not only directly and inversely by hopping of a localized particle between these centers, but also by hopping chains that pass through centers located nearby. Eliminating from consideration the coupling between the populations of two neighboring centers via double, triple, etc. hopping events is equivalent to elimination from consideration the correlations between configurations of the local environment $\{\varepsilon_i,r_i\}$ of these centers. This simplified model allows us to derive a closed kinetic equation for the average occupation $F(\varepsilon,\varepsilon',r')$ of a state with energy $\varepsilon$, which necessarily has a neighbor with energy $\varepsilon'$ at a distance $r'$. In fact, our refusal to include correlations makes it possible to carry out an independent averaging over the configuration of the local environment of a neighboring center in the expression for arrival along a single hopping channel. The validity of the averaging procedure is formally related to replacing $f^{m+1}_{\varepsilon'}\{\varepsilon,r;\varepsilon_i,r_i\}$ by $F(\varepsilon',\varepsilon,r)$. In accordance with the usual averaging rules

$$F(\varepsilon,\varepsilon',r')=\sum_{m=0}^{\infty}\int f^{m+1}_{\varepsilon}\{\varepsilon',r';\varepsilon_i,r_i\}P^m\{\varepsilon_i,r_i\}\times\prod_{i=1}^{m} d\varepsilon_i dr_i, \tag{2}$$

where the integration is carried out over all energies of distances to neighboring center $r_i<R$.

Total escape is defined by the reverse hops ${}^{n}\{\omega(\varepsilon,\varepsilon_i,r_i)f^n_\varepsilon\{\varepsilon_i,r_i\}\}$ and escape of a particle from the system $\omega_0(\varepsilon)$ [for example, by radiative and (or) nonradiative recombination for the excitons]. In those places where this will not cause ambiguity, we will omit the set $\{\varepsilon_i,r_i\}$ from the formulas in what follows.

The total escape rate from a state with energy $\varepsilon$ and set of neighbors ${}^{n}\{\varepsilon_i,r_i\}$ is written formally as a function $\Omega[\alpha]$ of the escape rate of particles from the system $\alpha\equiv\omega_0(\varepsilon)$:

$$\Omega[\alpha]=\alpha+\sum_{i=1}^{n}\omega(\varepsilon,\varepsilon_i,r_i). \tag{3}$$

The balance equation for arrival and departure, taking into account internal notation, reduces to

$$\Omega[\omega_0(\varepsilon)]f^n_\varepsilon=\Gamma^{(0)}(\varepsilon)+\sum_{i=1}^{n}\omega(\varepsilon_i,\varepsilon,r_i)F(\varepsilon_i,\varepsilon,r_i). \tag{4}$$

Let us divide the right and left sides of Eq. (4) by $\Omega[\omega_0(\varepsilon)]$ and substitute the expression for the population of the state $f^n_\varepsilon$ into the definition (2). As a result, we obtain a closed equation for the kinetics of an average occupation of a state with a fixed neighboring center:

$$\begin{aligned}F(\varepsilon,\varepsilon'',r'')={}&T_\varepsilon[\omega_0(\varepsilon)+\omega(\varepsilon,\varepsilon'',r'')]\\&\times\{\Gamma^{(0)}(\varepsilon)+\omega(\varepsilon'',\varepsilon,r'')F(\varepsilon'',\varepsilon,r'')\}\\&+\int d\varepsilon'dr'g(\varepsilon')S(r')\omega(\varepsilon',\varepsilon,r')\\&\times F(\varepsilon',\varepsilon,r')T_\varepsilon[\omega_0(\varepsilon)+\omega(\varepsilon,\varepsilon'',r'')\\&+\omega(\varepsilon,\varepsilon',r')],\end{aligned} \tag{5}$$

where the average lifetime of a state with energy $\varepsilon$ is introduced as a function $T_\varepsilon[\alpha]$ of the parameter $\alpha$ analogous to the definition (3):

$$T_\varepsilon[\alpha]=\sum_{m=0}^{\infty}\int\frac{P^m}{\Omega[\alpha]}\prod_{i=1}^{m} d\varepsilon_i dr_i. \tag{6}$$

Note that if the average lifetime of a state with energy $\varepsilon$ is $T_\varepsilon[\omega_0(\varepsilon)]$, the average lifetime of the same state when it necessarily has $(\varepsilon',r')$ as a neighbor will be different; specifically, $T_\varepsilon[\omega_0(\varepsilon)+\omega(\varepsilon,\varepsilon',r')]$.

Let us multiply the right and left sides of Eq. (6) by $\alpha$, take one of the integrations over the pair of other variables $(\varepsilon',r')$ outside the range of the sum, and relabel what is left by $T_\varepsilon[\alpha+\omega(\varepsilon,\varepsilon',r')]$. As a result, we obtain an integral equation for $T_\varepsilon[\alpha]$:

$$\alpha T_\varepsilon[\alpha]=1-\int d\varepsilon' dr' g(\varepsilon')S(r')\omega(\varepsilon,\varepsilon',r') \times T_\varepsilon[\alpha+\omega(\varepsilon,\varepsilon',r')]. \tag{7}$$

We note that the limit $R\to\infty$ can be taken in the integral equations (2) and (7). As a result, the dependence on the fictitious radius of sensitivity now disappears.

The integral equation (7) is considerably simpler to analyze than the infinite sum of multidimensional integrals in the definition (6). It turns out that the solution $T_\varepsilon[\alpha]$ can be written in the form of quadratures using the inverse Laplace transform. We thus find that

$$T_\varepsilon[\alpha]=\int_0^\infty dt \exp\left\{-\alpha t - \int d\varepsilon' dr' g(\varepsilon')S(r')(1-\mathrm{e}^{-\omega(\varepsilon,\varepsilon',r')t})\right\}.$$

Ordinarily, experimental methods are not sensitive to the local configuration of centers, and we are allowed to specify only the particle distribution in the system with respect to energy:

$$N(\varepsilon)=g(\varepsilon)\sum_{n=0}^{\mathrm{inf}ty}\int f_\varepsilon^n P^n \prod_{i=1}^{n} d\varepsilon_i dr_i\,.$$

For example, if we ignore nonradiative channels for recombination of excitons in heterostructures, then the observed shape of the stationary exciton luminescence line is $L(\varepsilon)\propto\omega_0(\varepsilon)N(\varepsilon)$.

Note that

$$\omega_0(\varepsilon)N(\varepsilon)=g(\varepsilon)\left(\Gamma^{(0)}(\varepsilon)+\int d\varepsilon' dr' g(\varepsilon')S(r') \times\{\omega(\varepsilon',\varepsilon,r')F(\varepsilon',\varepsilon,r') - \omega(\varepsilon,\varepsilon',r')F(\varepsilon,\varepsilon' r')\}\right) \tag{8}$$

and the law of conservation of the total number of particles in this system is obvious:

$$\int d\varepsilon\,\omega_0(\varepsilon)N(\varepsilon)=\int d\varepsilon\, g(\varepsilon)\Gamma^{(0)}(\varepsilon).$$

Thus, the results of analytic computations is the integral equation (5), whose solution can be written in explicit form in a number of special cases; otherwise, it must be solved numerically. In this formulation of the model we do not require methods of numerical simulation such as the Monte Carlo to analyze the processes of hopping relaxation .

## 3. RELAXATION AT LOW TEMPERATURES

At low temperatures, only hopping of particles to centers with large localization energy is possible. Thus, $\omega(\varepsilon,\varepsilon',r')\equiv 0$ for $\varepsilon>\varepsilon'$. This leads to a considerable simplification of the kinetic equation (5), which reduces to a pair of equations

$$F(\varepsilon,\varepsilon'',r'')=T_\varepsilon[\omega_0(\varepsilon)+\omega(\varepsilon,\varepsilon'',r'')] \times\left[\Gamma^{(0)}(\varepsilon)+\int^{\varepsilon} d\varepsilon' g(\varepsilon') \times\int dr' S(r')\omega(\varepsilon',\varepsilon,r')F(\varepsilon',\varepsilon,r')\right] \tag{9}$$

and

$$F(\varepsilon,\varepsilon'',r'')=T_\varepsilon[\omega_0(\varepsilon)]\left[\Gamma^{(0)}(\varepsilon)+\omega(\varepsilon'',\varepsilon,r'') \times F(\varepsilon'',\varepsilon,r'')+\int^{\varepsilon} d\varepsilon' g(\varepsilon') \times\int dr' S(r')\omega(\varepsilon',\varepsilon,r')F(\varepsilon',\varepsilon,r')\right] \tag{10}$$

for states with $\varepsilon<\varepsilon''$ and $\varepsilon>\varepsilon''$, respectively. The lower limit of integration with respect to energy is determined by the exciton mobility edge. Denoting the average arrival of a particle at level $\varepsilon$ by

$$\Gamma(\varepsilon)=\frac{F(\varepsilon,\varepsilon'',r'')}{T_\varepsilon[\omega_0(\varepsilon)+\omega(\varepsilon,\varepsilon'',r'')]},$$

we find from Eq. (9) that

$$\Gamma(\varepsilon)=\Gamma^{(0)}(\varepsilon)+\int^{\varepsilon} d\varepsilon' g(\varepsilon')\int dr' S(r')\omega(\varepsilon',\varepsilon,r') \times T_{\varepsilon'}[\omega_0(\varepsilon')+\omega(\varepsilon',\varepsilon,r')]\Gamma(\varepsilon') \tag{11}$$

with a distribution of particles with respect to energy

$$N(\varepsilon)=g(\varepsilon)\Gamma(\varepsilon)T_\varepsilon[\omega_0(\varepsilon)]. \tag{12}$$

This relation has a very simple explanation since $T_\varepsilon[\omega_0(\varepsilon)]$ is the average lifetime of a state with energy $\varepsilon$.

In the approximation $\omega(\varepsilon,\varepsilon',r')=\theta(\varepsilon'-\varepsilon)\omega(r')$, where $\theta(x)$ denotes the Heaviside unit step function, the analytic solution to Eq. (9) can be written down in terms of quadratures. Thus,

$$\Gamma(\varepsilon)=\Gamma^{(0)}\exp\left(\int^{\varepsilon} d\varepsilon' \frac{g(\varepsilon')}{\rho(\varepsilon')}\{1-\omega_0 T_{\varepsilon'}[\omega_0]\}\right), \tag{13}$$

where

$$T_{\varepsilon[\alpha]}=\int_0^\infty dt \exp\left(-\alpha t-\rho(\varepsilon)\times\int dr' S(r')\{1-\mathrm{e}^{-\omega(r')t}\}\right). \tag{14}$$

For compactness of the expressions we used the simplest dependence of the generation rate $\Gamma^{(0)}$ and escape rate $\omega_0$ on the state energy: $\Gamma^{(0)}(\varepsilon)=\mathrm{const}$, $\omega_0(\varepsilon)=\mathrm{const}$ and the concentration of states with energy $\varepsilon'>\varepsilon$ is

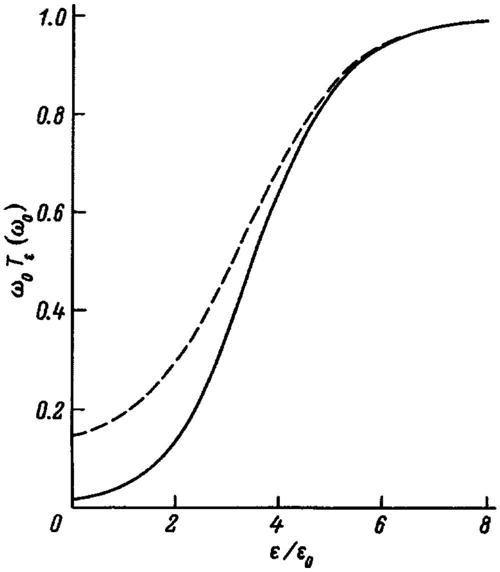

FIG. 1. Dependence of the average lifetime of a localized particle on energy calculated within the framework of the model used (solid curve) and in the approximation of hopping to the nearest center (dashed curve). $g_0\varepsilon_0 a^2=1$, $\omega_0/\omega(0)=0.1$

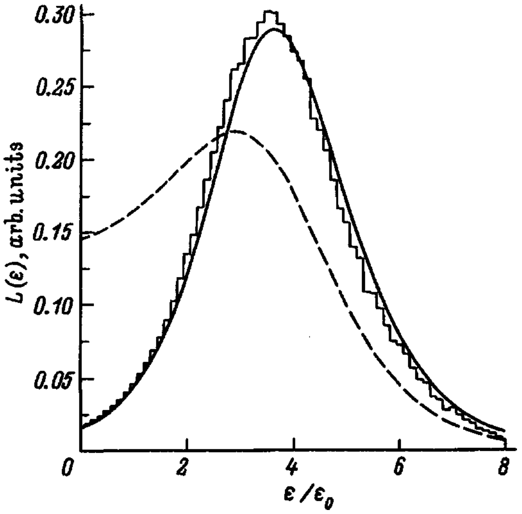

FIG. 2. Spectra of low-temperature steady-state luminescence from the tail of localized states. The solid curve shows a calculation taking into account all possible intercenter transitions, the dashed curve is obtained under the approximation of hopping to the nearest center. The staircase curve is a result of a computer simulation for a system of localization centers located randomly in space. $g_0\varepsilon_0 a^2=1$, $\omega_0/\omega(0)=0.1$

$$\rho(\varepsilon)=\int_\varepsilon^\infty d\varepsilon' g(\varepsilon').$$

Let us examine on the basis of this model the steady-state distribution of excitons in the tail of localized states with density $g(\varepsilon)=g_0 e^{-\varepsilon/\varepsilon_0}$ in a two-dimensional (2D) system ($S=2\pi r$). For definiteness, let the transition $\varepsilon\rightarrow\varepsilon'$ be caused by a tunneling mechanism $\omega(r)=\omega(0)e^{-r/a}$. In Fig. 1 the solid curve represents the dependence of the average lifetime $T_\varepsilon$ of a localized state on localization energy $\varepsilon$ [Eq. (14), $\alpha=\omega_0$]. In these calculations we used the following values of the dimensionless parameters: $g_0\varepsilon_0 a^2=1$ and $\omega_0/\omega(0)=0.1$. We note immediately that the choice of a tunneling mechanism for hopping imposes a strict limitation on the total concentration of localized centers, since this mechanism determines the possibility of forming very localized states in the random potential of the system. Thus, when the total concentration of centers increases to the point where $g_0\varepsilon_0 a^2\gtrsim 1$, the states become delocalized. Other mechanisms for intercenter transitions do not impose such a strict limitation on the concentration of localized states. Keeping this in mind, let us turn out attention to the possibility of analyzing systems with $\rho a^2>1$ within the framework of this model.

At low energies $\varepsilon$, where the concentration of localization centers that are accessible by hopping $\varepsilon\rightarrow\varepsilon'$, i.e., the function $\rho(\varepsilon)$, is large, the average lifetime of a state is determined by hopping (formally, $T_\varepsilon\rightarrow 0$ as $\rho(\varepsilon)a^2\rightarrow\infty$). For larger localization energies the concentration $\rho(\varepsilon)$ is small, so that intercenter transitions are practically impossible, and $T_\varepsilon$ is determined by the rate of departure from the system $\omega_0$. For comparison, we show on this plot the average lifetime $D_\varepsilon$ in the approximation of nearest-neighbor hopping:[14]

$$D_\varepsilon[\omega_0]=\int dr'\frac{P_\varepsilon(r')}{\omega_0+\omega(r')},$$

where

$$P_\varepsilon(r')=\rho(\varepsilon)S(r')e^{-\rho(\varepsilon)V(r')}.$$

Note that $D_\varepsilon[\omega_0]\rightarrow[\omega_0+\omega(0)]^{-1}$ for $\rho(\varepsilon)a^2$ large, so that the approximation of hopping to nearest neighbors does not work. It is obvious that for the set of parameters we have chosen the region of low localization energies is at the boundary of applicability of the nearest-neighbor hopping approximation. Here the values of $T_\varepsilon$ and $D_\varepsilon$ differ significantly.

The shape of the luminescence line $L(\varepsilon)=\omega_0 N(\varepsilon)$ in the tail of localized states is shown in Fig. 2. This calculation was done using the methods developed here (the solid curve) and the nearest-neighbor hopping approximation (the dashed curve). The result of direct computer simulation of the hopping process of relaxation in a 2D system of localized centers with a preset form of the functions $\omega(r)$ and $g(\varepsilon)$ is shown by the stepped curve. The dashed curve deviates considerably from the solid and step-like curves in the region of small localization energies. This reflects the rapid growth of the density of states function $g(\varepsilon)$ and the escape, as we mentioned above, of parameters from the range of applicability of the approximate approach. Conversely, by developing the analytic model in this paper we obtain the correct result for high and for low concentrations of localized centers.

## 4. CONCLUSIONS

In deriving our balance equation we assume that after the next hop a particle completely forgets about the local configuration of neighboring centers except for the center from which it hopped [see Eq. (4)]. This simplification in analyzing the relaxation process for localized particles allows us to frame the entire discussion in terms of the average occupation of a state with fixed neighboring centers. In this paper we have set aside the question of corrections to the population $N(\varepsilon)$ connected with non-Markovian sequential hops of a localized particle from one center to another. This problem was investigated in detail in Ref. 15. In the approximation of hopping to nearest centers it was shown that the correlation effects arise as the dimensionality of the system decreases, but as a whole this is not a large effect. The shift in the maximum of the step-like curve (computer modeling) relative to the maximum of the solid curve (model calculation) can be used as an estimate of the effect of correlation of localized centers.

At finite temperature $\Theta$, transitions $\varepsilon\rightarrow\varepsilon'$ with $\varepsilon'<\varepsilon$ turn out to be possible, and the peak of the luminescence line shifts toward the region of smaller $\varepsilon$. For example, let the dependence of the hopping rate on the energy of the initial and final states be approximated by the function $\theta_{\Theta}(\varepsilon'-\varepsilon)=\{1+\mathrm{e}^{(\varepsilon-\varepsilon')/\Theta}\}^{-1}$, which becomes the ordinary Heaviside omit step function for $\Theta=0$. Then, for $\Theta>\varepsilon_0$ the total escape rate to states with $\varepsilon'<\varepsilon$ diverges, which attests to the effective delocalization of particles at high temperature (in comparison with $\varepsilon_0$). In this regime a particle is trapped at a center, is excited into the continuum of delocalized states, is once again trapped by a center, etc. (one of the two mechanisms for thermalizing carriers listed in Ref. 12). The approach proposed here, which lifts the limitation on the largest permissible density of exciton states, allows analysis of various regimes within the framework of a single model.

The author is deeply grateful to L. A. Balakeĭnikov and L. E. Golub for useful discussions.

This work was supported in part by the Russian Fund for Fundamental Research (Grant 96-02-17849a), the Volkswagon Foundation, and a grant from the ‘‘The Japan–Former Soviet Union Scientists Collaboration Program of Japan Society for the Promotion of Science (JSPS).’’

[1] J. Christen, in *Advances in Solid State Physics*, P. Grosse [Ed.] (Pergamon, Braunschweig, 1990), V. 30, p. 239.
[2] C. Weisbuch, R. C. Miller, R. Dingle, A. C. Gossard, and W. Wiegmann, Solid State Commun. **37**, 219 (1981).
[3] P. S. Kop'ev, V. Ya. Mel'tser, I. N. Ural'tsev, Al. L. Ĕfros, and D. R. Yakovlev, JETP Lett. **42**, 402 (1985).
[4] G. Bastard, C. Delalande, M. H. Meynadier, P. M. Frijlink, and M. Voos, Phys. Rev. B **29**, 7042 (1984).
[5] P. S. Kop'ev, V. Ya. Mel'tser, I. N. Ural'tsev, Al. L. Ĕfros, D. R. Yakovlev, and A. V. Vinokurova, Fiz. Tekh. Poluprovodn. **22**, 424 (1988) [Sov. Phys. Semicond. **22**, 259 (1988)].
[6] M. Wilkinson, Frang Yang, E. J. Austin, and K. P. O'Donnell, J. Phys.: Condens. Matter **4**, 8863 (1992).
[7] S. D. Baranovskii, U. Doerr, P. Thomas, A. Naumov, and W. Gebhardt, Phys. Rev. B **48**, 17149 (1993).
[8] S. Glutsch and F. Bechstedt, Superlattices Microstruct. **15**, 5 (1994).
[9] Y. Masumoto, S. Shionoya, and H. Okamoto, in *Proceedings 17th International Conference on the Physics of Semiconductors*, J. D. Chadi and W. A. Harrison [Eds.] (Springer, N. Y., 1985) p. 349.
[10] H. Kalt, J. Collet, S. D. Baranovskii, Rosari Saleh, P. Thomas, Le Si Dang, and J. Cibert, Phys. Rev. B **45**, 4253 (1992).
[11] J. F. Donegan, R. P. Stanley, J. P. Doran, J. Hegarty, J. Lumin. **58**, 216 (1994).
[12] Don Monroe, Phys. Rev. Lett. **54**, 146 (1985).
[13] T. Takagahara, J. Lumin. **44**, 347 (1989).
[14] A. G. Abdukadyrov, S. D. Baranovskii, S. Yu. Verbin, E. L. Ivchenko, A. Yu. Naumov, and A. N. Reznitskiĭ, Zh. Éksp. Teor. Fiz. **98**, 2056 (1990) [Sov. Phys. JETP **71**, 1155 (1990)].
[15] L. E. Golub, E. L. Ivchenko, and A. A. Kiselev, J. Opt. Soc. Am. B **13**, 1199 (1996).
[16] E. L. Ivchenko and L. V. Takunov, Fiz. Tekh. Poluprovodn. **10**, 1334 (1976) [Sov. Phys. Semicond. **10**, 791 (1976)].

Translated by Frank J. Crowne

SEMICONDUCTORS VOLUME 32, NUMBER 5 MAY 1998

# Analysis of changes in the intensity of intrinsic luminescence after diffusion of copper into semi-insulating undoped gallium arsenide crystals

F. M. Vorobkalo, K. D. Glinchuk, and A. V. Prokhorovich

*Institute of Semiconductor Physics, Ukraine National Academy of Sciences, 252023 Kiev, Russia*

(Submitted September 15, 1997; accepted for publication November 26, 1997)
Fiz. Tekh. Poluprovodn. **32**, 570–573 (May 1998)

The effect of copper diffusion into semi-insulating undoped GaAs crystals on the intensity of intrinsic luminescence is analyzed. It is shown that diffusion of copper into semi-insulating undoped GaAs crystals can lead either to an increase or a decrease in the intensity of intrinsic luminescence. Analytic relations, which connect the magnitude and sign of the effect with recombination parameters in these crystals, and also with the intensity of the excitation luminescence, are obtained. © *1998 American Institute of Physics.* [S1063-7826(98)01205-8]

## 1. INTRODUCTION

A well known and commonly used way to increase the uniformity of semi-insulating, undoped crystals of gallium arsenide is to heat them to a high temperature ($T=$ 800–900 °C) (see, for example, Refs. 1 and 2 and also the review Ref. 3). During this exposure to heat, copper can diffuse into the bulk of the semi-insulating undoped GaAs crystal, which greatly changes its spectrum of local centers.[1–3] Therefore, in recent years interest has focused on the study of how copper affects the electrical properties (in particular, luminescence) of crystals of semi-insulating undoped gallium arsenide. As a result of this interest, it is now possible to obtain reliable information on the changes induced by copper in the energy structure of these crystals (see, e.g., Refs. 4 and 5, and also the review article Ref. 3). There is also reliable work related to the study of the effect of copper on their luminescence properties: in Refs. 1 and 2 the authors observed a considerable change in the intensity of intrinsic luminescence from semi-insulating undoped GaAs crystals after copper was diffused into them. In discussing their data, the authors of Refs. 1 and 2 limited the discussion to explaining the phenomena they observed and to their qualitative evaluation, which prevented them from elucidating the character of the patterns they reported or giving them a convincing physical description. In contrast to Refs. 1 and 2, in this paper we present a detailed analysis of how copper diffusion into crystals of semi-insulating undoped GaAs affects the intensity of intrinsic luminescence from these crystals, along with a real picture of the physical phenomena that take place in this situation.

## 2. CHANGES IN THE INTENSITY OF INTRINSIC LUMINESCENCE AFTER COPPER DIFFUSION INTO CRYSTALS OF SEMI-INSULATING UNDOPED GaAs (THEORY)

Let us calculate the intrinsic luminescence intensity (caused by direct radiative recombination of free electrons and holes corresponding to a recombination coefficient $c$) in starting crystals of semi-insulating undoped GaAs, and crystals of $p$-GaAs obtained after copper is diffused into them (the electrical properties of these crystals were described in detail in Refs. 4 and 5). In the original crystals of semi-insulating undoped GaAs, the concentration of equilibrium electrons and holes is very small compared to their excess concentrations $\delta n_1$ and $\delta p_1$ created by illumination. Diffusion of copper into these semi-insulating undoped crystals converts them into low-resistance crystals of $p$-GaAs.[4,5] Therefore, in crystals of $p$-GaAs doped with copper the concentration of equilibrium electrons is very small compared to their excess concentration $\delta n_2$, while the concentration of equilibrium holes $p_0$ can be either larger or smaller than the concentration of excess holes $\delta p_2$. In this case, the intensity of intrinsic luminescence in the original semi-insulating undoped GaAs crystals $I_1$ and the intensity $I_2$ obtained after diffusion of copper into them are determined by the following relations (we assume that the thickness of the crystals $d$ in the direction of propagation of the light $y$ greatly exceeds the diffusion length for electron-hole pairs $I_d$ and the depth of penetration of the excitation light $1/k$):

$$I_1=c\int_0^\infty \delta p(y)\,\delta n(y)\,dy, \tag{1}$$

$$I_2=c\int_0^\infty [p_0+\delta p(y)]\,\delta n(y)\,dy. \tag{2}$$

Furthermore, we assume that in both types of crystals the luminescence is dominated by the linear bulk recombination of excess electrons (with lifetimes $\tau_{n1}$ in the original crystals of semi-insulating undoped GaAs and $\tau_{n2}$ in $p$-GaAs crystals doped with copper) and holes (with lifetimes $\tau_{p1}$ in starting crystals of semi-insulating undoped GaAs and $\tau_{p2}$ in $p$-GaAs crystals doped with copper) for the excitation intensities we used, i.e., the quantities $\tau_{n1}$, $\tau_{n2}$, $\tau_{p1}$, and $\tau_{p2}$, and also the diffusion lengths for electron-hole pairs $l_{d1}$ in the original semi-insulating undoped GaAs crystals and $l_{d2}$ in crystals doped with copper, do not depend on the intensity of the excitation luminescence $L$.[1] We also assume that luminescence is excited by strongly absorbed light (i.e., the optical

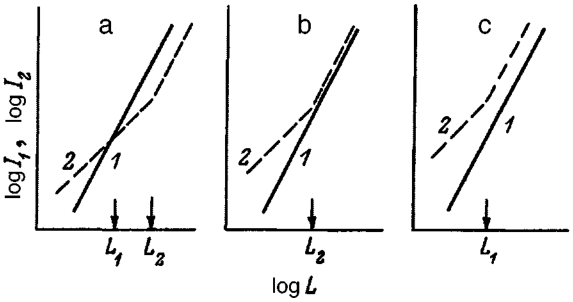

FIG. 1. Schematic dependence [from Eqs. (5) and (6)] of the intrinsic luminescence intensity on the intensity of excitation in initial crystals of semi-insulating undoped GaAs $I_1$ (*1*) and crystals obtained after diffusion of copper atoms $I_2$ (*2*) for various relations between their recombination parameters— $\tau_{n2}\tau_{p2}/l_{d2}<\tau_{n1}\tau_{p1}/l_{d1}$ (a), $\tau_{n2}\tau_{p2}/l_{d2}=\tau_{n1}\tau_{p1}/l_{d1}$ (b), and $\tau_{n2}\tau_{p2}/l_{d2}>\tau_{n1}\tau_{p1}/l_{d1}$ (c).

absorption coefficient $k$ is considerably larger than $1/l_d$).[2] In this case the concentration distribution of excess electrons and holes is given by the relations[6]

$$\delta n(y)=\delta n(0)\exp(-y/l_d), \tag{3}$$

$$\delta p(y)=\delta p(0)\exp(-y/l_d), \tag{4}$$

where $\delta n(0)=L\tau_n/l_d$, and $\delta p(0)=L\tau_p/l_d$ are the values of $\delta n$ and $\delta p$ at $y=0$.

Then, as follows from Eqs. (1)–(4), the intensity of intrinsic luminescence in the original crystals of semi-insulating undoped GaAs, and after copper is diffused into them are determined by the relations (obviously we have $I_1,I_2\ll L$):

$$I_1=\frac{c}{2l_{d1}}\tau_{n1}\tau_{p1}L^2, \tag{5}$$

$$I_2=cp_0L\tau_{n2}\left(1+\frac{L\tau_{p2}}{2p_0l_{d2}}\right) \tag{6}$$

[$I_2=cp_0L\tau_{n2}$ for $L\ll L_2=2p_0l_{d2}/\tau_{p2}$, i.e., $\delta p_2(0)=L_2\tau_{p2}/l_{d2}\ll 2p_0$, and $I_2=c\tau_{n2}\tau_{p2}L^2/2l_{d2}$ for $L\gg L_2$, i.e., $\delta p_2(0)\gg 2p_0$; obviously, the point where the function $I_2(L)$ changes slope is located at $L=L_2$, i.e., $\delta p_2(0)=2p_0$].

Figure 1 shows schematically the functions $I_1,I_2=\varphi(L)$ that follow from Eqs. (5) and (6) for various relations between recombination parameters of the original semi-insulating undoped GaAs crystals ($\tau_{n1},\tau_{p1},l_{d1}$), and the crystals of $p$-GaAs obtained by diffusing copper into the original crystals ($\tau_{n2},\tau_{p2},l_{d2}$). It is clear that, depending on the relation between recombination parameters for the crystals under study (in particular, between the quantities $\tau_{n1}\tau_{p1}/l_{d1}$ and $\tau_{n2}\tau_{p2}/l_{d2}$),[3] and also the intensity used to excite the luminescence in the experiments, after incorporating copper into the semi-insulating undoped GaAs crystals we can observe either a decrease ($I_2<I_1$) or an increase of the intensity of intrinsic luminescence ($I_2>I_1$), i.e., the magnitude and sign of these effect depend not only on the changes of the values $\tau_n,\tau_p$, and $l_d$ induced by the copper, but also on the rate of generation of electron-hole pairs $L$ (the latter is a consequence of the different dependences of the intensities $I_1$ and $I_2$ on $L$; namely, $I_1\sim L^2$ for any $L$ while $I_2\sim L$ for $L\ll L_2$ and $I_2\sim L^2$ for $L\gg L_2$). Actually, it follows from Eqs. (5) and (6) that when the luminescence is excited by strongly absorbed light we have:

1) $I_2>I_1$ for $L<L_1=2(\tau_{n2}/\tau_{n1})p_0l_{d1}/\tau_{p1}$, $I_2=I_1$ for $L=L_1$ and $I_2<I_1$ for $L>L_1$, if $\tau_{n2}\tau_{p2}/l_{d2}<\tau_{n1}\tau_{p1}/l_{d1}$ (see Fig. 1a);

2) $I_2>I_1$ for $L<L_2$ and $I_2=I_1$ for $L\geqslant L_2$, if $\tau_{n2}\tau_{p2}/l_{d2}=\tau_{n1}\tau_{p1}/l_{d1}$ (see Fig. 1b);

3) $I_2>I_1$ for any $L$ if $\tau_{n2}\tau_{p2}/l_{d2}>\tau_{p1}\tau_{n1}/l_{d1}$ (see Fig. 1c).

In principle, we can use Eqs. (5) and (6) to explain what caused the changes in the intrinsic luminescence intensity observed in Refs. 1 and 2 (increase in Ref. 1 and both increase and decrease in Ref. 2) after diffusion of copper into the semi-insulating undoped GaAs crystals (i.e., the roles played by changes in the quantities $\tau_n$, $\tau_p$, and $l_d$ induced by copper). However, these papers reported no data on the quantities $\tau_n$, $\tau_p$, and $l_d$ for the crystals under study. In addition, the magnitude of the intensity used in Refs. 1 and 2 to excite the luminescence makes it impossible to use relations (5) and (6) for a quantitative analysis of their data, although these data also qualitatively match the possible relations between quantities $I_1$ and $I_2$ shown in Fig. 1 (both $I_2>I_1$ and $I_2<I_1$ are possible). Therefore, in what follows we present measured results for copper-induced changes in the intrinsic luminescence intensity for crystals whose recombination parameters $\tau_n$, $\tau_p$, $l_d$ and rate of excitation of electron-hole pairs $L$ in them are known. This allows us to make quantitative estimates of the effect and identify the primary reasons for these changes.

## 3. METHOD

The crystals used at the beginning of the experiments were made of semi-insulating undoped GaAs (with a resistivity $\rho=2\times10^8\ \Omega\cdot$ cm at $T=300$ K that increased with decreasing temperature like $\rho(T)\sim\exp(0.75\ \mathrm{eV}/kT)$). Their conductivity was determined by ionization of EL2 defects (whose concentration $N_{EL2}=1.6\times10^{16}\ \mathrm{cm}^{-3}$, and the energy position of the levels they create is $\varepsilon_{EL2}=0.75$ eV) partially compensated by shallow carbon acceptors (with a concentration $N_{\mathrm{C}}\simeq3\times10^{15}\ \mathrm{cm}^{-3}<N_{EL2}$). The properties of these initial semi-insulating undoped GaAs crystals are described in detail in Ref. 5.

Atoms of copper were introduced into the semi-insulating undoped GaAs crystals via diffusion at 750 °C for 4.5 hours (their concentration was $N_{\mathrm{Cu}}\simeq1\times10^{17}\ \mathrm{cm}^{-3}$). Due to passivation of the EL2 defects by copper atoms in the doped crystals, the concentration of EL2 defects was considerably lower than the concentration of carbon atoms ($N_{\mathrm{EL2}}<1.5\times10^{15}\ \mathrm{cm}^{-3}=N_{\mathrm{C}}/2$).[5] Therefore, the conductivity of crystals diffusely doped with copper was determined by thermal ionization of carbon and copper atoms, and was quite large ($\rho=0.8-0.24\ \Omega\cdot\mathrm{cm}$ for $T=77-300$ K) and hole-like in character (the concentration of equilibrium holes was $p_0\simeq3\times10^{15}-8\times10^{16}\ \mathrm{cm}^{-3}$ at $T=77-300$ K). The properties of the crystals obtained after incorporating copper into semi-insulating undoped GaAs is described in detail in Ref. 5.

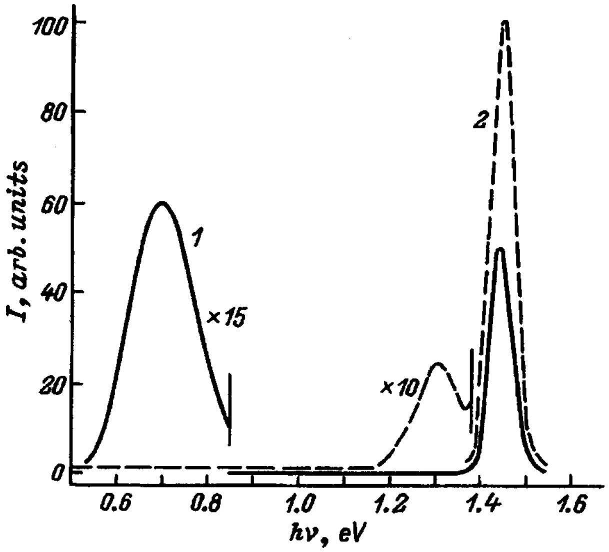

FIG. 2. Typical shape of photoluminescence spectra of initial semi-insulating undoped GaAs crystals (*1*) and crystals obtained by diffusion of copper (*2*) at 300 K and $L = 3\times10^{22}$ kW/cm$^2\cdot$ s.

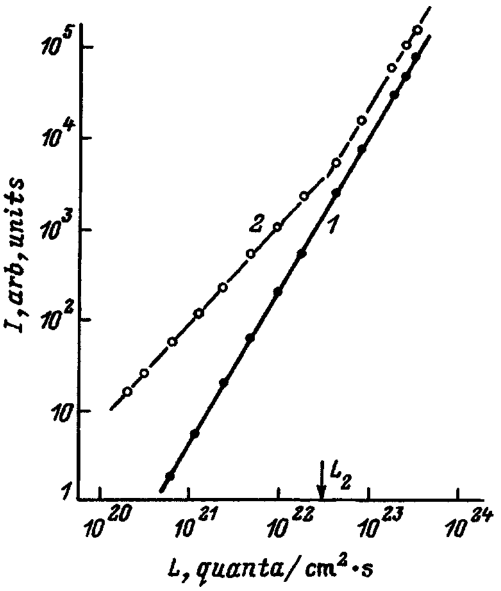

FIG. 3. Dependence of the intrinsic luminescence intensities in initially semi-insulating undoped GaAs crystals $I_1$ (*1*) and crystals obtained after copper diffusion $I_2$ (*2*) on the excitation energy $L$ at 300 K.

We studied the intrinsic luminescence of gallium arsenide crystals, both initial and doped with copper, at 300 K and at various levels of excitation. The luminescence was excited by strongly absorbed radiation from a He–Ne laser (photon energy $h\nu' =$ 1.96 eV, absorption coefficient $k=4\times10^4$ cm$^{-1}$, and excitation intensity $L=10^{18}-10^{22}$ kW/cm$^2\cdot$ s) and a ruby laser ($h\nu' =$ 1.79 eV, $k=3.4\times10^4$ cm$^{-1}$, $L=10^{22}-10^{24}$ kW/cm$^2\cdot$ s). The size of the luminescent region of gallium arsenide was determined by the diffusion length of excess current carriers $l_d$ [the quantity $l_d \simeq 10^{-4}$ cm exceeds the generation length for electron-hole pairs by the radiation $1/k \simeq (0.25-0.3)\times10^{-4}$ cm and was considerably lower than the crystal thickness $d(l_d, 1/k \ll d)$ ].

At the excitation levels we used, the intensity of intrinsic luminescence was considerably less than the excitation intensity, i.e., $I_1, I_2 \ll L$. Typical shapes of the luminescence spectra for initial crystals and crystals doped with copper are shown in Fig. 2 (in these crystals, in addition to the intrinsic emission band with its maximum at $h\nu_m =$ 1.44 eV, we also observed luminescence bands caused by the EL2 defects and copper atoms with energies $h\nu_m \simeq$ 0.7 and 1.30 eV, respectively). A detailed analysis of these spectra, in particular, the luminescence caused by EL2 defects that is quenched by Cu, can be found in Ref. 5.

## 4. CHANGE IN INTRINSIC LUMINESCENCE INTENSITY AFTER DIFFUSION OF COPPER INTO SEMI-INSULATING UNDOPED GaAs CRYSTALS (EXPERIMENT)

Figure 3 shows the experimental dependence of the intrinsic luminescence intensity on the level of excitation in initial semi-insulating undoped GaAs crystals and crystals obtained after diffusion of copper. It is clear that the introduction of copper leads to an increase in the intensity of intrinsic luminescence at any level of excitation, i.e., $I_2 > I_1$ for any $L$. From analysis of these experimental functions [see relations (5) and (6), and also Fig. 1c] it follows that the recombination parameters of the original semi-insulating undoped GaAs crystals are related to those obtained after diffusion of copper atoms as follows: $\tau_{n2}\tau_{p2}/l_{d2} > \tau_{n1}\tau_{p1}/l_{d1}$. This relation is actually satisfied in our experiments (because the Cu causes the value of $\tau_p$ to increase while leaving the quantities $\tau_n$ and $l_d$ unchanged), since direct measurement of the recombination parameters of the original crystals and those doped with copper at 300 K shows that in these crystals (in particular, when $L=3\times10^{22}$ kW/cm$^2\cdot$ s) we have $\tau_{n1} \simeq \tau_{n2} \simeq 10^{-10}$ s, $\tau_{p1} \simeq 1.6\times10^{-10}$ s, $\tau_{p2} \simeq 5\times10^{-10}$ s, and $l_{d1} \simeq l_{d2} \simeq 10^{-4}$ cm (for the methods of measuring $\tau_n, \tau_p$ and $l_d$, see Ref. 7).[4]

## 5. CONCLUSIONS

The increase in intrinsic luminescence intensity observed after copper is introduced into semi-insulating undoped crystals of gallium arsenide, which occurs at any level of excitation, is due to the increased lifetime of free holes induced by copper. The magnitude and sign of the effect are described satisfactorily by theoretical relations that take into account the dependence of the intensity of radiative recombination of free electrons and holes on the rate of their generation $L$ and their lifetimes $\tau_n$ and $\tau_p$.

---

1)The phenomena which we are describing will be observed if the lifetimes of excess current carriers are determined by the rate of their recombination via local centers whose occupation changes only slightly under excitation; i.e., the lifetimes of minority current carriers relative to their recombination at local centers are considerably lower than the lifetimes for electrons and holes relative to their direct radiative recombination $\tau = 1/c(p_0+\delta p)$.

2)The expressions given here for $\delta n$, $\delta p$, $I_1$, and $I_2$ are easily generalized to the case of an arbitrary relation between $k$ and $1/l_d$.[6] Thus, in particular, when weakly absorbed light is used to excite luminescence [$k \ll 1/l_d$], the relations given below for $\delta n$, $\delta p$, $I_1$, and $I_2$ are correct if we replace $1/l_d$ by $k$ in them.

---

[3] When weakly absorbed radiation is used to excite luminescence $(k \ll 1/l_d)$, we must also consider relations between the quantities $\tau_{n1}\tau_{p1}$ and $\tau_{n2}\tau_{p2}$ in analyzing the relations between intensities $I_1$ and $I_2$ (see above).

[4] In these experiments we observed a relatively weak nonlinearity in the recombination of excess electrons and holes, i.e., a relatively weak dependence of $\tau_n, \tau_p$, and $l_d$ on $L$ (in particular, $\tau_{n1}, \tau_{p1} \sim L^{-0.25}$). This implies that the forms of the experimental functions $I_1, I_2 = \varphi(L)$ we have obtained deviate somewhat from the theoretical form considered above [see Eqs. (5) and (6)]. In these experiments (see Fig. 3) we had $I_1 \sim L^{1.6}$ for any $L$, while $I_2 \sim L^{1.1}$ for $L < 3\times10^{22}$ kW/cm$^2$· s and $I_2 \sim L^{1.6}$ for $L > 3\times10^{22}$ kW/cm$^2$· s. A point where the function $I_2(L)$ changes slope is observed, as we expected, for $L = L_2 = 2p_0 l_{d2}/\tau_{p2} = 3\times10^{22}$ kW/cm$^2$· s (see Fig. 3), i.e., for $\delta p_2(0) = L_2\tau_{p2}/l_{d2} = 1.5\times10^{17}$ cm$^{-3} = 2p_0$.

[1] C. E. Third, F. Weinberg, L. Young, and M. Thewalt, Appl. Phys. Lett. **58**, 714 (1991).

[2] U. Jahn and H. Menniger, Phys. Status Solidi A **128**, 145 (1991).

[3] K. D. Glinchuk, V. I. Guroshev, and A. V. Prokhorovich, Optoelectron. and Semicond. Tech. **24**, 66 (1992) [in Russian].

[4] W. J. Moore, R. J. Henry, and J. S. Blakemore, Phys. Rev. B **46**, 7229 (1992).

[5] F. M. Borobkalo, K. D. Glinchuk, and A. V. Prokhorovich, Fiz. Tekh. Poluprovodn. **31**, 1045 (1997) [Semiconductors **31**, 893 (1997)].

[6] G. E. Pikus, *Principles of the Theory of Semiconductor Devices* (Moscow, 1965) [in Russian].

[7] N. M. Litovchenko and L. G. Shepel', Optoelectron. and Semicond. Tech. **29**, 108 (1995) [in Russian].

Translated by Frank J. Crowne

# Differential resistance of Au/GaAs$_{1-x}$Sb$_x$ tunneling contacts in the zero-bias anomaly region. I. Contacts to $n$-GaAs$_{1-x}$Sb$_x$

T. A. Polyanskaya,[a] T. Yu. Allen,[b] Kh. G. Nazhmudinov, S. G. Yastrebov, and
I. G. Savel'ev

*A. F. Ioffe Physicotechnical Institute, Russian Academy of Sciences, 194021 St. Petersburg, Russia*

(Submitted December 9, 1997; accepted for publication December 23, 1997)
Fiz. Tekh. Poluprovodn. **32**, 574–578 (May 1998)

The current-voltage characteristics and the differential resistance $R(V)=dV/dI$ of Au/$n$-GaAs$_{1-x}$Sb$_x$ tunneling contacts were investigated. Schottky barriers were prepared on $n$-GaAs$_{1-x}$Sb$_x$ epitaxial layers, which were specially not doped, in the composition range $0.01<x<0.125$. It was shown that the curves $R(V)$ in the electron density range $2\times10^{18}\leqslant n\leqslant7\times10^{18}$ cm$^{-3}$ and temperature range $4.2\leqslant T\leqslant295$ K are described well by the tunneling theory employing a self-consistent calculation of the potential in the Schottky barrier region. A square-root dependence of the conductance $G(V)=(dV/dI)^{-1}$ on the bias voltage $V$ was observed in the zero-bias anomaly region in accordance with the Al'tshuler–Aronov theory of quantum corrections introduced in the density of states at the Fermi level by the characteristic features of the electron-electron interaction in disordered metals. © *1998 American Institute of Physics.* [S1063-7826(98)01305-2]

## 1. INTRODUCTION

We undertook to investigate the differential resistance $R(V)=dV/dI$ of Au/GaAs$_{1-x}$Sb$_x$ barrier structures formed on epitaxial layers of a solid solution with a degenerate electron or hole gas in order to determine whether or not it is possible to observe for Schottky barriers by means of tunneling spectroscopy an anomaly in the density of states at the Fermi level $E_F$

$$\delta\nu\propto\sqrt{|E-E_F|},\tag{1}$$

predicted by Al'tshuler and Aronov for weakly disordered metals.[1–3] Here $E$ is the electron energy. The anomaly $\delta\nu$ (1) is due to a characteristic feature arising in the electron-electron interaction in the process of electron diffusion in the weakly disordered field of impurities and other lattice defects. As a result, an additional component $\Delta G(V)$ (so-called zero-bias anomaly) of the type

$$\frac{\Delta G(V)}{G(0)}=\gamma\sqrt{|V|}\tag{2}$$

appears in the tunneling conductance $G(V)=(dV/dI)^{-1}$ of the contact in the limit $V\to0$ but $|eV|\gg kT$ ($V$ is the bias voltage). Here $G(0)\equiv G(V=0)$ and the coefficient $\gamma$ depends on the resistivity $\rho$ and the electron-electron constant $\lambda_\nu$ (for the density of states)

$$\gamma\propto\lambda_\nu/\rho^{3/2}.$$

To distinguish the anomalous contribution to the conductance it is necessary to know the behavior of the "background" dependence of the differential resistance $R_N(V)$, determined by the normal density of states, which for a spherical isoenergetic surface is given by

$$\nu_0(E)=\frac{1}{2\pi^2}\left(\frac{2m^*}{\hbar^2}\right)^{3/2}(E-E_c)^{1/2},\tag{3}$$

where $m^*$ is the effective mass, and the electron energy $E$ is measured from the conduction-band bottom $E_c$. For this reason, the first problem of our investigations was to check the correspondence between the experimental and theoretical voltage dependences $R_N(V)$ in the temperature $T$ and voltage $V$ ranges where the anomaly in the tunneling conductance is not observed. This problem raises the question of whether the theory of tunneling in Schottky barriers adequately describes the experimentally observed dependences $R_N(V)$ for real surface-barrier structures.

It is well known that the theory developed in Refs. 4–7 for the density of states (3) satisfactorily describes the experimental current-voltage characteristics and the dependences $R_N(V)$ for Schottky barriers in the thermal-field emission region. However, in Ref. 8 it was noted (see Sec. 3.2.2) that this agreement between theory and experiment is surprising, considering that the space charge associated with impurities in a semiconductor is more likely macroscopically than microscopically nonuniform within the space charge region. This should result in large fluctuations in the form of the barrier[6] and in the tunneling probability. Indeed, the agreement between the theory[4–7] and the experimental data is markedly worse for diodes fabricated on the basis of "dirtier" semiconductors, for example, semiconductors with compensating impurities. An example of this is the well-known problem of the excess dark currents at low (of the order of liquid-nitrogen) temperatures in barrier structures fabricated on the basis of epitaxial layers of III–V solid solutions.

This question was greatly clarified after the development of the fluctuation theory of a barrier[9] and the consequent appearance of the field of research called incoherent mesoscopics. A theory of thermal-field emission was developed for Schottky barriers.[10] We checked this theory on Au/$n$-GaAs$_{1-x}$Sb$_x$ structures with electron density[11] $n=N_d-N_a\cong 10^{16}-10^{17}$ cm$^{-3}$. It was found that the theory of Ref. 10 makes it possible to explain the experimental data at the qualitative (voltage and temperature dependences of the current) and quantitative levels. Specifically, the low-temperature (excess) currents in Au/$n$-GaAs$_{1-x}$Sb$_x$ structures are explained by the presence of compensating levels of residual impurity with density[1)] $N_t=N_d+N_a=(3.0\pm 0.4)\times 10^{19}$ cm$^{-3}$.

We could not employ the theory of Ref. 10 to calculate the tunneling resistance $R_N(V)$, since bias voltages $V$ close to zero were not studied in Refs. 9 and 10 . However, we assume that the influence of fluctuations of the tunneling length on the current-voltage characteristics decreases substantially when the electron density $n=N_a-N_d$ in GaAs$_{1-x}$Sb$_x$ is 1.5–2 orders of magnitude higher than in the samples studied in Ref. 11 with the same residual impurity density $N_t=N_a+N_d$. As a result, we calculated the background dependence $R_N(V)=dV/dI$ with the density of states (3) on the basis of the conventional theory of field and thermal-field emission. The model of Ref. 14 was used to calculate $R_N(V)/R_N(0)$. In the present work it was shown (for the example of the tunneling conductance of Au/$n$-GaAs structures) that good agreement between theory and experiment can be obtained if the self-consistent solution of the Poisson equation for an electrostatic potential of the electron at the metal–semiconductor boundary is used to calculate the barrier transmittance.

## 2. EXPERIMENTAL PROCEDURE

Epitaxial layers of the solid solution GaAs$_{1-x}$Sb$_x$ were grown by liquid-phase eptiaxy in a purified-hydrogen atmosphere. The growth temperature was varied in the range 750–850 °C with cooling rate from 0.3 to 2 deg/min. The layers ranged in thickness from 10 to 45 $\mu$m. The components of the fluxed solution were Ga (99.9997%), AGN-1 nondoped $n$-GaAs with electron density $n\cong 10^{16}$ cm$^{-3}$ (As source), and nondoped $p$-GaAs with hole density $p\cong 10^{17}$ cm$^{-3}$ (Sb source). The Sb content was varied from $x=0.015$ to $x=0.125$. The substrate consisted of Te-doped $n$-GaAs with electron density $n\cong 10^{18}$ cm$^{-3}$ and (111)A orientation. The nondoped GaAs$_{1-x}$Sb$_x$ epitaxial layers had $n$-type conductivity and electron density $n=N_d-N_a=10^{16}-10^{17}$ cm$^{-3}$. These values are determined by the purity of the initial components of the fluxed solution, the degree of purification of hydrogen, and the characteristic features of the technological process. To obtain the layers with a wider range of electron densities, several series of epitaxial layers were doped with Te.

The Schottky barriers were fabricated by vacuum deposition of Au. First, the GaAs$_{1-x}$Sb$_x$ surface was cleaned with concentrated HCl for 30 sec in order to remove the natural oxide from the film surface. The wafers were gradually heated up to 200 °C (to anneal the surface of the epitaxial layer) with a residual pressure of $10^{-6}$ Torr and then cooled to 120 °C, at which temperature Au was deposited. Next, the structures were annealed at 200–250 °C for 3–4 min (in order to ‘‘secure’’ the Au film), after which Au/GaAs$_{1-x}$Sb$_x$/GaAs structures with diameter from 0.2 to 1 mm were formed by photolithography. A clamping contact consisting of a small In drop, attached to the Au film and protected by a lacquer coating, made it possible to perform measurements in the temperature range $4.2<T<450$ K.

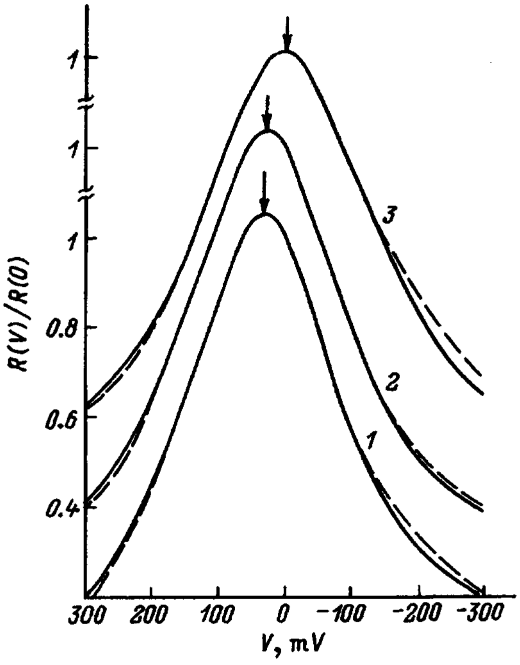

FIG. 1. $R_N(V)/R_N(0)$ versus the applied voltage $V$ for a Au/$n$-GaAs$_{0.96}$Sb$_{0.04}$ structure (sample 7$n$ in Table I) at temperatures $T$, K: *1* — 4.2, *2* — 77.4, *3* — 295. The arrows mark the values of $V_{\max}$.

The differential resistance $R(V)=dV/dI$ was measured as a function of the bias voltage $V$ by a bridge scheme at signal modulation frequency 22 kHz. Regulation of the bias voltage made it possible to pass smoothly through the value $V=0$. The apparatus made it possible to measure signals with voltage amplitude $2\times 10^{-5}-2\times 10^{-4}$ V with a modulating current of $10^{-7}$ A, which remained constant to within no worse than 5% in the course of the measurements. Depending on the resistance of the sample, the amplitude of the output signal of the generator was changed in discrete steps, but did not exceed $kT$.

## 3. EXPERIMENTAL RESULTS

In Refs. 14 and 15 it is shown that the experimentally easily identifiable parameters of the curve $R_N(V)$ for Au/$n$-GaAs contacts — the voltage $V_{\max}$ in the direct-bias region (marked by arrows in Figs. 1 and 2) at which a maximum of the resistance $R_N(V)=R_N^{\max}(V_{\max})$ is observed and the half-width of the curve $R_N(V)$ — are not determined uniquely by $E_F$ (i.e., the current carrier density $n$ in the semiconductor with a degenerate electron gas) and the barrier height $\varphi_{b0}(V=0)$. These parameters can be determined only as adjustable parameters when fitting the theoretical dependences $R_N(V)/R_N(0)$ to the the experimental data. We checked this method of determining $n$ and $\varphi_{b0}$ on

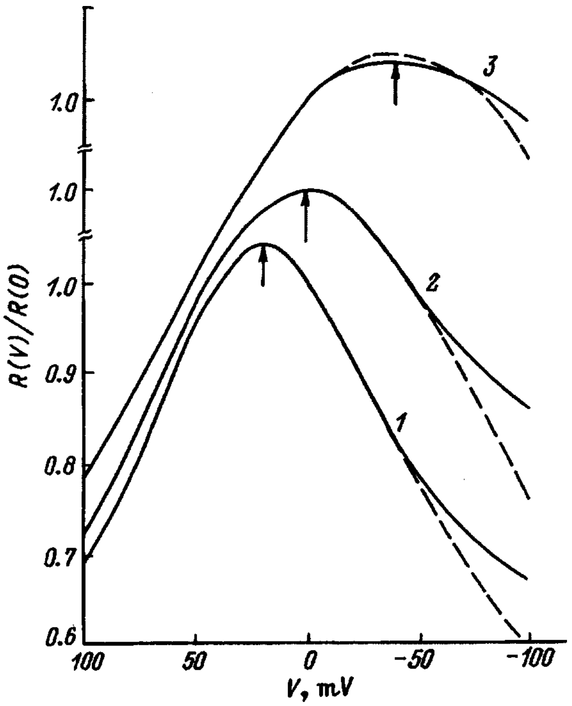

FIG. 2. Same as Fig. 1 but for the structure Au/$n$-GaAs$_{0.98}$Sb$_{0.02}$ (sample $2n$ in Table I).

Au/$n$-GaAs structures with electron density in GaAs $(1.5-5)\times10^{18}$ cm$^{-3}$, which is known from the Hall measurements. The densities determined by comparing the theoretical and experimental curves $R_N(V)/R_N(0)$ agree, to within no worse than 15%, with the results of the Hall measurements.

We used the same procedure for Au/$n$-GaAs$_{1-x}$Sb$_x$ structures. Figures 1 and 2 show the results obtained by comparing the experimental (solid lines) and theoretical (dashed lines) curves of $R_N(V)/R_N(0)$ for the samples Au/GaAs$_{0.96}$Sb$_{0.04}$ (Fig. 1) and Au/$n$-GaAs$_{0.98}$Sb$_{0.02}$ (Fig. 2). The theoretical curves were calculated in the model of Ref. 14 . The additional contribution $\Delta R(V)$ to the differential resistance in the region of the anomaly in the limit $V\rightarrow 0$ and $T=4.2$ K did not exceed 2–3% of the value of $R_N(0)$, so that it is not noticeable on the corresponding curves displayed in Figs. 1 and 2. Figure 2 illustrates well the effect of the temperature on the shape of the curve $R_N(V)$. We see that as temperature increases, the width of the curve increases, while the position of $V_{\max}$ shifts in the direction of reverse-bias voltages. The position $V_{\max}<0$ at high temperatures is manifested in structures with a relatively low electron density and is explained by an increase in the contribution of thermal-field emission with increasing temperature.

Table I gives the values of the density $n=N_d-N_a$ and barrier heights $\varphi_{b0}$ determined by fitting the theoretical curves to the experimental data. Earlier, photoelectric measurements gave the barrier height $\varphi_{b0}^{ph}=0.88\pm0.03$ ev at $T=77$ K, independent of the solid-solution composition in the range $0.03<x<0.125$, for Au/$n$-GaAs$_{1-x}$Sb$_x$ structures with $n=N_d-N_a=10^{16}-10^{17}$ cm$^{-3}$ in the solid solution.[16] Comparing the values of $\varphi_{b0}$ given in TableI with these data, we see that, except for the structures $7n$ and $8n$, they cluster around the values of $\varphi_{b0}^{ph}$ presented above.

In Ref. 15 it is shown that for Schottky barriers on $n$-GaAs the position of the maximum of $R_N(V)=R_N^{\max}$ with direct bias voltage $V=V_{\max}$ is always much less than $E_F$. In our case — for structures based on the solid solution $n$-GaAs$_{1-x}$Sb$_x$ — the values $V_{\max}=38$ meV at $T=4.2$ K for sample $7n$ in Fig. 1 and 22 meV for sample $2n$ in Fig. 2 are also much lower than the values of $E_F(T=4.2\text{ K})\cong190$ and 120 meV, respectively.

Proceeding now to the main purpose of our investigations — to check the applicability of the Al'tshuler–Aronov model[1–3] of the zero-bias anomaly in the tunneling conductivity of weakly disordered conductors — and to the description of the same phenomenon in Schottky barriers, we note the smallness of the anomalous contribution to the tunneling resistance, observed for our Au/$n$-GaAs$_{1-x}$Sb$_x$ structures. Figure 3 shows the conductance change $\Delta G=G(V)-G(0)$ in the region of the zero-bias anomaly as a function of $\sqrt{|V|}$ for the two samples for which it could be distinguished with adequate accuracy. As one can see from the figure, the voltage dependence $\Delta G(V)$ in the region of the anomaly satisfied the relation (2). In our view, this attests to the fact that a quantum correction to the Al'tshuler–Aronov density of states (1) also appears in the tunneling conductance of Schottky barriers, despite the fact that the theory of Refs. 1 –3 was formulated for contacts with weakly disordered metals.

TABLE I. Characteristics of Au/$n$-GaAs$_{1-x}$Sb$_x$ structures and parameters determined from variations of $dV/dI$.

| Sample No. | Sb content, $x$ | Film thickness $d$, $\mu$m | Te content, at. % | Barrier height $\varphi_{b0}$, eV | | | Density $N_d-N_a$, $10^{18}$ cm$^{-3}$ |
|---|---|---|---|---|---|---|---|
| | | | | 42 K | 77.4 K | 295 K | |
| $1n$ | 0.01 | 34 | 1.5 | 0.64 | 0.63 | 0.68 | 3.0±1.5 |
| $2n$ | 0.02 | 11 | 1 | 0.74 | 0.74 | 0.73 | 3.4±0.3 |
| $3n$ | 0.02 | 11 | 1 | 0.912 | 0.905 | 0.89 | 3.9±0.4 |
| $4n$ | 0.04 | 17 | 0.5 | 0.86 | 0.82 | 0.80 | 4.5±1.5 |
| $5n$ | 0.04 | 17 | 0.5 | 0.74 | 0.73 | 0.73 | 2.7±0.1 |
| $6n$ | 0.04 | 17 | 0.5 | 0.80 | 0.80 | 0.80 | 2.6±0.2 |
| $7n$ | 0.04 | 43 | 1.5 | 1.05 | 1.04 | 1.03 | 6.6±0.3 |
| $8n$ | 0.04 | 43 | 1.5 | 1.04 | 1.01 | 1.05 | 6.0±1.5 |
| $9n$ | 0.06 | 16 | 0.2 | 0.80 | 0.80 | 0.80 | 2.0±0.4 |
| $10n$ | 0.06 | 16 | 0.2 | 0.81 | 0.80 | 0.77 | 1.9±0.6 |

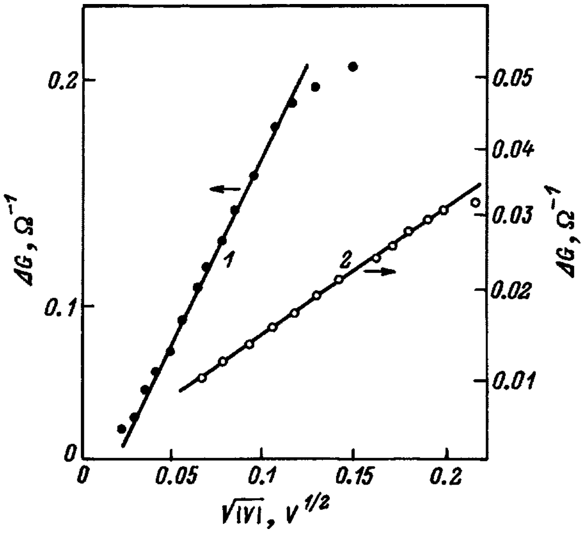

FIG. 3. $\Delta G = G(V) - G(0)$ in the region of the zero-bias anomaly versus $\sqrt{|V|}$ at $T = 4.2$ K for the structures *1* — Au/*n*-$GaAs_{0.96}Sb_{0.04}$ (sample 4*n*), *2* — Au/*n*-$GaAs_{0.98}Sb_{0.02}$ (sample 2*n*).

## 4. CONCLUSIONS

The differential resistance $dV/dI$ in Au/*n*-$GaAs_{1-x}Sb_x$ Schottky barriers versus the bias voltage and temperature in the range $4.2 < T < 295$ K is described satisfactorily by the tunneling theory employing a self-consistent calculation of the potential in the region of the Schottky barrier.[14] For low biases up to $|V| = 10 - 40$ meV a square-root dependence of the conductance $G(V) = (dV/dI)^{-1}$ on the bias voltage $V$ is observed. This agrees with the Al'tshuler–Aronov theory for quantum corrections introduced in the density of states at the Fermi level by the characteristic features of the multiparticle interaction in a disordered conductor.[1–3]

[a] E-mail: pta@nano.ioffe.rssi.ru

[b] Present address: University of Tennessee at Chattanooga, Chattanooga, TN 37403 USA; E-mail: tbilgild@cecasun.utc.edu.

[1] This value of the residual impurity density $N_t$ in our solid-solution layers agrees with estimates obtained previously from the results of an investigation of the mobility[12] and current-voltage characteristics in $GaAs_{1-x}Sb_x$-based $p-n$ junctions.[13]

---

[1] B. L. Altshuler and A. G. Aronov, Solid State Commun. **30**, 115 (1979).

[2] B. L. Al'tshuler and A. G. Aronov, JETP Lett. **37**, 175 (1983).

[3] B. L. Altshuler and A. G. Aronov, in *Electron-Electron Interactions in Disordered Systems*, edited by A. L. Efros and M. Pollak, Elsevier Science Publishers, B. V., 1985, Ch. 1.

[4] F. A. Padovani and R. Stratton, Solid-State Electron. **9**, 695 (1966).

[5] C. R. Crowell and V. L. Rideout, Solid-State Electron. **12**, 89 (1969).

[6] C. Y. Chang and S. M. Sze, Solid-State Electron. **13**, 727 (1970).

[7] V. L. Rideout and C. R. Crowell, Solid-State Electron. **13**, 993 (1970).

[8] E. H. Roderick, in *Metal-Semiconductor Contacts*, Clarendon Press, Oxford, 1978 [Russian trans. Radio, Moscow, 1982].

[9] M. É. Raĭkh and I. M. Ruzin, Zh. Éksp. Teor. Fiz. **92**, 2257 (1987) [Sov. Phys. JETP **65**, 1273 (1987)].

[10] M. É. Raĭkh and I. M. Ruzin, Fiz. Tekh. Poluprovodn. **21**, 456 (1987) [Sov. Phys. Semicond. **21**, 283 (1987)].

[11] T. A. Polyanskaya and Kh. G. Nazhmudinov, Fiz. Tekh. Poluprovodn. **21**, 1737 (1987) [Sov. Phys. Semicond. **21**, 1053 (1987)].

[12] Yu. F. Biryulin, V. N. Karyaev, I. Yu. Novikova, T. A. Polyanskaya, V. V. Chaldyshev, and Yu. V. Shmartsev, Fiz. Tekh. Poluprovodn. **15**, 2288 (1981) [Sov. Phys. Semicond. **15**, 1330 (1981)].

[13] A. Ya. Vul' and S. V. Kidalov, Fiz. Tekh. Poluprovodn. **20**, 451 (1986) [Sov. Phys. Semicond. **20**, 285 (1986)].

[14] I. N. Kotel'nikov, D. K. Chepikov, E. G. Chirkova, and A. Ya. Shul'man, Fiz. Tekh. Poluprovodn. **21**, 1854 (1987) [Sov. Phys. Semicond. **21**, 1123 (1987)].

[15] R. Stratton and F. A. Padovani, Solid-State Electron. **10**, 813 (1967).

[16] L. V. Sharonova, T. A. Polyanskaya, Kh. G. Nazhmudinov, V. N. Karyaev, and L. A. Zaĭtsev, Fiz. Tekh. Poluprovodn. **22**, 93 (1988) [Sov. Phys. Semicond. **22**, 57 (1988)].

Translated by M. E. Alferieff

SEMICONDUCTORS VOLUME 32, NUMBER 5 MAY 1998

# Differential resistance of Au/GaAs$_{1-x}$Sb$_x$ tunneling contacts near the zero-bias anomaly. II. Contacts to $p$-GaAs$_{1-x}$Sb$_x$

T. A. Polyanskaya,*) T. Yu. Allen,†) Kh. G. Nazhmudinov, and I. G. Savel'ev

*A. F. Ioffe Physicotechnical Institute, Russian Academy of Sciences, 194021 St. Petersburg, Russia*

(Submitted December 9, 1997; accepted for publication December 23, 1997)
Fiz. Tekh. Poluprovodn. **32**, 579–582 (May 1998)

The differential resistance $R(V)=dV/dI$ of Au/$p$-GaAs$_{1-x}$Sb$_x$ tunneling contacts was investigated. Schottky barriers were prepared on epitaxial layers of the solid solution $p$-GaAs$_{1-x}$Sb$_x$ $(0.045<x<0.125)$, which were doped with Ge from 0.01 to 5 at.%. It was shown that substantial features are present in the voltage dependences $R(V)$ for Au/$p$-GaAs$_{1-x}$Sb$_x$ contacts as compared with the data for Au/$n$-GaAs$_{1-x}$Sb$_x$ structures. A square-root voltage dependence was observed for the conductance $G(V)=(dV/dI)^{-1}$ versus the bias voltage $V$ near the zero-bias anomaly, in agreement with Al'tshuler–Aronov theory for quantum corrections introduced in the density of states at the Fermi level by the characteristic features of the electron-electron interaction in disordered metals. © *1998 American Institute of Physics.* [S1063-7826(98)01405-7]

A method for preparing GaAs$_{1-x}$Sb$_x$ epitaxial layers is described in Ref. 1. As the substrate for growing the $p$-type solid solution we used $p$-GaAs with hole density $p\cong 10^{19}\text{cm}^{-3}$ and (111)A orientation. To obtain layers with a wide range of hole densities several series of samples were doped with Ge (from 0.01 to 5 at. %). The Schottky barriers to the $p$-GaAs$_{1-x}$Sb$_x$ layers were also prepared in the manner described in Ref. 1 .

The measurements of the differential resistance curves $R(V)=dV/dI$ for barrier structures formed on GaAs$_{1-x}$Sb$_x$ epitaxial layers with a degenerate hole gas showed that the dependences differ substantially from the corresponding dependences for $n$-GaAs$_{1-x}$Sb$_x$-based structures.[1] The Au/$n$-GaAs$_{1-x}$Sb$_x$ structures investigated in Ref. 1 were characterized by a small additional maximum on the $R(V)$ curve near $V\cong 0$ (the so-called zero-bias anomaly), which did not exceed 2–3%.

The typical curves $R(V)$ for Au/$p$-GaAs$_{1-x}$Sb$_x$ structures are shown in Fig. 1; the parameters of some samples are given in Table I. As one can see from the figure, in contrast to the data for contacts based on the $n$-type solid solution,[1] here the additional resistance $\Delta R(V)=R(V)-R_N(V)$ near $V\cong 0$ for some samples reaches or exceeds the maximum value of the background resistance $R_N(V)$. Here $R_N(V)$ is the bias voltage dependence of the normal or background differential resistance due to the standard density of states

$$\nu_0(E)=\frac{1}{2\pi^2}\left(\frac{2m^*}{\hbar^2}\right)^{3/2}(E_v-E)^{1/2}, \tag{1}$$

where $m^*$ is the effective mass, and the electron energy $E$ is measured from the valence band top $E_v$. We observed similar phenomena (called the ''giant resistance peak'') — when the zero-bias anomaly is of the order of or greater than the normal resistance — in the differential conductance of metal–insulator–metal[2,3] or metal–insulator–amorphous semiconductor[4] structures.

The theory of hole tunneling in semiconductors with a complex valence band has not been adequately developed. As a result, we made no effort to compare the background dependence $R_N(V)$ with the theoretical dependence, as done in Ref. 1 for Au/$n$-GaAs$_{1-x}$Sb$_x$ structures. However, a number of characteristic features of the voltage dependences $R(V)$ for Au/$p$-GaAs$_{1-x}$Sb$_x$ barriers can be represented as follows.

**1**. According to calculations[5] for Schottky barriers prepared on the basis of $p$-GaAs, the position of $V_{\max}$ in the direct-bias region, to which the maximum $R_N(V)=R_{\max}(V_{\max})$ corresponds, coincides with $E_F/e$ (in contrast to the situation in the case of $n$-GaAs). Assuming that this also is true for our Au/$p$-GaAs$_{1-x}$Sb$_x$ structures, we determined the hole density from the values of $E_F=eV_{\max}$ and we present in Fig. 2 the conductance $G(V)=(dV/dI)^{-1}$ in the limit $V\to 0$ per unit contact area $(s)$

$$\frac{G(0)}{s}=\frac{1}{s(dV/dI)|_{V=0}} \tag{2}$$

as a function of hole density $p$, determined in the manner indicated. The solid line in Fig. 2 shows the fitted curve

$$G(0)/s=G_{c0}(p-p_c)^{\gamma} \tag{3}$$

with the parameters

$$G_{c0}\cong(24.5\pm 9.5)\Omega^{-1}\ \text{cm}^{-2},$$

$$p_c=(6.4\pm 0.6)\times 10^{18}\ \text{cm}^{-3},\quad \gamma=0.84\pm 0.16.$$

A dependence of the type (3) was observed earlier[6] for the conductivity $\sigma$ versus the hole density at $T=4.2$ K in an investigation of the galvanomagnetic phenomena in our epitaxial layers[1)] $p$-GaAs$_{1-x}$Sb$_x$. From this comparison it can be concluded that the contact resistance of our Schottky bar-

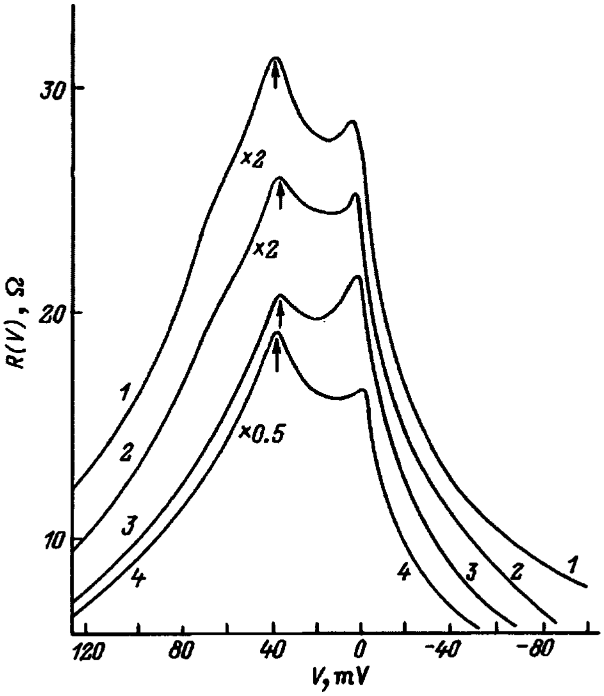

FIG. 1. $R=dV/dI$ versus the applied voltage $V$ at $T=4.2$ K for Au/$p$-GaAs$_{1-x}$Sb$_x$ structures (see Table I): *1* — 8$p$, *2* — 3$p$, *3* — 10$p$, *4* — 13$p$. The arrows indicate the values of $V_{\max}$.

riers $R_c=s/G(0)$ in the limit $V\rightarrow 0$ is determined mainly by the conductivity $\sigma$ of the semiconductor, as assumed in the theory of contacts.[7] This does not agree with the classical theory of field emission in Schottky barriers,[8] according to which $R_c$ depends exponentially on the current carrier density

$$R_c \sim \exp(\varphi_b/E_{00}),$$

where $E_{00}\sim(N_a-N_d)^{1/2}$.

**2**. Figure 3 shows the anomalous correction $A(V)$ to $R_N(V)$ for several Au/$p$-GaAs$_{1-x}$Sb$_x$ structures at $T=4.2$ K. The values of $A(V)$ were calculated as

$$A(V)=[R(V)-R_N(V)]/R(0), \tag{4}$$

TABLE I. Characteristics of GaAs$_{1-x}$Sb$_x$ epitaxial layers in Au/$p$-GaAs$_{1-x}$Sb$_x$ structures, results for which are presented in Figs. 1, 3, and 5.

| Sample No. | Sb content, $x$ | Film thickness $d$, $\mu$m | Ge content, at. % |
|---|---|---|---|
| 1$p$ | 0.06 | 18 | 0.2 |
| 2$p$ | 0.06 | 18 | 2 |
| 3$p$ | 0.06 | 18 | 5 |
| 4$p$ | 0.085 | 15 | 0.1 |
| 5$p$ | 0.085 | 15 | 0.2 |
| 6$p$ | 0.085 | 15 | 2 |
| 7$p$ | 0.105 | 13 | 0.05 |
| 8$p$ | 0.105 | 13 | 0.1 |
| 9$p$ | 0.105 | 13 | 0.2 |
| 10$p$ | 0.105 | 13 | 0.5 |
| 11$p$ | 0.125 | 18 | 0.1 |
| 12$p$ | 0.125 | 18 | 0.2 |
| 13$p$ | 0.125 | 18 | 0.5 |

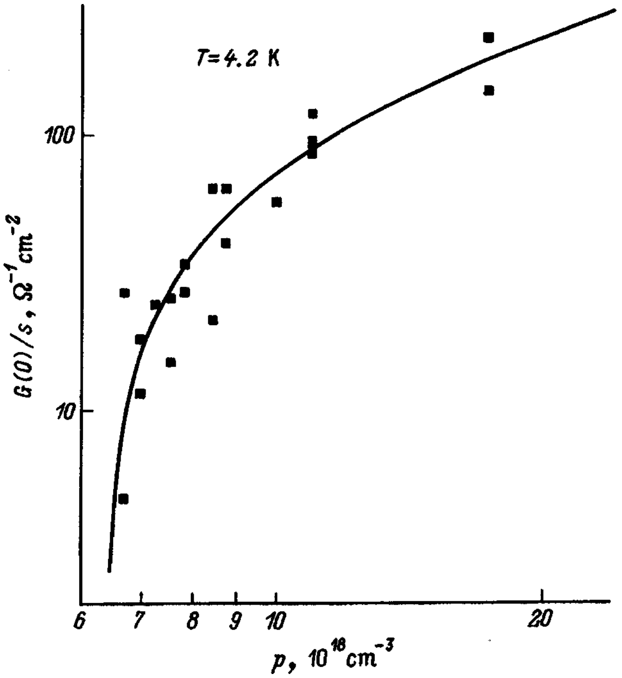

FIG. 2. Conductance $G_c$ [see Eq. (2)] for $V=0$ and $T=4.2$ K versus the hole density $p$ in GaAs$_{1-x}$Sb$_x$, determined according to the value of $eV_{\max}$ in the direct bias region (see Fig. 1). The solid line corresponds to the expression (2).

where $R(V)$ is the experimental differential resistance at $T=4.2$ K, and in the expression (4) we used for $R_N(V)$ not the computed dependence, as for Au/$n$-GaAs$_{1-x}$Sb$_x$ structures in Ref. 1 , but rather the curve $R(V)$ measured at $T=55$ K. The problem is that the zero-bias anomaly decreases substantially with increasing temperature, while the

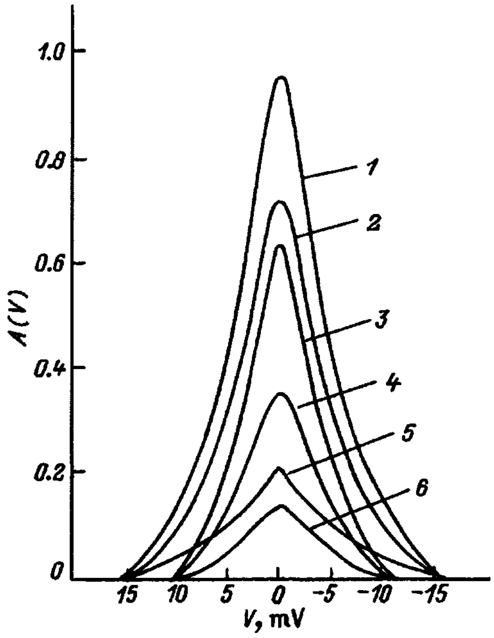

FIG. 3. Relative magnitude of the zero-bias anomaly $A(V)$ at $T=4.2$ K, separated from the background resistance $R_N(V)$ measured at $T=55$ K, for Au/$p$-GaAs$_{1-x}$Sb$_x$ samples (see Table I): *1* — 10$p$, *2* — 4$p$, *3* — 11$p$, *4* — 5$p$, *5* — 7$p$, *6* — 1$p$.

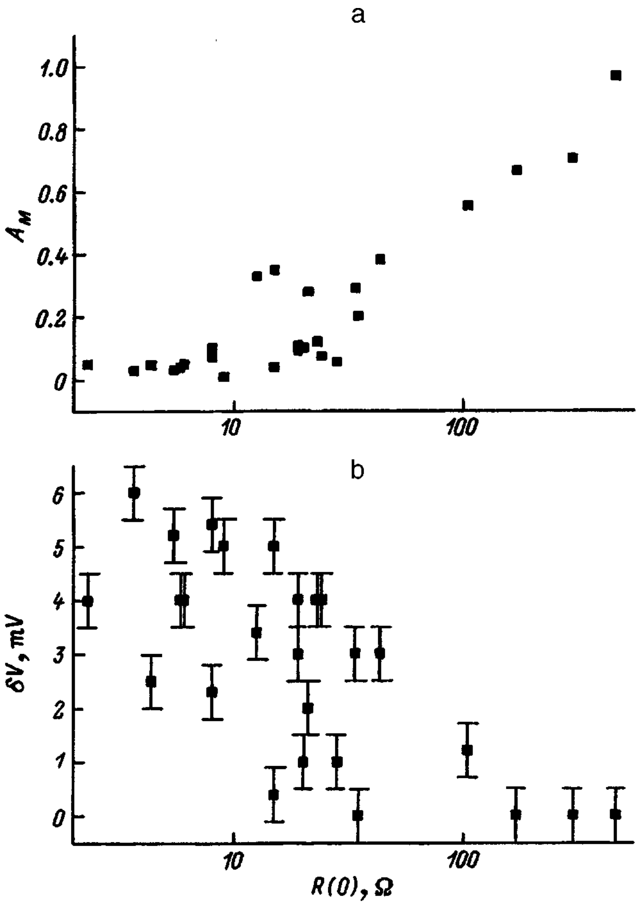

FIG. 4. Amplitude of the zero-bias anomaly $A_M$ (a) and its asymmetry parameter $\delta V$ (b) versus the resistance $R(V=0)$ for Au/$p$-GaAs$_{1-x}$Sb$_x$ contacts at $T=4.2$ K.

background dependence $R_N(V)$ remains unchanged in the region $4.2<T<55$ K, as follows from the tunneling theory. As temperature increases further $T>55$ K, the zero-bias anomaly vanishes, but then the form of the differential resistance curve $R(V)$ also changes, as observed in structures based on the $n$-type solid solution at high temperatures.[1] At $T=55$ K the amplitude $A(V=0)$ of the anomaly is negligible and the quantity $R_N(V,T=4.2\ \mathrm{K})\cong R_N$ $(V,\ T=55\ \mathrm{K})$ can be easily obtained for the purpose of calculating $A(V)$ at $T=4.2$ K according to the relation (4).

**3**. As one can see from Fig. 3, the amplitude of the zero-point anomaly (4) $A_M\equiv A(V\cong 0)$ for Au/$p$-GaAs$_{1-x}$Sb$_x$ samples reaches 96%, but the maximum of $A(V)$ does not always lie exactly at $V=0$. This asymmetry of the zero-bias anomaly relative to $V=0$ is expressed as a shift of the maximum of $A(V)$ on the voltage scale by an amount $\delta V<6$ meV, always in the direction of direct biases.

Figure 4a shows the values of the amplitude

$$A_M=[R(\delta V)-R_N(0)]/R(\delta V), \tag{5}$$

and Fig. 4b shows $\delta V$ as a function of $R(0)$. The amplitude $A_M$ increases with $R(0)$ (i.e., with decreasing hole density). This corresponds to the appearance of a giant peak on the curve $R(V)$ as the electrical parameters of the epitaxial layer approach the metal–insulator transition.

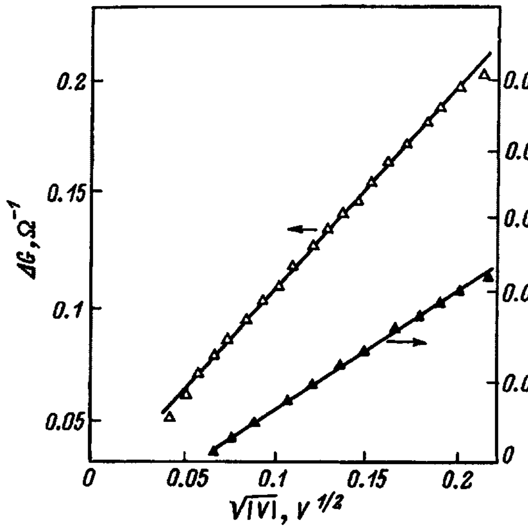

FIG. 5. The conductance $\Delta G=G(V)-G(0)$ versus $\sqrt{|V|}$ near the zero-bias anomaly at $T=4.2$ K for the structures (see Table I): *1* — $2p$; *2* — $6p$.

At the same time, $\delta V$ is much greater when the zero-bias anomaly is small — for small values of $R(0)$ (Fig. 4b). The error in measurements of $\delta V$ was eliminated by continuously scanning the voltage near the value $V=0$ from negative to positive biases and back. Moreover, the values found from $\Delta V$ fall outside the limits of the possible measurement error. The appearance of a shift $\delta V$ of the zero-bias anomaly in $R(V)$ relative to $V=0$ was also observed earlier[9,10] and was attributed to a strong compensation of the semiconductor. In our solid-solution layers the degree of compensation is indeed high, but it is due to the residual impurities[1,11] and therefore should decrease with increasing hole density and decreasing resistance, while we observe, in contrast, an increase in $\delta V$, which characteresizes the asymmetry effect. Thus the data presented in Fig. 4b do not agree with the model proposed in Refs. 9 and 10 for the origin of the aymmetry of the zero-bias anomaly.

**4**. An explanation of the zero-bias anomaly in the conductance of tunneling contacts was proposed in Refs. 12 –14. The authors calculated the quantum correction for the density of states depending in the dependence of tunneling conductance $G(V)=(dV/dI)^{-1}$ on the bias voltage for $|V|>kT$:

$$\frac{\Delta G(V)}{G(0)}=\gamma\sqrt{|V|}. \tag{6}$$

Here

$$\gamma\propto\lambda_\nu\rho^{3/2}\nu_F^{1/2},$$

$\nu_F$ is the density of states (1) with $E_\nu-E=E_F$, and $\lambda_v$ is a multiparticle interaction constant (for the density of states) in a weakly disordered current-carrier gas. Earlier, a square-root dependence of the type (6) was observed in the tunneling conductance of contacts of metals with thin films of granular metals and amorphous materials with metallic conductivity.[15–18] It was also observed at the Au/$n$-GaAs$_{1-x}$Sb$_x$ Schottky barriers.[1]

Figure 5 shows the change in the conductance

$\Delta G = G(V) - G(0)$ near the zero-bias anomaly (for $|V| < 40$ meV) as a function of $\sqrt{|V|}$ for two Au/$p$-GaAs$_{1-x}$Sb$_x$ structures. As one can see from the figure, the dependence $\Delta G(V)$ in this bias range satisfies Eq. (6). This also applies to Au/$n$-GaAs$_{1-x}$Sb$_x$ structures. This shows that probably there are quantum corrections for the Al'tshuler–Aronov density of state in tunneling spectroscopy of Schottky barriers.[12–14]

*)E-mail: pta@nano.ioffe.rssi.ru

†)Present address: University of Tennessee at Chattanooga, Chattanooga, TN 37403 USA; E-mail: tbilgild@cecasun.utc.edu.

1)However, in Ref. 6 the critical density for the dependence $\sigma(p - p_c)$ was found to be $p_c \simeq 4 \times 10^{18}$ cm$^{-3}$.

---

[1] T. A. Polyanskaya, T. Yu. Allen, Kh. G. Nazhmudinov, S. G. Yastrebov, and I. G. Savel'ev, Fiz. Tekh. Poluprovodn. **32**, 574 (1998) [*sic*].

[2] L. Y. L. Shen and J. M. Rowell, Phys. Rev. **165**, 566 (1968).

[3] P. Nielson, Phys. Rev. B **2**, 3819 (1970).

[4] R. A. Logran and J. M. Rowell, Phys. Rev. Lett. **13**, 404 (1964).

[5] R. Stratton and F. A. Padovani, Solid-State Electron. **10**, 813 (1967).

[6] T. Yu. Allen and T. A. Polyanskaya, Fiz. Tekh. Poluprovodn. **31**, 587 (1997) [Semiconductors **31**, 498 (1997)].

[7] R. Holm and E. Holm, *Electric Contacts Handbook*, Springer-Verlag, Berlin, 3rd edition [Russian trans., Inostr. Lit., Moscow, 1961].

[8] A. Y. C. Yu, Solid-State Electron. **13**, 239 (1970).

[9] E. L. Wolf, R. H. Wallis, and C. J. Adkins, Phys. Rev. B **2**, 1603 (1975).

[10] J. W. Osmun, Solid-State Electron. **13**, 1035 (1973).

[11] T. A. Polyanskaya and Kh. G. Nazhmudinov, Fiz. Tekh. Poluprovodn. **21**, 1737 (1987) [Sov. Phys. Semicond. **21**, 1053 (1987)].

[12] B. L. Altshuler and A. G. Aronov, Solid State Commun. **30**, 115 (1979).

[13] B. L. Al'tshuler and A. G. Aronov, JETP Lett. **37**, 175 (1983).

[14] B. L. Altshuler and A. G. Aronov, in *Electron–Electron Interactions in Disordered Systems*, edited by A. L. Efros and M. Pollak, Elsevier Science Publishers, B. V., 1985, Chap. 1.

[15] B. R. Sood, Phys. Rev. B **23**, No. 9 (1967).

[16] R. C. Dynes and J. P. Garno, Phys. Rev. Lett. **46**, 137 (1981).

[17] G. Hertel, D. J. Bishop, E. G. Spencer, J. M. Rowell, and R. C. Dynes, Phys. Rev. Lett. **50**, 743 (1971).

[18] W. L. McMillan and J. Mochal, Phys. Rev. Lett. **46**, 556 (1981).

Translated by M. E. Alferieff

# Binding energy of exciton-impurity complexes in semiconductors with diamond and zinc blende structure

S. M. Zubkova[a)] and E. I. Shul'zinger

*I. N. Frantsevich Institute of Materials Sciences, Ukrainian National Academy of Sciences, 252680 Kiev, Ukraine*

E. V. Smelyanskaya

*National Technical University ''Kiev Polytechnical Institute'', 252056 Kiev, Ukraine*

(Submitted April 18, 1997; accepted for publication October 21, 1997)
Fiz. Tekh. Poluprovodn. **32**, 583–587 (May 1998)

The binding energies of four complexes — exciton + charged impurity, exciton + neutral impurity — were calculated by a variational method in semiconductors with diamond and zinc blende structure taking into account the degeneracy of the valence-band edge. The numerical calculations were performed for exciton–impurity complexes in a series of II–VI, III–V, and IV–IV crystals. © *1998 American Institute of Physics.* [S1063-7826(98)01505-1]

## 1. INTRODUCTION

The existence of several types of exciton-impurity complexes (EICs) was first predicted in Ref. 1. Absorption and emission lines of several EICs, identified according to the value of the $g$ factor as EICs on a neutral acceptor, neutral donor, and ionized donor, were first observed in hexagonal CdS at $T=1.6$ K.[2,3] The first calculations of the binding energy of an exciton with an ionized impurity were performed in the effective mass approximation (EMA) using simple parabolic electron and hole dispersion laws. In Ref. 4 the binding energy of an exciton with an ionized impurity in semiconductors was calculated by a variational principle. It was shown that the bound state exciton + $D^+$ exists for $m_h>5m_e$, while an exciton + $A^-$ exists for $m_h>4m_e$.

The energies and wavefunctions of the complexes exciton + $D^+$ and exciton + $A^-$ were calculated in variational calculations for a wide range of values of the ratio $m_e/m_h$, covering the experimental values in InSb, InAs, InP, GaAs, GaSb, and so on.[5] In Ref. 5 it was concluded that bound excitons exist for $1.4\leqslant m_e/m_h\leqslant 4.5$.

The energy of an exciton bound on an ionized impurity was also calculated in Ref. 6 by a direct variational method in II–VI and III–V semiconductors with the sphalerite structure, taking account of the degeneracy of the valence-band edge and in the average effective mass approximation. It was shown that the exciton complexes in ionic semiconductors can form only on singly-charged impurities. The stability of excitons on a neutral donor or acceptor was studied in Refs. 7–9. The authors showed that for an EIC to be stable the critical parameter must lie in the interval $1<(\sigma_{\text{cr}}=(m_e/m_h))<2$. The binding energies of EICs were calculated by a variational method using 46- and 35-term trial atomic-type wavefunctions. Numerical calculations were performed for CdS, CdSe, ZnO, GaAs, and InP crystals neglecting the complicated band structure of these crystals.

In a later work[10] the ground-state energy of the EIC exciton + $D^0$ was calculated by a variational method in an approximation of simple parabolic bands for an arbitrary value of the ratio $\sigma=m_e/m_h$. It was shown that this complex is stable for any ratio of the electron and hole effective masses.

In summary, despite the fact that EICs in crystals have been studied for almost 35 years there are substantial discrepancies right up to contradictions in the theoretical results obtained by different authors concerning the conditions of existence and stability of EICs as well as the specific values of the binding energy of different complexes. Moreover, most theoretical calculations were performed in the approximation of a model band structure using simple parabolic dispersion laws. In other words the problem of EICs in semiconductors has not been solved conclusively. This concerns first and foremost the development of a single method of efficient and reliable calculation of the binding energies of the four most important EICs — exciton + $D^+$, exciton + $A^-$, exciton + $D^0$, and exciton + $A^0$ — in real semiconductors with a complicated band structure using a single approach for describing both exciton and impurity states as well as EIC states, determining at the same time the possibility of their existence in a specific crystal.

## 2. FORMULATION OF THE PROBLEM. HAMILTONIAN OF AN EXCITON–IMPURITY COMPLEX

Our work is devoted to the calculation of the ground-state energies of the four EICs listed above, taking into account the degeneracy of the valence-band top in semiconductors with diamond and zinc blende structure.

In Refs. 11 and 12 the EMA equations,[13,14] describing the state of an exciton in diamond- and sphalerite-like semiconductors, taking account of the degeneracy of the upper valence band, spin-orbit interaction, and anisotropy and nonparabolicity of the conduction band, were derived on the basis of the multielectron problem. The system of four second-order partial differential equations describing an exciton neglecting the spin-split off valence band is

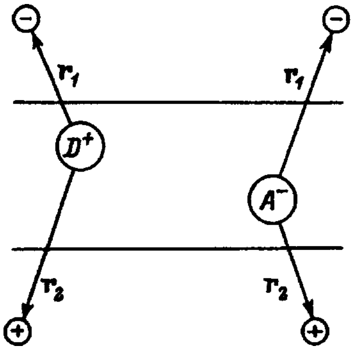

FIG. 1. Exciton on an ionized impurity.

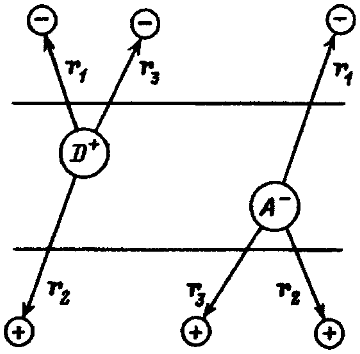

FIG. 2. Exciton on a neutral impurity.

$$\begin{cases}(\hat{b}_1-E)\Phi+(\hat{\mathcal{P}}+i\hat{Q})\chi=0;\\ (\hat{\mathcal{P}}-i\hat{Q})\Phi+(\hat{b}_4-E)\chi=0;\end{cases}$$

$$\Phi=\begin{pmatrix}\Psi_1\\ \Psi_4\end{pmatrix};\quad \chi=\begin{pmatrix}\Psi_2\\ \Psi_3\end{pmatrix}, \tag{1}$$

where

$$(\hat{\mathcal{P}}+i\hat{Q})=\sqrt{C^2+3B^2}\left(-I\frac{\partial^2}{\partial x\partial z}\pm i\sigma_3\frac{\partial^2}{\partial y\partial z}\mp i\sigma_2\frac{\partial^2}{\partial x\partial y}\right)_2 \mp\frac{i\sqrt{3}}{2}B\sigma_1\left(\frac{\partial^2}{\partial x^2}-\frac{\partial^2}{\partial y^2}\right)_2, \tag{2}$$

$$\hat{b}_{1,4}=-|A|\Delta_2\pm\frac{B}{2}\left(\frac{\partial^2}{\partial x^2}+\frac{\partial^2}{\partial y^2}-2\frac{\partial^2}{\partial z^2}\right)_2 -\frac{\hbar^2}{2m_e}\Delta_1-\frac{e^2}{\varepsilon_\infty|\mathbf{r}_2-\mathbf{r}_1|}+V, \tag{3}$$

$A$, $B$, and $C$ are the Dresselhaus–Kip–Kittel parameters; $\sigma_1$, $\sigma_2$, and $\sigma_3$ are the Pauli matrices; $I$ is the unit matrix; $\mathbf{r}_1$ and $\mathbf{r}_2$ are the electron and hole radius vectors in the exciton; and, $V$ is the potential energy of an impurity center.

For an exciton bound on an ionized impurity we have

$$V(\mathbf{r}_1,\mathbf{r}_2)=\frac{ze^2}{\varepsilon_0 r_2}-\frac{ze^2}{\varepsilon_0 r_1}, \tag{4}$$

where $z$ is the charge of the impurity center (see Fig. 1) — $z=1$ for the complex exciton $+\ D^+$ and $z=-1$ for the complex exciton $+\ A^-$.

For an exciton bound on a neutral impurity

$$V(\mathbf{r}_1,\mathbf{r}_2,\mathbf{r}_3)=V(\mathbf{r}_1,\mathbf{r}_2)-\frac{\hbar^2}{2m_e(m_h)}\Delta_3-\frac{e^2}{\varepsilon_0 r_3} -\frac{ze^2}{\varepsilon_0|\mathbf{r}_2-\mathbf{r}_3|}+\frac{ze^2}{\varepsilon_0|\mathbf{r}_1-\mathbf{r}_3|}. \tag{5}$$

Here $\mathbf{r}_3$ is the radius vector of the electron (hole) neutralizing the impurity and $z=\pm 1$ in the case of a neutral donor or acceptor, respectively (see Fig. 2).

## 3. CALCULATION OF THE GROUND STATE ENERGY OF AN EXCITON-IMPURITY COMPLEX

The systems (1)–(6) were solved numerically by a direct variational method. The trial function was approximated with a multiplicative form. For an electron ($\mathbf{r}_1$) in the exciton and for the intrinsic electron (hole) ($\mathbf{r}_3$) of a neutral impurity hydrogen-like functions were chosen with variational parameters $\alpha$ and $\beta$

$$\Psi=\sqrt{\frac{\alpha^3}{\pi}}e^{-\alpha r_1}\sqrt{\frac{\beta^3}{\pi}}e^{-\beta r_3} \times(\psi_1(r_2)\psi_2(r_2)\psi_3(r_2)\psi_4(r_2))^+. \tag{6}$$

The column vector $(\psi_1\psi_2\psi_3\psi_4)^+$ describes the state of a hole in a 4-fold degenerate valence band with a total angular momentum $j=3/2$. The trial functions $\psi_i$ in accordance with the symmetry of the hole part of the Hamiltonian (1)–(3) were chosen in the form of an expansion in terms of hydrogen-like $s$ and $d$ states of the type

$$\psi_i=\varphi_i(r,\theta)e^{-\alpha_i r}e^{im_i\varphi}. \tag{7}$$

The axial symmetry of the problem[15] makes it possible to assign to the four functions $\psi_i$ the following dependences on the angle $\varphi$:

$$m_1=m,\quad m_2=m+1,\quad m_3=m-2,\quad m_4=m-1. \tag{8}$$

The lowest 4-fold degenerate hole state corresponds to $m=0$, $1$. Then, for each of the four components we have

$$\psi_1=c_1e^{-\alpha_1 r_2}+c_5(x^2+y^2-2z^2)e^{-\alpha_5 r_2};$$

$$\psi_2=c_2z(x+iy)e^{-\alpha_2 r_2};\quad \psi_3=c_3i(x-iy)^2e^{-\alpha_3 r_2};$$

$$\psi_4=c_4iz(x-iy)e^{-\alpha_4 r_2}. \tag{9}$$

For the complexes exciton + charged impurity the second cofactor in Eq. (6) is absent; $\alpha$, $\beta$, $\alpha_i$, and $c_i$, $i=1,\ \ldots.\ 5$, are variational parameters. Substituting the expressions (6) and (9) into Eqs. (1)–(4) and using the normalization $\int\Psi^+\Psi d\tau=1$ we obtain for the complexes exciton $+\ D^+$ or $A^-$ the functional

$$E(\alpha,\alpha_i,c_i)=\int \Psi^+\hat{H}\Psi d\tau=\frac{\alpha^2}{2m_e}+As_1(\alpha_i,c_i)$$
$$\pm\frac{B}{2}s_2(\alpha_i,c_i)+\sqrt{3}Bs_3(\alpha_i,c_i)$$
$$+\sqrt{C^2+3B^2}S_4(\alpha_i,c_i)+\frac{z\alpha}{\varepsilon_0}$$
$$-zs_5(\alpha_i,c_i)/\varepsilon_0-s_6(\alpha,\alpha_i,c_i)/\varepsilon_\infty, \qquad (10)$$

where

$$s_1=\pi(\varepsilon_2\alpha_1^4+3\varepsilon_2+12\varepsilon_3+3\varepsilon_4+18\varepsilon_5);$$
$$s_2=6\pi(32\omega_{15}/5-\varepsilon_2/7+8\varepsilon_3/7+1\varepsilon_4/7+12\varepsilon_5/7);$$
$$s_3=32\pi(1\omega_{13}/5-96\delta_{35}/7+24\delta_{24}/7);$$
$$s_4=32\pi[-(\omega_{12}+\omega_{13})/5+48(2\delta_{35}-\delta_{25})/7$$
$$+24(2\delta_{34}-\delta_{24})/7];$$
$$s_5=\pi(\varepsilon_1\alpha_1^3+\varepsilon_2/\alpha_2+4\varepsilon_3/\alpha_3+\varepsilon_4/\alpha_4+6\varepsilon_5/\alpha_5);$$
$$s_6=s_5-\pi\left[C_1^2\frac{2\alpha+\alpha_1}{(\alpha+\alpha_1)^3}+\gamma_2+4\gamma_3+\gamma_4+6\gamma_5\right];$$
$$\varepsilon_i=c_i^2/\alpha_i^5; \quad \omega_{ij}=\frac{c_ic_j\alpha_i(5\alpha_i+\alpha_j)}{(\alpha_i+\alpha_j)^5};$$
$$\delta_{ij}=\frac{c_ic_j\alpha_i\alpha_j}{(\alpha_i+\alpha_j)^7}; \quad \gamma_i=\frac{c_i^2(4\alpha+\alpha_i)}{(\alpha+\alpha_i)^7}.$$

The functional (10) was written so that the contributions of the kinetic energy of the excitonic electron (term 1), the kinetic energy of the excitonic hole taking account of the 4-fold degeneracy of the valence-band edge (terms 2–5), the screened Coulomb interaction of the electron (hole) with a charged impurity (terms 6–7), and the screened interaction of an electron and a hole in the exciton (term 8) are seen explicitly. We note that analysis of the equation $\partial E(\alpha,\alpha_i,c_i)\partial\alpha=0$ showed that it is satisfied only if $z<\varepsilon_0/\varepsilon_\infty$. Therefore the EICs exciton + $D^+$ or $A^-$ can form only on single-charged impurities, in agreement with the results of Ref. 6 .

The normalization condition gives

$$\pi(\varepsilon_1\alpha_1^2+3\varepsilon_2/\alpha_2^2+12\varepsilon_3/\alpha_3^2$$
$$+3\varepsilon_4/\alpha_4^2+18\varepsilon_5/\alpha_5^2)=1. \qquad (11)$$

The derivation of Eqs. (10)–(11) used the important property of the operators $\hat{b}_2$ and $\hat{b}_3$

$$\int \psi_n^*\hat{b}_{2,3}\psi d\tau=\int \psi\hat{b}_{2,3}\psi_n^* d\tau. \qquad (12)$$

The functional (10) and all subsequent formulas are written in the dimensionless variables

$$\varepsilon=E\frac{\hbar^2}{m_0e^4}, \quad \rho=r\frac{m_0e^2}{\hbar^2}.$$

For EICs with neutral impurities the following terms are added to Eq. (10):

$$\frac{\beta^2}{2m_e(m_h)}-\frac{|z|\beta^2}{\varepsilon_0}+\frac{sign(z)}{\varepsilon_\infty}\left[\frac{\alpha^2(\alpha+2\beta)}{(\alpha+\beta)^3}-\alpha-\pi\right.$$
$$\left.\times\left(c_1^2\frac{\alpha_1+2\beta}{(\alpha_1+\beta)^3}+c_2^2\chi_2+4c_3^2\chi_3+c_4^2\chi_4+6C_5^2\chi_5\right)\right],$$
$$\chi_i=\frac{\alpha_i+4\beta}{(\alpha_i+\beta)^7}, \quad i=2,3,4,5. \qquad (13)$$

These terms include the kinetic energy of the electron (hole) neutralizing the impurity, the Coulomb interaction of this electron (hole) with a charged impurity center, and the Coulomb interaction of the excitonic electron and hole with the electron (hole) of the neutral impurity.

The functionals (10) and (13), taking account of Eq. (11), were minimized numerically with respect to the 10–11 parameters by the steepest-descent method (gradient method). The working program makes it possible to obtain

TABLE I. Binding energies (meV) of the ground state of EICs exciton $+D^+$ and exciton $+D^0$ for a number of semiconductors.

| | | GaAs | | ZnTe | | ZnSe | | CdTe | | GaSb | | GaP | | InSb | | InP | |
|---|---|---|---|---|---|---|---|---|---|---|---|---|---|---|---|---|---|
| EIC Exciton $D^+$ | This work | −5.65 | | −32.2 | | −34 | | −15.5 | | −2.5 | | −16.7 | | −0.706 | | −6.95 | |
| | Theoretical calculations | −5.5 | [6] | −11.5 | [4] | −17.1 | [23] | −14.6 | [18] | −2.7 | [18] | −22.8 | [18] | −1.06 | [23] | −6.8 | [18] |
| | | $\sigma=0.25$ | | | | | | $\sigma=0.27$ | | $\sigma=0.16$ | | $\sigma=0.18$ | | | [18] | $\sigma=0.18$ | |
| | | −6.15 | [18] | −13 | [18] | −37.1 | [18] | | | | | | | −0.7 | [18] | | |
| | | $\sigma=0.11$ | | $\sigma=0.15$ | | $\sigma=0.28$ | | | | | | | | $\sigma=0.04$ | | | |
| | Experiment | −7.2 | [19] | | | −34.3 | [24] | −14 | [25] | | | | | | | | |
| | | −6.1 | [20] | | | −37.3 | [24] | −19 | [26] | | | | | | | | |
| EIC Exciton $+D^0$ | This work | −5.6 | | −30.05 | | −32.5 | | −12.8 | | −2.43 | | −15.38 | | −0.695 | | −6.45 | |
| | Theoretical calculations | −6.4 | [21] | −25.9 | [22] | −31.4 | [22] | −12.9 | [21] | −2.5 | [21] | | | | | −8.1 | [21] |
| | | $\sigma=0.14$ | | | | $\sigma=0.21$ | | | | | | | | | | | |
| | Experiment | −6 | [19] | −12.1 | [21] | −26.9 | [21] | −21.3 | [22] | | | | | | | | |
| | | | | | | −33.3 | [24] | | | | | | | | | | |

TABLE II. Binding energies (meV) of the ground state of EICs exciton $+A^-$ and $+A^0$ for a number of semiconductors.

| | | GaAs | | ZnTe | | CdTe | | GaSb | | GaP | |
|---|---|---|---|---|---|---|---|---|---|---|---|
| | This work | $-29.5$ | | $-118.5$ | | $-73.1$ | | $-10.8$ | | $-30.1$ | |
| | Theoretical calculations | $-22.1$ | [16] | $-106$ | [4] | | | $-7.2$ | [6] | $-36$ | [6] |
| | | $\sigma=0.25$ | | | | | | $\sigma=0.28$ | | $\sigma=0.40$ | |
| EIC | | $\varepsilon_0=12.9$ | | | | | | $-8.75$ | [6] | $-47.1$ | [6] |
| Exciton | | $-28.1$ | [6] | | | | | $\sigma=0.34$ | | $\sigma=0.34$ | |
| $+A^-$ | | $\sigma=0.25$ | | | | | | $-18$ | [4] | | |
| | | $\varepsilon=11.6$ | | | | | | | | | |
| | Experiment | $-31.9$ | [19] | | | | | $-8$ | [28] | $-30$ | [29] |
| | | | | | | | | $-17$ | [28] | | |
| | This work | $-34.4$ | | $-74.2$ | | $-74.6$ | | $-12.6$ | | $-26.1$ | |
| | Theoretical calculations | $\sigma=0.28$ | | $\sigma=0.39$ | | $\sigma=0.16$ | | $\sigma=0.25$ | | | |
| Exciton | | $-29.3$ | [27] | | | | | | | | |
| $+A^0$ | | $\sigma=0.22$ | | | | | | | | | |
| | Experiment | $-34$ | [20] | | | $-76.8$ | [27] | | | | |
| | | $-39$ | [27] | | | | | | | | |
| | | 36.7 | [19] | | | | | | | | |

the binding energies of four EICs for Ge, Si, and II–VI and III–V semiconductors with zinc-blende structure.

## 4. DISCUSSION

The calculations were performed for 16 crystals of the types indicated above. A comparative analysis of the contributions of individual terms in the functionals (10) and (13) permits making a judgement as to the possibility of the existence of a given complex in a specific crystal for given parameters $m_e$, $A$, $B$, and $C$. For example, in the EIC exciton $+ A^-$ in Si with $A=-4.25$, $B=-0.7$, and $C^2=21.72$, in units of $\hbar^2/2m_0$, the interaction of the excitonic electron and hole and the interaction of an electron with $A^-$ are almost four orders of magnitude weaker than the interaction of the hole with $A^-$, i.e. we have obtained a shallow acceptor level with $E_b=-30.3$ meV, which is in good agreement with $E_b=-30.6$ meV calculated in Ref. 16 with the same parameters.

In Tables I and II the ground-state energies which we obtained for the four EICs for a number of crystals are compared with the calculations performed by other authors and with existing experimental data. Table III gives the values of the parameters $m_e$, $A$, $B$, $C^2$, $\varepsilon_0$, and $\varepsilon_\infty$ as well as the average value of $m_h$ and $\sigma=m_e/m_h$ which were used. A comparison shows satisfactory agreement with experimental data, while for GaAs, CdTe, GaSb, InSb, and InP the agreement is good. The discrepancies can be attributed, first and foremost, to the large difference in the parameters of the band structure which were obtained by different authors both experimentally and theoretically.

We note that the concept of the so-called average hole effective mass employed in most works on EICs itself depends on the method used to determine the effective mass. For example, in GaAs the value of $m_h$ determined from the binding energy of a free exciton equals $0.17m_0$; the value determined from the binding energy of a shallow acceptor is $0.3m_0$; and, the value determined as the arithmetic mean of the effective masses of heavy ($m_{hh}$) and light ($m_{lh}$) holes equals $0.27m_0$.[10] We note once again that in our work we did not resort to this concept, and we operated with the D–K–K parameters $A$, $B$, and $C$ describing the structure of the upper valence band. Table III gives the values of $m_h$ as the arithmetic mean of the effective masses of the heavy and light holes

$$m_{hh(lh)}=\frac{m_0}{\gamma_1\mp 2|\gamma|},\quad \gamma=\frac{2\gamma_2+3\gamma_3}{5},\quad \frac{\gamma_1}{m_0}=-\frac{2A}{\hbar^2},$$

$$\frac{\gamma_2}{m_0}=-\frac{B}{\hbar^2},\quad \frac{\gamma_3}{m_0}=\frac{\sqrt{C^2+3B^2}}{\sqrt{3}\hbar^2},\tag{14}$$

where $\gamma_1$, $\gamma_2$, and $\gamma_3$ are the well-known Luttinger

TABLE III. Crystal parameters.

| | $A\left(\frac{\hbar^2}{2m_0}\right)$ | $B\left(\frac{\hbar^2}{2m_0}\right)$ | $C^2\left(\frac{\hbar^4}{4m_0^2}\right)$ | $\epsilon_0$ | | $\epsilon_\infty$ | | $m_e$ | $m_h$ | $\sigma$ |
|---|---|---|---|---|---|---|---|---|---|---|
| GaAs | $-5.5$ | $-4.5$ | $-1$ | 12.9 | [6] | 10.9 | [6] | 0.066 | 0.55 | 0.12 |
| ZnTe | $-1.2$ | $-2.38$ | $-0.2$ | 8.7 | [30] | 7.2 | [30] | 0.17 | 0.58 | 0.29 |
| ZnSe | $-1.71$ | $-2.39$ | 4.5 | 8.6 | [30] | 5.9 | [30] | 0.21 | 0.82 | 0.26 |
| CdTe | $-3.9$ | $-4$ | $-14$ | 10.7 | [30] | 7.1 | [30] | 0.11 | 2.56 | 0.043 |
| GaSb | $-10.2$ | $-8.6$ | 16 | 16.1 | [6] | 14.2 | [6] | 0.046 | 0.38 | 0.12 |
| GaP | $-4.7$ | $-2.6$ | 9 | 10.7 | [6] | 8.5 | [6] | 0.13 | 0.34 | 0.38 |
| InSb | $-31.5$ | $-29.3$ | 113 | 17.2 | [30] | 15.3 | [30] | 0.015 | 0.27 | 0.056 |
| InP | $-6.3$ | $-5.3$ | 0 | 12.3 | [30] | 9.5 | [30] | 0.072 | 0.54 | 0.133 |

parameters[17] and $\gamma = m_e / m_h$. Our values of $\sigma$, calculated using Eq. (14), often differ substantially from the values presented by other authors, making accurate comparison of the results difficult.

The calculations showed that the terms originating from the nondiagonal parts of the Hamiltonian (1)–(3) and corresponding to taking account of the degeneracy of the upper valence band contribute 10–30% to the binding energy of complexes in many crystals. This justifies a departure from the model band structure and introducing an average hole effective mass. This contribution turned out to be especially large in the crystals ZnS, InAs, GaP, AlSb, GaSb, and AlAs for the EIC exciton $+ A^-$, SiC, ZnTe, and ZnS for the EIC exciton $+ D^+$, and GaAs, ZnS, Si, CdTe, GaP, GaSb, and ZnSe for the EIC exciton $+ A^0$. In the case of the EIC exciton $+ D^0$ the contribution from the terms due to the degeneracy of the valence band was found to be negligibly small in all crystals investigated.

It is evident from Table I that the energies of EICs with $D^+$ and $D^0$ are very close and the energy of the complex exciton $+ D^+$ is higher than that of the complex exciton $+ D^0$ on the average by 5–7%. The variance of the binding energies is much larger for the complexes with $A^-$ and $A^0$.

To improve the calculations further the spin-orbit split off valence band must be taken into account. This is especially important for light crystals (Si, SiC, ZnS), where the spin-orbit splitting is comparable to the binding energy of a localized state. In this case it is necessary to solve a system of six partial differential equations.[32]

[a] Fax: (380-44)444-20-78

---

[1] M. A. Lampert, Phys. Rev. Lett. **1**, 450 (1958).
[2] J. J. Hopfield and D. G. Thomas, Phys. Rev. **122**, 35 (1961).
[3] D. G. Thomas and J. J. Hopfield, Phys. Rev. **128**, 2135 (1962).
[4] R. R. Sharma and S. Rodrigues, Phys. Rev. **153**, 823 (1967).
[5] O. S. Zinets and V. I. Sugakov, Ukr. Fiz. Zh. **12**, 344 (1967) .
[6] Sh. N. Gifeĭsman and V. P. Koropchanu, Fiz. Tekh. Poluprovodn. **18**, 671 (1984) [Sov. Phys. Semicond. **12**, 417 (1984)]
[7] G. Munschy, Phys. Status Solidi B **53**, 377 (1972).
[8] G. Munschy and C. Carabatos, Phys. Status Solidi **57**, 523 (1973).
[9] B. Stébe and G. Munschy, Phys. Status Solidi **88**, 713 (1978).
[10] T. D. Clark, K. K. Bajaj, W. M. Theis, and D. E. Phelps, Phys. Status Solidi B **110**, 341 (1982).
[11] S. M. Zubkova and K. B. Tolpygo, Fiz. Tverd. Tela (Leningrad) **19**, 556 (1977) [Sov. Phys. Solid State **19**, 318 (1977)].
[12] S. M. Zubkova and K. B. Tolpygo, Fiz. Tverd. Tela (Leningrad) **21**, 1210 (1979) [Sov. Phys. Solid State **21**, 701 (1979)].
[13] C. Kittel and A. Mitchell, in *Problems of Semiconductor Physics*, edited by V. L. Bonch-Bruevich, Inostr. Lit., Moscow, 1957, p. 505
[14] J. Luttinger and W. Kohn, in *ibid.*, p. 515 (1957).
[15] V. N. Dem'yankov, S. M. Zubkova, K. B. Tolpygo, and V. G. Filin, Fiz. Tverd. Tela (Leningrad) **25**, 3114 (1983) [Sov. Phys. Solid State **25**, 1795 (1983)].
[16] S. M. Zubkova, V. G. Filin, E. V. Smelyanskaya, and K. B. Tolpygo, Phys. Status Solidi B **183**, 497 (1994).
[17] J. M. Luttinger, Phys. Rev. **102**, 1030 (1956).
[18] G. Mahler and U. Schröder, Phys. Rev. Lett. **27**, 1358 (1971).
[19] E. H. Bogardus and H. B. Bebb, Phys. Rev. **176**, 993 (1968).
[20] M. A. Gilleo, P. T. Bailey, and D. E. Hill, Phys. Rev. **174**, 898 (1968).
[21] F. Mokross and H. Buttner, Phys. Status Solidi **94**, 107 (1979).
[22] W. Ungier, M. Suffczynski, and J. Adamowski, Phys. Rev. B **24**, 2109 (1981).
[23] M. Suffczynski, Phys. Lett. A **24**, 453 (1967).
[24] J. L. Merz, H. Kukimoto, K. Nassau, and J. W. Shiever, Phys. Rev. B **6**, 545 (1972).
[25] G. Babonas and A. Sileika, Phys. Status Solidi **42**, 577 (1970).
[26] G. L. Bir, B. S. Razbirin, and I. N. Ural'tsev, Fiz. Tverd. Tela (Leningrad) **14**, 360 (1972) [Sov. Phys. Solid State **14**, 300 (1972)].
[27] A. N. Lobaev and A. P. Silin, Fiz. Tverd. Tela (Leningrad) **24**, 1457 (1982) [Sov. Phys. Solid State **24**, 827 (1982)].
[28] E. J. Johnson and H. Y. Fan, Phys. Rev. A **139**, 1991 (1965).
[29] R. K. Willardson and A. C. Beer [Eds.], *Semiconductors and Semimetals, Vol. 3, Optical Properties of III–V Compounds,* Academic Press, N. Y., 1967 [Russian trans. Mir, Moscow, 1989, p. 488].
[30] A. N. Pikhtin and A. D. Yas'kov, Fiz. Tekh. Poluprovodn. **12**, 1047 (1978) [Sov. Phys. Semicond. **12**, 622 (1978)].
[31] M. Cardona, J. Phys. Chem. Solids **24**, 1543 (1963).
[32] V. N. Dem'yankov, S. M. Zubkova, K. B. Tolpygo, and V. G. Filin, Fiz. Tverd. Tela (Leningrad) **25**, 3114 (1983) [Sov. Phys. Solid State **25**, 1795 (1983)].

Translated by M. E. Alferieff

## SEMICONDUCTOR STRUCTURES, INTERFACES, AND SURFACES

# Heterojunction based on semiconductors with the chain structure TlSe–TlInSe$_2$

I. V. Alekseev*

*Joint Institute of Nuclear Research, 141980 Dubna, Russia*

(Submitted June 16, 1997; accepted for publication November 11, 1997)
Fiz. Tekh. Poluprovodn. **32**, 588–590 (May 1998)

A heterojunction based on semiconductors with a chain crystal structure $p$-TlSe–$p$-TlInSe$_2$ was obtained. Liquid-phase epitaxy from TlSe melt on the natural (110) cleavage surface of a TlInSe$_2$ crystal was used. The structure obtained is sensitive to light and hard radiation. Some photoelectric properties of the heterojunctions were investigated. © *1998 American Institute of Physics.* [S1063-7826(98)01605-6]

It is well known that one of the factors stimulating the development of heterojunctions in II–VI semiconductors was the impossibility of producing a $p-n$ heterojunction in many compounds of this group because of self-compensation, which impedes doping.[1,2]

A similar situation arises in anisotropic, for example, layered, semiconductors whose doping is complicated by the ''self-purification'' effect — release of impurities from layers into the interlayer space of the crystal.[3] On the other hand, the anisotropy of layered semiconductors makes it possible to obtain by lamination perfect natural surfaces with a low density of states, which is important for obtaining high-quality heterojunctions (HJs). In recent years intense efforts have been made to produce HJs in layered crystals by van der Waals epitaxy, specifically, on semiconductors such as InSe and GaSe.[4,5] It is of interest to investigate in this direction a different class of anisotropic semiconductors — semiconductors with a chain structure.

Interesting examples of such semiconductors are TlSe and TlInSe$_2$. They are isostructural and crystallize in a tetragonal lattice. Some crystal parameters are given in Table I. In contrast to III–IV–V compounds with a crystal chain structure, there exists for them a well-developed technology for growing large single crystals.[9] TlInSe$_2$ crystals exhibit high sensitivity to near-IR and hard radiation, and they exhibit high radiation resistance.[10] The present paper reports the first results on the fabrication of TlSe–TlInSe$_2$ heterojunctions by van der Waals epitaxy. TlSe epitaxy on a (110) TlInSe$_2$ surface was conducted from TlSe melt with direct melt–substrate contact.

The crystals for the experiment were grown by oriented crystallization, which is described in Ref. 9 and which consists of a modified Bridgman method. The single-crystal ingots possessed a crystallographic orientation with the **c** axis directed along the ingot, $p$-type conductivity, and hole density at 290 K $1.7\times10^{17}$ and $2.1\times10^{11}$ cm$^{-3}$ for TlSe and TlInSe$_2$, respectively.

The substrates were prepared by cleaving an ingot along two mutually perpendicular {110} natural cleavage surfaces. They were bar-shaped with approximate dimensions $0.5\times2\times10$ mm. The reflecting surfaces bounding the samples were not additionally worked.

The heterostructures were prepared in a horizontal quartz tube in vacuum under residual pressure 0.13 Pa. Two quick-response heaters provided a vertical temperature gradient in the reactor.

Two variants of the relative arrangement of TlSe and the substrate were used in the preparation for epitaxy: TlSe below and above the substrate. In the first variant the substrate was arranged with the freshly cleaved surface on a crystal or TlSe powder loaded into a thin-wall quartz ''boat.'' In the second variant a TlSe sample, which was slightly smaller than the substrate, was placed on the substrate. Next, the temperature in the reactor was raised in 7–10 min to the melting point of TlSe, held at that level for 3–5 min, and then rapidly (within 30 s) lowered by 10–15 °C. The temperature was further decreased at a rate of 3–4 °C/min.

In both variants the obtained epitaxial layers were single-crystal layers when the substrate temperature was lower than the melt temperature. However, in the first variant the epitaxial layers were permeated with small voids, apparently, as a result of overheating of the bottom layers of the melt and release of a volatile component. The epitaxial layers were 100–200 $\mu$m thick.

Ohmic indium contacts were deposited on the prepared heterostructures. The contacts were continuous on the TlSe side and in the form of a narrow longitudinal strip on the opposite side. Figure 1 shows a photomicrograph of the side cleavage surface of the heterostructure. Cleaving was done in the (110) plane perpendicular to the junction boundary. An

TABLE I. Crystal parameters.

| Compound | $a$, Å | $c$, Å | $E_g$, eV | $T_m$, °C | Reference |
|---|---|---|---|---|---|
| TlSe | $8.02\pm0.01$ | $7.00\pm0.02$ | 0.56 | 334 | 6, 7 |
| TlInSe$_2$ | 8.075(3) | 6.847(4) | | | 7 |
| TlInSe$_2$ | 8.02 | 6.826 | 1.2 | 772 | 8 |

*Note:* $a,c$—crystal lattice constants, $E_g$—band gap, $T_m$—melting temperature.

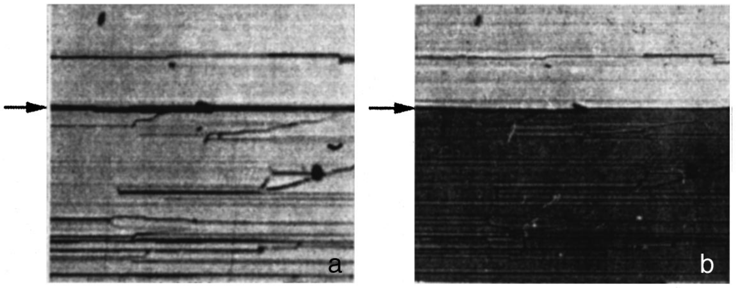

FIG. 1. Photomicrograph of a side cleavage surface of the heterostructure in natural (a) and polarized (b) light. Magnification: ×250.

epitaxial TlSe layer is located on top. The section of the junction boundary marked by the arrows is clearly distinguished in polarized light.

The isotypic HJs obtained exhibited appreciable sensitivity to light and hard radiation. The current-voltage characteristics were almost symmetric with a rectification factor 1.5–2 at 0.5 V. The currents consisted of several tens of $\mu$A. In view of the large serial resistance, determined by the high-resistance substrate, it was of no interest to analyze the current-voltage and current-capacitance characteristics.

The maximum short-circuit current density ($TlInSe_2$-side illumination) was $I_{sc}=0.5-0.6$ mA/cm$^2$. The open-circuit voltage $U_{oc}$ with concentrated solar radiation reached 0.39–0.40 V at room temperature. The polarity of the photoresponse on all HJs corresponded to a positive potential on TlSe relative to $TlInSe_2$.

The currents excited by 80–100 keV x-rays were equal to approximately 0.5 $\mu$A with an exposure dose rate of 10 rad/min.

Figure 2 shows the spectral characteristic of the photoresponse of HJ in the short-circuit current mode (curve *1*). One can see from the spectrum that carriers photogenerated in the narrow-gap component of the pair do not participate in the photoresponse. This could be due to the fact that because of the large difference of the majority carrier density between TlSe and $TlInSe_2$ the space-charge region is concentrated in the latter. It is interesting that the maximum in the spectral characteristic of the HJ is shifted in the short-wavelength direction relative to the maximum in the spectrum of the photoconductivity $I_{\rm ph}$ of a uniform $TlInSe_2$ crystal (curves *3* and *4*). The observed shift is probably due to the Dember effect, since in the experimental high-resistance $TlInSe_2$ crystals with high $\mu_p\tau_p=10^{-2}$ cm$^2\cdot$ V$^{-1}$ ($\mu_p$ is the mobility, and $\tau_p$ is the lifetime of the holes) the diffusion hole current, directed away from the illuminated surface in the direction of the HJ, should make a large contribution to the photoresponse. This is confirmed by the fact that this shift is not observed under illumination along the heterojunction, performed through a side cleavage surface of the heterostructure (Fig. 2, curve *2*). The curves *3* and *4* in Fig. 2 are the photoconductivity spectra of a uniform $TlInSe_2$ crystal illuminated in the direction of and perpendicular to the electric field, respectively. The intensity of the field in the samples was equal to 100 V/cm, so that the diffusion component of the photoresponse could not be large compared with the photocurrent. For this reason, the shift in the photoconductivity spectra is very small compared with the corresponding shift in the $I_{sc}$ spectra. We underscore, however, that the conclusion as to the role of the Dember effect is tentative.

The temporal parameters of the heterojunctions obtained were estimated from the kinetics of the short-circuit voltage, excited by square pulses of radiation from an injection laser with wavelength $\lambda=0.91$ $\mu$m. The rise and fall time constants of the photoresponse were equal to $10^{-4}$ s. The large value of the response time is determined by the *RC* of the HJ. We note that the corresponding times for a detector based on a uniform $TlInSe_2$ crystal, which are determined by the generation-recombination processes in $TlInSe_2$, are two orders of magnitude larger.

Special investigations showed that in TlSe and $TlInSe_2$

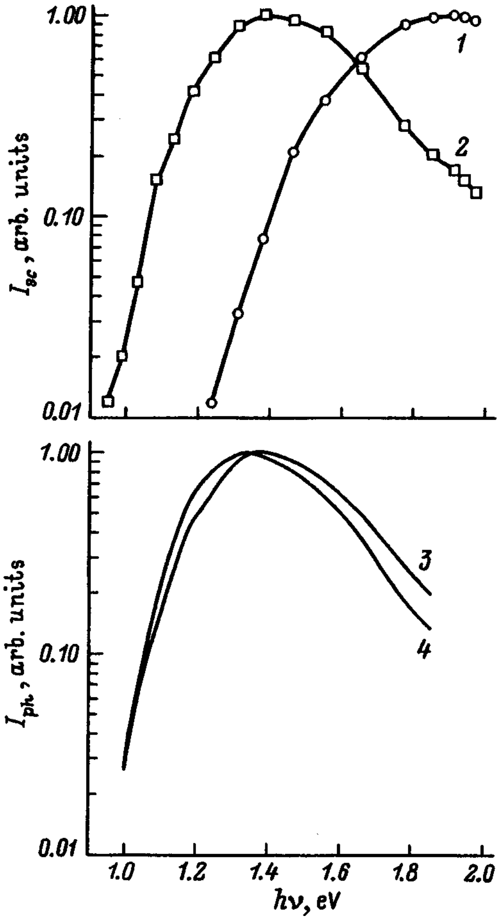

FIG. 2. $I_{sc}$ spectra of a heterojunction illuminated on the $TlInSe_2$ side (*1*) and through the side cleavage surface along the junction boundary (*2*) and the photoconductivity spectra of a $TlInSe_2$ crystal illuminated in the direction of (*3*) and perpendicular to (*4*) the electric field.

an excess and deficit of the metal component does not change the type of conductivity, while excess selenium forms a shallow acceptor in them. Considering the relatively low epitaxy temperature and the similar composition of the materials in a pair, it can be assumed that cross doping and formation of parasitic $p-n$ junctions during the formation of the HJ are unlikely.

The closeness of the crystal lattice parameters and the natural surface of the crystals forming the heteroboundary give hope that it will be possible to realize in this system HJs with a low density of local states at the boundary.

The use of a low-resistance substrate and perfection of the fabrication technology will make it possible to investigate HJs in greater detail and improve their characteristics — extend the spectral sensitivity range, increase $I_{sc}$, decrease the response time, and so on. In this case the HJs TlSe–$TlInSe_2$ could find applications as detectors of hard radiation and as radiation-resistant solar cells.

---

*E-mail: aleks@nf.jinr.ru

---

[1] H. H. Woodberry, in *Physics and Chemistry of III–VI Compounds* [Russian translation], Mir, Moscow, 1970.

[2] R. W. Dutton and R. S. Muller, Solid-State Electron. **11**, 749 (1968).

[3] K. D. Tovstyuk, *Semiconductor Materials Science* [in Russian], Naukova Dumka, Kiev, 1984.

[4] O. Lang and A. Klein, J. Cryst. Growth **146**, 439 (1995).

[5] O. Lang, C. Peterkoffer *et al.*, in *Proceedings 13th Photovoltaic Conference*, Nizza, 1995.

[6] *Reference Data on the Physical and Chemical Properties of Semiconductor Materials* [in Russian], Nauka, Moscow, 1979.

[7] D. Muller, G. Eulenberger, and H. Hahn, Z. Anorg. Allg. Chem. **398**, 207 (1973).

[8] G. D. Guseinov, E. Mooser, and I. V. Alekseev *et al.*, Phys. Status Solidi **34**, 33 (1969).

[9] I. V. Alekseev, Izv. Akad. Nauk SSSR, Neorg. Mater. **26**, 1401 (1990).

[10] I. V. Alekseev, Izv. Akad. Nauk SSSR, Neorg. Mater. **28**, 2404 (1992).

Translated by M. E. Alferieff

SEMICONDUCTORS VOLUME 32, NUMBER 5 MAY 1998

# Mechanism of anodic electroluminescence of porous silicon in electrolytes

D. N. Goryachev,[a] L. V. Belyakov, and O. M. Sreseli

*A. F. Ioffe Physicotechnical Institute, Russian Academy of Sciences, 194021 St. Petersburg, Russia*

G. Polisskiĭ

*Technical University of Munich, D-85747 Garching, Germany*

(Submitted December 9, 1997; accepted for publication December 23, 1997)
Fiz. Tekh. Poluprovodn. **32**, 591–595 (May 1998)

A mechanism of charge-carrier transfer from an electrolyte into porous silicon, which explains the efficient anodic electroluminescence of porous silicon, is proposed and analyzed in detail. It is shown that when a current flows through the interface, electrically active particles accumulate in the electrolyte — atomic hydrogen and oxygen, which with respect to porous silicon are efficient electron donors and acceptors. Visible-range electroluminescence arises as a result of bipolar electron and hole injection from the electrolyte into high-resistance quantum-well crystallites of porous silicon. It is shown that the overall mechanism is the same for anodic and cathodic electroluminescence. This explains the well-known similarity of these two processes. The detailed physicochemical processes, which are the basis for anodic luminescence, are explained. [S1063-7826(98)01705-0]

## 1. INTRODUCTION

Electroluminescence (EL) of porous silicon (*por*-Si) in contact with electrolytes is observed with porous layers grown on *n*- or *p*-type silicon substrates when both negative and positive biases are applied to them (cathodic and anodic EL, respectively).[1–5] By studying such EL it is possible to form judgements about charge-carrier transport processes in the complex multicomponent system *por*-Si. Numerous investigations of the cathodic EL of *por*-Si in contact with an oxidizing electrolyte have shown that it is highly efficient.[2,3]

In Refs. 6 and 7 the processes occurring in such a system under a cathodic bias were analyzed in detail and a generalized model of the cathodic EL of *por*-Si in electrolytes was proposed. This model was based on the idea that *por*-Si consists of crystallites of different sizes. The largest crystallites are essentially a continuation of the silicon substrate. The smallest crystallites do not exceed several nanometers in size. The visible photo- and electroluminescence of *por*-Si is observed as a result of the quantum-well broadening of the band gap of such crystallites up to 2–3 eV.[8]

But the small size of the microcrystallites gives rise to not only a broadening of their band gap, but also account for their high electrical resistance, irrespective of the type of conductivity and charge-carrier density in the initial silicon substrate. The free-carrier (both electrons and holes) density in the microcrystallites is exceedingly low. For this reason, simultaneous injection of charge carriers of both signs (bipolar injection) into the microcrystallites is necessary in order to obtain efficient electroluminescence. However, the band offsets at the Si/*por*-Si heterojunction impede the entry of carriers from the substrate, while a low-resistance electrolyte, which penetrates into the porous layer, shunts the high-resistance microcrystallites, and most of the electrical current flows from the silicon substrate directly into the electrolyte, bypassing the microcrystallites.[9,10] Therefore, carrier injection from both the substrate and the electrolyte is impeded.

In Ref. 6 it was shown that electrically active particles, which can inject both types of carriers into the microcrystallites, are generated at the electrolyte–substrate boundary as a result of electrochemical processes occurring during current flow. The carriers recombine in the microcrystallites, giving rise to EL in the visible range. In the cathodic process, ions–radicals $SiO_4^{\cdot -}$ (acceptors) and neutral hydrogen atoms $H^0$ (electron donors) participate as concrete, electrically active particles. This model has explained virtually all characteristic features of the visible and infrared cathodic EL.

Cathodic luminescence arises only when a strong oxidizer is present in the electrolyte, whereas anodic EL occurs in water solutions with virtually any composition. Thus, very similar results have been obtained with solutions of HCl, KCl, $H_2SO_4$, and $NaNO_3$.[5,11,12] We also observed intense EL with the use of a 0.1 $M$ NaOH solution and buffer solutions of $Na_2B_4O_7$ with $pH=9.18$. In these cases the maximum of the anodic EL spectrum was shifted to higher energies.

As a rule, anodic EL is no less intense than cathodic EL, though it is accompanied by more rapid degradation. The spectral characteristics of anodic EL are very reminiscent of the characteristics of cathodic EL of *por*-Si. For both cathodic and anodic EL the onset of luminescence is delayed. This delay time ordinarily ranges from 0.01 s up to several seconds. At low current densities (1 mA/cm$^2$) the delay of anodic EL increases to several minutes. It has been found that the delay time is directly proportional to the thickness of the *por*-Si layer and inversely proportional to the current density.[5] In the process of anodic EL a ‘‘blue’’ shift of the spectral maximum of the EL with increasing voltage on the electrolytic cell[13] and with increasing duration of electrolysis[5] is observed.

The mechanism leading to the appearance of anodic EL has not been studied adequately and has been interpreted differently in different studies.[4,5] In our study the basic assumptions of the model, which were formulated in Refs. 6 and 7, are extended to anodic EL of *por*-Si, and the specific physicochemical processes which occur are uncovered. The electrically active particles are identified — donors and acceptors, providing bipolar injection of carriers into the microcrystallites. The observed characteristic features of anodic EL are explained.

## 2. ELECTROCHEMICAL AND CHEMICAL PROCESSES ACCOMPANYING THE PASSAGE OF AN ANODIC CURRENT

Anodic electrochemical processes on a silicon surface proceed with the participation of the valence band of the semiconductor and are associated with the consumption of holes.[14] In the case of *p*-Si these holes come from the volume of the semiconductor. In the case of *n*-Si the hole sources are generation-recombination processes at the interface of the semiconductor with the oxide layer that is formed.[15]

The main anodic process is oxidation of silicon, i.e., ionization of the surface silicon atoms with trapping of holes and formation of silicon monoxide and then silicon dioxide:

$$\mathrm{Si}+2h^{+}+\mathrm{H_2O}\rightarrow\mathrm{SiO}+2\mathrm{H}^{+}, \tag{1a}$$

$$\mathrm{SiO}+2h^{+}+\mathrm{H_2O}\rightarrow\mathrm{SiO_2}+2\mathrm{H}^{+}. \tag{1b}$$

Dissolution of silicon is ruled out here, because the electrolyte contains no fluoride ions, which are capable of binding silicon ions into a soluble complex.

If the current is virtually completely expended at the first stages of electrolysis on the oxidation of silicon, then after the first $\mathrm{SiO_2}$ layer has formed on its surface the anode potential increases and water molecules[14] and hydroxide ions start to oxidize in the reactions

$$\mathrm{H_2O}+2h^{+}\rightarrow\mathrm{O}^{0}+2\mathrm{H}^{+}\,(\text{in an acidic medium}) \tag{2a}$$

or

$$2(\mathrm{OH})^{-}+2h^{+}\rightarrow\mathrm{O}^{0}+\mathrm{H_2O}\ \ (\text{in an alkaline medium}) \tag{2b}$$

with atomic oxygen $\mathrm{O}^0$ being formed in each case. Each of these electrochemical processes is followed by a chain of chemical transformations. Specifically, silicon monoxide SiO, formed by the reaction (1a), can react with water

$$\mathrm{SiO}+2\mathrm{H_2O}\rightarrow\mathrm{SiO_2}+2\mathrm{H}^{0}+2\mathrm{H}^{+} \tag{3}$$

with atomic hydrogen $\mathrm{H}^0$ being formed, similarly to the manner in which this happens in the electrolytic production of *por*-Si.[16] The existence of the reaction (3) is confirmed experimentally by the fact that the oxygen released at the anode ordinarily contains an admixture of hydrogen. Along with molecule formation from hydrogen and oxygen atoms, some oxygen atoms are used up in the oxidation of silicon. Nonetheless, it is obvious that in the presence of a current flow atomic hydrogen and oxygen are always present in the electrolyte in quasiequilibrium concentrations that are proportional to the current.

## 3. MODEL OF ANODIC ELECTROLUMINESCENCE

When a current flows in the system ⟨silicon substrate⟩/*por*-Si the initial porous layer is shunted by the low-resistance electrolyte, and a larger fraction of the current passes from the silicon substrate directly into the electrolyte, bypassing the microcrystallites. For this reason, the reactions (1)–(3) occur inside the porous layer — at the boundary of the electrolyte with the silicon substrate. The atomic hydrogen and oxygen formed in the process can diffuse into the electrolyte and become adsorbed on the surface of the electrically neutral, quantum-well nanocrystallites.

Comparison of the standard electrochemical potentials $\varphi$ of atomic hydrogen and oxygen (which equal $-2.10$ V and $+2.42$ V, respectively, relative to a normal standard electrode[17]) with the position of the Fermi level and the band edges in silicon and *por*-Si[18] shows that they are extremely electrically active particles: hydrogen atoms are donors and oxygen atoms are acceptors. The adsorbed atomic hydrogen injects electrons into the conduction band of the microcrystallites, while oxygen atoms remove electrons from the valence band, which is equivalent to injection of holes into it. In the process the microcrystallites remain electrically neutral, while bipolar injection of carriers into the microcrystallites gives rise to visible-range EL. In this process the semiconductor essentially plays the role of a solid-state catalyst, which facilitates electron exchange between electrically active particles:

$$\overset{\ulcorner\; 2e^{-} \;\urcorner}{2\mathrm{H}^{0}+\mathrm{O}^{0}}\rightarrow\mathrm{H_2O}. \tag{4}$$

Some of the energy released in such a reaction goes into luminescence. In accordance with the Franck–Condon principle,[19] such exchange is more likely to occur not directly in the electrolyte but rather with the participation of a solid surface, in the present case *por*-Si.

It should also be noted that electron injection occurs by the simple scheme

$$\mathrm{H}^{0}\rightarrow\mathrm{H}^{+}+e^{-}, \tag{5}$$

whereas hole injection is complicated by the chemical interaction of oxygen with *por*-Si. Initially, atomic oxygen interacts with hydrogen chemisorbed on the *por*-Si surface:

$$2(\equiv\mathrm{Si}-\mathrm{H})+\mathrm{O}^{0}\rightarrow2\,\mathrm{Si}+\mathrm{H_2O}+2h^{+} \tag{6a}$$

or, equivalently,

$$\mathrm{O}^{0}\rightarrow\mathrm{O}^{2-}+2h^{+}. \tag{6b}$$

However, after the chemisorbed hydrogen is removed from the surface of the microcrystallites the hole injection process is accompanied by oxidation of silicon atoms. This ultimately leads to the formation of silicon oxide microcrystallites on the surface:

$$\mathrm{Si}+2\mathrm{O}^{0}\rightarrow\mathrm{SiO_2}+4h^{+}. \tag{6c}$$

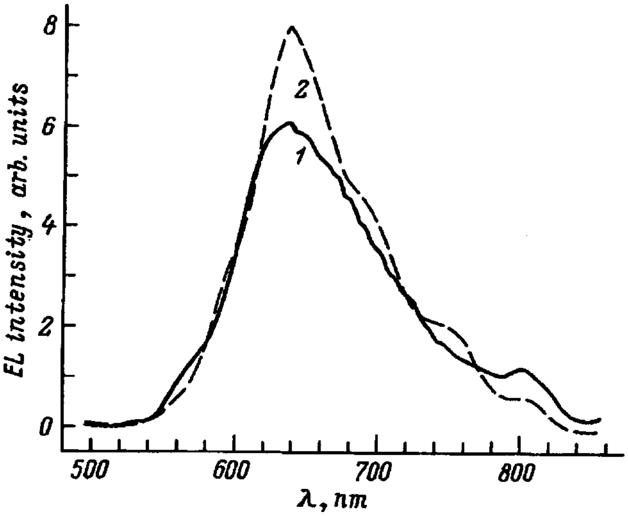

FIG. 1. Anodic (*1*) and cathodic (*2*) electroluminescence spectra obtained for the same *por*-Si sample in solutions: *1* — 1 N $H_2SO_4$, *2* — 1 N $H_2SO_4$ + 0.1 N $K_2S_2O_8$. The *por*-Si samples were prepared by the method of Ref. 10.

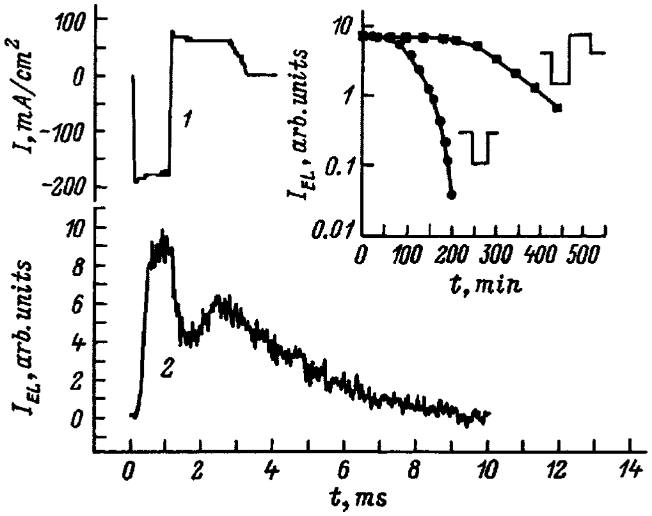

FIG. 2. Temporal characteristics of the electroluminescence of *por*-Si in an oxidizing electrolyte during passage of sign-alternating current pulses: *1* — current amplitude, *2* — intensity of electroluminescence measured at wavelength 700 nm. Inset: Variation of the intensity of electroluminescence accompanying repeated passage of current pulses.

## 4. DISCUSSION OF THE RESULTS ON THE BASIS OF THE PROPOSED MODEL

It should be noted first that the overall model proposed above applies to anodic and cathodic electroluminescence. For this reason, for the same *por*-Si sample, i.e., for the same crystallite-size distribution, identical cathodic and anodic EL spectra are observed (Fig. 1).

The long delay times for onset of EL relative to onset of current passage are explained by the fact that charge-carrier transport to *por*-Si microcrystallites is mainly ionic and not electronic. This is confirmed by the experiments of Ref. 20, where very weak anodic EL with virtually no delay was observed in the absence of wetting of *por*-Si by electrolyte and in the presence of an anodic current flow (for sufficiently high potentials). Under good wetting conditions, however, the same current was achieved with substantially lower potentials, and the EL was several orders of magnitude more intense but appeared after a delay of more than 1 min. In the first case EL associated with direct current passage through microcrystallites occurred. The appearance of efficient EL becomes possible only after the electrolyte penetrates deep into the porous layer and hydrogen and oxygen atoms have accumulated in sufficient numbers and diffuse to the microcrystallites. Improving the wettability of *por*-Si by the electrolyte improves the penetration of the electrolyte to the substrate and at the same time allows the electrolyte to come into contact with a large number of microcrystallites and therefore improves the conditions for the appearance visible-range EL.

The delay times in the anodic process for low current densities are at least an order of magnitude longer than the ‘‘cathodic’’ delay times. This could be due to the fact that when anodic current starts to flow, it is almost completely expended on the formation of silicon oxide. Oxygen is not released at this stage of electrolysis and therefore acceptors, which inject holes into the microcrystallites, are absent at these initial stages of electrolysis.

The proposed model makes it possible to explain the dependence of the delay of EL onset on the thickness of the *por*-Si layer. Electrically active particles are formed on the inner boundary of *por*-Si with the substrate and reach the *por*-Si surface only to the extent that they diffuse in the electrolyte. Correspondingly, as assumed in Ref. 5, EL initially arises inside the *por*-Si layer and reaches the *por*-Si surface only after the passage of a certain period of time, which depends on the layer thickness. This was confirmed experimentally in Ref. 12. The inverse relation between the EL delay and the anodic current density is obvious, since a definite amount of electricity must pass in order to achieve a definite threshold concentration of electrically active particles.

The mechanism of anodic EL proposed above makes it possible to explain the effects associated with the appearance of the ‘‘blue’’ shift of the spectral maximum of EL as a function of the applied voltage. The energies of the electrically active particles (donors and acceptors) in the electrolyte are determined by their standard electrochemical potentials $\varphi$ and concentrations. Their concentration in the electrolyte increases with increasing difference in the energies of electron donors and acceptors which are formed during electrolysis. Therefore, wider-gap microcrystallites will be entrained into the EL process. Since the equilibrium concentrations of electrically active particles are determined by the current density and correspondingly the voltage, the higher the current density at the working electrode, the larger the shift of the maximum of the EL spectrum in the direction of higher energies is. This pertains equally to both anodic and cathodic EL and is confirmed by experiments.[13,21,9]

In accordance with the reaction (6c), atomic oxygen oxidizes the surface of *por*-Si microcrystallites by injecting holes into them. In the process the silicon microcrystallites become smaller, and an increasingly larger shift of the maximum of EL into the short-wavelength region of the spectrum is observed as the duration of electrolysis increases. Subsequently, as a result of the formation of an oxide film, the surface of the microcrystallites becomes blocked and, correspondingly, irreversible degradation of the EL occurs. The blue shift of the maximum of EL that we observed in the case of alkaline electrolytes is also evidently due to a decrease in microcrystallite size as a result of partial dissolution of microcrystallites in the alkali.

The similarity of the mechanisms leading to the appearance of EL at a *por*-Si boundary with electrolytes in anodic and cathodic regimes is confirmed by the experiments described in Ref. 9. When sign-alternating current pulses with a low repetition rate ($\sim 10$ Hz) pass through the electrolytic cell, both pulses are accompanied by EL with the same spectral composition, but the anodic EL is characterized by much longer rise and fall times (Fig. 2). A typical feature of this regime is a substantial decrease of the degradation of EL (inset in Fig. 2). In our opinion, the liberation of hydrogen during cathodic polarization of the electrode and hydrogen adsorption by the surface of microcrystallites play a definite role in decreasing the degradation of the EL. During the next anodic current pulse a substantial fraction of the atomic oxygen formed is expended on removal of adsorbed hydrogen in the reaction (6a) and not on oxidation of the surface. Next, the cathodic current pulse restores the layer of chemisorbed hydrogen atoms and the entire sequence of processes is repeated. Thus, blocking of the surface of microcrystallites by silicon oxides is largely averted and bipolar carrier injection into microcrystallites is maintained.

## 5. CONCLUSIONS

A model explaining the appearance of intense anodic electroluminescence of porous silicon in contact with electrolytes was proposed. It was shown that when current flows through the interface of the silicon substrate with the electrolyte, atomic hydrogen and oxgyen, which with respect to porous silicon are effective electron donors and acceptors, accumulate in the electrolyte. Diffusing into the electrolyte, they are adsorbed on the surface of the microcrystallites porous silicon and give rise to bipolar injection of charge carriers into them. Subsequent recombination of these carriers serves as a source of visible electroluminescence. The detailed mechanism of physicochemical processes leading to the appearance of luminescence was identified and explained. It was shown that the degradation of electroluminescence of porous silicon can be reduced substantially.

This work was supported by the Russian Fund for Fundamental Research (Grant 96-02-17903), the program ‘‘Physics of solid-state nanostructures’’ sponsored by the Ministry of Science (Projects 96-1012 and 97-1035), and also INTAS (Grant 93-3325-2-ext).

[a] Fax: (812)2471017; e-mail: dng@olgas.ioffe.rssi.ru

---

[1] P. M. M. Bressers, J. W. J. Knaper, E. A. Meulenkamp, and J. J. Kelly, Appl. Phys. Lett. **61**, 108 (1992).
[2] L. T. Canham, W. Y. Leong, M. I. J. Beale, T. I. Cox, and L. Taylor, Appl. Phys. Lett. **61**, 2563 (1992).
[3] D. N. Goryachev, O. M. Sreseli, and I. D. Yaroshetskiĭ, Fiz. Tekh. Poluprovodn. **27**, 1815 (1993) [Semiconductors **27**, 999 (1993)].
[4] A. Halimaoui, C. Oules, G. Bomchil, A. Bsiesy, F. Gaspard, R. Herino, M. Ligeon, and F. Muller, Appl. Phys. Lett. **59**, 304 (1991).
[5] P. C. Searson, S. M. Prokes, and O. J. Glembocki, J. Electrochem. Soc. **140**, 3327 (1993).
[6] D. N. Goryachev, O. M. Sreseli, and L. V. Belyakov, Fiz. Tekh. Poluprovodn. **31**, 1383 (1997) [Semiconductors **31** 716 (1997)].
[7] O. Sreseli, D. Goryachev, G. Polisski, L. Belyakov, and F. Koch, in *Pits and Pores: Formation, Properties and Significance for Advanced Luminescent Materials*, edited by D. J. Lockwood, P. Schmuki and A. Bsiesy, Pennington, N.J., Electrochemical Society Inc., 1997, **PV97-7**, p. 184.
[8] L. T. Canham, Appl. Phys. Lett. **57**, 1046 (1990).
[9] O. M. Sreseli, G. Polisski, D. Kovalev, D. N. Goryachev, L. V. Belyakov, and F. Koch, in *Advanced Luminescent Materials*, edited by D. J. Lockwood, P. M. Fauchet, N. Koshida and S. R. J. Brueck, Pennington, NJ, Electrochemical Society Inc., 1995, **PV95-25**, p. 24.
[10] D. N. Goryachev, O. M. Sreseli, and L. V. Belyakov, Pis'ma Zh. Tekh. Fiz. **23**, 58 (1997) [Tech. Phys. Lett. **23**, 35 (1997)].
[11] M. Ligeon, F. Muller, R. Herino, F. Gaspard, J. C. Vial, R. Romestain, S. Billat, and A. Bsiesy, J. Appl. Phys. **74**, 1264 (1993).
[12] M. I. J. Beale, N. I. Cox, L. T. Canham, and D. Brumhead, in *Microcrystalline Semiconductors: Materials Science and Devices*, edited by P. M. Fauchet *et al.*, Pittsburg, Pa., 1993 [MRS Proc., **283**, 377 (1993)].
[13] A. Bsiesy, M. A. Hory, F. Gaspard, R. Herino, M. Ligeon, F. Muller, R. Rommestain, and J. C. Vial, in *Microcrystalline and Nanocrystalline Semiconductors*, Pittsburg, Pa., 1995 [MRS Proc., **358**, 619 (1995)].
[14] V. A. Myamlin and Yu. V. Pleskov, *Electrochemistry of Semiconductors*, Plenum Press, N. Y., 1967 [Russian original, Nauka, Moscow, 1965].
[15] S. O. Izidinov, A. P. Blokhina, and L. A. Ismaĭlova, Elektrokhimiya **24**, 1220 (1988).
[16] Y. Kang and J. Jorne, J. Electrochem. Soc. **144**, 3104 (1997).
[17] D. Dobos, *Electrochemical Data*, Academiai Kiado, Budapest, 1977 [Russian trans., Mir, Moscow, 1980].
[18] L. V. Belyakov, D. N. Goryachev, D. I. Kovalev, F. Kokh, V. Petrova-Kokh, O. M. Sreseli, and I. D. Yaroshetskiĭ, Fiz. Tekh. Poluprovodn. **29**, 1288 (1995) [Semiconductors **29**, 667 (1995)].
[19] S. R. Morrison, *The Chemical Physics of Surfaces*, Plenum Press, N. Y., 1977 [Russian trans., Mir, Moscow, 1980].
[20] A. Halimaoui, Appl. Phys. Lett. **63**, 1264 (1993).
[21] A. Bsiesy, F. Muller, M. Ligeon, F. Gaspard, K. Herino, R. Romestain, and J. C. Vial, Phys. Rev. Lett. **71**, 637 (1993).

Translated by M. E. Alferieff

SEMICONDUCTORS VOLUME 32, NUMBER 5 MAY 1998

## LOW DIMENSIONAL SYSTEMS

# Transport properties of magnetoexcitons in coupled quantum wells

Yu. E. Lozovik

*Institute of Spectroscopy, Russian Academy of Sciences, 142092 Troitsk*

A. M. Ruvinskiĭ

*Department of Theoretical Physics, Moscow State Institute of Steels and Alloys, 117936 Moscow, Russia*

(Submitted July 28, 1997; accepted for publication September 16, 1997)
Fiz. Tekh. Poluprovodn. **32**, 596–601 (May 1998)

The transport times $\tau(P)$ and the mean free paths of magnetoexcitons in a quantum well and of spatially direct and indirect magnetoexcitons in coupled quantum wells in a random potential produced by thickness fluctuations of the quantum wells or a random distribution of impurity centers in quantum wells ($P$ is the magnetic momentum of an exciton) are calculated. The function $\tau(P)$ is nonmonotonic, but as the distance $D$ between the quantum wells increases, the maximum $\tau_{\max}(P)$ gradually vanishes in the presence of scattering by surface terraces. As the magnetic field ($H$) increases, $\tau(0)$ decreases as $1/\sqrt{H}$ for $D \ll l$ ($l=\sqrt{\hbar c/eH}$ is the magnetic length) and as $1/H^2$ for $D \gg l$. The behavior of the computed values of $\tau$ for large $H$ agrees qualitatively with the experimental data. The mean free path length of a magnetoexciton exhibits at $P \neq 0$ a maximum whose magnitude decreases as the parameter $D/l$ increases. *© 1998 American Institute of Physics.* [S1063-7826(98)01805-5]

## 1. INTRODUCTION

In recent years low-dimensional semiconductor structures — dots and wires — have aroused a great deal of interest (see Refs. 1–3 and the literature cited there). Electron-hole systems in coupled quantum wells (CQWs) are attracting special attention because of the prediction of superfluidity[4–6] of indirect excitons, consisting of spatially separated electron ($e$) and hole ($h$), in them. In these systems superfluidity appears in the form of undamped electrical currents in each quantum well. These systems can also exhibit interesting effects due to entrainment of quasiparticles of one layer by quasiparticles of another layer.[7] A strong magnetic field increases the binding energy of two-dimensional (2D) magnetoexcitons[8,9] and can strongly influence the formation of the superfluid phase.

Other phases can also form in these systems.[6] Some of these phases are similar to those in three-dimensional excitonic systems.[10] They can exist if the exciton lifetime is much longer than the thermalization time. A sharp decrease of the lifetime of indirect excitons with increasing magnetic field $H$ for $H>7$ T has been observed experimentally[1] at low temperatures $T<1$ K. The exciton lifetime is determined by radiative and nonradiative recombination mechanisms. Excitons with electrons and holes in different quantum wells (QWs) are characterized by long recombination times as a result of the weak overlapping of the $e$ and $h$ wave functions. For this reason, the magnetoexciton lifetime under such conditions is in all likelihood determined by the transport time. We shall study the effect of impurity centers and surface nonuniformities, caused by fluctuations of the width (layer thickness) of $e$ and $h$ QWs, on the low-temperature transport properties of excitons in a single QW and in CQWs in a strong transverse magnetic field. The problem of the diffusion and localization of 2D excitons in the absence of a magnetic field was studied in Refs. 11–14. The transport properties of volume excitons were studied in Refs. 15 and 16. Magnetoexcitonic transport in double QWs was studied in Ref. 17.

In the present paper we shall show that the transport relaxation time $\tau$ of an indirect magnetoexciton depends strongly on the exciton magnetic momentum $\mathbf{P}$ and the distance $D$ between the $e$ and $h$ quantum wells. The transport relaxation time $\tau$ of magnetoexcitons in QWs and CQWs for small $D$ on surface terraces exhibits a maximum at a nonzero exciton momentum. As the parameter $D/l$ ($l=\sqrt{\hbar c/eH}$ is the magnetic length) increases, the maximum gradually decreases and then vanishes. As $H$ increases, $\tau$ decreases as $\tau \sim 1/\sqrt{H}$ for $D/l \ll 1$ and $P=0$ and as $\tau \sim 1/H^2$ for $D/l \gg 1$. The decrease of $\tau$ and the theoretically computed values of $\tau$ agree qualitatively with the experimental results obtained in Ref. 1 in high magnetic fields.

In Sec. 2 the transport relaxation times and mean free path of magnetoexcitons (MEs) in a single QW in a random potential produced by thickness fluctuations of the quantum well are calculated; in Sec. 3 the transport relaxation time and the mean free path of magnetoexcitons in CQW is calculated; in Sec. 4 the relaxation times and the mean free path of magnetoexcitons in a single QW and in CQWs in the field of randomly distributed impurity centers is calculated. In the last section of this paper we discuss the results which we obtained.

## 2. MAGNETOEXCITON IN A QUANTUM WELL. SCATTERING BY THE TERRACES OF A QUANTUM WELL

Thickness fluctuations of a QW, which arise during the fabrication process, result in the appearance of a random potential. The interaction between an exciton and such a random field has the form[11,14,17]

$$V(\mathbf{r}_e,\mathbf{r}_h)=\alpha_e[\xi_1(\mathbf{r}_e)-\xi_2(\mathbf{r}_e)]+\alpha_h[\xi_1(\mathbf{r}_h)-\xi_2(\mathbf{r}_h)], \tag{1}$$

where $\alpha_{e,h}=\partial E^{(0)}_{e,h}/\partial d$, $E^{(0)}_{h,e}$ are the lower energy levels of a hole and an electron in the valence band and in the conduction band, and $\xi_{1,2}(\mathbf{r})$ are the thickness fluctuations on the top and bottom surfaces of the QW. We assume that the fluctuations occurring on different surfaces are statistically independent, while fluctuations occurring on the same surface are described by a Gaussian correlation function

$$\langle\langle\xi_i(\mathbf{r}_1)\xi_j(\mathbf{r}_2)\rangle\rangle=\delta_{ij}\Delta_i^2\exp\left[-\frac{(\mathbf{r}_1-\mathbf{r}_2)^2}{3\Lambda_i^2}\right]. \tag{2}$$

In what follows we shall study strong transverse magnetic fields $l\ll a_{e,h}$ ($a_{e,h}=\varepsilon\hbar^2/m_{e,h}e^2$ are the effective electron and hole Bohr radii, $\varepsilon=(\varepsilon_1+\varepsilon_2)/2$, $\varepsilon_{1,2}$ are the permittivities of the media surrounding the $e$- and $h$-QWs) and thin quantum wells, whose thickness $d$ satisfies the inequalities $d^2\ll a_{e,h}l$ and $\Delta_i\ll d$. The quantity $\Delta_i$ corresponds to the thickness of one monolayer and equals $\sim 3$ Å (see Ref. 18 and the literature cited there). The value of $\Lambda_i$ depends strongly on the method used to prepare the QW.[19] Depending on the value of $\Lambda_i/r_{\text{exc}}$ ($r_{\text{exc}}$ is the size of an exciton in the plane of the QW; in a strong electric field $r_{\text{exc}}\sim l$ (Refs. 8 and 9), two characteristic transport regimes can be distinguished. For $\Lambda_i\gg r_{\text{exc}}$ excitons become localized in a region of size $\Lambda_i$ at the minimum of the random potential. Zero-dimensional excitonic states,[18] similar to states in quantum dots,[20,21] form here. In the latter case exciton transport is apparently thermally activated with hopping between states at the minima of the potential well of different quantum dots.[12] In the present paper we shall examine the opposite case $\Lambda_i\ll r_{\text{exc}}$, i.e., a smooth surface potential, which, as shown in Refs. 18 and 22 with the aid of scanning tunneling microscopy, is realized at the boundaries of the intensely investigated AlGaAs–GaAs structures. The condition for the random potential to be smoth can be expressed more rigorously in the form[23]

$$r_{\text{exc}}\sqrt{\langle\langle\nabla V^2\rangle\rangle}\ll E_I, \tag{3}$$

where $E_I$ is the exciton ionization energy. We obtain from Eq. (3)

$$\Lambda\gg\frac{a^z_{e,h}l^2\Delta}{d^3}\sqrt{2\pi^3} \tag{4}$$

for $D\ll l$ and

$$\Lambda\gg\frac{a^z_{e,h}lD\Delta}{d^3}\sqrt{2\pi^3} \tag{5}$$

for $D\gg l$ ($a^z_{e,h}=\varepsilon\hbar^2/m^z_{e,h}e^2$ is the effective Bohr radius of $e$ and $h$ in the $z$ direction, perpendicular to the QW plane). We note that since in strong magnetic fields the radius of an exciton decreases as $l\sim\sqrt{H}$, the magnetoexciton transport regime can change as $H$ increases.

The transport relaxation time of excitons will be calculated in the Born approximation, which is valid for $\hbar^2/M(D/l)\Lambda^2\gg\Delta\hbar^2/\pi^2 m^z_{e,h}d^3_{e,h}$, i.e., if

$$\pi\sqrt{\frac{d^3_{e,h}}{\Delta}\frac{m^z_{e,h}}{M(D/l)}}\gg\Lambda. \tag{6}$$

As $D$ or $H$ increases, the magnetoexciton effective mass $M(D/l)$ increases,[8,9] decreasing the upper limit of $\Lambda$. The magnetoexciton ionization energy decreases with increasing $D$, increasing the lower limit of $\Lambda$, and it increases with $H$, decreasing the lower limit.

The transport relaxation time of an exciton is given in the Born approximation by the expression[14,16,17]

$$\tau^{-1}(P)=\frac{2\pi}{\hbar}\sum_{P'}\langle\langle|\langle P'|V(\mathbf{r}_e,\mathbf{r}_h)|P\rangle|^2\rangle\rangle \times[1-\cos(\phi_{PP'})\delta[\mathscr{E}(P)-\mathscr{E}(P')]], \tag{7}$$

where $\mathscr{E}(P)$ corresponds to the magnetoexciton dispersion law in a QW at the lower Landau level $n=m=0$:[8]

$$\mathscr{E}(P)=\frac{1}{2}\hbar\omega_c-\frac{e^2}{\varepsilon l}\sqrt{\frac{\pi}{2}}I_0\left(\frac{P^2l^2}{4\hbar^2}\right)\exp\left(-\frac{P^2l^2}{4\hbar^2}\right), \tag{8}$$

where $\omega_c=eH/\mu c$ is the cyclotron frequency, $\mu=m_em_h/(m_e+m_h)$ is the reduced mass of a magnetoexciton in the QW plane, $P$ is the exciton magnetic momentum, and $I_0(x)$ is a zero-order modified Bessel function. The matrix element (1) of the transition from the state $\langle n=m=0,\mathbf{P}|$ into the state $\langle n=m=0,\mathbf{P}'|$ is

$$\begin{aligned}\langle\mathbf{P}'|V(\mathbf{r}_e,\mathbf{r}_h)|\mathbf{P}\rangle&=\frac{1}{S}\exp[-(\mathbf{P}'-\mathbf{P})^2l^2/4\hbar^2]\\&\times\{V_e(\mathbf{P}'-\mathbf{P})\exp(il^2\mathbf{H}[\mathbf{P},\mathbf{P}']/2\hbar H)\\&+V_h(\mathbf{P}'-\mathbf{P})\exp(-il^2\mathbf{H}[\mathbf{P},\mathbf{P}']/2\hbar^2H)\}\end{aligned} \tag{9}$$

($S$ is the area of the QW). Then

$$\begin{aligned}&\langle\langle|\langle\mathbf{P}'|V(\mathbf{r}_e,\mathbf{r}_h)|\mathbf{P}\rangle|^2\rangle\rangle\\&=\frac{\pi}{2S}\{\alpha_e^2+\alpha_h^2+2\alpha_e\alpha_h\cos(l^2[\mathbf{P},\mathbf{P}']/\hbar^2)\}\\&\times\sum_{i=1,2}\exp\{-(\mathbf{P}'-\mathbf{P})^2l^2\beta_i/2\hbar^2\}(\Delta_i\Lambda_i)^2.\end{aligned} \tag{10}$$

Substituting the expression (7) into Eq. (4), we obtain an expression for the magnetoexciton transport relaxation time in the QW

$$\tau^{-1}(P)=\tau_e^{-1}(P)+\tau_h^{-1}(P)+\tau_{eh}^{-1}(P), \tag{11}$$

where

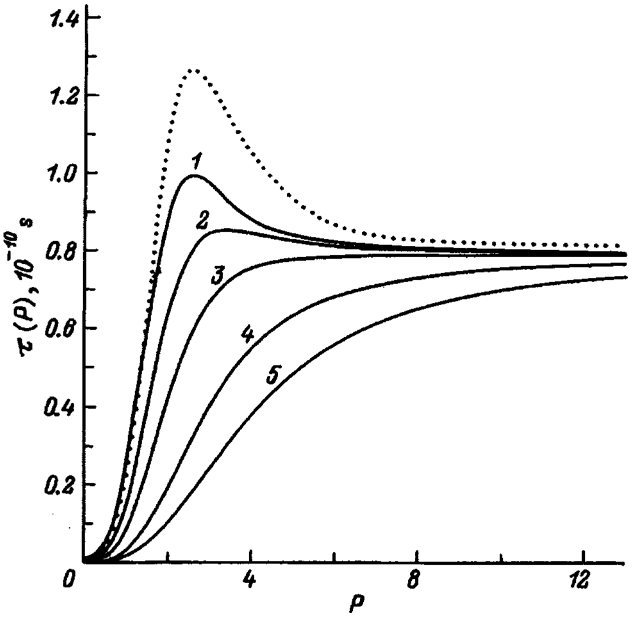

FIG. 1. Direct (dotted line) and indirect (solid lines) magnetoexciton transport relaxation time due to surface terraces in coupled quantum wells as a function of the magnetic momentum $P$ (in units $\hbar/l$) for $H=2\times10^5$ Oe. The curves *1–5* correspond to different distances between the $e$ and $h$ quantum wells $D/l=0.1$, 0.5, 1, 2, 3.

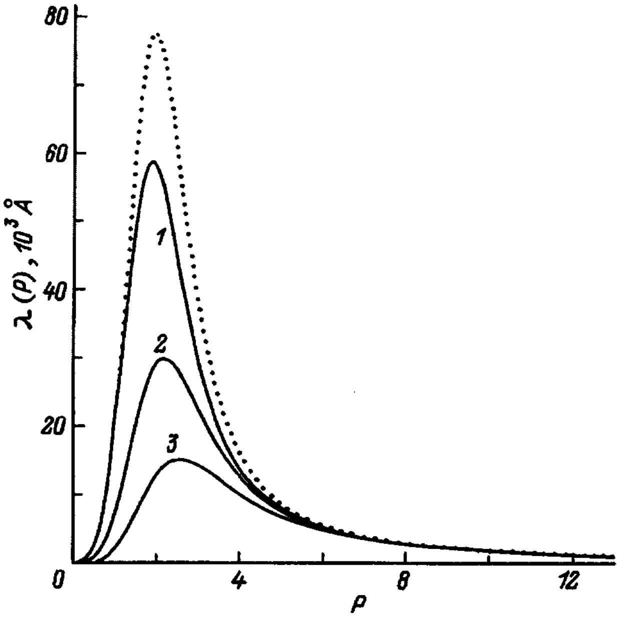

FIG. 2. Average mean free path length of direct (dotted lines) and indirect (solid lines) magnetoexcitons taking account of scattering by surface terraces in coupled quantum wells as a function of the magnetic momentum $P$ (in units of $\hbar/l$) with $H=2\times10^5$ Oe. The curves *1–3* correspond to $D/l=0.1$, 0.5, and 1.

$$\tau_{e,h}^{-1}=\frac{\pi}{4\hbar^3}\left|\frac{\partial\mathscr{E}(P)}{\partial P^2}\right|^{-1}\alpha_{e,h}^2\sum_{i=1,2}(\Delta_i\Lambda_i)^2\exp(-P^2l^2\beta_i/\hbar^2)\times[I_0(P^2l^2\beta_i/\hbar^2)-I_1(P^2l^2\beta_i/\hbar^2)] \tag{12}$$

and

$$\tau_{eh}^{-1}(P)=\frac{\pi\alpha_e\alpha_h}{2\hbar^3}\left|\frac{\partial\mathscr{E}(P)}{\partial P^2}\right|^{-1}\sum_{i=1,2}(\Delta_i\Lambda_i)^2\times\exp(-P^2l^2\beta_i/\hbar^2)\left\{I_0(P^2l^2\sqrt{\beta_i^2-1}/\hbar^2)-\frac{\beta_i}{\sqrt{\beta_i^2-1}}I_1(P^2l^2\sqrt{\beta_i^2-1}/\hbar^2)\right\}, \tag{13}$$

where $\beta_i=1+\Lambda_i^2/l^2$, and $I_1(x)$ is a first-order modified Bessel function. For $l\ll a_{e,h}$ and $d^2\ll a_{e,h}l$ taking account of the $e$ and $h$ motion along the magnetic field does not produce any qualitative changes in the magnetoexcitonic spectrum,[8,9] so that we assume, similarly to Ref. 14, that $\alpha_{e,h}=-\pi^2\hbar^2/m_{e,h}^zd^3$.

Figure 1 shows the magnetoexciton transport scattering time in a GaAs/Al$_x$Ga$_{1-x}$As quantum well. The following parameter values were used in the calculation: $d=40$ Å, $\Lambda_1=10$ Å, $\Lambda_2=3$ Å, $\Lambda_1=\Lambda_2=3$ Å, electron and hole effective masses in AlAs(GaAs), according to Ref. 24, are $m_e^z=1.1(1.3)$ and $m_h^z=0.75(0.34)$. For $P=2.6\hbar/l$ a maximum of $\tau(P)$ is observed. The asymptotic relaxation times (11) are

$$\tau(P)=\frac{\hbar e^2l}{\sqrt{2\pi}\varepsilon}\frac{1}{(\alpha_e+\alpha_h)^2}\times\begin{cases}[(\Delta_1\Lambda_1)^2+(\Delta_2\Lambda_2)^2]^{-1}, & P=0,\\ 8[(\Delta_1\Lambda_1)^2/\beta_1^{3/2}+(\Delta_2\Lambda_2)^2/\beta_2^{3/2}]^{-1}, & Pl/\hbar\gg1.\end{cases}$$

We shall calculate the magnetoexciton mean free path as $\lambda(P)=\nu(P)\tau(P)$ (Fig. 2), where $\nu(P)=\partial\mathscr{E}(P)/\partial P$. We note that for $P=0$ we have $\lambda(0)=0$ $(\nu(0)=0)$, while for $Pl/\hbar\gg1$ we obtain

$$\lambda(P)=\frac{4\sqrt{2}\hbar^2e^4}{\sqrt{\pi}\varepsilon^2P^2l}\frac{1}{(\alpha_e+\alpha_h)^2}\left[\frac{(\Delta_1\Lambda_1)^2}{\beta_1^{3/2}}+\frac{(\Delta_2\Lambda_2)^2}{\beta_2^{3/2}}\right]^{-1}. \tag{14}$$

In the regions $Pl/\hbar\ll1$ and $Pl/\hbar\gg1$ the magnetoexciton mean free path is less than or comparable to the correlation length $\Lambda$. This indicates that MEs tend to localize in such states (the problem of the localization of magnetoexcitons in random fields in CQWs will be examined elsewhere).

## 3. MAGNETOEXCITON IN COUPLED QUANTUM WELLS. SCATTERING BY TERRACES OF ELECTRON AND HOLE QUANTUM WELLS

The interaction of an exciton, whose electron and hole are located in different spatially separated quantum wells, with a random field produced by thickness fluctuations of the $e$- and $h$-QWs is

$$V(\mathbf{r}_e,\mathbf{r}_h)=\alpha_e[\xi_1(\mathbf{r}_e)-\xi_2(\mathbf{r}_e)]+\alpha_h[\xi_3(\mathbf{r}_h)-\xi_4(\mathbf{r}_h)], \tag{15}$$

where $\alpha_{e,h}=\partial E_{e,h}^{(0)}/\partial d_{e,h}$ and $\xi_i(\mathbf{r})$ are the thickness fluctuations at the top and bottom surfaces of the electron and hole QWs. We once again that the fluctuations on different surfaces of a QW are statistically independent, and that the fluctuations on the same surface are described by the Gaussian correlation function (2). This is possible if the distance $D$

between the $e$- and $h$-QWs is greater than the thickness fluctuations of the $e$- and $h$-QWs on the nearest surfaces.1)

$$\langle\langle|\langle \mathbf{P}'|V(\mathbf{r}_e,\mathbf{r}_h)|\mathbf{P}\rangle|^2\rangle\rangle$$
$$=\frac{\pi}{2S}\Bigg\{\alpha_e^2\sum_{i=1,2}\exp[-(\mathbf{P}'-\mathbf{P})^2l^2\beta_i/2\hbar^2](\Delta_i\Lambda_i)^2$$
$$+\alpha_h^2\sum_{i=3,4}\exp[-(\mathbf{P}'-\mathbf{P})^2l^2\beta_i/2\hbar^2](\Delta_i\Lambda_i)^2\Bigg\}. \tag{16}$$

Substituting the expression (16) into Eq. (7), we obtain the magnetoexciton relaxation time in the coupled quantum wells

$$\tau^{-1}(P,D)=\tau_e^{-1}(P,D)+\tau_h^{-1}(P,D), \tag{17}$$

where

$$\tau_{e,h}^{-1}(P,D)=\frac{\pi}{4\hbar^3}\left|\frac{\partial\mathscr{E}(P,D)}{\partial P^2}\right|^{-1}\alpha_{e,h}^2$$
$$\times\sum_{i=1,2(3,4)}(\Delta_i\Lambda_i)^2\exp(-P^2l^2\beta_i/\hbar^2)$$
$$\times[I_0(P^2l^2\beta_i/\hbar^2)-I_1(P^2l^2\beta_i/\hbar^2)], \tag{18}$$

$D$ is the distance between the $e$- and $h$-QWs, $\mathscr{E}(P,D)$ is the energy of a magnetoexciton in the $n=m=0$ level in coupled quantum wells (see Ref. 9)

$$\mathscr{E}(\mathscr{P},\mathscr{D})=\frac{1}{2}\hbar\omega_c-\frac{e^2}{\varepsilon l}\frac{1}{\sqrt{2}}f(\mathscr{D},\mathscr{P}), \tag{19}$$

$$f(\mathscr{P},\mathscr{D})=\sum_{k=0}^{\infty}P_{2k}(g)\frac{(-1)^k(2k)!}{2^{2k}(k!)^2}$$
$$\times\left\{\left(\frac{2}{(\mathscr{D}^2+\mathscr{P}^2)}\right)^{k+1/2}\gamma\left(k+1,\frac{\mathscr{D}^2+\mathscr{P}^2}{2}\right)\right.$$
$$\left.+\left(\frac{\mathscr{D}^2+\mathscr{P}^2}{2}\right)^k\Gamma\left(-k+\frac{1}{2},\frac{\mathscr{D}^2+\mathscr{P}^2}{2}\right)\right\}, \tag{20}$$

where $\mathscr{D}=D/l$, $\mathscr{P}=Pl/\hbar$, $g=[1+(\mathscr{P}/\mathscr{D})^2]^{-1/2}$, $\Gamma(a,x)$ is the complete gamma function, $\gamma(a,x)$ is the incomplete gamma function, and $P_k(x)$ is a Legendre polynomial. Figure 1 shows the computational results obtained for the relaxation time using Eqs. (17) and (18) for an indirect magnetoexciton, which consists of an electron in an AlAs QW and a hole in a GaAs QW. The parameters of the $e$- and $h$-QWs are identical to the parameters employed for calculating the relaxation time of a direct magnetoexciton (see Sec. 2).

In the momentum range $Pl/\hbar\ll 1$ we find

$$\tau(0,D)=\frac{2\hbar^3}{\pi}\frac{1}{M(D/l)}$$
$$\times\frac{1}{\alpha_e^2\sum_{i=1,2}(\Delta_i\Lambda_i)^2+\alpha_h^2\sum_{i=3,4}(\Delta_i\Lambda_i)^2}, \tag{21}$$

where

$$M(D/l)=\frac{M_0}{(1+\mathscr{D}^2)\exp(\mathscr{D}^2/2)\operatorname{erfc}(\mathscr{D}/\sqrt{2})-\mathscr{D}\sqrt{2/\pi}} \tag{22}$$

is the effective mass of an indirect magnetoexciton in the state $n=m=0$ in CQWs (see Ref. 9), and $M_0=2^{3/2}\varepsilon\hbar^2/e^2l\sqrt{\pi}$ is the mass of a direct magnetoexciton.[8] The relaxation time (21) decreases with increasing magnetic field as $\sim 1/\sqrt{H}$ in the case $D\ll l$ and as $\sim 1/H^2$ in the case $D\gg l$, in agreement with experimentally observed times.[1] In the momentum ranges $Pl/\hbar\gg 1$ and $PD/\hbar\gg 1$ the magnetoexciton dispersion has the form[9] $\mathscr{E}\simeq -e^2\hbar/\varepsilon Pl^2$. Therefore, for large magnetic momenta the relaxation time

$$\tau\simeq\frac{4\sqrt{2}\hbar e^2 l}{\varepsilon\sqrt{\pi}}\left[\alpha_e^2\sum_{i=1,2}\frac{(\Delta_i\Lambda_i)^2}{\beta_i^{3/2}}+\alpha_h^2\sum_{i=3,4}\frac{(\Delta_i\Lambda_i)^2}{\beta_i^{3/2}}\right]^{-1} \tag{23}$$

does not depend on $P$ and $D$ and decreases with increasing magnetic field as $\sim 1/\sqrt{H}$. As the distance $D$ between the quantum wells increases, the magnitude of the peak ($\tau_{\max}$) decreases, and for $D$ exceeding some critical value the function $\tau(P)$ becomes monotonically increasing (Fig. 1). The $P$ and $D$ dependences of the mean free path are shown in Fig. 2. Because of the quadratic dependence (19) on the magnetic momentum for $Pl/\hbar\ll 1$ we have $\nu(0,D)=0$ and therefore $\lambda(0,D)=0$. For $Pl/\hbar\gg 1$ we obtain $\lambda\sim 1/P^2$. As the parameter $D/l$ increases, the magnitude of the peak $\lambda(P,D)$ decreases.

## 4. IONIZED IMPURITIES IN COUPLED QUANTUM WELLS

Let us consider the case where the Coulomb impurities $q_1$ and $q_2$ with densities $n_1$ and $n_2$ are distributed randomly in electron and hole quantum wells. The interaction of an exciton with the impurities in CQWs is described by the potential

$$V(\mathbf{r}_e,\mathbf{r}_h)=V_e(\mathbf{r}_e)+V_h(\mathbf{r}_h), \tag{24}$$

where

$$V_e(\mathbf{r}_e)=\sum_i\frac{-eq_1}{\varepsilon|\mathbf{r}_e-\mathbf{r}_i|}+\sum_j\frac{-eq_2}{\varepsilon\sqrt{(\mathbf{r}_e-\mathbf{r}_j)^2+D^2}}, \tag{25}$$

$$V_h(\mathbf{r}_h)=\sum_i\frac{eq_1}{\varepsilon\sqrt{(\mathbf{r}_h-\mathbf{r}_i)^2+D^2}}+\sum_j\frac{eq_2}{\varepsilon|\mathbf{r}_h-\mathbf{r}_j|}. \tag{26}$$

The impurity centers $q_1$ and $q_2$ occupy in the CQWs the positions $\mathbf{r}_i$ and $\mathbf{r}_j$, respectively. For $D=0$ all impurities are located in the same QW. The matrix element of the exciton-impurity interaction (24) is

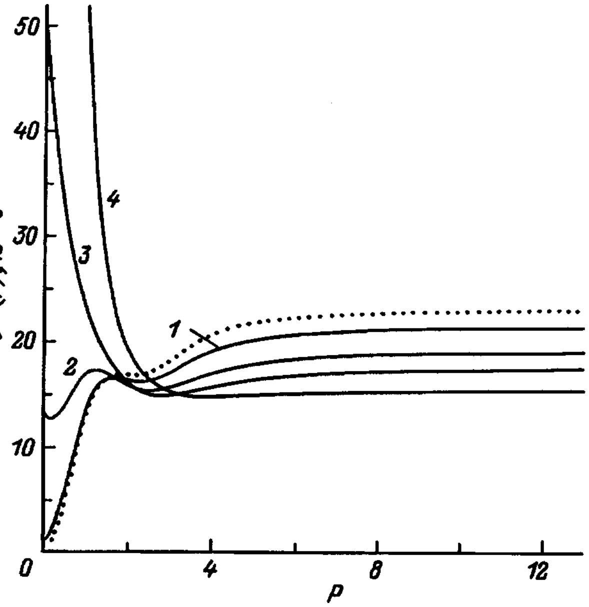

FIG. 3. Reciprocal of the direct (dotted line) and indirect (solid lines) magnetoexciton transport relaxation time due to impurities in coupled quantum wells as a function of the magnetic momentum $P$ (in units $\hbar/l$) for $H=2\times10^5$ Oe. Curves *1–4* correspond to $D/l=0.1$, 0.3, 0.5, and 1 and impurity densities $c_1=c_2=2\times10^{10}$ cm$^{-2}$.

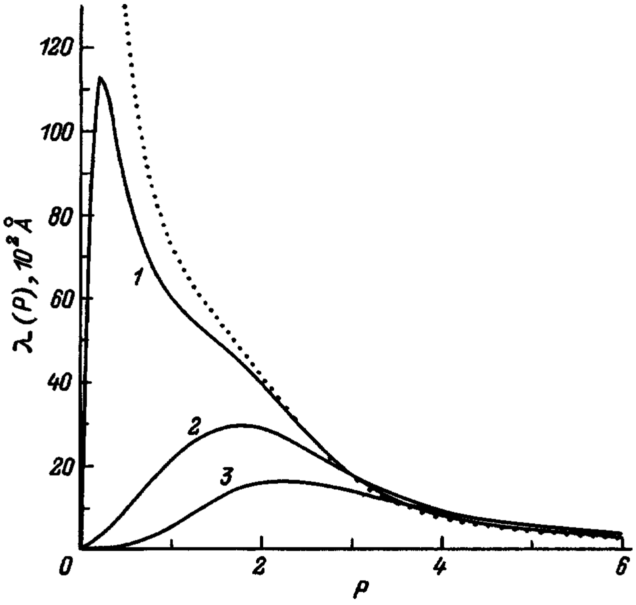

FIG. 4. Average mean free path length of direct (dotted lines) and indirect (solid lines) magnetoexcitons taking account of scattering by impurities in coupled quantum wells as a function of the magnetic momentum $P$ (in units of $\hbar/l$) with $H=2\times10^5$ Oe. The curves *1–3* correspond to $D/l=0.1$, 0.5, and 1 and impurity densities $c_1=c_2=2\times10^{10}$ cm$^{-2}$.

$$\langle\langle|\langle\mathbf{P}'|U(\mathbf{r}_e,\mathbf{r}_h)|\mathbf{P}\rangle|^2\rangle\rangle=\exp\left[-\frac{(\mathbf{P}'-\mathbf{P})^2l^2}{2\hbar^2}\right]\times\left(\frac{2\pi\hbar e}{\mathbf{P}'-\mathbf{P}}\right)^2\frac{n_1q_1^2+n_2q_2^2}{S\varepsilon^2}\times\left\{1+\exp\left(-\frac{2D|\mathbf{P}'-\mathbf{P}|}{\hbar}\right)-2\exp\left(-\frac{D|\mathbf{P}'-\mathbf{P}|}{\hbar}\right)\times\cos\left(\frac{[\mathbf{P},\mathbf{P}']l^2}{\hbar^2}\right)\right\}. \qquad (27)$$

Using Eqs. (7) and (27), we find the magnetoexciton relaxation time

$$\frac{1}{\tau_i(P,D)}=\frac{\pi}{2\hbar}\left(\frac{e}{\varepsilon^2P}\right)^2\left|\frac{\partial\mathscr{E}(P,D)}{\partial P^2}\right|^{-1}\exp\left(-\frac{P^2l^2}{\hbar^2}\right)\times(n_1q_1^2+n_2q_2^2)\int_0^{2\pi}\exp\left(\frac{P^2l^2\cos\phi}{\hbar^2}\right)\times\left[1+\exp\left(-\frac{2PD\sqrt{2-2\cos\phi}}{\hbar}\right)-2\exp\left(-\frac{PD\sqrt{2-2\cos\phi}}{\hbar}\right)\times\cos\left(\frac{P^2l^2}{\hbar^2}\sin\phi\right)d\phi\right]. \qquad (28)$$

Figure 3 shows the $P$ and $D$ dependences of the relaxation time, which is described by the expression (28). For $P=0$ we obtain the following expression from Eq. (28):

$$\tau_i(0,D)=\frac{\hbar^3}{4\pi^2}\frac{\varepsilon^2}{e^2D^2M(D/l)}\frac{1}{(n_1q_1^2+n_2q_2^2)}. \qquad (29)$$

The divergence in Eq. (29) in the limits $P\to0$ and $D\to0$ is caused by the use of an unscreened $e(h)$–impurity interaction potential. As $D$ increases, the time $\tau_i(0,D)$ decreases more rapidly than $\tau(0,D)$. For $Pl/\hbar\gg1$ and $PD/\hbar\gg1$ the transport relaxation time does not depend on $P$ and $D$:

$$\tau_i\simeq\frac{\hbar\varepsilon}{\sqrt{2}\pi^{3/2}l(n_1q_1^2+n_2q_2^2)}. \qquad (30)$$

Figure 4 shows the magnetoexciton mean free path in the field produced by impurities randomly distributed in the CQWs. As $D/l$ increases, the maximum of $\lambda_i(P,D)$ gradually decreases.

## 5. CONCLUSIONS

We have examined The low-temperature transport properties of an exciton whose electron and hole occupy the same GaAs/Al$_x$Ga$_{1-x}$As quantum well or in different spatially separated quantum wells in a strong transverse magnetic field. The transport relaxation times of the direct and indirect magnetoexcitons in the presence of scattering by surface terraces and impurity centers in CQWs were calculated in the Born approximation. The relaxation time of a direct ME with momenta $Pl/\hbar\ll1$ is determined by scattering by surface terraces, since in this case the relaxation time on impurity ions $\tau_i\to\infty$ and $\tau(P)$ is a nonmonotonic function of $P$, exhibiting a maximum a the momentum$P=2.6\hbar/l$. As the distance $D$ between the $e$ and $h$ quantum wells or the magnetic field increases, in the presence of scattering by surface terraces the maximum of $\tau(P,D)$ decreases and then vanishes. At the same time, the transport relaxation time of an indirect magnetoexciton in a state with arbitrary $P$ decreases, in agreement with experiment.[1] For $D/l$ greater than a certain critical value, the relaxation time on surface terraces and impurities is a monotonically increasing function of $P$. The average mean free path of direct and indirect magnetoexcitons is a nonmonotonic function of $P$, which possess at $P \neq 0$ a maximum whose magnitude decreases as $D/l$ increases. The magnetoexciton mean free path in the presence of scattering by impurities is found to be an order of magnitude smaller than in the case of scattering by surface terraces.

This work was supported by the Russian Fund for Fundamental Research, INTAS, and the program ''Physics of solid-state nanostructures.''

[1)] The opposite case $D \ll \Delta$ obtains in double quantum wells. The case $D=0$ is studied in Ref. 17 .

---

[1] L. V. Butov, A. Zrenner, G. Abstreiter, G. Böhm, and G. Weigmann, Phys. Rev. Lett. **73**, 304 (1994).
[2] L. V. Butov, A. Zrenner, G. Abstreiter, A. V. Petinova, and K. Eberl, Phys. Rev. B **52**, 12 153 (1995).
[3] M. Bayer, V. B. Timofeev, F. Faller, T. Gutbrod, and A. Forchel, Phys. Rev. B **54**, 8799 (1996).
[4] Yu. E. Lozovik and V. I. Yudson, JETP Lett. **22**, 274 (1975).
[5] Yu. E. Lozovik and V. I. Yudson, Zh. Éksp. Teor. Fiz. **71**, 738 (1976) [Sov. Phys. JETP **44**, 389 (1976)].
[6] Yu. E. Lozovik and O. L. Berman, Zh. Éksp. Teor. Fiz. **111**, 1879 (1997) [J. Exp. Theor. Phys. **84**, 1027 (1997)].
[7] Yu. E. Lozovik and M. V. Nikitkov, Zh. Éksp. Teor. Fiz. **111**, 1107 (1997) [J. Exp. Theor. Phys. **84**, 612 (1997)].
[8] I. V. Lerner and Yu. E. Lozovik, Zh. Éksp. Teor. Fiz. **78**, 1167 (1980) [Sov. Phys. JETP **51**, 588 (1980)].
[9] Yu. E. Lozovik and A. M. Ruvinsky, Phys. Lett. A **227**, 271 (1997).
[10] L. V. Keldysh and A. N. Kozlov, Zh. Éksp. Teor. Fiz. **54**, 978 (1968) [Sov. Phys. JETP **27**, 1521 (1968)].
[11] Zh. S. Gevorkyan and Yu. E. Lozovik, Fiz. Tverd. Tela (Leningrad) **27**, 1800 (1985) [Sov. Phys. Solid State **27**, 1079 (1985)].
[12] T. Takagahara, Phys. Rev. B **31**, 6552 (1985).
[13] H. Hillmer, A. Forchel, S. Hansmann, M. Morohashi, E. Lopez, H. P. Meier, and K. Ploog, Phys. Rev. B **39** 10901 (1989).
[14] P. K. Basu and P. Ray, Phys. Rev. B **44**, 1844 (1991).
[15] A. I. Ansel'm and Yu. A. Firson, Zh. Éksp. Teor. Fiz. **1**, 151 (1995).
[16] V. M. Agranovich and M. D. Galanin, in *Electronic Excitation Energy Transfer in Condensed Matter, Series on Modern Problems in Condensed Matter Science*, Vol. 3, edited by V. M. Agranovich and A. A. Maradudin, North−Holland, Amsterdam, 1982, Chap. 5.
[17] A. B. Dzyubenko and G. E. W. Bauer, Phys. Rev. B **51**, 14 524 (1995).
[18] A. Zrenner, L. V. Butov, M. Hagn, G. Abstreiter, G. Böhm, and G. Weigmann, Phys. Rev. Lett. **72**, 3382 (1994).
[19] M. Tanaka and H. Sakaki, J. Cryst. Growth **81**, 153 (1987).
[20] V. Halonen, T. Chakraborty, and P. Pietiläinen, Phys. Rev. **45**, 5980 (1992).
[21] R. I. Dzhioev, B. P. Zakharchenya, E. L. Ivchenko, V. L. Korenev, Yu. G. Kusraev, N. N. Ledentsov, V. M. Ustinov, A. E. Zhukov, and A. F. Tsatsul'nikov, JETP Lett. **65**, 804 (1997).
[22] R. Grousson, V. Voliotis, N. Grandjean, J. Massies, M. Leroux, and C. Deparis, Phys. Rev. **55**, 5253 (1997).
[23] V. L. Bonch-Bruevich, I. P. Zvyagin, R. Kaĭper, A. G. Mironov, R. Enderlein, and B. Esser, *Electronic Theory of Disordered Semiconductors*, Nauka, Moscow, 1981, p. 125.
[24] B. Rejaei Salmassi and G. E. W. Bauer, Phys. Rev. B **39**, 1970 (1989).

Translated by M. E. Alferieff

SEMICONDUCTORS VOLUME 32, NUMBER 5 MAY 1998

# Electron tunneling between two-dimensional electronic systems in a heterostructure with a single doped barrier

V. G. Popov, Yu. V. Dubrovskiĭ, Yu. N. Khanin, and E. E. Vdovin

*Institute of Microelectronics Technology and Ultrapure Materials, Russian Academy of Sciences, 142432 Chernogolovka, Russia*

D. K. Maude and J.-C. Portal

*High Magnetic Field Laboratory, CNRS, 38042 Grenoble Cedex, France*

T. G. Andersson and J. Thordson

*Department of Physics, Chalmers University of Technology, Göteborg, Sweden*

(Submitted August 6, 1997; accepted for publication November 11, 1997)
Fiz. Tekh. Poluprovodn. **32**, 602–606 (May 1998)

Electron tunneling in a heterostructure with a single doped barrier was investigated. Analysis of the experimental data showed that all features in the tunneling conductance are due to electron tunneling between two-dimensional electron sheets which appear on different sides of the barrier as a result of ionization of impurities in the barrier. Electron transport between the two-dimensional electron sheets and three-dimensional contact regions does not introduce significant distortions in the measured tunneling characteristics. In such structures there is no current flow along the two-dimensional electron gas; such a current ordinarily makes it difficult to investigate tunneling between two-dimensional electronic systems in magnetic fields.
[S1063-7826(98)01905-X]

## INTRODUCTION

Tunneling spectroscopy is an effective method for investigating low-dimensional electronic systems. As the dimension of electronic systems decreases, new physical phenomena appear. These phenomena are manifested in the characteristic features of electron tunneling between such systems, specifically, it makes it possible to employ structures with low-dimensional electronic systems for practical applications. For example, resonance-tunneling diodes (RTDs), whose principle of operation is based on resonance tunneling between a three-dimensional electron gas and a two-dimensional electronic state in double-barrier heterostructures, are well known in microwave electronics.[1] It has been found that as the dimension of the emitter in a RTD decreases, the ratio of the peak resonance current to the background nonresonance current increases. This greatly improves the characteristics of RTDs.[2] Moreover, investigations of electron tunneling processes between two-dimensional systems (2D–2D tunneling) have revealed a number of new physical phenomena: tunneling between Landau levels with different indices,[3,4] tunneling between $\Gamma$ and $X$ valleys,[5] appearance of a tunneling pseudogap in the density of states at the Fermi levels of two-dimensional systems in a quantizing magnetic field.[6,7] 2D–2D tunneling has made it possible to investigate in greater detail electron tunneling processes with emission of optical phonons[8] and plasmons,[9] as well as nonparabolicity effects in two-dimensional systems.[10]

Tunneling between two-dimensional electronic systems has been investigated on two types of structures: 1) two quantum wells separated by a nondoped tunneling barrier[6,7] and 2) a heterostructure with a single doped barrier, in which two two-dimensional electron gases appeared on both sides of the barrier as a result of ionization of impurities in the barrier.[4,10] Structures with ohmic contacts to separate two-dimensional (2D) sheets were used in the experiments. This made it possible to investigate directly tunneling processes between 2D electronic systems. However, the measurement of the tunneling current in such structures in strong magnetic fields presents definite difficulties. Indeed, in these samples the contact regions are spatially separated from the tunneling region. In tunneling current measurements the two-dimensional electron gas (2DEG) plays the role of a series resistance. In a strong magnetic field, in the quantum Hall effect regime current flows through 2DEG along edge states and tunneling occurs between these states. Thus, in tunneling experiments in a strong magnetic field the area of the tunneling region depends strongly on the population of the Landau levels in parallel 2D sheets.

In the present work we investigated tunneling between 2D electronic systems in samples where current flow along a 2D sheet is excluded. The samples were produced on the basis of a heterostructure with a doped $Al_xGa_{1-x}As$ barrier bounded on both sides by weakly doped GaAs layers (spacers) which separate the barrier layer from the strongly doped $n^+$-GaAs contact regions. Enriched 2D sheets appeared on both sides of the barrier as a result of ionization of impurities in the barrier. Differential tunneling conductance measurements with different magnetic field orientations were performed on such samples. Analysis of the data obtained showed that all features of the tunneling conductance are due

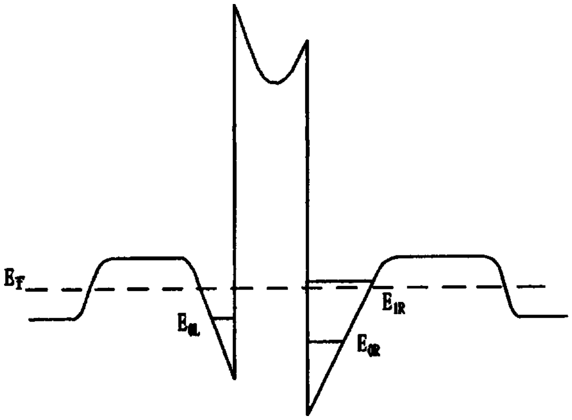

FIG. 1. Schematic diagram of the relief of the conduction-band bottom of the experimental heterostructure and system of quantum-well levels $E_{0L}$, $E_{0R}$, and $E_{1R}$ in enriched sheets; $E_F$ is the Fermi level.

to tunneling between 2D systems, while electron transport in the regions between the 2DEG and the three-dimensional contact regions contributes small perturbations to the measured tunneling characteristics.

## EXPERIMENTS AND DISCUSSION

The experimental samples were grown by molecular-beam epitaxy on strongly doped $n^+$-GaAs substrates and possessed the following sequence of layers:

200-nm-thick GaAs layer, $n^+=5\times10^{17}$ cm$^{-3}$ ;
200-nm-thick GaAs layer (spacer), $n^-=3\times10^{15}$ cm$^{-3}$;
10-nm-thick nondoped GaAs layer;
2-nm-thick nondoped $Al_{0.4}Ga_{0.6}As$ layer;
10-nm-thick $Al_{0.4}Ga_{0.6}As$ layer, $n^+=6\times10^{17}$ cm$^{-3}$;
2-nm-thick nondoped $Al_{0.4}Ga_{0.6}As$ layer;
10-nm-thick nondoped GaAs layer;
200-nm-thick GaAs layer (spacer), $n^-=3\times10^{15}$ cm$^{-3}$;
200-nm-thick GaAs layer, $n^+=5\times10^{17}$ cm$^{-3}$;
200-nm-thick GaAs contact layer, $n^+=3\times10^{18}$ cm$^{-3}$.

Ohmic contacts were produced by depositing Ni–Ge–Au systems followed by thermal annealing. The standard chemical etching technology was used to produce 50 $\mu$m in diameter mesa structures. The band structure of the enriched layers is shown schematically in Fig. 1

Peaks and a region of negative differential conductance were observed in the curve of the tunneling differential conductance versus the bias voltage (Fig. 2, curve *1*). We attribute these features to the appearance of resonance tunneling (RT), when the applied voltage aligns the energy position of the quantum levels in the enriched layers on different sides of the barrier. The peak of the differential conductance at $V_b=6$ mV is due to RT, when the level $E_{0L}$ lines up with the level $E_{0R}$ (0–0 transition), while the peak at $Vb=-14$ mV appears when $E_{0L}$ lines up with $E_{1R}$ (0–1 transition) (Fig. 1). It is assumed that the voltage drop on the spacers is small. The tunneling conductance measurements performed in magnetic fields with different orientations confirmed the correctness of this explanation.

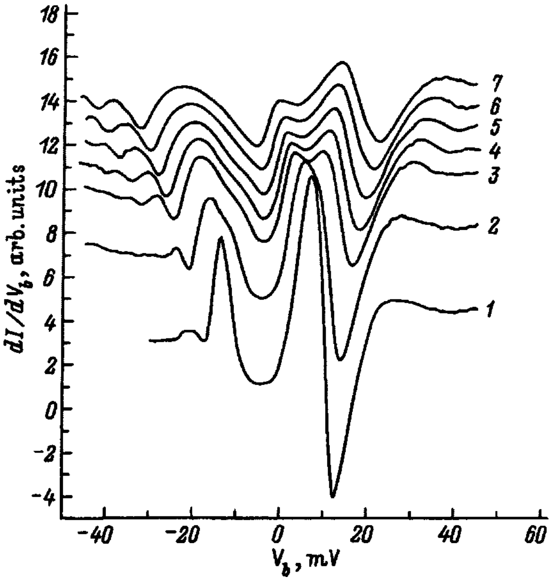

FIG. 2. Differential tunneling conductance $dI/dV_b$ versus bias voltage $V_b$ in a magnetic field perpendicular to the tunneling current. $B$, T: *1*—0, *2*—0.22, *3*—0.44, *4*—0.55, *5*—0.66, *6*—0.77, *7*—0.88. Curves *2–7* are shifted arbitrarily in the vertical direction.

Splitting of the peak due to a 0–0 transition and a shift of the peak due to a 0–1 transition were observed in a magnetic field **B**⊥**J** (**J** is the tunneling current density) (Fig. 2). The behavior of the resonance peaks in a magnetic field **B**⊥**J** has been studied quite well.[4,10] In Ref. 10 it was shown that the peaks due to resonances between filled 2D subbands split, while peaks due to RT via empty subbands broaden and shift in the direction of high bias voltages. To compare our experimental data for the 0–0 transition with the theory proposed in Ref. 4 , we presented in Fig. 3 the experimental and computed [obtained from the expressions (8) in Ref. 4] values of the external bias voltage, corresponding to falling ''into'' or ''out of'' resonance, depending on the magnetic field. The experimental values were obtained as follows: The experimental dependences $dI/dV_b=f(V_b)$ were integrated,

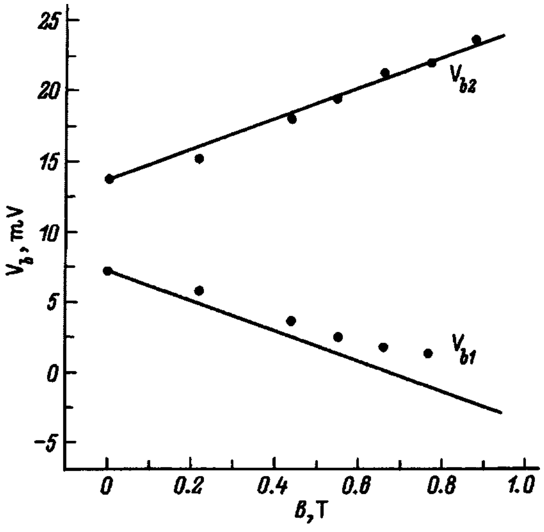

FIG. 3. Broadening of the resonance peak due to the 0–0 transition versus magnetic field $B$. The values of $V_{b1}$ correspond to the onset of resonance tunneling, while $V_{b2}$ corresponds to completion of tunneling. The details are discussed in the text.

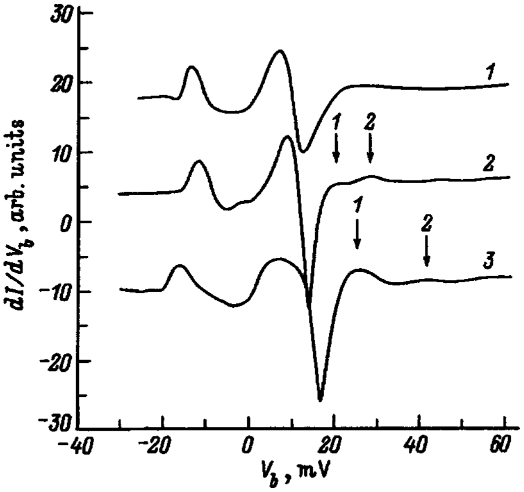

FIG. 4. Differential tunneling conductance $dI/dV_b$ versus bias voltage $V_b$ in a magnetic field parallel to the tunneling current. $B$, T: *1*—0, *2*—4.8, *3*—7.5. The arrows mark the additional maxima. The curves are shifted arbitrarily in the vertical direction.

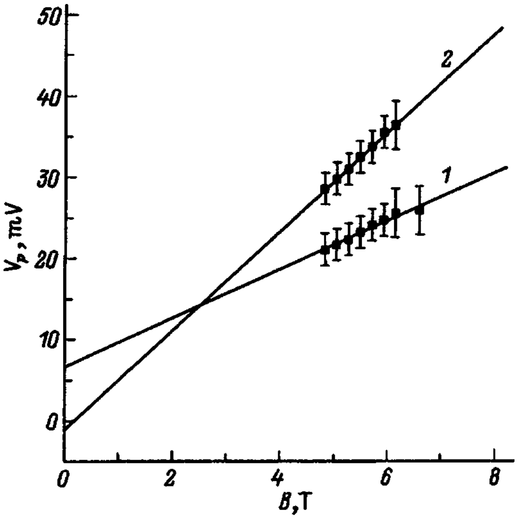

FIG. 5. Position $V_p$ of additional peaks indicated in Fig. 4 as a function of the magnetic field $B$. The numbers on the curves correspond to the numbers of the peaks in Fig. 4.

the background nonresonant current was subtracted out, and the voltage values of interest to us were determined for a current equal to 10% of the peak value at resonance. When comparing the computed values with the experimental data, we varied the difference the average positions of the 2D electrons along the $z$ axis, which was oriented in the direction of the current. The best agreement between the experimental and computed values was obtained for $\langle z_R\rangle-\langle z_L\rangle=35$ nm; here $\langle z_R\rangle$ is the average position of the 2D electrons in the $E_{0R}$ level, and $\langle z_L\rangle$ is the average position of the 2D electrons in the $E_{0L}$ level (see Fig. 1). The computed value equals 29 nm and agrees quite well with the experimental value.

In a magnetic field $\mathbf{B}\|\mathbf{J}$ additional peaks (marked by arrows in Fig. 4), whose positions depend on the magnetic field, were observed in the dependences $dI/dV_b=f(V_b)$. These features can appear for two reasons.

The first reason is electron tunneling between Landau levels with different indices. Indeed, the presence of impurities in the barrier increases the role of tunneling with elastic scattering. In this process the momentum components parallel to the interface are not conserved, only the electron energy is conserved, while tunneling with elastic scattering between Landau levels with different indices is possible in a quantizing magnetic field,[4] i.e., for certain discrete values of the bias voltage in a fixed magnetic field

$$V_n=\Delta E\pm n\hbar\omega_c, \tag{1}$$

where $n$ is an integer, $\Delta E$ is the energy difference between states of the 2D subbands with zero bias voltage, $\hbar$ is the Planck constant, and $\omega_c$ is the cyclotron frequency.

The second reason is the presence of Shubnikov–de Haas oscillations (periodic in the inverse magnetic field) in the tunneling conductance with period depending on the bias voltage. This can also result in the appearance of additional features in the dependences $dI/dV_b=f(V_b)$.[11] In this case the position of the additional peaks on the voltage axis depends linearly on the magnetic field. Figure 5 shows the magnetic field dependences of the positions of two peaks. We note that these dependences are linear and the position of the peak closest to resonance is described well by the expression (1) with $n=2$ and $\Delta E=6$ mV; the other features behave differently. For this reason, we attribute the first peak to tunneling between Landau levels with different indices. As mentioned in Ref. 4 , the probability of tunneling with elastic scattering by impurities decreases as electron energy increases, i.e., as the bias voltage increases, the magnitude of such peaks should decrease. This is probably why features with large $n$ are not observed. The feature with $n=1$ is not present, since it should appear in the region of nonlinearity of the tunneling conductance, making it much more difficult to observe.

To determine the nature of the other features it is convenient to study the dependence $dI/dV_b=f(B)$ for different fixed bias voltages. Oscillations of the differential conductance, which are periodic in the inverse field, were found in such dependences for different bias voltages $V_b$ ($\mathbf{B}\|\mathbf{J}$). Oscillations with two periods were observed. The dependence $B_f$ — the fundamental fields determining the period of the observed oscillations — on $V_b$ is presented in Fig. 6. Note that one period (curve *1*) depends strongly on the bias voltage, while the dependence of the other period (curve *2*) on the bias voltage is much weaker. A strong dependence can arise as a result of modulation of the density of unoccupied states in the collector 2DEG, into which the electrons tunnel, as a result of Landau quantization.[12] The number of these states is determined by the bias voltage, so that the period of such oscillations depends strongly on $V_b$. A weak dependence could be due to a change in the 2DEG density as a result of the application of a voltage, since this change is determined by the small capacitance of the barrier.[13] However, there are a number of factors which must be considered. In the first place, in the present system there exist two 2DEGs and each one should contribute to the oscillations of the tunneling conductance. In the second place, when the sign of the applied voltage changes ($V_b<0$, Fig. 6), oscilla-

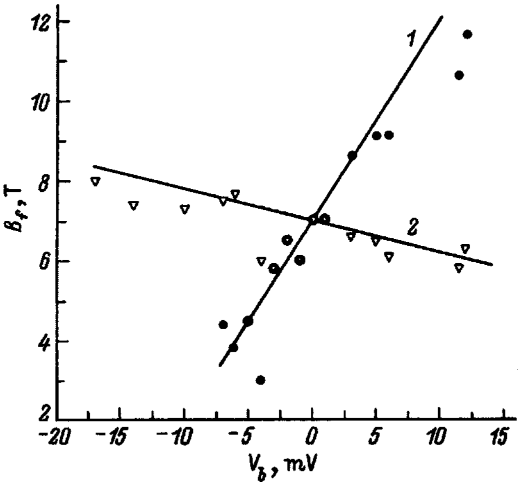

FIG. 6. Fundamental field $B_f$ for Shubnikov-de Haas oscillations in the tunneling differential conductance as a function of the bias voltage $V_b$. The error in determining $B_f$ equals 2 T.

tions associated with empty states of the collector 2DEG, accompanied by an increase in $B_f$ and not a decrease as in our experiments (curve *2*), should be observed. Such behavior can be explained by taking into account the broadening of the quantum levels in 2D enriched sheets. Since the oscillations of the differential tunneling conductance are investigated near resonance, it can be assumed that tunneling occurs between 2D systems and the tunneling current density in a magnetic field has the form

$$J=\frac{2e}{h}\int_{\mu_C}^{\mu_E} G_L(\varepsilon,B)T(\varepsilon)G_R(\varepsilon,B)d\varepsilon, \qquad (2)$$

where $\mu_E$ and $\mu_C$ are chemical potentials of the emitter and collector, respectively. It is assumed that

$$\mu_E-\mu_C=eV, \qquad (3)$$

$G_L(\varepsilon,B)$ and $G_R(\varepsilon,B)$ are the densities of states in the 2D enriched sheets on different sides of the barrier, and $T(\varepsilon)$ is the squared modulus of the tunneling transition matrix element. We note that in a magnetic field the electron density of states in a 2DEG is modulated by the system of Landau levels and the degree of modulation is determined by the broadening of these levels. In one 2DEG (for example, in the gas on the left-hand side; see Fig. 1) the degree of modulation is small compared with that in the other 2DEG because of the strong broadening of the levels, while in the expression (2) the functions $T(\varepsilon)$ and $G_R(\varepsilon,B)$ must be treated as constants at low bias voltages. Then

$$J=\frac{2e}{h}T\,G_R\int_{\mu_C-E_{0L}}^{\mu_E-E_{0L}} G_L(\varepsilon_k,B)d\varepsilon_k, \qquad (4)$$

where $\varepsilon_k$ is the electron kinetic energy in the plane of the 2D sheet. The expression for the experimentally measured differential tunneling conductance can be easily obtained from the expression (4), taking into account the relation (3):

$$\frac{dJ}{dV}=\frac{2e}{h}T\,G_R \times\left[G_L(\mu_C-E_{0L})\left(\frac{dE_{0L}}{dV}+e\right)-G_L(\mu_E-E_{0L})\frac{dE_{0L}}{dV}\right].$$

As is well known from the theory of the Shubnikov-de Haas effect, in this case the resonance current as a function of the magnetic field will oscillate with two frequencies, which are determined by the following expressions, taking into account the relation (3):

$$B_{f1}=\frac{m^*}{\hbar e}(\mu_E-E_{0L}), \quad B_{f2}=\frac{m^*}{\hbar e}(\mu_E-eV-E_{0L}), \qquad (5)$$

where $m^*$ is the electron effective mass in GaAs. It is evident from the expressions (5) that $B_{f2}$ depends strongly on the bias voltage, while $B_{f1}$ varies little, since it is determined by the electron density in the 2DEG emitter. The electron densities in enriched 2D sheets vary with the applied voltage in accordance with the barrier capacitance, so that

$$\mu_E-E_{0L}(V)=\mu_E-E_{0L}(0)+CV/eG_{2\mathrm{D}},$$

where $C$ is the specific capacitance of the barrier, and $G_{2D}$ is the density of states of the 2DEG. The computed straight lines presented in Fig. 6 were obtained from the expressions (5).

We therefore attribute the observation of only two oscillation periods in our experiments to the substantially different broadening of the quantum-well levels in the enriched sheets near the barrier. In our case the oscillations of the tunneling conductance in a magnetic field are determined by the level $E_{0L}$ in the enriched sheet on the bottom side of the barrier (the growth direction of the structure is up), which agrees with the well-known fact that a 2DEG is of a higher quality near an interface, where the AlGaAs layers are grown on a GaAs surface.

## CONCLUSIONS

Our analysis of the experimental data shows that all features of electron transport in heterostructures with a single, doped barrier are due to tunneling processes between two-dimensional electronic systems, while electron transport between two-dimensional sheets and three-dimensional contact regions introduces a small perturbation into the observed features. Thus, we have investigated 2D–2D tunneling in structures where electron transport along two-dimensional sheets is excluded.

This work was performed under the partial support of the State Scientific and Technical Programs ‘‘Physics of solid-state nanostructures’’ (97-1057) and ‘‘Physics of quantum and wave processes,’’ direction ‘‘Statistical physics’’ (V.3), as well as the Russian Fund for Fundamental Research (95-02-06310), INTAS–RFFI (95-0849), and CRDF (RC1-220).

[1] H. Mizuta and T. Tanoue, *The Physics and Applications of Resonant Tunneling Diodes*, Cambridge Univeristy Press, N.Y., 1995.
[2] P. Cheng and J. S. Harris, Jr., Appl. Phys. Lett. **55**, 572 (1989).

[3] M. L. Leadbeater, F. W. Sheard, and L. Eaves, Semicond. Sci. Technol. **6**, 1021 (1991).
[4] W. Demmerle, J. Smoliner, G. Berthold, E. Gornik, G. Weimenn, and W. Schlapp, Phys. Rev. B **44**, 3090 (1991).
[5] E. E. Mendez and L. L. Chang, Surf. Sci. **229**, 173 (1990).
[6] J. P. Eisenstein, L. N. Pfeifer, and K. W. West, Phys. Rev. Lett. **69**, 3804 (1992).
[7] K. M. Brown, N. Turner, J. T. Nicholls, E. H. Linfield, M. Pepper, D. A. Ritchie, and G. A. C. Jones, **50**, Phys. Rev. B 15 465 (1994).
[8] B. Deveaud, A. Chomette, F. Clerot, P. Auvray, R. Regreny, R. Ferreira, and G. Bastard, Phys. Rev. B **42**, 7021 (1990).
[9] T. Suski, J. Smoliner, C. Gschlobl, W. Demmerle, G. Bohm, and G. Weimenn, in ‘‘*Proceedings of the 5th International Conference on High Pressure in Semiconductor Physics,* Kyoto, 1992 [Jpn. J. Appl. Phys. **32**, Suppl. 32-1, 138 (1993)].
[10] G. Rainer, J. Smoliner, E. Gornik, G. Böhm, and G. Weimann, Phys. Rev. B **51**, 17 642 (1995).
[11] A. Nogaret, L. A. Cury, D. K. Maude, J. C. Portal, D. L. Sivco, A. Y. Cho, and G. Hill, Semicond. Sci. Technol. **8**, 1810 (1993).
[12] Yu. V. Dubrovskii, Yu. N. Khanin, I. A. Larkin, and S. V. Morozov, Phys. Rev. B **50**, 4897 (1994).
[13] L. Eaves, B. R. Snel, D. K. Maude, P. S. S. Guimares, D. C. Taylor, and F. W. Troombs, in *Proceedings International Conference on the Physics of Semiconductors,* Stockholm, World Scientific, 1986, p. 1615.

Translated by M. E. Alferieff

SEMICONDUCTORS VOLUME 32, NUMBER 5 MAY 1998

# Numerical analysis of the longitudinal electric current during resonance current flow in a *n*-GaAs/Al$_x$Ga$_{1-x}$As superlattice with doped quantum wells

S. I. Borisenko and G. F. Karavaev

*V. D. Kuznetsov Siberian Physicotechnical Institute at Tomsk State University, 634040 Tomsk, Russia*

(Submitted July 7, 1997; accepted for publication November 19, 1997)
Fiz. Tekh. Poluprovodn. **32**, 607–612 (May 1998)

The electric current density in the resonance electron transport along the axis of a $n$-GaAs/Al$_{0.36}$Ga$_{0.64}$As superlattice with doped quantum wells at low temperatures was analyzed numerically. The energy spectrum of the conduction-band minibands was calculated in the Kane and effective-mass approximations. The current density was calculated using the well-known formula obtained on the basis of the density-matrix method for a uniform electric field ignoring heating of the electron gas. The effect of an interaction between the minibands in an electric field on the electrical conductivity and intersubband optical absorption was studied. © *1998 American Institute of Physics.* [S1063-7826(98)02005-5]

As is well known, the numerical analysis of the electric current density due to electron transitions between Stark ladders of different minibands in strong electric fields in the direction of the axis of a superlattice (SL) is a difficult problem, to the solution of which a great deal of attention is now being devoted.[1,2] The difficulty of the problem lies in the fact that the electron transport of interest is a purely quantum effect, and this requires knowledge of the nonequilibrium density matrix. Moreover, the solution of this problem is complicated by the nonuniformity of the electric field arising in real SLs in connection with the presence of a negative differential conductivity and a quite substantial free charge-carrier density, which leads to the appearance of a strong-field domain at the anode contact.[3,4]

As a result of the problems indicated above, quasiclassical methods have been used to analyze the longitudinal current transport in SLs with doped quantum wells (QWs) in a strong electric field.[5,6] However, in the region of resonance current transport, when the strong-field domain encompasses the entire SL,[7] as well as for nondoped SLs[8] it can be assumed that the electric field is uniform and the quantum transport theory[9] can be used to calculate the current density, if the heating of the electron gas is negligible.

In this paper we numerically analyze the resonance current density and intersubband optical absorption for GaAs/Al$_x$Ga$_{1-x}$As SLs, used as IR photodetectors, with donor-doped QWs.[10–12] The QWs in these SLs have two minibands, whose width is equal to virtually zero due to the wide barriers. The resonance current in them is determined by electron transitions from the Stark states of the first miniband into the Stark states of the second miniband of neighboring QWs. The resonance current density was calculated at low temperatures taking into account electron scattering by impurity ions using the well-known formula obtained on the basis of the density-matrix method.[9]

## 1. METHOD FOR CALCULATING THE RESONANCE CURRENT DENSITY

The resonance current density $j_r$ in a uniform electric field $F$ parallel to the SL axis was calculated according to the standard formula[9]

$$j_r = en\tau_\perp \tilde{d}|\tilde{\Omega}_{12'}|^2, \tag{1}$$

where $n$ is the volume-averaged electron density, $\tau_\perp$ is the phase-difference relaxation time averaged over the transverse electron energy, the parameter

$$\tilde{d} = \langle \tilde{w}_{21}|z|\tilde{w}_{21}\rangle - \langle \tilde{w}_{10}|z|\tilde{w}_{10}\rangle \tag{2}$$

is close in magnitude to the period $d$ of the SL, and the matrix element

$$\hbar\tilde{\Omega}_{12'} = \langle \tilde{w}_{10}|\hat{H}_0 - eFz|\tilde{w}_{21}\rangle \tag{3}$$

determines the probability of electron tunneling between the Stark states of neighboring QWs. In Eqs. (2) and (3) $\tilde{w}_{il}$ are the wave functions of electrons in an electric field in the envelope approximation, which correspond to the energy

$$E_{il} = E_i - eFdl, \tag{4}$$

where $i$ is the number of the state in the $l$th QW, $\hat{H}_0$ is a single-particle Hamiltonian operator for electrons in the SL in the absence of an electric field, and $z$ is the coordinate along the axis of the SL. The orthonormalized functions $\tilde{w}_{il}$, calculated in the approximation of isolated QWs, are linear combinations of orthonormalized Wannier functions

$$\tilde{w}_{il} = \sum_j c_{ji} w_{jl}, \tag{5}$$

where

$$w_{il}(z) = w_i(z - ld) = \frac{1}{\sqrt{N}} \sum_q e^{-iqld} \psi_{iq}(z) \tag{6}$$

is the Wannier function corresponding to the $i$th miniband in the conduction band localized in the $l$th QW, and $\psi_{iq}$ are the Bloch-type electron wave functions with wave number $q$ in the envelope approximation with the corresponding energies $E_{iq}$. The energies $E_i$ and the corresponding coefficients $c_{ji}$ are solutions of the system of linear equations

$$\sum_j \left[(I_{i0}-E)\delta_{ij}-eFZ_{ij0}\right]c_j=0, \tag{7}$$

where

$$I_{i0}=\frac{1}{N}\sum_q E_{iq} \tag{8}$$

is the average energy in the $i$th miniband,

$$Z_{ij0}=\langle \tilde{w}_{i0}|z|\tilde{w}_{j0}\rangle=\int_L w_{i0}^{*}zw_{j0}dz \tag{9}$$

is the matrix element of the coordinate operator, and $L=Nd$ is the length of the SL along the symmetry axis. Using Eq. (5) and the orthonormality of the functions $\psi_{iq}$, we obtain the following expressions for the parameter $\tilde{d}$ and the matrix elements determining the probability of a tunneling transition

$$\tilde{d}=d+\sum_{ij}(c_{i2}^{*}c_{j2}-c_{i1}^{*}c_{j1})Z_{ij0}, \tag{10}$$

$$\hbar\tilde{\Omega}_{12'}=\sum_{ij}c_{i1}^{*}c_{j2}(I_{i1}\delta_{ij}-eFZ_{ij1}), \tag{11}$$

where

$$I_{i1}-\frac{1}{N}\sum_q e^{iqd}E_{iq}, \tag{12}$$

$$Z_{ij1}=\langle \tilde{w}_{i0}|z|\tilde{w}_{j1}\rangle. \tag{13}$$

The envelopes $\psi_{iq}$ and energies $E_{iq}$ were calculated taking into account the Kane nonparabolicity for III–V semiconductors in the three-band approximation, which we shall call the Kane approximation. In this approximation the functions $\psi_{iq}$ are three-component column vectors with components $\psi_{iq\nu}$, which satisfy the orthonormality condition

$$\langle \psi_{iq}|\psi_{jq}\rangle=\sum_{\nu=1}^{3}\langle \psi_{iq\nu}|\psi_{jq\nu}\rangle=\delta_{ij}. \tag{14}$$

According to Ref. 13 , the functions $\psi_{iq\nu}$ and energies $E_{iq}$ are solutions of the system of linear differential equations

$$\begin{gathered}
-\sqrt{\frac{2}{3}}P\hat{P}_z\psi_2+\frac{1}{\sqrt{3}}P\hat{P}_z\psi_3+V_s(z)\psi_1=E\psi_1,\\
-\sqrt{\frac{2}{3}}P\hat{P}_z\psi_1+V_p(z)\psi_2=(E+E_g)\psi_2,\\
\sqrt{\frac{1}{3}}P\hat{P}_z\psi_1+V_\delta(z)\psi_3=(E+E_g+\Delta)\psi_3,
\end{gathered} \tag{15}$$

where $\hat{P}_z$ is the $z$ component of the momentum operator, $E_g$ and $\Delta$ are, respectively, the band gap and the spin-orbit splitting of the valence-band top in the semiconductor where the QW is located; $P$ is a matrix element determining the interaction of the valence-band edge and the conduction band in the Kane model and was assumed to be constant over the entire SL; $V_s$, $V_p$, and $V_\delta$ are functions describing the edges of the conduction band, the light-hole band, and the spin-orbit splitoff band, which are measured from the edges of these bands in the QW. These functions are periodic with the period of the SL and differ from zero near the barriers, where they are constant. For the GaAs/Al$_x$Ga$_{1-x}$As SLs, which we are studying, with square QWs and barriers, these functions are constant near the barriers:

$$V_p=E_g(0)-E_g(x)+V_s,\quad V_\delta=\Delta(0)-\Delta(x)+V_p, \tag{16}$$

where

$$E_g(x)=E_g(1)x+E_g(0)(1-x)-C_gx(1-x),$$

$$\Delta(x)=\Delta(1)x+\Delta(0)(1-x)$$

are, respectively, the band gap and the spin-orbit splitting of the valence band in Al$_x$Ga$_{1-x}$As.

According to Ref. 13 , the system of equations (15) reduces to a Kronig–Penney type equation for the function $\psi_1$

$$\left\{\frac{1}{2}\hat{P}_z\frac{1}{m(E,z)}\hat{P}_z+V_s(z)\right\}\psi_1=E\psi_1 \tag{17}$$

with boundary conditions following from continuity of $\psi_1$ and $m^{-1}\psi_1'$ at the heterojunction, where

$$\frac{1}{m(E,z)}=\frac{2}{3}P^2\left(\frac{2}{E+E_g-V_p(z)}+\frac{1}{E+E_g+\Delta-V_\delta(z)}\right). \tag{18}$$

According the Eq. (15), the functions $\psi_2$ and $\psi_3$ are determined in terms of $\psi_1$ according to the formulas

$$\psi_2=-\sqrt{\frac{2}{3}}\frac{P}{E+E_g-V_p(z)}\hat{P}_z\psi_1,$$

$$\psi_3=\sqrt{\frac{1}{3}}\frac{P}{E+E_g+\Delta-V_\delta(z)}\hat{P}_z\psi_1. \tag{19}$$

Since, according to the theory of Ref. 13 , the matrix element $P$ should not depend on the coordinate, it was determined as the average value over the period of the SL:

$$P^2=\frac{P^2(x)b+P^2(0)a}{d}, \tag{20}$$

where $a$ and $b$ are, respectively, the width of the QW and the SL barrier,

$$P^2(x)=\frac{E_g(x)[E_g(x)+\Delta(x)]}{2m_c(x)\left[E_g(x)+\frac{2}{3}\Delta(x)\right]},$$

$m_c(x)=xm_c(1)+(1-x)m_c(0)$ is the electron effective mass at the point $\Gamma$ in Al$_x$Ga$_{1-x}$As.

For $E=0$ in Eq. (18), Eq. (17) becomes the ordinary Schrödinger equation for the envelope function $\psi_{iq}$. We call it the effective-mass approximation.

Taking into account the symmetry of the superlattice potential and choosing the coordinate system at the center of the zeroth QW, the functions $\psi_{iq}(z)$ and $w_{il}(z)$ can be chosen so as to satisfy the following symmetry conditions

$$\psi_{iq}(-z)=\psi_{iq}^{*}(z)=(-1)^{\alpha_i}\psi_{i-q}(z),$$

$$w_{il}(-z)=w_{i-l}^{*}(z)=(-1)^{\alpha_i}w_{i-l}(z), \tag{21}$$

where $\alpha_i=0,1$. According to these conditions, the even functions $\psi_{i0}(z)$ and $w_{i0}(z)$ are real, while the odd functions are imaginary. In what follows, we call the minibands with $\alpha_i=0$ odd and vice versa. Using the expressions (6), (14), and (21), we obtain for the matrix element $Z_{ijn}$

$$Z_{ijn}=\frac{i}{\pi}\sum_{\nu}\int_0^{\pi/d}\left(e^{-iqdn}-(-1)^{\alpha_i+\alpha_j}e^{iqdn}\right)Z_{ij\nu}(q)\,dq, \tag{22}$$

where

$$Z_{ij\nu}(q)=\int_0^{d/2}\left\{z\ \mathrm{Im}(\psi_{iq\nu}^{*}\psi_{jq\nu})-\mathrm{Re}\left(\psi_{jq\nu}\frac{\partial}{\partial q}\psi_{iq\nu}^{*}\right)\right\}dz, \tag{23}$$

and the matrix elements satisfy the symmetry condition

$$Z_{ijn}=-Z_{jin}. \tag{24}$$

It follows from Eq. (22) that the matrix elements $Z_{ij0}$, which determine in the approximation of isolated QWs the energy spectrum in an electric field, are different from zero only between minibands of different parity. This corresponds to the selection rules for intersubband optical absorption.

## 2. PARAMETER VALUES EMPLOYED AND ANALYSIS OF COMPUTATIONAL RESULTS

The resonance value of the dark current density was calculated for GaAs/$\mathrm{Al_{0.36}Ga_{0.64}As}$ superlattices with 70-Å-wide doped QWs and a 140-Å-thick barrier using Eq. (1). The dopant density $N_D$, according to the experiment of Ref. 11 , was assumed to be $1.4\times10^{18}\ \mathrm{cm}^{-3}$. The following formulas and values of the independent variables were used to calculate the parameters appearing in the system of equations (15) and Eq. (17):[14]

$$E_g=E_g(0)=\left(1.52-\frac{5.408\times10^{-4}T^2}{204+T}\right)\mathrm{eV},$$

$$E_g(1)=\left(3.10-\frac{8.208\times10^{-4}T^2}{204+T}\right)\mathrm{eV}$$

are the band gaps in GaAs and AlAs as functions of temperature $T$;

$$\Delta=\Delta(0)=0.34\ \mathrm{eV},\quad \Delta(1)=0.28\ \mathrm{eV}$$

are the spin-orbit splittings of the valence-band top in GaAs and AlAs;

$$m_c(0)=0.067\,m_0,\quad m_c(1)=0.15\,m_0$$

are the electron effective masses at the point Γ in GaAs and AlAs; the parameter $C_g=0.37$ eV takes into account the nonlinear character of the variation of the band gap in the alloy $\mathrm{Al}_x\mathrm{Ga}_{1-x}\mathrm{As}$ as a function of the molar fraction $x$.[15]

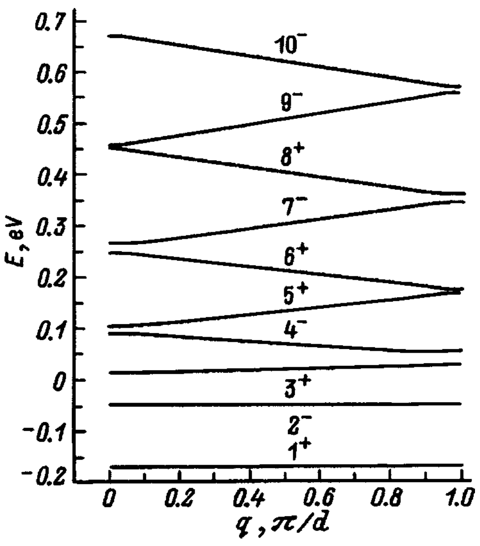

FIG. 1. Energy spectrum of minibands of the conduction band near the point Γ of the superlattice GaAs/$\mathrm{Al_{0.36}Ga_{0.64}As}$.

Figure 1 shows the energy spectrum of the ten lowest minibands for our SL at $T=15$ K, as calculated from the solution of Eq. (17) in the Kane approximation. The index on a miniband number indicates the parity of the band: + for even and − for odd. It follows from the figure that the QW contains two minibands with very small dispersion, between which, according to selection rules, intersubband absorption with energy $\hbar\omega_0=I_{20}=I_{10}=121$ meV can be observed. The computed spectrum was obtained with an effective height of the potential barrier $V_s=218$ meV, whose value was adjusted so as to obtain agreement between the experimental and computed data on intersubband optical absorption.[11] The value obtained for $V_s$ is less than the offset of the conduction

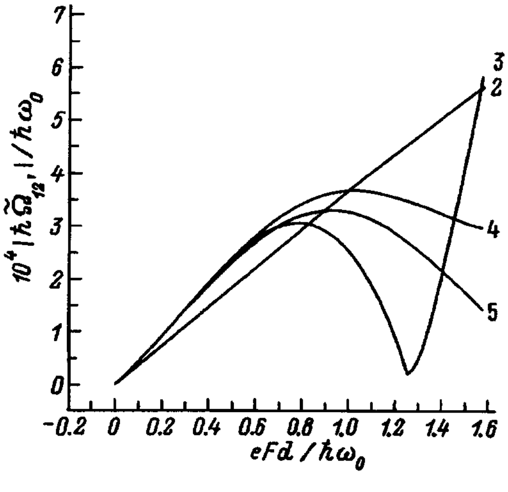

FIG. 2. Modulus of the matrix element giving the probability of a tunneling transition between the ground state and the first excited state of neighboring quantum wells as a function of the intensity of the electric field in the Kane approximation. The number on each curve is the number of minibands taken into account in calculating the curve.

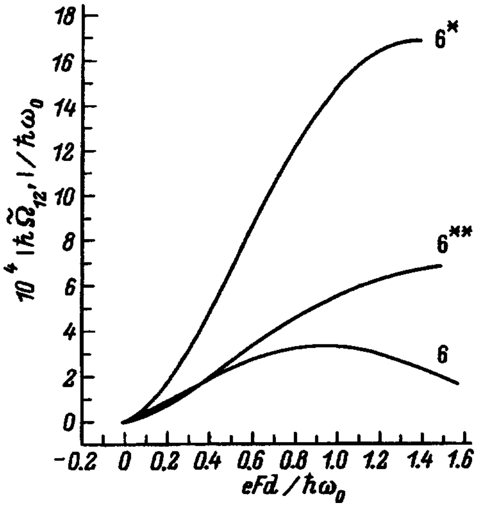

FIG. 3. Modulus of the matrix element giving the probability of a tunneling transition between the ground state and the first excited state of neighboring quantum wells as a function of the intensity, six-miniband approximation: *6* — Kane approximation ($V_s=218$ meV), *6**—effective-mass approximation ($V_s=189$ meV), *6***—effective-mass approximation ($V_s=218$ meV).

band edge at the heteroboundary, equal to 285 meV; here the computed value is $\hbar\omega_0=136$ meV. The effective barrier height in the effective mass approximation is $V_s=189$ meV. The fact that the effective height $V_s$ of the potential barrier is smaller than the offset of the bands at the heterojunction could be due to the additional interaction energy of an electron with neutral impurity atoms, whose density at the temperature studied is high.

Figure 2 shows the matrix element $|\hbar\tilde{\Omega}_{12'}|$, calculated according to Eqs. (7), (11), (12), and (22) in the Kane approximation, versus the electric field intensity. The numbers on the curves in the figure are the numbers of the lower minibands taken into account in the calculation of the indicated curve. It is evident from the figure that in the region of the resonance value of the field $F_r=\hbar\omega_r/ed$, where $\hbar\omega_r\approx\hbar\omega_0$ is the intersubband absorption energy ($\hbar\omega=E_2-E_1$) in an electric field $F_r$, the value of the matrix element depends strongly on the number of minibands taken into account. Convergence of the calculation was attained in a six-miniband approximation. For the resonance value of the field the matrix element is $|\hbar\tilde{\Omega}_{12'}|=4.0\times10^{-5}$ eV, which is much lower than the corresponding value calculated in the effective-mass approximation (Fig. 3). It should be noted that the character of the field dependence of this matrix element near the resonance value is different in different approximations. In the effective-mass approximation the matrix element increases with the field, while in the Kane approximation a maximum is observed in this region.

Figure 4 shows $\Delta\hbar\omega=\hbar\omega-\hbar\omega_0$ — the shift of the intersubband optical absorption energy — as a function of the electric field calculated in the six-miniband approximation. It follows from the figure that as the field increases, the inter-

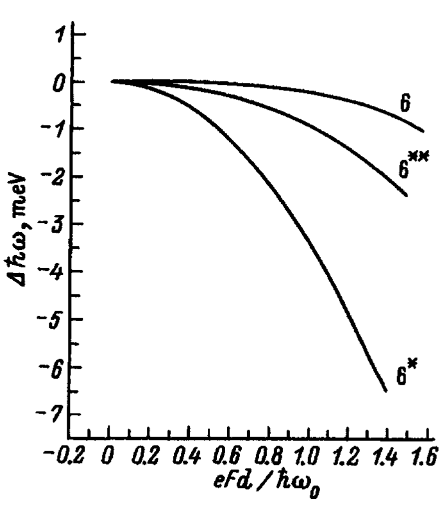

FIG. 4. Energy shift of intersubband optical absorption versus the electric field intensity, six-miniband approximation. $\hbar\omega_0$, meV: *6* — 121, *6**—120, *6***—130.

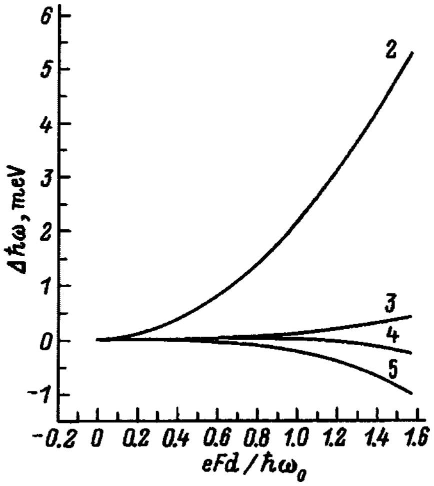

FIG. 5. Energy shift of intersubband optical absorption versus the electric field intensity, Kane approximation. The number on each curve is the number of the minibands taken into account in calculating the curve.

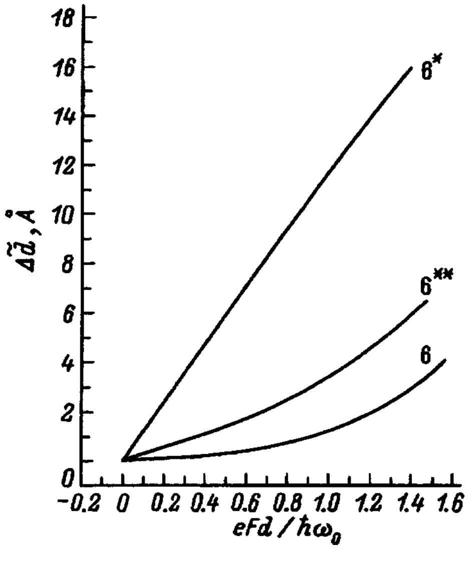

FIG. 6. $\Delta\tilde{d}$ (deviation of the parameter $\tilde{d}$ from the superlattice period $d=210$ Å) versus the electric field intensity. The calculation was performed in the six-miniband approximation.

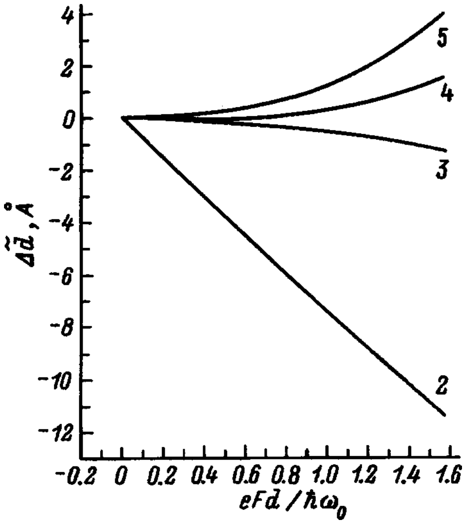

FIG. 7. $\Delta\tilde{d}$ (deviation of the parameter $\tilde{d}$ from the superlattice period) versus the electric field intensity. The calculation was performed in the Kane approximation. The number on each curve is the number of minibands taken into account in the calculating the curve.

subband absorption energy decreases, i.e., a ''red'' shift occurs. This shift, calculated in the region of the resonance field in the Kane approximation, in contrast to the effective-mass approximation, was found to be very small ($\sim 0.2$ meV). It should be noted that in the two-miniband approximation this shift was found to be a ''blue'' shift and much larger in absolute value, $\sim 2$ meV (Fig. 5). Our numerical analysis gives an explanation of the small value of $\Delta\hbar\omega$ that is different from Ref. 12 , where the shift was attributed to screening of the electric field in the QW by free electrons.

Figure 6 shows the parameter $\Delta\tilde{d}=\tilde{d}-d$ as a function of the field, calculated using Eqs. (7), (10), and (22) in different approximations using six minibands. According to the figure, the value of $\tilde{d}$ calculated in any approximation increases with the field. This increase can be explained by the fact that the electron motion in the second miniband is freer than in the first miniband. However, in the approximation with a small number of minibands this parameter can decrease as the field increases (Fig. 7). The increase in this parameter in the region of a resonance field was found in the Kane approximation to be approximately 1 Å, which is much less than the period of the SL under study, so that the difference between $\tilde{d}$ and $d$ can be ignored in the range of fields investigated.

Using the value presented above for the matrix element of the probability of a tunneling transition, the computed resonance value of the current density $j_r$ was found to be of the order of 1.25 A/cm$^2$, which is in good agreement with the experimental value of 0.9 A/cm$^2$ determined from the current-voltage characteristic of the dark current at $V=6$ V (Ref. 11). According to Ref. 7 , for this voltage the electric field in the SL studied is uniform; i.e., the strong-field domain encompasses the entire SL, and in the case of 50 periods, since $\hbar w_r \approx 120$ meV, it corresponds to the resonant value. To calculate $j_r$ the electron density $n=1.3\times10^{15}$ cm$^{-3}$ was used and the relaxation time of the phase difference was assumed to be $\tau_\perp = 7.8\times10^{-13}$ s at $T=15$ K. The quantity $\tau_\perp$ was limited by the scattering by impurity ions, while the interaction of electrons with neutral atoms was taken into account by introducing an effective height $V_s$ of the potential barrier for electrons.

Our numerical analysis of the longitudinal current density under the conditions of resonance current flow and intersubband optical absorption in a SL with weakly interacting QWs showed that agreement between the theoretical and experimental data on the phenomenon studied at low temperatures can be obtained by introducing an effective height of the potential barrier at a heterojunction and assuming scattering by impurity ions to be the main scattering mechanism. As the calculations showed, in the analysis of the optical and kinetic properties in the region of quantum electric fields the interaction of the Stark states, which lie in isolated QWs, with the excited states is strong. Disregarding this interaction can change the numerical result not only quantitatively, but also qualitatively. The use of the effective mass method to calculate the energy spectrum of the minibands, instead of methods which take into account the nonparabolicity of the volume spectrum near the conduction-band edge, can also give qualitatively incorrect results when analyzing the physical properties of the superlattices studied.

[1] J. Potvig, Jauho Anti-Pekka, and H. Smith, Phys. Rev. Lett. **74**, 1831 (1995).
[2] H. Grahn, J. Kastrup *et al.*, Jpn. J. Appl. Phys. **34**, 4526 (1995).
[3] K. K. Choi, B. F. Levin *et al.*, Phys. Rev. B **3**, 4172 (1987).
[4] H. T. Grahn, H. Schider, and K. Klitzing, Phys. Rev. B **41**, 2890 (1990).
[5] R. E. Kunz and E. Scholl, Phys. Rev. B **47**, 4337 (1993).
[6] F. Prengel, A. Wacker, and E. Scholl, Phys. Rev. B **50**, 1705 (1994).
[7] S. H. Kwok, T. B. Norris *et al.*, Phys. Rev. B **51**, 10 171 (1995).
[8] F. Capasso, K. Mohammed, and A. Y. Cho, Appl. Phys. Lett. **48**, 478 (1986).
[9] R. F. Kazarinov and R. A. Suris, Fiz. Tekh. Poluprovodn. **6**, 148 (1972) [Sov. Phys. Semicond. **6**, 120 (1972)].
[10] B. F. Levine, K. K. Choi *et al.*, Appl. Phys. Lett. **50**, 1092 (1987).
[11] K. K. Choi, B. F. Levine *et al.*, Appl. Phys. Lett. **50**, 181 (1987).
[12] B. F. Levine, C. G. Bethea *et al.*, Appl. Phys. Lett. **53**, 231 (1988).
[13] *Molecular-Beam Epitaxy and Heterostructures* [in Russian], Nauka, Moscow, 1989.
[14] Landolt-Börnstein, in *Zahlenwerte und Funktionen aus Naturwissenshaften und Technik,* edited by O. Madelung, Springer-Verlag, N.Y., 1987, Vol. 5, No. 3, Part 22A.
[15] J. Batey and S. L. Wright, Surf. Sci. **174**, 320 (1986).

Translated by M. E. Alferieff

## AMORPHOUS, GLASSY, AND POROUS SEMICONDUCTORS

# Investigation of the photovoltage in *por*-Si/*p*-Si structures by the pulsed-photovoltage method

V. Yu. Timoshenko* and E. A. Konstantinova

*M. V. Lomonosov Moscow State University, 119899 Moscow, Russia*

T. Dittrich

*Munich Technical University, D-85747 Garching, Germany*

(Submitted May 26, 1997; accepted for publication June 7, 1997)
Fiz. Tekh. Poluprovodn. **32**, 613–619 (May 1998)

Photovoltaic phenomena in the structures *por*-Si/*p*-Si were investigated by the pulsed photovoltage method in the time interval 100 ns–10 ms using irradiation with nanosecond laser pulses with photon energies 1.4, 2.0, 2.8, and 3.7 eV. The data obtained show that besides the barrier photovoltage, due to the separation of nonequilibrium charge carriers in the space-charge region of *p*-Si at the *por*-Si/*p*-Si interface, there also exists an efficient mechanism of photovoltage formation due to charging of the surface of the *por*-Si nanostructure. This mechanism is explained as ‘‘optical doping’’ of a semiconductor and develops in a manner peculiar to semiconductor nanostructures. © *1998 American Institute of Physics.* [S1063-7826(98)02105-X]

## 1. INTRODUCTION

Electronic phenomena in porous Si (*por*-Si) have recently been studied extensively. The structural, optical, and luminescence properties of *por*-Si have been studied in greatest detail.[1,2] It has been established that a quantum-well effect and molecular coating of the nanostructures play a determining role in photoluminescence (PL) phenomena. In Refs. 3 and 4 the conductivity of *por*-Si was investigated and it was concluded that charge carriers are transported by a hopping mechanism, which attests to the presence of a large number of traps — charge trapping centers. Photovoltaic phenomena in this material have been studied separately. A barrier photovoltage in a metal/*por*-Si structure was observed and investigated in Ref. 5 . The photoconductivity[6,7] and photovoltage[8,9] in metal/*por*-Si/*p*-Si structures have been studied in the visible range of the spectrum. In Ref. 10 a lateral photovoltage was found in *por*-Si layers. However, the mechanisms leading to the formation of a photovoltage in *por*-Si remain controversial. Moreover, in most cases uncontrollable contact phenomena at the metal/*por*-Si interface complicate the interpretation of the experimental results.

In our previous studies it was shown that a contact-free method of measuring the contact potential difference (CPD) in the Kelvin scheme can be successfully used to investigate photovoltaic effects in *por*-Si.[11,12] Charge trapping with relaxation times of the order of several minutes and longer was detected in oxidized *por*-Si. Both positive and negative CPD signals were detected when the samples were illuminated with radiation with different photon energies. But the mechanisms leading to the formation of a photovoltage were not completely determined, since the CPD was measured at times greater than 0.1 s. In Ref. 13 photovoltaic effects in *por*-Si were investigated with a resolution of 100 ns by the pulsed photovoltage method (PPV). Unfortunately, in this work the PPV measurements were performed for only two photon energies, which makes it impossible to draw an unequivocal conclusion about the nature of the photovoltage formed. Moreover, to determine the characteristic features of the photovoltage in *por*-Si nanostructures it is necessary to perform comparative experiments on *c*-Si surfaces with a similar molecular coating.

In the present work *por*-Si/*p*-Si structures were investigated by the PPV method using nanosecond laser pulses with photon energies 1.4, 2.0, 2.8, and 3.7 eV. Photovoltaic phenomena in as-grown and oxidized samples were analyzed and, for comparison, *p*-Si single crystals were investigated under similar conditions. A model of photovoltage formation, which explains the experimental results and which is in good agreement with the CPD data, is proposed.[11,12]

## 2. EXPERIMENTAL PROCEDURE

*por*-Si/*p*-Si structures were formed by anodic treatment of *p*-Si wafers ($\rho = 10\ \Omega \cdot$ cm) with (100) orientation in a HF:$C_2H_5OH$:$H_2$ (1:2:1) solution with current density 30 mA/cm$^2$ for 5 min. The porous layer was about 5 $\mu$m thick. Some samples were investigated immediately after preparation. The other samples were allowed to stand in air for several months (oxidized samples). The *p*-Si wafers employed for comparison were held in HF without passing a current. The volume charge-carrier lifetime in *p*-Si single crystals was $\tau_0 = 20\ \mu$s.[14] According to our IR-transmission data,[12] the surface of the freshly prepared samples was pas-

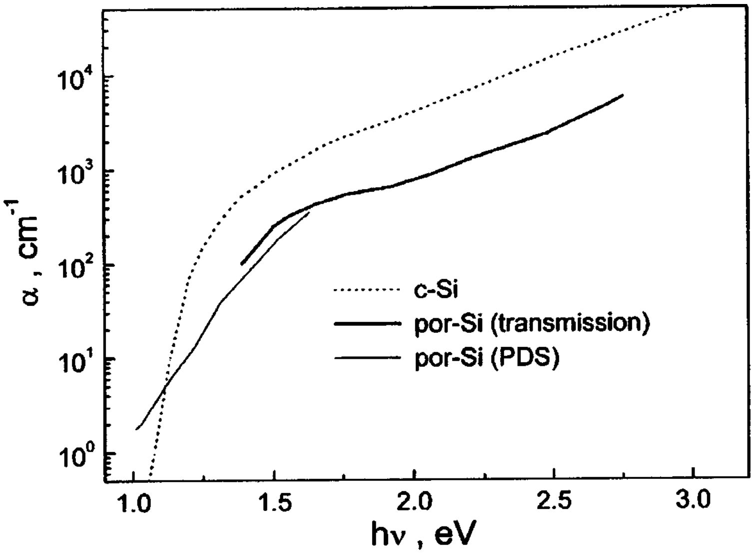

FIG. 1. Absorption coefficients of *por*-Si (solid lines) and *c*-Si (dotted lines) versus the energy of optical photons. The absorption coefficients $\alpha(h\nu)$ for *por*-Si were obtained from measurements of the transmission of peeled-off films (thick line) and from Ref. 20 according to photothermal deflection spectroscopy data (PDS, thin line). The values of $\alpha(h\nu)$ for *c*-Si were taken from Ref. 21 .

sivated with hydrogen. Si–O bonds predominate in oxidized *por*-Si.[12] The surface of HF-treated single-crystal *p*-Si is characterized by a hydrogen coating.[15]

The measurements were performed in a dry-nitrogen atmosphere using a capacitor scheme in which one capacitor plate served as the experimental sample and the other as a half-transmitting metal electrode, separated from the *por*-Si surface by a 100-$\mu$m-thick mica plate. The PPV signal was measured relative to the half-transmitting metal electrode. The kinetics of the photovoltage excited by single-pulse laser radiation was recorded with a Tektronix RTD 710A digital voltmeter. The transmission band in our experiments was $10^2-10^7$ Hz. The following lasers were employed for excitation: a semiconductor diode laser ($h\nu_1=1.4$ eV, $\tau=150$ ns, $W=1$ $\mu$J/cm$^2$), a nitrogen laser, and dye lasers pumped by the nitrogen laser ($h\nu_2=2.0$ eV, $h\nu_3=2.8$ eV, $h\nu_4=3.7$ eV, $\tau\sim1$ ns, $W=0.01-0.02$ $\mu$J/cm$^2$). Additional information was obtained from optical measurements of the photoluminescence and absorption. We used for this purpose *por*-Si films peeled off at the end of the electrochemical process.

## 3. RESULTS AND DISCUSSION

### 3.1. Optical properties of porous Si

The peaks in the PL spectra of freshly prepared and oxidized samples were located near $\lambda=700$ nm in the case of excitation by UV light with photon energy $h\nu_4$. However, the luminescence of oxidized *por*-Si was seven times more intense than that of as-grown material. This is probably due to better surface passivation of the nanostructures by the oxide layer. Our measured value of the external quantum yield $\eta$ of the oxidized samples is equal to approximately 0.2%.

Figure 1 shows the absorption coefficient $\alpha(h\nu)$ for *por*-Si, calculated on the basis of optical transmission measurements and photothermal deflection spectroscopy data. The results are presented without any correction for porosity. The values of $\alpha(h\nu)$ for *c*-Si, which were taken from a handbook, are shown in the figure for comparison. According to Fig. 1, the penetration depth $\alpha^{-1}$ of light in *por*-Si exceeds 10 $\mu$m for $h\nu<2$ eV and is less than 1 $\mu$m for $h\nu>2.5$ eV. Therefore, it can be assumed that the *por*-Si layers employed are virtually transparent for $h\nu\leqslant2$ eV and opaque for $h\nu>2.5$ eV.

### 3.2. Measurements of the pulsed photovoltage for *p*-Si wafers

The kinetics of the photovoltage $U_{PV}(t)$ after the action of laser pulses with the maximum intensity on single-crystalline *p*-Si wafers is shown in Fig. 2. As one can see from the figure, the time position of the maximum of the signal amplitude is virtually identical to the time position of the laser pulse. For excitation energies in the interval $h\nu_1-h\nu_3$ the curves $U_{PV}(t)$ are similar to one another. The character of the relaxation is close to exponential (compare curves *1–3* and the computed exponential curve *5*). For photon energy $h\nu_4$ the departure of $U_{PV}(t)$ from an exponential increases. The photovoltage relaxation time, measured according to the decay of the photovoltage amplitude by a factor of $e$, equals approximately 50 $\mu$s for all excitation photon energies.

The amplitude and sign of the PPV attest to the fact that the detected signal is due mainly to the barrier photovoltage resulting from the separation of nonequilibrium charge carriers (NCCs) in the electric field near the surface. Nonetheless, a number of features in $U_{PV}(t)$ at the initial stage and at times exceeding 100 $\mu$s are apparently due to trapping of NCCs in surface states. Let us discuss these states. As one can see from Fig. 2, $|U_{PV}|$ decreased sharply in a time $\tau\simeq0.2$ $\mu$s after illumination. We assume that this feature is due to the surface photovoltage resulting from the formation of a positive charge in surface states. According to Ref. 16 , fast states strongly influence the photovoltage amplitude when the injection level is high. Charge trapping in fast states is most pronounced, in our view, for the case where a region near the surface is excited by light with photon energy $h\nu_4$ (Fig. 2, curve *4*). The character of the dependences $U_{PV}(t)$ at times longer than 100$\mu$s and their departure from an exponential dropoff (''tails'') could be due to the ejection

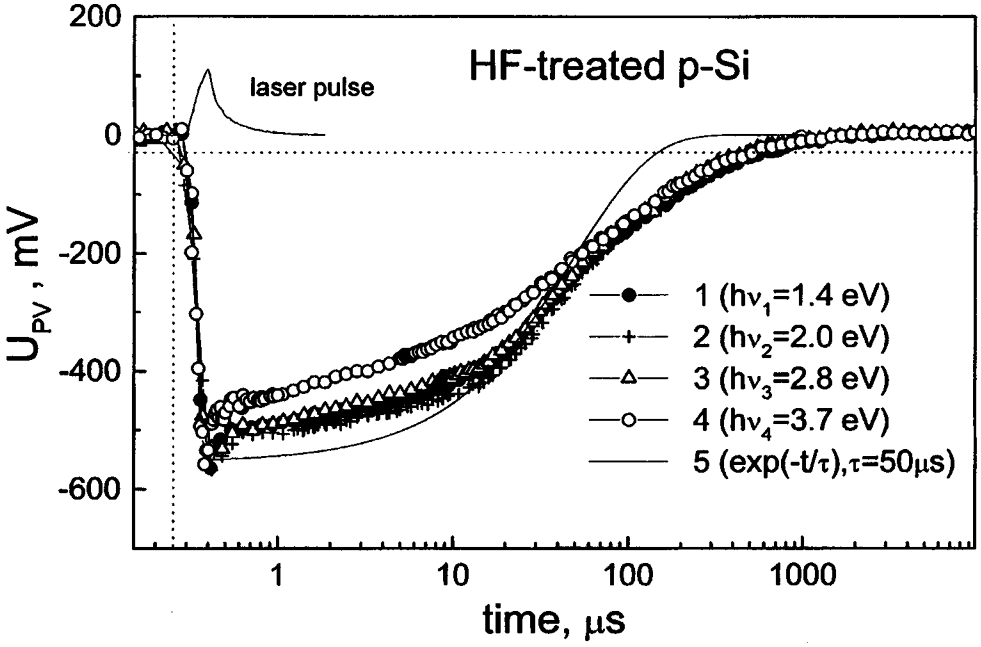

FIG. 2. Kinetics of the photovoltage $U_{PV}$ for $p$-Si after illumination with laser pulses (the photon energy $h\nu_i$ is indicated in the figure). Curve *5* corresponds to the computed exponential relaxation of the photovoltage with $\tau=50$ μs.

of trapped positive charge and (or) trapping of negative charge.

It was observed that the dependence of $|U_{PV}^{\max}|$ on the illumination intensity saturates (Fig. 3, curves *1* and *2*). This indicates that bands in the layer near the surface rectify under maximum excitation intensity conditions. The maximum excess charge carrier density was equal to $\delta n \simeq W\alpha/h\nu = 5\times 10^{15}$ cm$^{-3}$ for irradiation with $h\nu_1$ and $\delta n \simeq 10^{15}$ cm$^{-3}$ for pulses in the range $h\nu_2 - h\nu_4$, which corresponds to injection level $\delta n/n_i \simeq 10^5$, where $n_i = 10^{10}$ cm$^{-3}$ is the intrinsic charge carrier density. This is sufficient for band rectification in the experimental samples.[16,17] If the fast states are ignored, then the maximum PPV amplitude is given by

$$|U_{PV}|^{\max} = Y_0 - U_D, \tag{1}$$

where $Y_0$ is the initial surface potential. The Dember photovoltage $U_D$ is given by the expression

$$U_D = \frac{b-1}{b+1}\ln\left[1+\frac{\delta n}{n_i}\left(\frac{b+1}{\lambda+b/\lambda}\right)\right], \tag{2}$$

where $b=\mu_e/\mu_n$ is the ratio of the electron and hole mobilities, the parameter $\lambda = n_i/n_0 = p_0/n_i$ characterizes the ''nonintrinsic nature'' of the semiconductor, and $n_0$ and $p_0$ are, respectively, the electron and hole densities in the equilibrium state. For $\delta n/n_i \simeq 10^5$, $b=3$, and $\lambda = 10^5$ the Dember photovoltage equals approximately 30 mV. Therefore, we obtain $Y_0 = 0.63$ eV, which indicates the presence of a layer which is depleted of majority carriers and enriched with minority carriers in a near-surface region in $p$-Si. The presence of a conduction inversion layer at the surface can probably explain the fact that the PPV relaxation time is longer than the volume time $\tau_0$.[18]

### 3.3. PPV measurements for freshly prepared *por*-Si/*p*-Si structures

We shall now discuss the kinetics of PPV of as-prepared *por*-Si/$p$-Si structures (Fig. 4). Since *por*-Si is virtually transparent for light with photon energies $h\nu_1$ and $h\nu_2$, it can be assumed that the PPV is formed in $p$-Si at the *por*-Si/$p$-Si interface. The dependence of $|U_{PV}|^{\max}$ on the excitation intensity is presented in Fig. 3 (curve *3*). Taking into consideration the fact that this dependence saturates and using the

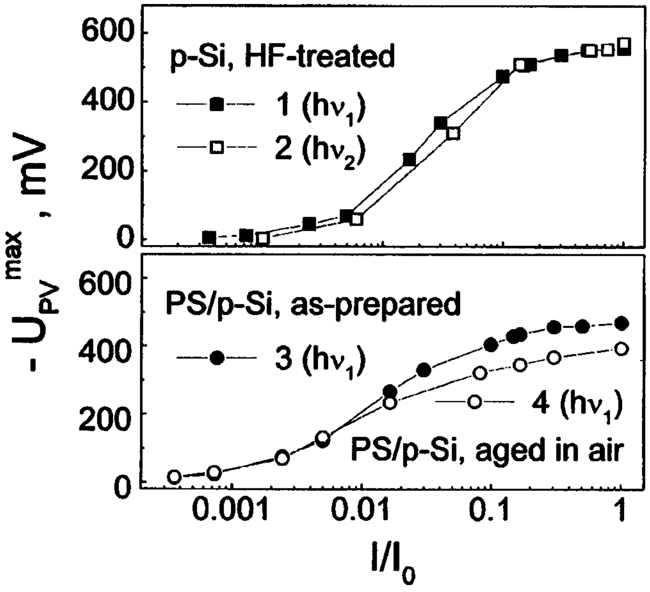

FIG. 3. Maximum photovoltage amplitude $|U_{PV}|^{\max}$ versus excitation intensity $I$ under illumination with light with photon energies $h\nu_1$ and $h\nu_2$ for $p$-Si (1, 2) and *por*-Si/$p$-Si samples: 3—freshly prepared, 4—oxidized. In the figure *por*-Si is designated as PS.

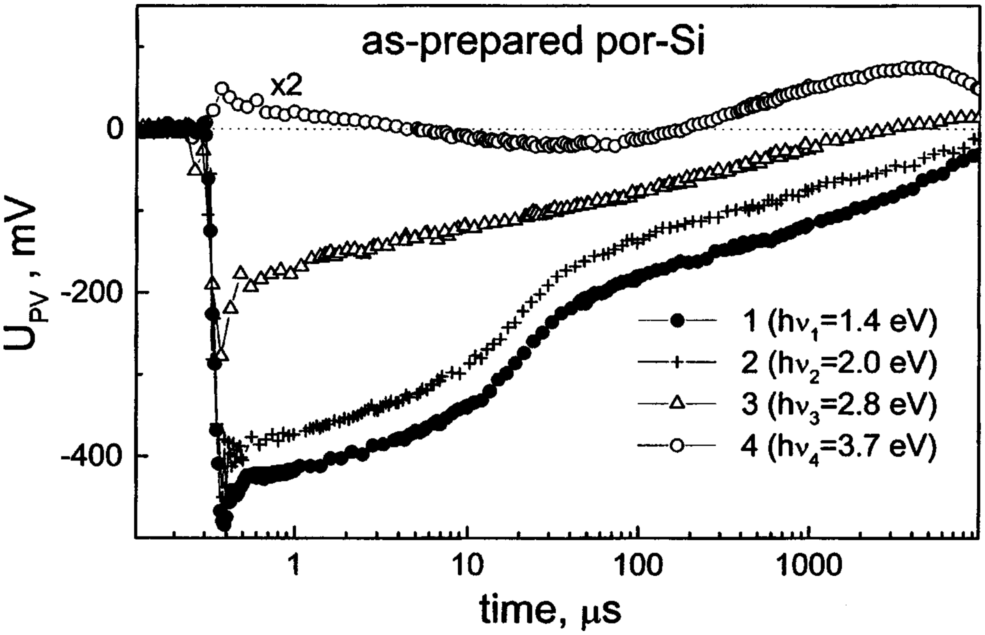

FIG. 4. Kinetics of the photovoltage $U_{PV}$ for as-prepared *por*-Si/*p*-Si structures upon excitation with laser pulses with the photon energies $h\nu_i$ indicated in the figure.

expressions (1) and (2) presented above, we obtain that the initial bending of the energy bands in *p*-Si at the *por*-Si/*p*-Si interface is of the order of 0.51 eV. This value is less than $Y_0$ for the *p*-Si surface treated in the same electrolyte. The value of $Y_0$ can decrease as a result of charge trapping and (or) differences in the electron energies in *por*-Si and *c*-Si. The latter is a result of the quantum confinement of charge carriers in *por*-Si nanostructures.

An important feature of the kinetics of PPV of freshly prepared *por*-Si/*p*-Si structures is the presence of persistent ''tails'' and the sharp decrease of the amplitude under illumination with photons with energies $h\nu_3$ and, especially, $h\nu_4$ (Fig. 4). The tails of the functions $U_{PV}(t)$ are probably due to charge transfer processes occurring in the porous layer itself. The weak signal for $h\nu_3$ could be due to light absorption in *por*-Si itself. According to Fig. 1, on account of absorption in the porous layer the intensity of light with $h\nu_3$ reaching the substrate is ten times lower than that of radiation with $h\nu_1$. Since *por*-Si is not transparent for photons with energies $h\nu_4$, the PPV amplitude has its lowest value. This value ($U_{PV} \simeq 20$ mV) is close to $U_D$. In our view, this means that there is no built-in electric field in as-prepared porous layers. However, electric fields can be induced by charging under illumination. Positive charging can explain the tails in the curves $U_{PV}(t)$ for $t > 100$ μs (Fig. 4, curve *4*).

### 3.4. PPV measurements for oxidized *por*-Si/*p*-Si structures

Let us discuss the results obtained for oxidized *por*-Si/*p*-Si structures (Fig. 5). As one can see from the figure, there are some differences in the PPV kinetics between oxidized and as-prepared samples. In the first place, the value of $|U_{PV}|^{\max}$ is lower. It was found from the saturating dependences $|U_{PV}|^{\max}$ versus excitation intensity (Fig. 3, curve *4*) that the bending of energy bands at the *por*-Si/*p*-Si interface of oxidized structures was equal to approximately 0.43 eV. In the second place, the PPV kinetics under excitation with photons in the range $h\nu_1 - h\nu_3$ is markedly nonexponential. This is probably due to strong trapping of positive charge in the porous layer. The nonmonotonic behavior of the PPV kinetics was observed 2 μs after illumination with $h\nu_1$ and $h\nu_2$ photons (Fig. 5). In our view, this is due to trapping and rapid ejection of positive charge. In the third place, an appreciable PPV amplitude occurred in the case where *por*-Si was irradiated with strongly absorbed light with $h\nu_4$ (Fig. 5). As follows from our analysis, the form and amplitude of the PPV after illumination with ultraviolet light can be explained by reabsorption of the *por*-Si PL by the *p*-Si substrate. We note that the oxidized samples were characterized by a higher quantum yield of PL. According to our measurements, close values of $|U_{PV}|^{\max}$ were recorded upon illumination with $h\nu_4$ photons (Fig. 5) and upon illumination with $h\nu_1$ photons and amplitude which was reduced to the intensity $I_0/200$ (Fig. 3, curve 4). This gives $\eta$ of the order of 0.5% for PL excited by $h\nu_4$ light, in agreement with the value obtained from direct optical measurements (see above).

## 4. MODEL OF PHOTOVOLTAIC PHENOMENA

A scheme of photovoltaic processes in *por*-Si/*p*-Si structures can be proposed on the basis of the experimental results obtained by us (Fig. 6). It is based on two main assumptions:

1) separation of nonequilibrium charge carriers in the space-charge region of the silicon substrate at the interface with *por*-Si and

2) trapping of positive charge on the surface of the nanostructures.

The process (1) leads to rectification of the bands at the *por*-Si/*p*-Si interface. The photovoltage obtained under illu-

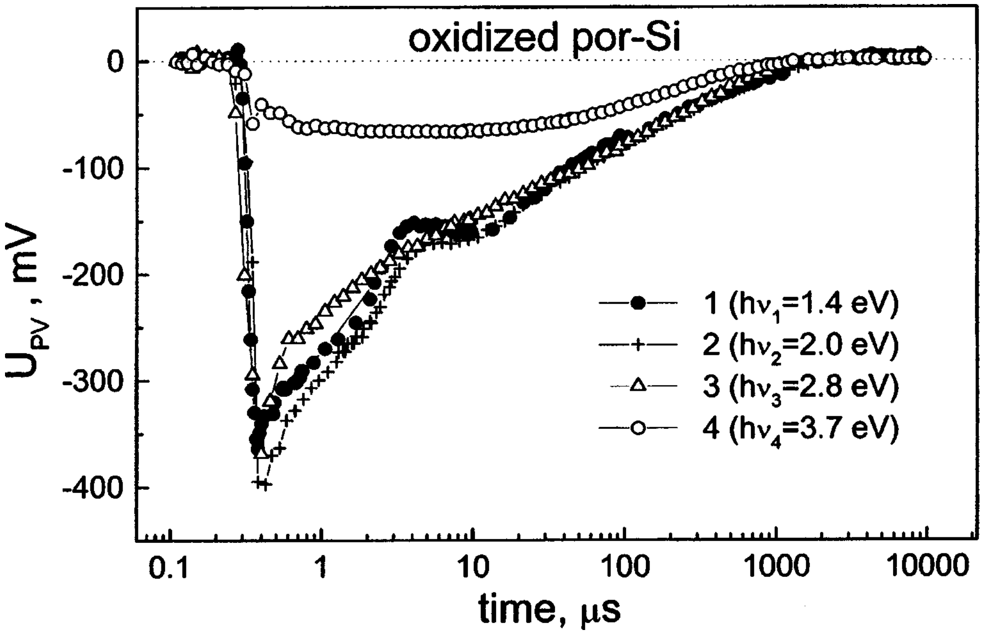

FIG. 5. Kinetics of the photovoltage $U_{PV}$ for oxidized *por*-Si/*p*-Si structures upon excitation with laser pulses with the same photon energies as in Fig. 3.

mination with weakly absorbed light with $h\nu=1-2$ eV was always negative. It should be noted that the component (1) can be induced by *por*-Si photoluminescence. This effect is strongest for ultraviolet irradiation of samples with a high quantum yield (Fig. 5, curve *4*).

When discussing the process (2), both fast and slow states should be taken into consideration. Fast states determine the nonexponential features of the kinetics $U_{PV}(t)$ and probably participate in the formation of the photovoltage signal in CPD measurements.[11,12] The charging of slow states engenders a photovoltage with a long relaxation time (greater than 1 s), so-called optical charging.[12] However, in our view, there is only one reason for the fast and slow photovoltage components—''optical doping'' of *por*-Si nanostructures as a result of charge separation in silicon ''wires'' and formation of a positive ''optical'' charge on the surface of the wires. In *por*-Si nanostructures, where the characteristic lengths are much less than the Debye screening length, charged surface defects play the role of charged impurities and produce a shift of the band edges relative to the Fermi level (Fig. 6). The process discussed is essentially optical doping of *por*-Si and determines the character of photovoltage formation in this material.

It can be shown that both the positive and negative photovoltages in the experimental samples are due to trapping of only the positive charge, which happens in different regions of the porous layer. Indeed, when light is absorbed only in the silicon substrate, rectification of the bands in *p*-Si (see above) and diffusion of nonequilibrium charge carriers from *p*-Si into *por*-Si occur. The density of charged centers decreases from the boundary with the substrate into the volume of *por*-Si on thicknesses of the order of the diffusion length of the charge carriers. This leads to band bending in *por*-Si and formation of a negative component of the photovoltage (Fig. 6). It is obvious that the tails of the PPV kinetics (Figs. 4 and 5) and the high amplitude of the CPD signal[12] under illumination with $h\nu=1.4-2$ eV photons could be due to these diffusion and charge-trapping processes.

When the exciting light is strongly absorbed in *por*-Si ($h\nu=3-4$ eV), optical doping is maximum near the sample surface and decreases in a direction toward the substrate. As a result, the curves $U_{PV}(t)$ become positive for freshly prepared samples under irradiation with $h\nu_4$ phtons (Fig. 4). For oxidized structures, together with the appearance of a positive photovoltage, there appears a signal due to absorption of the PL of the porous layer by the *p*-Si substrate (see above). As a result of competition between these two processes, the PPV kinetics upon irradiation with $h\nu_4$ photons exhibits

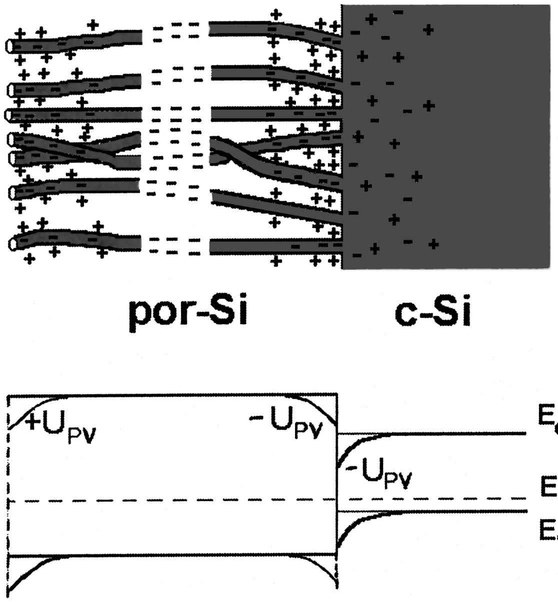

FIG. 6. Schematic diagram of the *por*-Si/*p*-Si structure and the energy diagram of the structure before illumination (thick lines) and after illumination (thin lines).

markedly nonexponential nature (Fig. 5). We note that the proposed mechanism explains the positive photovoltage observed in CPD experiments for irradiation with high-energy photons.[12] For oxidized samples the charge-exchange times for traps increase because of the potential barrier of the oxide, resulting in prolonged optical charging.[11,12]

As far as the nature of the traps participating in the photovoltage formation in *por*-Si is concerned, it is known that adsorbed molecules (for example, water) can form positively charged centers.[19] Indeed, we observed a decrease in the amount of trapped charge in CPD experiments after the samples are heated[11,12] at $T=450$ K, which is sufficient for desorption of weakly bound water molecules from the Si surface.[19]

## 5. CONCLUSIONS

In the present work photovoltaic phenomena in *por*-Si/$p$-Si structures were investigated by the contact-free pulsed-photovoltage method. Both as-prepared and oxidized structures were used. For comparison, HF-treated single-crystal $p$-Si samples were also analyzed. The data obtained by us indicate the presence of a barrier photovoltage at the boundary of the porous layer and the substrate, as well as the existence of a surface photovoltage. The latter forms as a result of positive charging of the surface of the nanostructures and the consequent optical doping of the porous layer. It was shown that the optical doping, which is nonuniform over the depth of the porous layer, produces positive and negative photovoltages.

We thank P. K. Kashkarov and S. N. Kozlov for valuable remarks and for helpful discussions of the results.

This work was supported in part by the Russian State Scientific and Technical Programs ''Surface atomic structures'' (Project 96-1.33) and ''Physics of solid-state nanostructures'' (Project 1-064).

*E-mail: vtim@ofme.phys.msu.su

---

[1] K. Jung, S. Shih, and D. Kwong, J. Electrochem. Soc. **140**, 346 (1993).

[2] B. Hamilton, Semicond. Sci. Technol. **10**, 1187 (1995).

[3] M. Ben-Chorin, F. Moller, and F. Koch, Phys. Rev. B **49**, 2981 (1994).

[4] M. Ben-Chorin, F. Moller, F. Koch, W. Schirmacher, and M. Eberhard, Phys. Rev. B **51**, 2199 (1995).

[5] J. P. Zheng, K. L. Liao, W. P. Shen, W. A. Anderson, and H. S. Kwok, Appl. Phys. Lett. **61**, 459 (1992).

[6] G. Smestad and M. Kunst, Sol. Energy Mater. Sol. Cells **26**, 277 (1992).

[7] T. Ozaki, M. Araki, S. Yoshimura, H. Koyama, and N. Koshida, J. Appl. Phys. **76**, 1986 (1994).

[8] F. Yan, X.-M. Bao, and T. Gao, Solid State Commun. **91**, 341 (1994).

[9] N. J. Pulsford, G. L. J. A. Rikken, Y. A. R. R. Kessener, E. J. Lous, and A. H. J. Venhuizen, J. Appl. Phys. **75**, 636 (1994).

[10] D. W. Boeringer and R. Tsu, Appl. Phys. Lett. **65**, 2332 (1994).

[11] Th. Dittrich, P. K. Kashkarov, E. A. Konstantinova, and V. Yu. Timoshenko, Thin Solid Films **255**, 74 (1995).

[12] P. K. Kashkarov, E. A. Konstantinova, A. B. Matveeva, and V. Yu. Timoshenko, Appl. Phys. A **62**, 547 (1996).

[13] V. Yu. Timoshenko, P. K. Kashkarov, A. B. Matveeva E. A. Konstantinova, H. Fliether, and Th. Dittrich, Thin Solid Films **276**, 216 (1996).

[14] V. Yu. Timoshenko, J. Rappich, and Th. Dittrich Jpn. J. Appl. Phys. **36**, L58 (1996).

[15] E. Yablonovitch, D. L. Allara, C. C. Chang, T. Gmitter, and T. B. Bright, Phys. Rev. Lett. **57**, 249 (1986).

[16] E. O. Johnson, Phys. Rev. **111**, 153 (1958).

[17] Th. Dittrich, M. Braue, and L. Elstner, Phys. Status Solidi **137**, K29 (1993).

[18] K. Watanabe, Semicond. Sci. Technol. **9**, 370 (1994).

[19] V. F. Kiselev and O. V. Krylov, *Electronic Phenomena in Adsorption and Catalysis on Semiconductors and Dielectric*, Springer-Verlag, Berlin, 1987.

[20] D. G. Yarkin, E. A. Konstantinova, and V. Yu. Timoshenko, Fiz. Tekh. Poluprovodn. **28**, 669 (1995) [Semiconductors **29**, 348 (1995)].

[21] N. B. Hannay [Ed.], *Semiconductors*, Reinhold Publishing Corp., N. Y., 1959 [Russian translation, Inostr. Lit., Moscow, 1962].

Translated by M. E. Alferieff

# Effect of annealing in an atomic-hydrogen atmosphere on the properties of amorphous hydrated silicon films and the parameters of *p–i–n* structures based on them

M. M. Mezdrogina, A. V. Abramov, G. N. Mosina, I. N. Trapeznikova, and A. V. Patsekin

*A. F. Ioffe Physicotechnical Institute, Russian Academy of Sciences, 194021 St. Petersburg, Russia*

(Submitted June 19, 1997, accepted for publication July 14, 1997)
Fiz. Tekh. Poluprovodn. **32**, 620–626 (May 1998)

The decrease in the density of dangling silicon–silicon bonds in *a*-Si:H films as a result of annealing in an atomic-hydrogen atmosphere is determined by their density in the initial (nonannealed) film. The change in the total hydrogen density in *a*-Si:H films, annealed in an atomic-hydrogen atmosphere, is determined by the type of silicon–hydrogen bonds and the impurity content: The hydrogen content can decrease to 1 at. % in the presence of monohydride bonds (2020 $\mathrm{cm}^{-1}$) and no change is observed in the hydrogen content in the presence of oxygen ($\lesssim 0.1$ at. %). A decrease in the defect density as a result of annealing in an atomic-hydrogen atmosphere is observed for all films. The Staebler–Wronski effect — AM-1 irradiation for 10 h — is observed for all films irrespective of the total hydrogen density, the type of silicon-hydrogen bonds, and the presence of oxygen. © *1998 American Institute of Physics.* [S1063-7826(98)02205-4]

## 1. INTRODUCTION

Even though amorphous hydrated silicon (*a*-Si:H) films are used in the fabrication of a number of devices — phototransducers, field-effect transistors, radiation sensors, the problem of controlling the density and types of defects in the disordered structural network and the problem of the formation of the morphology of the structure of the films remain urgent.

An entire series of deposition methods making it possible to reduce to a minimum the density of defects in the disordered structural network ($10^{14}-10^{15}\ \mathrm{cm}^{-3}$), local nonuniformities, and inhomogeneities of the microstructure, which arise during deposition of two-component amorphous films (*a*-Si:H), has been proposed.[1,2]

It is also known that the questions of the stability of the photoelectric parameters under the influence of irradiation (Staebler–Wronski effect), which arise in connection with defect formation as a result of the conversion of weak silicon–silicon bonds into dangling bonds, could be associated with the presence of ''excess'' hydrogen in the disordered structure of the *a*-Si:H network.

The problem of depositing *a*-Si:H films with a total hydrogen density equal to the density of dangling silicon–silicon bonds in the disordered structural network ($10^{19}-10^{20}\ \mathrm{cm}^{-3}$) of nonhydrated amorphous silicon cannot be solved on the basis of the conventional deposition methods (decomposition of silane mixtures in a high-frequency cyclotron resonance discharge, ''hot wall,'' and others), if the total defect density in the films (dangling silicon–silicon bonds) does not exceed $10^{16}\ \mathrm{cm}^{-3}$.

Films with hydrogen concentration less than 6 at. % cannot be obtained by varying the basic technological parameters of the deposition process — the growth rate, the substrate temperature, and the construction of the reactor.[2,3]

At the same time, the problem of obtaining *a*-Si:H films with the minimum hydrogen density equal to the density of dangling silicon–silicon bond is important not only from the standpoint of optimizing the optoelectronic parameters of *a*-Si:H and improving device parameters based on the films, specifically, suppressing the Staebler–Wronski effect, but also from the standpoint of investigating a single-component single-phase material with the minimum density of defects in the disordered structural network.

Another, no less important, problem is hydrogen passivation of dangling silicon–silicon bonds in the process of *a*-Si:H crystallization for the purpose of obtaining films with the maximum possible specific displacement $(\mu\tau)_n$ of the electrons, which is very important for the fabrication of thin-film field-effect transistors. In this case the films must contain at least 6–8 at. % hydrogen after high-temperature annealing.

There are several methods for solving these problems.

1. Deposition of *a*-Si:H films at high substrate temperatures. This makes it possible to decrease the hydrogen content in the films. The drawback of this method is that the hydrogen density profile over the film thickness is nonuniform.[2]

2. The hydrogen content can be decreased by high-temperature or very prolonged annealing in vacuum, but in this case the defect density in the films increases.[4]

3. Bombardment of the film surface with Si ions. This also increases the defect density.

4. Annealing in an atomic-hydrogen atmosphere. This is the so-called ''chemical etching'' method in which the total hydrogen density decreases as a result of a decrease in the density of weak, strained silicon–hydrogen bonds.[5]

Our objective in the present work is to investigate the effect of annealing in an atomic-hydrogen atmosphere on the parameters of *a*-Si:H films with different oxygen concentrations. Special attention will be given to films with a total hydrogen content of no more than 1 at. %.

TABLE I. Technological parameters of deposition and annealing of *a*-Si:H films.

| Technological parameters | *a*-Si:H films | | |
|---|---|---|---|
| | I | II | III |
| Deposition temperature, $T_s$ °C | 380 | 380 | 340 |
| Deposition rate, Å/s | 0.8−2.5 | 0.5−0.8 | 1−1.5 |
| Annealing temperature, $T_a$, °C | 380 | 380 | 380 |
| Gas mixture pressure (Torr) during deposition | $(2-3)\times10^{-2}$ | $(1-2)\times10^{-2}$ | $4\times10^{-2}$ |
| Gas mixture pressure during annealing | $(2-3)\times10^{-2}$ | $(1-2)\times10^{-2}$ | $4\times10^{-2}$ |
| Annealing regime, min | *a*,*c* | *a* | *a*,*b*,*c* |
| Annealing time, min | 30–60 | 30 | 30–60 |

## 2. PRODUCTION AND METHODS OF INVESTIGATION OF *a-SI:H FILMS*

Nondoped and doped films ($n$- and $p$-type conductivity) were obtained by the method of high-frequency decomposition of monosilane in tetrode and triode (using a mobile shutter) systems. As shown earlier,[6] the use of multielectronic systems (tetrode, triode) makes it possible to control the position of the Fermi level $\varepsilon_F$ by varying the impedance of the intermediate grids without changing the technological parameters.

The deposition parameters and the annealing regimes of the experimental films, which differ by the type of silicon-hydrogen bonds and the total hydrogen density, are presented in Table I. The deposition and annealing temperatures are the same for all types of films. The annealing regime was as follows: immediately after deposition, no exposure in air (a), alternate annealing and deposition (b), and annealing after exposure in air (c).

Table II shows the types of silicon-hydrogen bonds, the total hydrogen concentration before and after the films are annealed, the change in the position of $\varepsilon_F$, and the activation energy of the temperature dependence of the dark conductivity—$\Delta F_\sigma$.

Quartz, devitrified glass, and Corning 7059 glass were used as substrates. KDB-4.5 and KBD-10 single-crystal silicon with crystallographic orientations ⟨111⟩ and ⟨100⟩ was used for depositing films when determining the types of silicon-hydrogen bonds and the total hydrogen content by means of infrared spectroscopy (the 630 cm$^{-1}$ band was analyzed). An IR Fourier spectrometer was also used to determine the total hydrogen content and to identify the silicon-hydrogen and silicon-oxygen bonds. The doped layers were deposited from gas mixtures—silane–phosphine and silane-diborane. The doping level equals 0.3 at. % in the case of $p$-layer deposition and 0.25 at. % ($B_2H_6/SiH_4+B_2H_6$, $PH_3/SiH_4/PH_3$) in the case of $n$-layer deposition. As shown earlier,[7] a low doping level in the case of deposition of a $p$-layer makes it possible to shift the maximum of the photosensitivity into the short-wavelength region of the spectrum, while a low doping level in the case of $n$-layer deposition makes it possible to increase the specific displacement $(\mu\tau)_p$ of the holes.[7]

*p–i–n* Structures with a Shottky barrier (*n–i–*Pt) were deposited on different substrates: on devitrified glass with a current-conducting electrode and on glass with current-conducting layers of tin and indium oxides. All structures obtained were dried on the $p$-layer side.[6] The layer thicknesses were varied as follows: from 200 to 800 Å for the $p$-layer, 150 to 1000 Å for the $n$-layer, and 1500 to 8000 Å for the nondoped layer. The (*p–i–n, n–i–*Pt) structures were formed on different films — nonannealed, annealed after deposition of the $p$- and $i$-layers without exposure in air, and with alternate deposition and annealing in the case of deposition of $p$- and $i$-layers. Oxygen was added from water vapor during deposition of nondoped layers in order to shift the maximum of the photosensitivity into the short-wavelength region of the spectrum. The density of dangling silicon–silicon bonds for II–III-type films differed very little ($N_{D_{\mathrm{II}}}\sim N_{D_{\mathrm{III}}}$).

## 3. MEASUREMENTS OF THE FILM PARAMETERS

The absorption spectra were measured on an IFS-113V IR spectrometer in the range 530–4500 cm$^{-1}$ with a resolution of 2.0 cm$^{-1}$ and averaging over 1000 scans. Absorption lines due to the bending vibrational modes of Si–H bonds near 645 cm$^{-1}$ and stretching vibrations of the same bonds in the range 2000–2100 cm$^{-1}$ can be seen clearly in the spectra.

It was assumed on the basis of the data in Ref. 7 that annealing in an atomic-hydrogen atmosphere makes it pos-

TABLE II. Total hydrogen concentration ($C_H$) before and after annealing, type of silicon-hydrogen bonds, presence of oxygen, position of $\varepsilon_f$, activation energy of the temperature dependence of the dark conductivity ($\Delta E_\sigma$) in *a*-Si:H films.

| Film type | Total hydrogen content before annealing, $C_H$, % | Silicon-hydrogen bond type | Oxygen content, % | $\varepsilon_c-\varepsilon_f$, eV | $\Delta\varepsilon_\sigma$, eV | $C_H$ after annealing, % |
|---|---|---|---|---|---|---|
| I | 8−10 | Si–H (2000 cm$^{-1}$) | <0.1 | 0.63−0.79 | 0.73−1.05 | 5−8 |
| II | 8−15 | Si–H (2020 cm$^{-1}$) | <0.1 | 0.65−0.73 | 0.78−0.90 | 1−10 |
| III | 10−17 | Si–H (2020 cm$^{-1}$) | ~0.1 | 0.63−0.77 | 0.73−0.96 | 10−16 |

sible to obtain a more uniform hydrogen density profile over the film thickness, i.e., annealing promotes smoothing of the nonuniformities on the substrate–*a*-Si:H layer interface.

The microstructure of the obtained films was investigated by transmission electron microscopy with an accelerating voltage of 100 kV. Light-field image and microdiffraction regimes were used. The samples for investigating microstructure were prepared by chemical-dynamic etching from the substrate side.

The defect density (dangling silicon–silicon bonds), $N_D$, and the Urbach parameter were determined on the basis of optical absorption data obtained by the constant photocurrent method.

The photoconductivity was measured with photon flux $I = 10^{15}$ photons/cm$^2$ with $h\nu = 2$ eV at room temperature.

The refractive index of type-I and -III films was determined from ellipsometry data. The optical band gap and the refractive index were determined from the transmission spectra.

The photoluminescence of the films investigated was measured by the standard method at $T = 77$ K. Excitation was performed with a 120-mW Ar laser with photon energy 2.54 eV. The spectral characteristics were determined using illumination by a hydrogen lamp and an incandescent lamp (in the range from 0.25 to 0.80 $\mu$m).

## 4. RESULTS AND DISCUSSION

Figures 1a and 1b display the variation of the activation energy of the temperature dependence of the dark conductivity and photoconductivity of films before and after annealing in an atomic-hydrogen atmosphere (regime a) and curves of the photo- and dark conductivities $(\sigma_{ph}, \sigma_d)^{3,4}$ versus the quantity $\varepsilon_c - \varepsilon_F$ determined from the expression $\varepsilon_c - \varepsilon_F = kT\ln(\sigma_0/\sigma)$, where $\varepsilon_c$ is the conduction band edge, $\varepsilon_F$ is the position of the Fermi level, and $\sigma_0 = 150\ \Omega^{-1}\cdot$ cm$^{-1}$, and versus the activation energy $\Delta E_\sigma$ of the dark conductivity (determined experimentally). We see that the position of the Fermi level changes — it shifts to the center of the mobility gap — $E_g$. A similar shift of the Fermi level is also observed in the case of vacuum annealing.[4] In contrast to vacuum annealing, in the case of annealing in an atomic-hydrogen atmosphere the photoconductivity is observed to increase, i.e. the ratio of the photoconductivity after annealing to the photoconductivity before annealing depends on the position of the Fermi level and the activation energy of the dark conductivity in the initial film, and it is large for $\Delta E_\sigma \geqslant 0.90$ eV. The changes in the defect density in *a*-Si:H films as a result of annealing in an atomic-hydrogen atmosphere (Fig. 2) depend on the defect density in the initial film: The ratio $N_{D2}/N_{D1}$ is all the larger, the lower the preannealing defect density in the film. A change in the charge state of defects of the type $D^- \rightarrow D^0$ or $D^+ \rightarrow D^0$ could be the reason why the total defect density decreases. It was shown in Ref. 8 that the energy position of defects in the mobility gap is determined by the mechanism responsible for the production of the defects — during film growth. The variation of the growth kinetics, the conditions of annealing, determines the type and density of defects. A decrease of the density of ''floating'' bonds (quintuply coordinated silicon atoms) can also result in a decrease of $N_D$. The total defect density can also decrease as a result of the formation of nano- and microcrystallites, which decreases the stress in the structural network of amorphous silicon. The changes occurring in the defect density as a result of annealing are not correlated with a change in the hydrogen density. A small change in the total hydrogen density as a result of annealing in an atomic-hydrogen atmosphere could occur for different reasons:

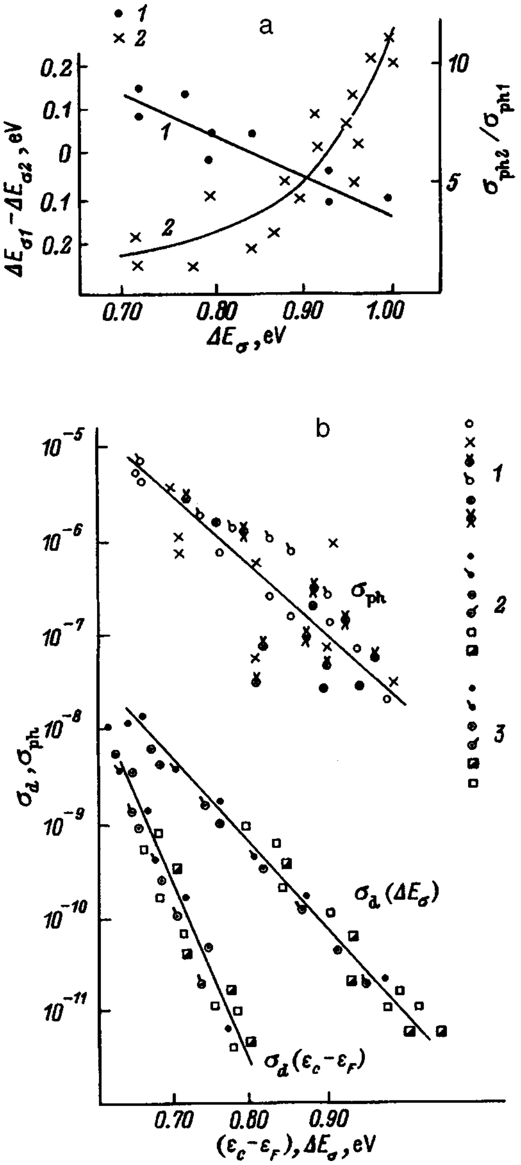

FIG. 1. a—Variation of the activation energy $\Delta E_\sigma$ of the temperature dependence of the dark conductivity (*1*) and photosensitivity $\sigma_{ph2}/\sigma_{ph1}$ (*2*) of *a*-Si:H films before and after annealing in an atomic-hydrogen atmosphere and b—photo- (*1*) and dark (*2, 3*) conductivities versus $\varepsilon_c - \varepsilon_F$ and $\Delta E_\sigma$ for *a*-Si:H films (types I, II, III) before and after annealing.

- Presence of homogeneous microstructure, low concentration of stressed, ''weak'' silicon-hydrogen bonds. It is known[7] that a homogeneous microstructure is observed in films with a low ratio of silicon dihydride to silicon monohydride, which corresponds to a low ratio of the intensities of the 2090 and 2000-cm$^{-1}$ lines.

The films investigated in the present work were distin-

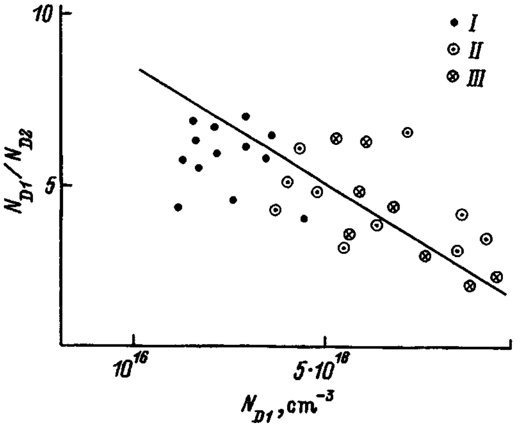

FIG. 2. Variation of the ratio of the defect densities in the disordered structural network in $a$-Si:H films (type I, II, III) before ($N_{D1}$) and after ($N_{D2}$) annealing in an atomic-hydrogen atmosphere.

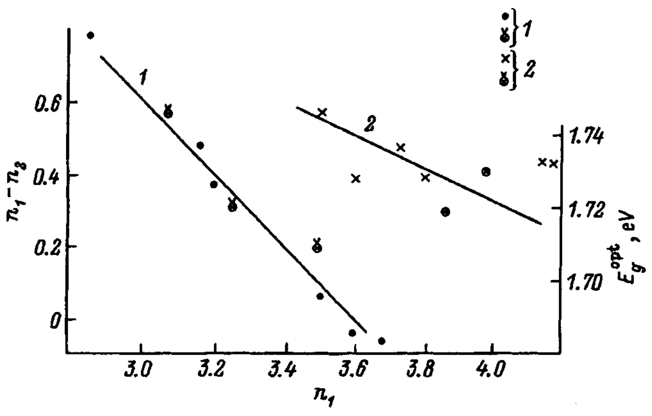

FIG. 3. Variation of the refractive index $n_1-n_2$ (*1*) and optical band gap $E_g^{\text{opt}}$ (*2*) of $a$-Si:H films before and after annealing as a function of the refractive index of the initial film.

guished by the degree of nonuniformity of the microstructure, and the different change in the total hydrogen density could be due to different values of the ratios of the concentrations of silicon dihydride to silicon monohydride in the initial film. For example, type-I films had only monohydride bonds (2000 $\text{cm}^{-1}$), type-II films had clustered monohydride bonds (2020 $\text{cm}^{-1}$), and type-III films had monohydride bonds (2020 $\text{cm}^{-1}$) and silicon-oxygen bonds (1060 $\text{cm}^{-1}$). A change in the total hydrogen content after annealing is not observed in type-III films and it is small in type-I films.

A small change in the hydrogen concentration as a result of annealing in an atomic-hydrogen atmosphere could be due to the following factors:

- Formation of monomolecular hydrogen ($H+H=H_2\uparrow$) and long $H_2$ lifetime in the presence of any third component. In this case the change in the total hydrogen content in $a$-Si:H films as a result of annealing in an atomic-hydrogen atmosphere will also be small, since the surface of the annealed film is coated with a layer of molecular hydrogen. Oxygen, small additions of which ($\lesssim$ 0.1 at. %), as shown in Ref. 7 , at deposition temperatures $T>300°\text{C}$ greatly increase the specific displacement $(\mu\tau)_n$ of electrons, can play a role as the ''third'' component, giving rise to a small change in the hydrogen concentration as a result of annealing. The increase in $(\mu\tau)_n$ is probably due to a modification of the film surface during annealing.

- Presence of nano- and microcrystallites in the initial film. In this case the observed changes in the defect density could be due to a decrease in the height of the potential barrier at the boundary between the amorphous and microcrystalline phases. The absence of changes in the hydrogen density in type-III films before and after annealing could be due to the presence of impurities and a second phase. Measurements of the optical parameters of photoluminescence and microstructure, presented in the following figures, attest to the presence of impurities.

Figure 3 shows data on the change in the refractive index $n$ and optical band gap as a function of the refractive index in the initial films. For type-III and -I films the refractive index is observed to decrease with a small change in hydrogen density. Annealing of type-III films in vaccuum ($T=400$ °C, annealing time — 2 h) and in an atomic-hydrogen atmosphere did not result in a large change in the photoelectric properties, while the hydrogen content decreased to 8 and 10 at. %, respectively. The values of the refractive index $n$ and $E_g^{\text{opt}}$ decreased. An increase in the refractive index and a small decrease in $E_g^{\text{opt}}$ were observed in type-I and -II films. A sharp decrease of $E_g^{\text{opt}}$ was not observed for films with a total postannealing oxygen content not exceeding 1 at. %. The photoluminescence spectrum for these films on single-crystal silicon also did not change much; only the intensity of photoluminescence increased (Fig. 4).

The decrease of the refractive index for films in which a small postannealing change in hydrogen density was observed could be due to an increase in the nonuniformity of the microstructure, since (Fig. 3) the decrease in the refractive index is all the larger, the lower its value in the initial

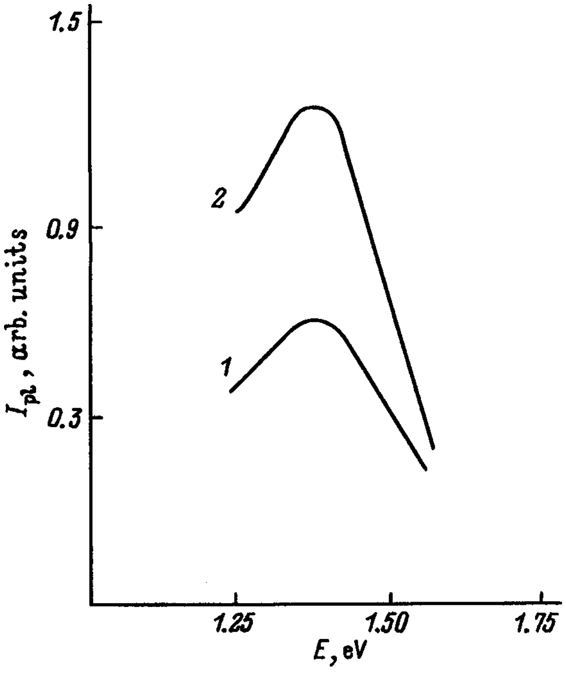

FIG. 4. Intensity of photoluminescence in $a$-Si:H films before (*1*) and after (*2*) annealing.

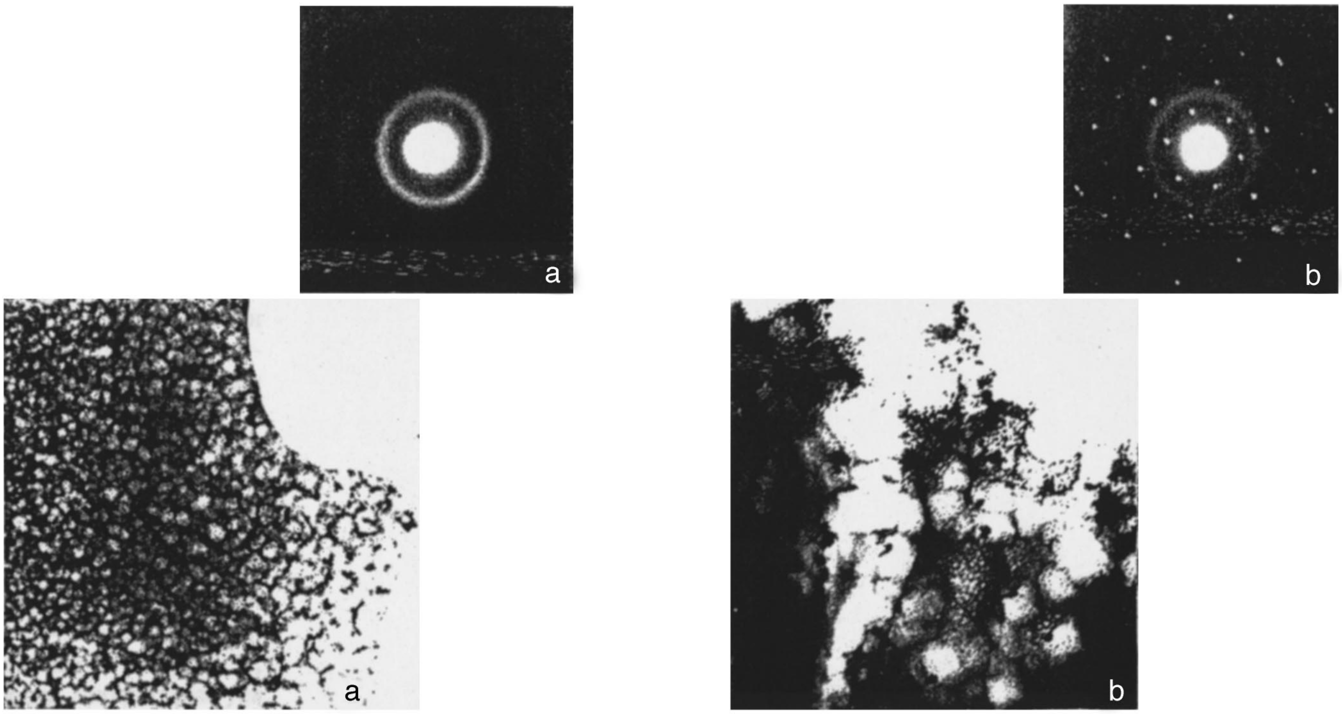

FIG. 5. a—Light-field contrast image of an $a$-Si:H film before annealing (hydrogen concentration 8.3 at. %, thickness 0.7 $\mu$m). Inset: Microdiffraction pattern of the same film. b—Light-field contrast image of $a$-Si:H:H film after annealing (hydrogen concentration less than 1 at. %, thickness 0.4 $\mu$m). Inset: Microdiffraction pattern of the same film.

film. An increase in the heterogeneity of the microstructure should lead to an increase in the dark conductivity and a decrease in the photoconductivity, which are not observed in this case (Fig. 1). An increase in the defect density is also not observed. According to the dc photocurrent method, the defect density decreases (Fig. 2).

It can be conjectured that microcrystallites form in the disordered structural network of amorphous silicon, as a result of which the stresses decrease and the height of the potential barriers (deformation) between the phases and therefore the defect density decrease. At the same time, the presence of an interface between the crystalline and amorphous phases increases the nonuniformity of the microstructure.

The changes occurring in the microstructure of $a$-Si:H films (type-I, where a decrease of hydrogen density is observed) deposited on a single-crystalline substrate and annealed in an atomic-hydrogen atmosphere are presented in Fig. 5. The insets in Figs. 5a and b show the changes in the microdiffraction pattern for the same films. One can see that prior to annealing the films were amorphous. Total crystallization occurs after annealing in the atomic-hydrogen atmosphere. The films crystallize in the orientation of the substrate on which they were deposited. The light-field image (Fig. 5a) attests to the presence of a columnar structure with grain size 100–250 nm. A high density of small formations, probably pores, with dimensions of 40–50 Å is seen inside the grains. The appearance of microcrystallites does not greatly change the photoluminescence spectra for the films. The intensity of photoluminescence at 1.36 eV increases; the energy position of this peak, characteristic for amorphous hydrated silicon, does not change (Fig. 4).

According to the IR spectroscopy data, the $a$-Si:H films deposited on different KDB silicon (4.5 and 10) substrates with different crystallographic indices ($\langle 100\rangle$ and $\langle 111\rangle$) have a different hydrogen content. The microstructure and microdiffraction pattern of the films are presented in Fig. 6. One can see that the information on the types of silicon-hydrogen bonds and the total hydrogen density is different for the same technological process and depends on the type of substrate.

Figure 7 shows the spectral characteristics of $p$–$i$–$n$ structures based on the $a$-Si:H films investigated. We see that the current sensitivity of the structures increases as a result of annealing in an atomic-hydrogen atmosphere. This agrees with the decrease in the defect density in nonhydrogenated layers subjected to annealing. This is valid for all structures formed on films which differ with respect to the initial defect density. A shift of the photosensitivity maximum is observed only in the case where the $p$-layer is subjected to annealing or $p$-layers were deposited alternately (with alternation of deposition and annealing). The maximum current sensitivity of the experimental structures at $\lambda = 0.35\ \mu$m equals 0.12 A/W.

Investigation of the Staebler–Wronski effect (AM-1 illumination for 10 h) on films before and after annealing showed that an increase of the defect density up to $8\times10^{16}-2\times10^{17}$ cm$^{-3}$ as a result of irradiation occurs for all types of films. For films whose hydrogen content does not exceed 1 at. % the change in the density of dangling bonds is small

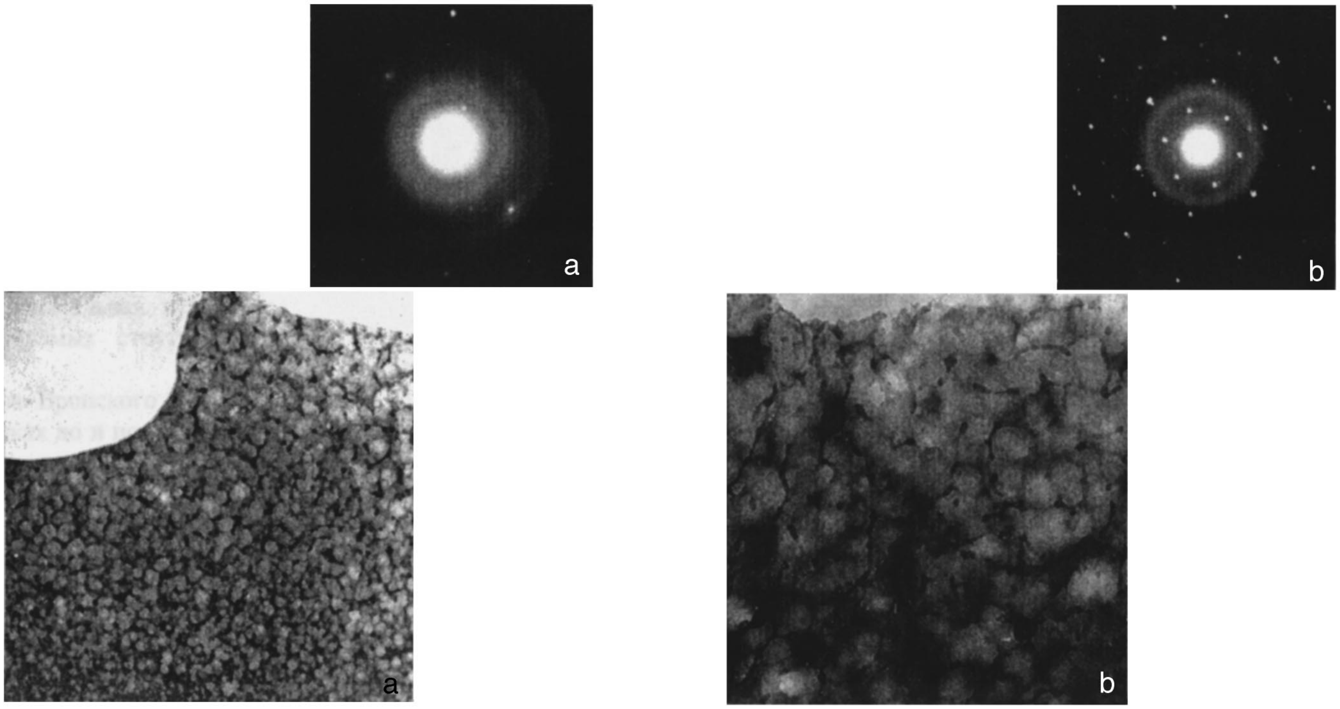

FIG. 6. a—Light-field contrast image of *a*-Si:H film deposited on a KDB-4.5 [100] substrate. Inset: Microstructural pattern of the same film. b—Light-field contrast image of an *a*-Si:H film deposited on a KDB-10 [111] substrate. Inset: Microstructural pattern of the same film.

— from $7\times10^{16}$ to $1.2\times10^{17}$ cm$^{-3}$. An increase in Urbach energy from 50–70 to 90–110 meV is observed at the same time.

The following conclusions can be drawn on the basis of the data obtained on the influence of annealing in an atomic-hydrogen atmosphere on the parameters of *a*-Si:H films and *p–i–n* structures based on such films.

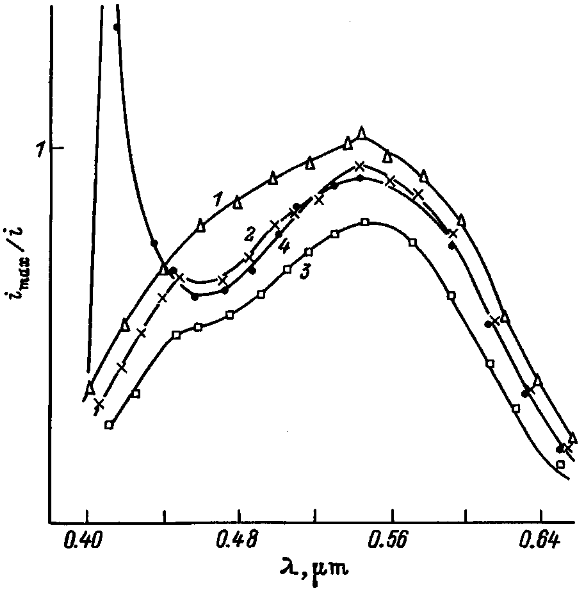

FIG. 7. Spectral characteristics of *p–i–n* structures based on *a*-Si:H films. *1*—Type-I *a*-Si:H films used as the *i*-layer, *2*—type-III *a*-Si:H films after annealing used as the *i*-layer, *3*—type-III *a*-Si:H:H films with alternate annealing of a *p*-layer during deposition was used as the *i*-layer.

1. The hydrogen content in films subjected to annealing can decrease to 1 at. %. The films have a total defect density not greater than $7\times10^{16}$ cm$^{-3}$. The optical band gap changes very little — from 1.76 to 1.73 eV.

2. The introduction of oxygen (0.1 at. %) from water vapor into the gas mixture makes it possible to keep the hydrogen density from changing as a result of annealing, but then the defect density in the disordered structural network decreases.

3. The change in the microstructure of *a*-Si:H films, the PL and refractive index intensities, and the shift of the Fermi level toward the center of the mobility gap are due to ''etching'' of the surface of the growing or deposited film by atomic hydrogen.

4. The total hydrogen content and the type of silicon-hydrogen bonds, which are determined by IR spectroscopy, depend on the type of crystallographic orientation of the single-crystal substrate.

5. The Staebler–Wronski effect is observed for films in which the total hydrogen content does not exceed 1 at. %. Conversion of weak silicon-silicon bonds into dangling bonds is probably due to the types of defects produced in the disordered structural network of amorphous silicon with the use of silicon-hydride radicals.

[1] T. Takahogi, S. Shiguba, H. Sakaia, K. Honishino, and H. Yashina, Jpn. J. Appl. Phys. **35**, L818 (1996).

[2] Q. Zhang, T. Nishino, H. Takasina, M. Kumeda, and T. Shimizu, Jpn. J. Appl. Phys. **35**, 4409 (1996).

[3] O. A. Golikova, M. M. Kazanin, O. I. Kon'kov, V. Kh. Kudoyarova, and E. I. Terukov, [Fiz. Tekh. Poluprovodn. **30**, 405 (1996) [Semiconductors **30**, 226 (1996)].

[4] O. A. Golikova, M. M. Kazanin, and Kh. Yu. Mavlyanov, Fiz. Tekh. Poluprovodn. **28**, 1329 (1994) [Semiconductors **28**, 752 (1994)].
[5] K. Asano, Appl. Phys. Lett. **56**, 533 (1989).
[6] M. M. Mezdrogina, O. A. Golikova, K. Arlauskas, G. Yushka, M. M. Kazanin, and R. Kaĭdarov, Neorg. Mater. **27**, 666 (1991).
[7] M. M. Mezdrogina, O. A. Golikova, M. M. Kazanin, and R. Ikramov, Zh. Tekh. Fiz. **62**, 108 (1992) [Sov. Phys. Tech. Phys. **37**, 55 (1992)].
[8] G. Schumm, Phys. Rev. B **49**, 2442 (1994).

Translated by M. E. Alferieff

SEMICONDUCTORS VOLUME 32, NUMBER 5 MAY 1998

# Nonmonotonic character of the growth-temperature dependence of the resistance of polycrystalline silicon films

D. V. Shengurov, D. A. Pavlov, V. N. Shabanov, V. G. Shengurov, and A. F. Khokhlov

*N. I. Lobachevskiĭ Nizhegorod State University, 603600 Nizhniĭ Novogorod, Russia*

(Submitted June 10, 1997; accepted for publication October 2, 1997)
Fiz. Tekh. Poluprovodn. **32**, 627–630 (May 1998)

The effect of the substrate temperature $T_s$ on the sheet resistance $R_s$ for polycrystalline Si films obtained by molecular-beam deposition was investigated. It was found that $R_s$ is a nonmonotonic function of $T_s$ for films doped with different impurities during the deposition process. An explanation based on a modified Setto model is proposed for the experimental results obtained. © *1998 American Institute of Physics.* [S1063-7826(98)02305-9]

## 1. INTRODUCTION

Polycrystalline silicon films (PSFs) are finding wide application in the preparation of thin-film transistors, solar cells, and integrated-circuit resistors.[1–3] The method of molecular-beam deposition (MBD) provides wide possibilities for varying the properties of PSFs.[4–6] It makes it possible to obtain PSFs at a low growth temperature and to vary independently over wide limits the growth rate and the dopant type and flux as well as to use certain factors which stimulate film growth (for example, application of an accelerating potential to the substrate).

In this paper we report the results of an experimental study of the variation of the sheet resistance of MBD-grown PSFs as a function of growth temperature and dopant type.

## 2. EXPERIMENTAL PROCEDURE

The layers were deposited by the MBD method using sublimating Si sources.[4] Rectangular 75×5×0.8 mm wafers grown from doped Si single crystals served as the sources of Si vapor and dopant. The sources were chosen with an impurity density so as to be able to obtain impurity fluxes which are close in magnitude. The computed values of the impurity fluxes obtained in the present experiment are presented in Table I. The Si flux was equal to $2\times10^{16}$ atoms/cm$^2\cdot$ s. The source was heated up to a working temperature of the order of 1380 °C by passing a current. The substrates consisted of Si plates, coated with a layer of thermally grown oxide of thickness $t\simeq0.4$ $\mu$m. The polycrystalline Si films were 0.15 and 1.5 $\mu$m thick.

The structure of the layers was monitored by electron diffraction in reflection and transmission. In films with thickness $d=0.15$ $\mu$m the size of the coherent scattering region (CSR) was determined according to the angular width $\Delta S$ of the diffraction maxima from the Scherrer formula

$$D=4\pi k/\Delta S, \tag{1}$$

where $k\approx1$ is the Scherrer constant. Film-surface morphology was investigated by electron microscopy on angular replicas. The sheet resistance of the PSFs was measured by the standard four-probe method.

## 3. RESULTS AND DISCUSSION

Figure 1 shows the diffraction patterns of films of thickness $d=0.15$ $\mu$m, grown at substrate temperatures $T_s=400$ and 450 °C. One can see that the transition from growth of amorphous to polycrystalline films occurs in this temperature interval. It should be noted that in the Si sublimation method a transition to epitaxial growth on a single-crystal substrate was observed in the same temperature interval.[7] The variation of the size of CSR and the grain size as a function of the film growth temperature is shown in Fig. 2.

Investigation of the 1.5-$\mu$m-thick films grown at $T_s>500$ °C established that they grow with a clearly defined texture in the growth direction (110). In addition, as the growth temperature increases, the angular spread of the texture decreases. Thus, the angular spread was equal to 58° for films grown at 570 °C and 17° for films grown at 640 °C.

The variation of the structural-morphological properties of PSFs as a function of deposition temperature is shown in Fig. 3. For example, in arsenic-doped films at low temperatures $T_s\simeq550$ °C films grow with round grains of uniform size. Grain size is observed to increase with $T_s$. As the growth temperature increases further ($T_s\simeq650$ °C), the contour of the film surface intensifies. Grains acquire a polyhedral shape, and their sizes become comparable to the film thickness ($d\simeq1$ $\mu$m). For PSFs doped with other impurities the structural-morphological properties vary with growth temperature similarly. Al-doped films are exceptions. At a growth temperature of $590\pm10$ °C grains up to 10 $\mu$m in size with an average size of 4.2 $\mu$m, which is much greater than the film thickness, were observed in the films.

Data on the substrate temperature $T_s$ dependences of the sheet resistance ($R_s$) of PSFs and epitaxial Si films with the same thickness grown under similar conditions on an oriented substrate as presented in Fig. 4. For all dopants the

TABLE I. Dopant flux from silicon source.

| Type of impurity | As | Sb | Al | Ga | B |
|---|---|---|---|---|---|
| Flux, atoms/cm$^2\cdot$ s | $6\times10^{12}$ | $1.2\times10^{12}$ | $1.6\times10^{12}$ | $8\times10^{12}$ | $8\times10^{12}$ |

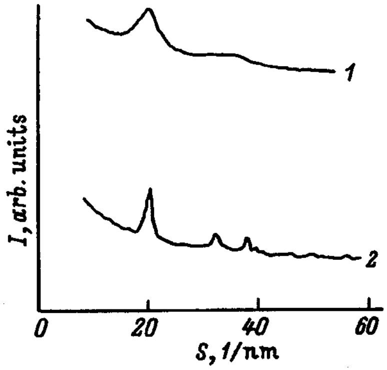

FIG. 1. Diffraction patterns of silicon films grown at substrate temperatures $T_s$, °C: *1* — 400, *2* — 450.

dependences $R_s(T_s)$ for PSFs are strongly nonmonotonic. For acceptor impurities $R_s(T_s)$ reaches a minimum in the range of growth temperatures $T_{s\,\mathrm{min}} \simeq 580-610$ °C, while for donor impurities $T_{s\,\mathrm{min}} \simeq 530$ °C. At the same time, $R_s$ for single-crystal films in the experimental temperature range is virtually constant and much lower than the minimum value for PSFs. The only exceptions are aluminum-doped PSFs, where the minimum value of $R_s$ is virtually identical to $R_s$ of single-crystal films.

The temperature dependences of the sheet resistance with the temperature decreasing from room temperature to liquid-nitrogen temperature were measured for separate PSFs. The observed dependences for most samples were of the form

$$R_s \sim \exp(-E/kT), \tag{2}$$

where $E$ is the activation energy, which is correlated with the value of $R_s$ at room temperature: The value of $E$ increases with increasing $R_s$. For the minimum values of $R_s$ the energy $E \leqslant 0.05$ eV, irrespective of the type of dopant, while for high-resistance films ($R_s \geqslant 10^8$ $\Omega/\square$)) $E = 0.45-0.5$ eV.

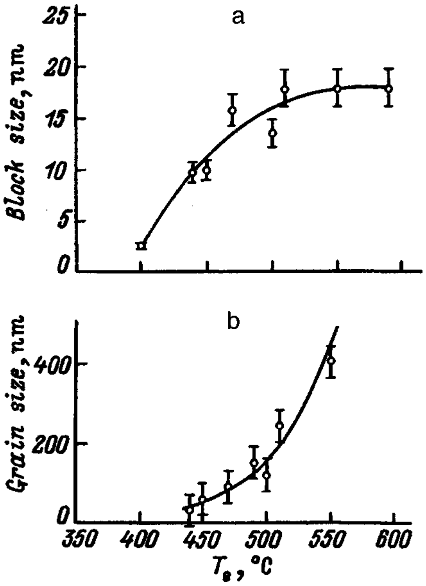

FIG. 2. Size of the coherent scattering regions (a) and grain size in polycrystalline Si films (b) versus growth temperature $T_s$.

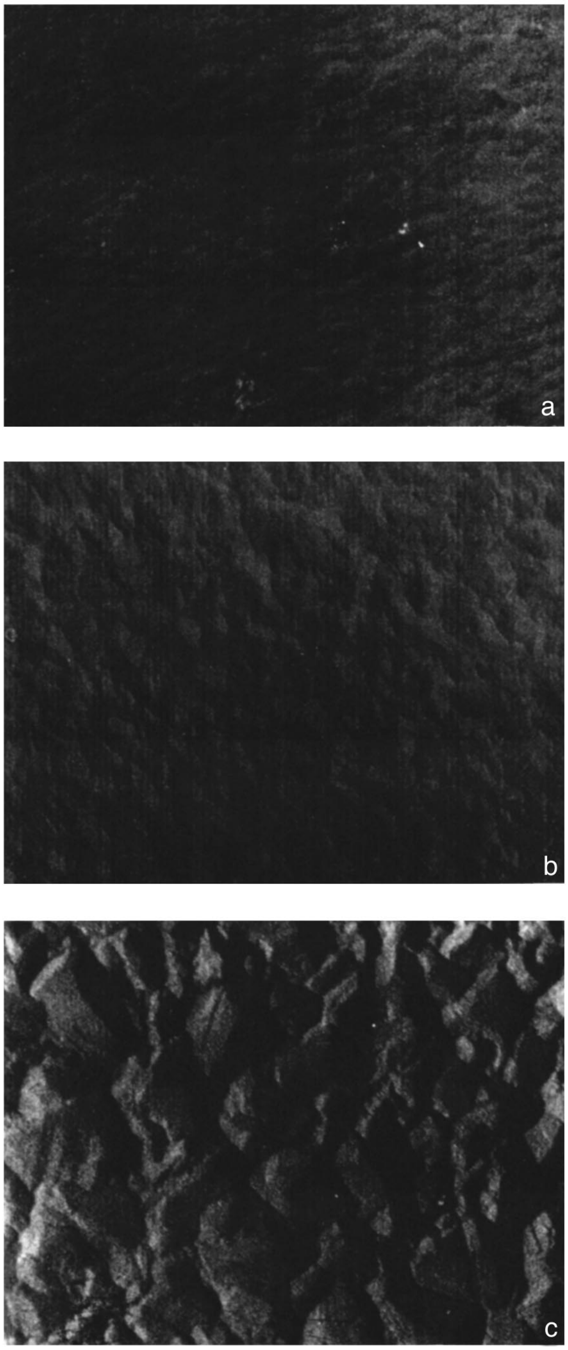

FIG. 3. Photomicrograph of angular replicas from the surface of polycrystalline Si films. The micrographs were obtained in an electron microscope (×15 000). Growth temperature $T_s$, °C: a — 550, b — 600, c — 650.

The observed variations of the film resistance as a function of growth temperature can be qualitatively explained on the basis of a modified Setto model[8,9] for partially depleted grains. The resistivity is given by

$$\rho = \frac{kN_c}{q\langle a\rangle ATN_G}\exp(qV_B/kT), \tag{3}$$

where $\langle a\rangle$ is the average grain size, $N_G$ is the density of the electrically active dopant, $V_B$ is the barrier height at grain

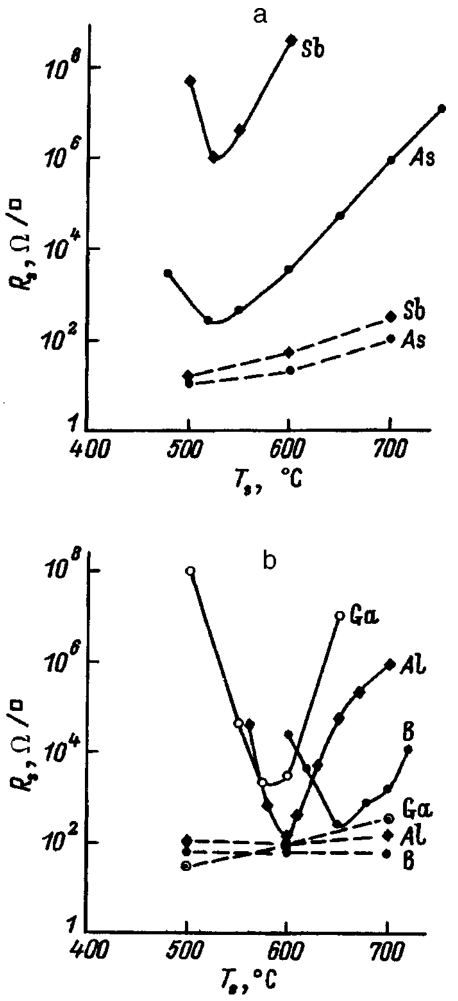

FIG. 4. Sheet resistance of polycrystalline Si films doped with donor impurities (a) and acceptor impurities (b) versus growth temperature $T_s$. The dashed lines show the same dependences for single-crystal films (data taken from Ref. 10 ).

boundaries, $A$ is the Richardson constant, $q$ is the electron charge, and $N_c \sim T^{3/2}$ is the effective density of states. The barrier height[9] is given by

$$V_B = Q_i^2/(8\varepsilon\varepsilon_0 q N_G), \quad (4)$$

where $Q_i$ is the charge on the grain interface.

In the substrate temperature range 500 °C $\leqslant T_s \leqslant T_{s\,\min}$ the grain size $\langle a \rangle$ increases and the boundary quality improves. As a result, $Q_i$ decreases, which results in a decrease of $V_B$ and $\rho$. In the range $T_s \approx T_{s\,\min}$ the grain size reaches almost its maximum value, while the resistance reaches its minimum value. As growth temperature increases further, mechanisms which decrease the density of electrically active impurity are apparently activated: impurity segregation on defects and intergrain boundaries and incomplete transport of the impurity from source to layer during growth.[10] As a result, $V_B$ starts to increase and this causes $R_s$ to increase. We explain the higher value of $T_{s\,\min}$ for B-doped films by weak segregation of B in Si.

## 4. CONCLUSIONS

The growth temperature dependence of the sheet resistance of polycrystalline Si films doped with different impurities in the process of molecular-beam deposition was investigated. In contrast to single-crystal films, where the resistance is virtually constant in the experimental temperature range, this dependence is nonmonotonic: The minimum value of $R_s(T_s)$ occurs at $T_{s\,\min} = 580-610$ °C for acceptor impurities and $T_{s\,\min} \simeq 530$ °C for donor impurities.

[1] M. K. Hatalis and D. M. Greve, IEEE Electron Device Lett. **EDL-8**, 361 (1987).
[2] Z. Shi and S. R. Wenham, Prog. Photovoltaics **2**, 153 (1994).
[3] P. H. L. Rasky, D. W. Greve, M. H. Kryder, and S. Dutta, J. Appl. Phys. **57**, 4077 (1985).
[4] D. A. Pavlov, V. G. Shengurov, D. V. Shengurov, and A. F. Khokhlov, Fiz. Tekh. Poluprovodn. **29**, 286 (1995) [Sov. Phys. Semicond. **29**, 142 (1995)].
[5] N. K. Annamalai *et al.*, Thin Solid Films **155**, 97 (1987).
[6] M. Matsui, Y. Shiraki, and E. Maruyama, J. Appl. Phys. **53**, 995 (1982).
[7] V. P. Kuznetsov, V. V. Postnikov, T. D. Komarova, E. A. Rozanova, T. N. Strizheva, and T. M. Zotova, Kristallografiya **20**, 626 (1975) [Sov. Phys. Crystallogr. **20**, 382 (1975)].
[8] J. Y. W. Setto, J. Appl. Phys. **46**, 5247 (1975).
[9] G. Harbeke [Ed.], *Polycrystalline Semiconductors. Physical Properties and Application*, Berlin, 1985 [Russian translation, Mir, Moscow, 1989].
[10] V. P. Kuznetsov and V. V. Postnikov, Kristallografiya **19**, 346 (1974) [Sov. Phys. Crystallogr. **19**, 211 (1974)].

Translated by M. E. Alferieff

SEMICONDUCTORS VOLUME 32, NUMBER 5 MAY 1998

# Characteristic features of the IR spectra of amorphous boron-doped hydrated silicon

I. A. Kurova and L. I. Belogorokhova*)

*Department of Physics, M. V. Lomonosov Moscow State University, 119899 Moscow, Russia*

A. I. Belogorokhov

*Institute of Rare Metals (Giredmet), 109017 Moscow, Russia*

(Submitted July 28, 1997; accepted for publication October 22, 1997)
Fiz. Tekh. Poluprovodn. **32**, 631–633 (May 1998)

Vibrational modes with wave numbers 1879 and 1848 $cm^{-1}$, previously observed only in the spectra of crystalline diborane, were observed in the optical spectra of $a$-Si:H(B) films. This indicates formation of complexes and bonds similar to those present in diborane, specifically, bridging hydrogen in the amorphous network. The change in the amplitudes of the observed modes after the films are annealed is attributed to structural rearrangements resulting in a decrease in the density of weakly bound bridging hydrogen and an increase in the density of quadruply coordinated boron. This explains the previously observed increase in the conductivity of annealed films. © *1998 American Institute of Physics.* [S1063-7826(98)02405-3]

The properties of amorphous hydrated silicon ($a$-Si:H) are determined by the presence of hydrogen and the microstructure of hydrogen bonds in the amorphous network. Hydrogen bonds can be successfully studied by infrared (IR) spectroscopy methods.[1] The hydrogen bonds with silicon in nondoped $a$-Si:H have been studied most extensively. The effect of impurities (specifically, boron) on hydrogen bonds has been investigated much less. In Ref. 2 , an absorption peak at frequency $\nu = 2475$ $cm^{-1}$ was observed in boron-doped films; this peak does not occur in the spectra of the nondoped material. The authors attribute the peak to a stretching vibrational mode of B–H bonds. No other features were observed in the spectrum. However, in Ref. 3 an absorption peak at $\nu = 1875$ $cm^{-1}$ was observed in crystalline silicon ($c$-Si) with hydrogen and attributed to a stretching vibrational mode of Si–H bonds which interact with nearby electrically inactive boron. On heating to temperature $T > 250$ °C Si–B bonds are formed instead of Si–H bonds as a result of hydrogen diffusion; boron becomes quadruply-coordinated, electrically active boron and the absorption peak at $\nu = 1875$ $cm^{-1}$ vanishes. The conductivity of $c$-Si increases with the degree of doping with boron. Similar conductivity increases after annealing were also observed in boron-doped $a$-Si:H.[4] For this reason, the investigation of the IR absorption spectra of boron-doped amorphous silicon $a$-Si:H(B) is of interest from the standpoint of the structure of the hydrogen bonds in $a$-Si:H in the presence of boron impurity and the change in this structure as a result of different external actions (including, high-temperature annealing) as well as for studying the correlation between structural rearrangements of the bonds and the change in the parameters of the material, for example, the conductivity.

In the present work we investigated boron-doped $a$-Si:H films deposited on $c$-Si and quartz glass substrates, as well as structures of the type $c$-Si/$p^+$-$a$-Si:H(B)/$p$-$a$-Si:H(B)/$a$-SiC. The films and structures were grown by deposition in the plasma of an rf glow discharge with substrate temperatures $T_s = 300 - 320$ °C. The boron density in the $a$-Si:H(B) layers studied was equal to $5 \times 10^{17} - 1 \times 10^{19}$ $cm^{-3}$ and was measured by secondary-ion mass spectrometry (SIMS). The absorption spectra were measured on structures and films with a $c$-Si substrate and the reflection spectra were measured on films with a quartz-glass substrate.

The optical spectra were obtained with a Bruker fast-scan IFS-113 v IR Fourier spectrometer with a resolution of 0.5 $cm^{-1}$ in the experimental wave number range 1000–4000 $cm^{-1}$. In a number of cases the measurements were performed by accumulating a signal and averaging over 1024 spectra. The absorption spectra of the $a$-Si:H layers in the structure were obtained by subtracting from the total spectrum the structure of the spectrum from the $c$-Si(B) substrate and the spectrum from the protective $a$-SiC layer, which were measured separately. Strong interference effects appeared in the absorption spectra of the structures and in the reflection spectra of the $a$-Si:H(B) films on quartz. They were taken into account by using the well-known relations to simulate interference.[5] The optical spectrum of the $a$-Si:H(B) layers which was analyzed was obtained after subtracting the simulated curve from the experimental data.

Figure 1 shows the absorption spectrum of the structure (solid line). The spectrum was obtained by subtracting out the spectra of the substrate ($c$-Si) and protective layer ($a$-SiC) and taking into account interference [the thickness and boron density in the $p^+$ and $p$ layers of $a$-Si:H(B) were as follows: $d_1 = 0.1$ $\mu$m, $d_2 = 5$ $\mu$m, $N_{B1} = 1 \times 10^{19}$ $cm^{-3}$, and $N_{B2} = 5 \times 10^{17}$ $cm^{-3}$]. We see from the figure that strong absorption occurs in the spectral region $\nu = 1800 - 2200$ $cm^{-1}$. The spectrum shown in Fig. 1 can be represented as a sum of several vibrational modes. These modes can be approximated by four Gaussians with different amplitudes and different half-widths. They are represented in Fig. 1 by dashed lines. Their maxima occur at the frequencies 2090, 2003, 1879, and 1848 $cm^{-1}$. The sum of these four Gaussians corresponds to the experimental curve. The spectral po-

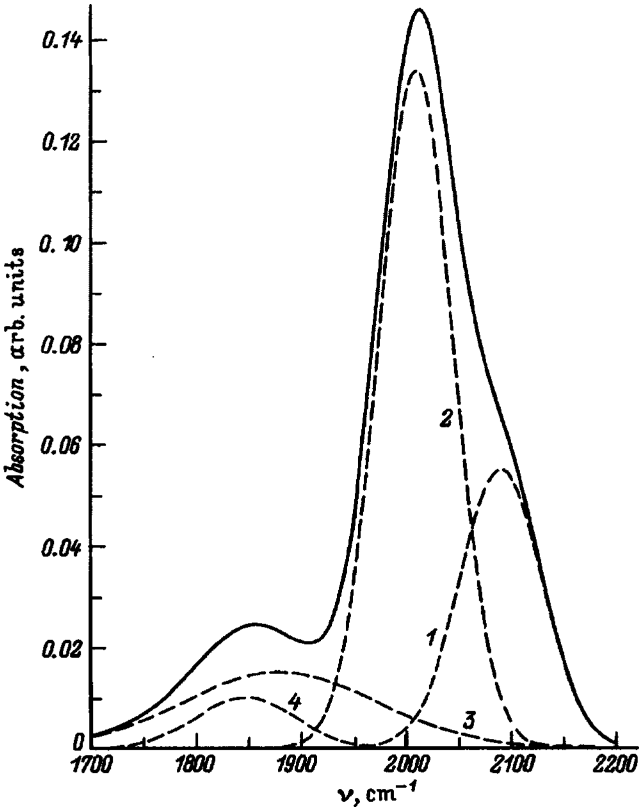

FIG. 1. Typical experimental absorption spectrum of the structure $p^+/p$ based on $a$-Si:H(B) (solid line) and four Gaussians into which this spectrum is decomposed (dashed lines). Positions of the maxima of the Gaussians $\nu$, cm$^{-1}$: *1* — 2090, *2* — 2003, *3* — 1879, *4* — 1848.

sitions of the first and second maxima (2090 and 2003 cm$^{-1}$) are due to absorption by vibrational stretching modes of the Si–H$_2$ and Si–H bonds.[6] The third and fourth maxima (1879 and 1848 cm$^{-1}$) coincide with the observed absorption peaks in the spectrum of the $a$-Si:H(B) films (film thickness $d = 1$ $\mu$m, boron density $N_B = 2 \times 10^{18}$ cm$^{-3}$) on the $c$-Si substrate (Fig. 2). In Fig. 2 the position of these peaks is shown by arrows for clarity. This absorption spectrum was obtained by subtracting out the substrate spectrum and taking into account the interference. We note that the ratio of the amplitudes of the absorption peak corresponding to the stretching mode of the Si–H bond with $\nu = 2003$ cm$^{-1}$ to the amplitude of the observed absorption peaks exceeds 100. Thus, the contribution of the observed modes to absorption is quite small and their observation was made possible only by the advantages of Fourier spectroscopy.

Figure 3 shows the reflection spectra of $a$-Si:H(B) films on quartz-glass substrates ($d = 1$ $\mu$m, $N_B = 2 \times 10^{18}$ cm$^{-3}$). The spectrum *1* corresponds to the control film, and the spectra *2* and *3* correspond to films annealed at temperatures $T_a = 360$ and 335 °C, respectively. The spectrum *3* can be represented as a sum of two Gaussians (dashed lines) with maxima at $\nu_3 = 1879$ cm$^{-1}$ and $\nu_4 = 1848$ cm$^{-1}$, the same as the positions of the maxima in the experimental spectra represented by curves *1* and *2*. The dashed line corresponds to a curve which is a sum of these two Gaussians. One can see from the figure that this curve is identical to the spectrum 3.

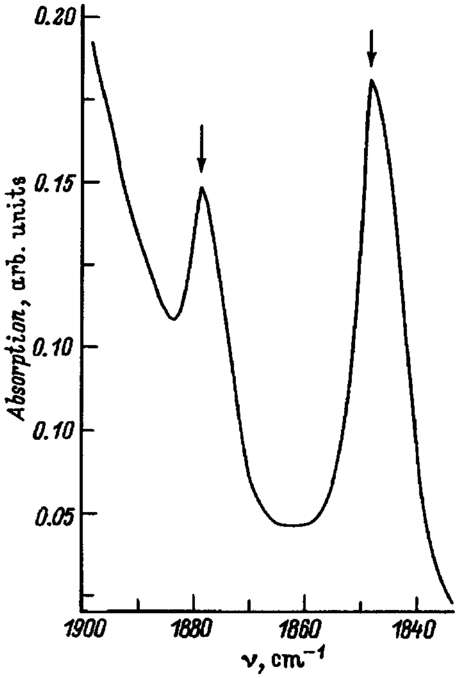

FIG. 2. Absorption spectrum of an $a$-Si:H(B) film. The spectrum was obtained after the $c$-Si substrate spectrum was subtracted out and the interference was taken into account. The arrows show the positions of the absorption maxima: 1879, 1848 cm$^{-1}$.

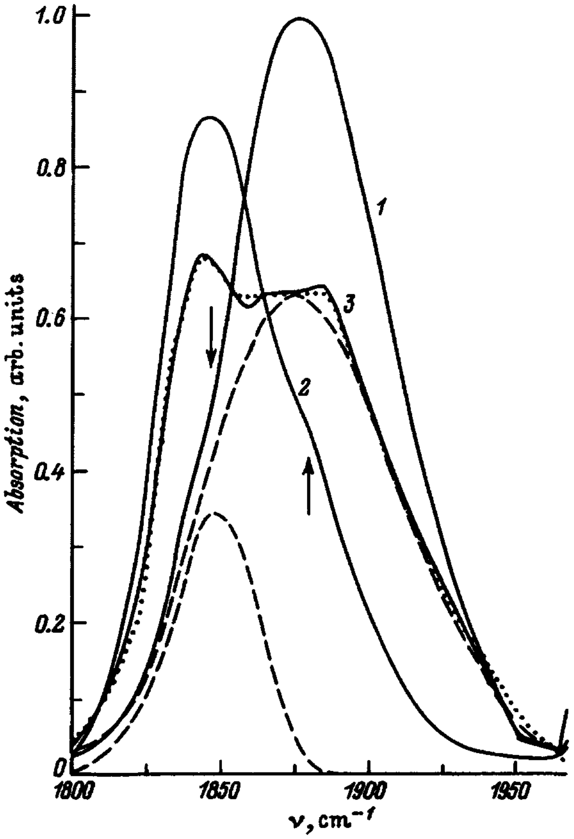

FIG. 3. Absorption spectrum of nonannealed (*1*) and annealed at temperatures 360 °C (*2*) and 335 °C (*3*) $a$-Si:H(B) films on quartz-glass substrates. The arrows show the position of the hidden absorption peaks in the spectra *1* and *2*. The dashed lines shows the position of two Gaussians into which spectrum *3* is decomposed; the dotted line shows sum of the Gaussians.

Moreover, the arrows show the presence of weak peaks which are present in spectra *1* and *2*. The spectral positions of the peaks correspond to the frequencies 1848 and 1879 $\mathrm{cm}^{-1}$; i.e., the main absorption in the spectrum of the control (nonannealed) film occurs at the frequency 1879 $\mathrm{cm}^{-1}$, while in the case of the film annealed at the maximum temperature (360 °C) the main absorption occurs at the frequency 1848 $\mathrm{cm}^{-1}$. The shift of the absorption maxima of $a$-Si:H(B) films into the IR region upon annealing can be explained by a change in the ratio of the amplitudes of their constituent modes with maxima at $\nu_3$ and $\nu_4$. Annealing increases the amplitude of mode *4* and decreases the amplitude of mode *3*. In the case of an intermediate annealing temperature ($T_a = 335$ °C) both modes are clearly seen in the optical spectrum.

According to the published data, the absorption peaks at $\nu_3 = 1879$ $\mathrm{cm}^{-1}$ and $\nu_4 = 1848$ $\mathrm{cm}^{-1}$ have not been previously observed in the optical spectra of $a$-Si:H and $a$-Si:H(B) layers. However, they have been observed in the polarized IR spectra of liquid and crystalline diborane $B_2H_6$ (Ref. 7). According to Ref. 7 , these modes are due to the presence of bridging hydrogen (1879 $\mathrm{cm}^{-1}$) and boron–boron type bonds (1848 $\mathrm{cm}^{-1}$). The vibrational modes, similar to those occurring in crystalline and liquid diborane, which we observed in the optical spectra of the $a$-Si:H(B) material, could indicate clustering of boron and hydrogen. As a result, structural bonds of the type occurring in diborane molecules form in $a$-Si:H(B). The mode *3* is due to the presence of weakly bound bridging hydrogen. At an annealing temperature $T_a = 360$ °C these bonds change, specifically, as a result of the diffusion of weakly bound hydrogen. For this reason, the intensity of the vibrations of mode *3* decreases, while the intensity of the vibrations of the mode associated with boron (mode *4*) increases.

In summary, vibrational modes with $\nu_3 = 1879$ $\mathrm{cm}^{-1}$ and $\nu_4 = 1848$ $\mathrm{cm}^{-1}$, not previously described in the literature, were observed in the optical spectra of all experimental $a$-Si:H(B) layers. The presence of these modes indicates clustering of boron and hydrogen and the presence of bridging hydrogen in a system consisting of a three-center bond with silicon and boron atoms, as well as bonds of the type B–B. It was determined that when the $a$-Si:H(B) films are annealed, the amplitudes of these modes change as a result of structural rearrangements of the bonds: decrease in the concentration of weakly bound bridging hydrogen and increase in the concentration of electrically active boron atoms, which determine mode *4*.

This work was supported by the Russian Fund for Fundamental Research, Project 96-02-18853.

*)Fax: (095)4387664; e-mail: abelog@glas.apc.org

---

[1] G. L. Kong, D. L. Zhang, J. P. Zhao, and X. B. Liao, Solid State Phenom. **44-46**, 677 (1995).
[2] S. C. Shen and M. Cardona, Phys. Rev. B **23**, 5322 (1981).
[3] J. I. Pankove, P. S. Zanzucchi, and C. W. Magee, Appl. Phys. Lett. **46**, 421 (1985).
[4] I. A. Kurova, A. N. Lupacheva, N. N. Meleshko *et al.*, Semiconductors **28**, 628 (1994).
[5] M. Cardona, *Modulation Spectroscopy*, Academic Press, N. Y., 1969.
[6] G. Lucovsky, R. S. Nemanich, and S. C. Knight, Phys. Rev. B **19**, 2064 (1979).
[7] I. Freund and R. S. Halford, J. Chem. Phys. **43**, 3795 (1965).

Translated by M. E. Alferieff

SEMICONDUCTORS VOLUME 32, NUMBER 5 MAY 1998

## PHYSICS OF SEMICONDUCTOR DEVICES

# Charge-carrier exclusion and accumulation intensified by ohmic contacts

V. K. Malyutenko, G. I. Teslenko, and V. V. Vaĭnberg

*Institute of Semiconductor Physics, Ukrainian National Academy of Sciences, 252028 Kiev, Ukraine*

(Submitted August 29, 1997; accepted for publication October 14, 1997)
Fiz. Tekh. Poluprovodn. **32**, 634–637 (May 1998)

The effect of the high generation-recombination power of an ohmic contact ($S$ contact) on exclusion–accumulation processes in structures with an antiblocking contact (asymmetric structures of the type $p^+-p-S$) was studied theoretically and experimentally. It is shown that, in contrast to the ordinarily studied symmetric structure $p^+-p-p^+$, the asymmetric structures, which is being studied, forms a region of accumulation or exclusion, depending on the direction of the current. The nonequilibrium carrier density in the accumulation layer is much higher while the exclusion region is longer than in the symmetric structure. A density $n$ 100 times higher than the equilibrium value $n_0$ was obtained experimentally for Ge at 300 K. The length of the exclusion region reached 96% of the sample length. Applications of structures with antiblocking and ohmic contacts based on narrow-gap materials are proposed. © *1998 American Institute of Physics.* [S1063-7826(98)02505-8]

### 1. INTRODUCTION

An electric field $E_x$ in a semiconductor crystal with antiblocking contacts at the ends (for definiteness, we consider the structure $p^+-p-p^+$) gives rise to a substantial redistribution of charge carriers $(n,p)$ in the longitudinal direction. As a result of bipolar carrier drift in the field $E_x$, a large portion of the base, comparable in size to the bipolar drift length $L_E$, is depleted of electron-hole pairs (exclusion). At the same time, a pair accumulation region, comparable in size to the bipolar diffusion length $L_d$ ($L_E \gg L_d$), appears at one of the $p^+$ contacts. This redistribution is especially large in semiconductors whose conductivity is close to the intrinsic value ($n_0$, $p_0 \cong n_i \gg N_a$, where $N_a$ is the density of noncompensated acceptors).

The extended high-resistance exclusion region determines mainly the characteristic features of current flow in the $p^+-p-p^+$ structure, and for this reason it has been investigated for a long time and in detail (see the review in Ref. 1). It has been established that the free charge-carrier density $n=p$ in this region can be easily one or two orders of magnitude lower than the equilibrium value $n_0 \cong p_0$. The exclusion effect has been used to determine the parameters of an electron-hole plasma,[2] decrease the response time of photodetectors,[3] and produce unconventional sources of radiation.[4]

There is less information about the parameters of the accumulation region. This is apparently due to the very low enrichment levels, which are of no practical interest compared with the injection phenomenon. It was shown recently[5,6] that a large increase in carrier density in the accumulation layer near the small-radius contact should be expected in $p^+-p-p^+$ structures with an exotic geometry (cylindrical and spherical). The effect is obviously due to the geometric factor.

In the present paper we examine the possibility of a large increase in charge carrier density in the accumulation region for a crystal with the classical rectangular square geometry. The accumulation effect is investigated in the presence of an ohmic ($S$) contact in the crystal ($p^+-p-S$ structure). By definition, as a result of thermal generation, the equilibrium carrier density $n_0=p_0$ should be preserved at an ohmic contact for any value of the current $j$. For this reason, in the presence of carrier drift toward the $p^+$ contact an ohmic contact will become an efficient source of nonequilibrium charge carriers. In our study we investigated, both theoretically and experimentally, the charge-carrier distributions in the base and the density of charge carriers in the accumulation layer, as well as the current-voltage characteristics (IVCs) of $p^+-p-S$ structures.For comparison, the same measurements were also performed on the standard $p^+-p-p^+$ structures. The experiments were conducted on pure $p$-Ge at room temperature. The unavoidable errors arising in the asymptotic solutions of the nonlinear continuity equation are eliminated by solving the problem numerically.

### 2. BASIC RELATIONS

We are studying a square semiconductor crystal with almost intrinsic conductivity ($p_0-n_0=N_a \ll n_i$) with base length $d$ ($0<x<d$) much longer than the diffusion length $L_d$. Generation–recombination processes on the side faces are ignored. It is assumed that bipolar diffusion-drift processes in the base do not lead to the appearance of a volume charge, and this fact is reflected by the quasineutrality equation

$$p=n+N_a. \tag{1}$$

The contacts used to apply an external electric field $E_x$ to the base of the structure can be of two types: In the standard situation the crystal is bounded on the faces by two $p^+-p$ junctions (symmetric structure) and in the other case an ohmic contact is present in the $x=d$ plane (asymmetric structure). Junctions of the type $p^+-p$ are treated as sharp potential barriers; we neglect space charge regions in them. It is also assumed that the carrier density on the ohmic contact remains at the equilibrium level for arbitrary currents.

The spatial distribution of the nonequilibrium charge-carrier density $n(x)$ is found from the continuity equation

$$D\frac{d^2n}{dx^2}+\mu_E E_x\frac{dn}{dx}=\frac{n-n_0}{\tau}, \tag{2}$$

where

$$D=\frac{n\mu_n D_p+p\mu_p D_n}{p\mu_p+n\mu_n}, \quad \mu_E=\frac{\mu_p\mu_n(p-n)}{p\mu_p+n\mu_n},$$

$$\tau_n=\tau_p=\tau=\text{const.}$$

Equation (2) is supplemented with boundary conditions for symmetric (3′) and asymmetric (3″) structures

$$j_n|_{x=0,d}=0\rightarrow D\left.\frac{dn}{dx}\right|_{x=0,d}=\frac{j}{e}\left.\frac{\mu_n n}{p\mu_p+n\mu_n}\right|_{x=0,d}, \tag{3′}$$

$$j_n|_{x=0}=0, \quad n|_{x=d}=n_0. \tag{3″}$$

The condition (3′) reflects the smallness of the electronic current through the $p^+-p$ contact, while the second condition (3″) corresponds to an ohmic contact at $x=d$.

We also use the expression for the total current density in the structure:

$$j=j_n+j_p=en\mu_n E_x+D_n\frac{dn}{dx}+ep\mu_p E_x-D_p\frac{dp}{dx}, \tag{4}$$

from which we obtain an expression for the field $E_x$

$$E_x=\left[\frac{1}{e}j+(D_p-D_n)\frac{dn}{dx}\right]\Big/(p\mu_p+n\mu_n). \tag{5}$$

The total voltage in the base is determined as

$$V=\frac{j}{e}\int_0^d\frac{dx}{p\mu_p+n\mu_n}+\int_0^d\frac{(D_p-D_n)\frac{dn}{dx}}{p\mu_p+n\mu_n}dx. \tag{6}$$

To solve the problem numerically are used the standard parameters of Ge at 300 K: $\mu_n=3800$ cm$^2$/(V·s), $\mu_p=1800$ cm$^2$/(V·s), $D_n=98$ cm$^2$/s, $D_p=47$ cm$^2$/s, $n_0=n_i=2.34\times10^{13}$ cm$^{-3}$, $d=1$ cm, and $\tau=100$ and 300 $\mu$s. The computational results are presented in Figs. 1–3.

## 3. EXPERIMENT

The experiment was performed at room temperature for long ($d\gg L_d$) $p$-type Ge samples with uncompensated acceptor density $N_a\cong10^{12}$ cm$^{-3}$ ($n_i\gg N_a$). The IVCs and the longitudinal charge-carrier distribution in the base were measured. An antiblocking contact was produced by fusing-in In in a hydrogen atmosphere at 500 °C and an ohmic contact was established by fusing-in pure Sn. To decrease the effect of surface generation-recombination processes, the free faces were etched in $H_2O_2$. According to our measurements, the effective charge-carrier lifetime $\tau$ did not exceed 100 $\mu$s. An electric field (constant-voltage regime) in the form of 500-$\mu$s square pulses was applied to the samples. The absence of Joule heating was specially monitored. The sample dimensions were 11.4×5.7×2.8 mm.

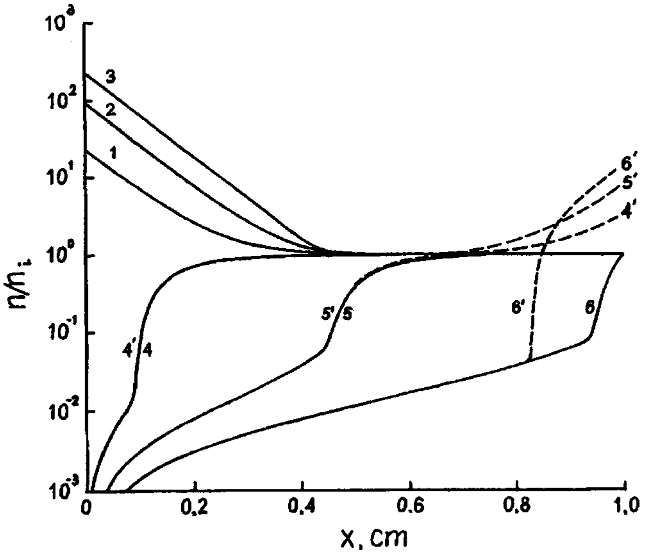

FIG. 1. Calculation of the longitudinal electron-hole pair density distribution in $p^+-p-S$ (solid lines *1–6*) and $p^+-p-p^+$ (dashed lines *4′*, *5′*, *6′*) structures with $\tau=100$ $\mu$s. Current density, mA/cm$^2$: *1* — 20; *2* — 100; *3* — 1000; *4, 4′* — 10; *5, 5′* — 30; *6, 6′* — 60.

The electron-hole pair distribution $n(x)$ along the base of the structures was investigated by the standard method of probing in the IR region of the spectrum beyond the intrinsic absorption edge of the material ($\lambda=2-10$ $\mu$m) in a direction perpendcular to the current lines. The width of the IR probe did not exceed 200 $\mu$m, and the scanning step was equal to 250 $\mu$m. The radiation transmitted through the crystal was detected with a cooled Ge:Au photodetector. It was assumed

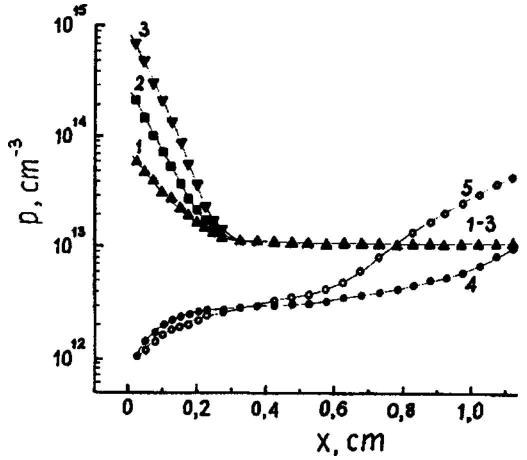

FIG. 2. Experimental data on the longitudinal free-carrier density distribution in $p^+-p-S$ (curves *1–4*, ohmic contact on the right-hand side) and $p^+-p-p^+$ (curve *5*) structures. Current density, mA/cm$^2$: *1* — 31, *2* — 103, *3* — 400, *4* — 23, *5* — 28.

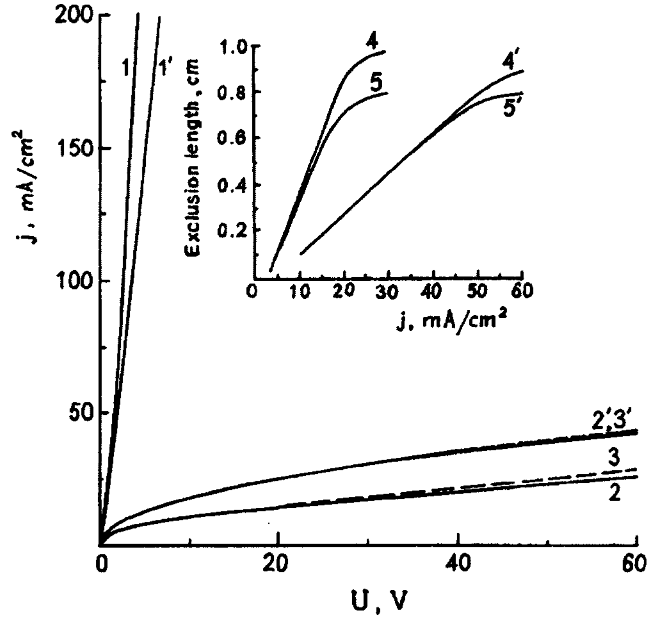

FIG. 3. Calculation of the current–voltage characteristics of $p^+-p-p^+$ (*3, 3'*) and $p^+-p-S$ (*1, 1'* and *2, 2'*) structures. *1, 1'* — accumulation regime; *2, 2'* — exclusion regime. Inset: Exclusion length versus current for $p^+-p-p^+$ (*5, 5'*) and $p^+-p-S$ (*4, 4'*) structures. The curves *1'* — *5'* correspond to $\tau=100$ $\mu$s ($d/L_d=12.5$); *1–5* — $\tau=300$ $\mu$s ($d/L_d=7.2$).

that the signal in the strong exclusion regime with $U=30$ V near the $p^+-p$ contact corresponds to complete extraction of the minority carriers (electrons) $\Delta n=\Delta p=n_0$.

## 4. RESULTS AND DISCUSSION

We now turn to the calculations of the spatial distribution of the minority charge carriers $n(x)$, presented in Fig. 1. The results for a symmetric structure (curves *4'*, *5'*, *6'*, carrier drift toward the contact $x=d$) confirm the characteristic features that are well-known from the asymptotic solutions of the problem. The accumulation region arising at the $p^+-p$ contact at $x=d$ is localized in a region with a length of the order of $L_d$. An exclusion region almost devoid of minority carriers arises at the opposite contact at $x=0$. The length of the exclusion region$^{1)}$ increases as the current (see the inset in Fig. 3), while the size of the accumulation region remains nearly constant. When the sign of the field $E_x$ changes, an accumulation region appears at the contact $x=0$ (not shown in Fig. 1). It is interesting to note that, as follows from the nature of the antiblocking contacts, the total number of charge carriers in the crystal is conserved under exclusion–accumulation conditions. This follows from the balance equation

$$\int_0^d [n(x)-n_0]dx=0, \tag{7}$$

which is obtained from the continuity equation (2) with the boundary conditions (3'). It is thus easy to estimate the maximum electron-hole pair density in the accumulation layer as $n(d)/n_0 \cong d/L_d$. For our case it should be expected that $n(d)/n_0 \cong 10$, which corresponds to the exact calculation (Fig. 1, curve *6'*).

A different picture arises in the asymmetric structure. First and foremost, the carrier distribution becomes asymmetric relative to the sign of $E_x$. In the presence of drift toward the ohmic contact the exclusion region extends over a larger region than in the case of the symmetric structure — virtually over the entire crystal, whereas the accumulation region is absent (Fig. 1, curves *4–6*). Thus, in the entire volume of the base the carrier density drops below the equilibrium value. The total number of carriers in the crystal, as one can easily see, decreases with increasing $E_x$. Conversely, for drift in the opposite direction there is no exclusion region, since the ohmic contact ''maintains'' the charge-carrier density in the base at the equilibrium value $n_0$. As a result, an accumulation region with carrier density higher than in the symmetric structure (curves *1–3*) forms near the $p^+$ contact, and the total number of carriers in the crystal increases with $E_x$. Using the relations (2) and (3'), we obtain$^{2)}$ in this case the following expression from the balance equation:

$$\int_0^d n(x)dx=n_0 d+\frac{j\tau}{e(1+\mu_p/\mu_n)}. \tag{8}$$

The experimental charge-carrier distributions shown in Fig. 2 qualitatively confirm the results presented above. Indeed, in an asymmetric structure the charge-carrier density in the accumulation layer is 15 times higher than in a symmetric structure (see curves *3* and *5*) with the same voltage $U=30$ V. There is virtually no density change at the ohmic contact. This indicates that the contact is of good quality.

We note that the increase in density above the equilibrium density by the amount $dn/n_0 \approx 10^2$ obtained experimentally in the asymmetric structure is high enough for considering practical applications of the accumulation effect. As follows from Fig. 2, the charge-carrier density near an antiblocking contact can be varied over a range of almost three orders of magnitude.

Let us now examine the characteristic features of the IVCs (see Figs. 3 and 4). In a symmetric structure for both current directions the well-known law $j\sim\sqrt{V}$, which is a consequence of the appearance and expansion of the exclusion region, is satisfied, while in an asymmetric structure the form of the IVC is sensitive to the sign of the applied field $E_x$. A carrier drift toward to the ohmic contact gives rise to the formation of an exclusion region in the base, which gives $j\sim\sqrt{V}$. The IVC of the structure with a $S$ contact is characterized by a lower current than in the case of a symmetric structure, since the total number of carriers decreases with increasing current, while the exclusion region is longer (see curves *4* and *5* in the inset in Fig. 3). The effect is especially noticeable in structures with a shorter base (lower value of $d/L_d$). According to our estimates, the exclusion length in an asymmetric structure reaches 0.96 cm as compared with 0.8 cm in a symmetric structure with $d/L_d=7.2$ and $j=30$ mA/cm$^2$. For the opposite direction of current flow a substantial portion of the crystal remains undisturbed and the accumulation layer decreases the total conductivity of a long crystal. As as result, the IVC becomes slightly superlinear. It

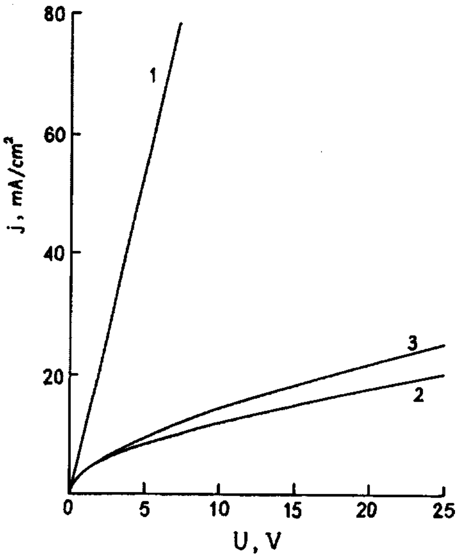

FIG. 4. Experimental current-voltage characteristics of $p^+-p-S$ (*1, 2*) and $p^+-p-p^+$ (*3*) structures.

is natural to expect the superlinearity of the IVC to be greater in a structure with a shorter base (Fig. 3, curves *1* and *1′*).

## 5. CONCLUSIONS

Exclusion–accumulation effects in a semiconductor with antiblocking contacts and almost intrinsic conductivity manifest qualitatively new features if one of the antiblocking contacts is replaced by an ohmic contact. Depending on the direction of charge-carrier drift, an ohmic contact is a region of effective generation or recombination of charge carriers. As a result, either accumulation or exclusion can be obtained in a $p^+-p-S$ structure. In the first case (drift toward the $p^+$ contact) an accumulation region with a higher carrier density than in the case of two antiblocking contacts appears in the sample. Such a situation could be helpful for producing modulators and IR-range emitters. Especially timely is the use of $S$ contacts as a method for ''pumping'' in narrow-gap semiconductors (InSb,HgCdTe) at high temperatures, where the standard injection method with the aid of a $p–n$ junction becomes inefficient because of the high rate of thermal generation of carriers.

In the exclusion regime an extended depletion region arises in the sample and the equilibrium carrier density is maintained only in a narrow layer adjoining the ohmic contact. Such a deep-depletion regime can be recommended for use in semiconductor solar coolers.[8]

This work was supported in part by the Ukrainian Science and Technology Center (Grant No. 394).

[1)] The exclusion length is defined as the distance from the $p^+-p$ junction to the point corresponding to a sharp decrease in the field $E_x$ at the boundary of the depleted region.[7]

[2)] The expression (8) for the total number of nonequilibrium carriers in the base is valid only for ''long'' structures, $d \gg L_d$.

---

[1] V. K. Malyutenko, Semicond. Sci. Technol. **8**, S390 (1993).
[2] A. G. Kollyukh, V. K. Malyutenko, and A. M. Rybak, Zh. Prikl. Spektrosk. **50**, 801 (1989).
[3] T. Ashley and G. T. Elliot, Electron. Lett. **21**, 451 (1985).
[4] S. S. Bolgov, B. R. Vardanyan, V. K. Malyutenko, V. I. Pipa, A. P. Savchenko, and A. E. Yunovich, Fiz. Tekh. Poluprovodn. **28**, 658 (1994) [Semiconductors **28**, 394 (1994)].
[5] A. A. Akopyan, S. A. Vitusevich, and V. K. Malyutenko, Fiz. Tekh. Poluprovodn. **28**, 21 (1994) [Semiconductors **28**, 12 (1994)].
[6] A. A. Akopyan, V. K. Malyutenko, and G. I. Teslenko, Fiz. Tekh. Poluprovodn. **28**, 1479 (1994) [Semiconductors **28**, 829 (1994)].
[7] A. M. White, Infrared Phys. **25**, 720 (1985).
[8] P. Berdahl, Sol. Energy Mater. **14**, 437 (1986).

Translated by M. E. Alferieff